Dissertation
submitted to the
Combined Faculties of Natural Sciences and Mathematics
of the Ruperto-Carola-University of Heidelberg, Germany
for the degree of
Doctor of Natural Sciences

Put forward by
Sven Meyer
born in: Düsseldorf
Oral examination: June, 15th

THE EVOLUTION OF LINEAR PERTURBATIONS IN LEMAÎTRE-TOLMAN-BONDI MODELS AND THE EFFECT ON LIGHT PROPAGATION

Referees: Prof. Dr. Matthias Bartelmann
Prof. Dr. Luca Amendola

Parentibus meis et uxori et luci futurae.

ABSTRACT

Spherical void models of Gpc-scale have widely been discussed in the literature as a possible alternative to the spatially homogeneous Friedmann models with dark energy. In this framework, the local universe is modeled by an exact solution of Einstein's field equations, the so-called Lemaitre-Tolman-Bondi (LTB) metric, which constitutes a spherically symmetric spacetime that is solely filled by pressureless dust. In extension to recent multi-probe analyses of void models in a cosmological context, we study the evolution of linear, gauge-invariant perturbations on top of LTB backgrounds starting from a full spectrum of Gaussian initial conditions. The relativistic framework of perturbation theory on radially inhomogeneous spacetimes is substantially more complicated than in standard homogeneous models of FLRW type, because the spacetime is intrinsically dynamical already at first order which causes gauge-invariant perturbations to couple. As shown by Clarkson et al. in 2009 ([29]), their evolution is constrained by a system of linear partial differential equations which need to be integrated numerically. We present a new numerical scheme based on finite element methods to solve this equation system and generate appropriate scalar initial conditions in the homogeneous asymptotic limit of the LTB patch. In this context, we involve realisations of Gaussian random fields with an underlying power spectrum for the Bardeen potential. After spherical harmonic decomposition, the initial fluctuations are mapped to the corresponding LTB gauge-invariant variables and those evolved into the radially inhomogeneous LTB regime. Estimates of angular power spectra of each gauge-invariant quantity are computed as functions of redshift on the past null cone. This enables us to analyse the coupling strength in a statistical way. We find significant couplings up to 25% for large and deep voids of Gpc scale as required to fit the distance redshift relations of SNe. As a major complication, LTB gauge-invariant perturbations are abstract mathematical objects that, although in principle observable, cannot feasibly be transformed to physically meaningful quantities. We therefore adapt a relativistic framework of light propagation to perturbed LTB models that allows to map the combined contribution of gauge-invariant metric and matter perturbations to sources of the optical tidal matrix. The corresponding Sachs equation is derived for generically perturbed LTB spacetimes and numerically investigated in case of negligible perturbation coupling.

ZUSAMMENFASSUNG

Sphärische Void Modelle mit einer Ausdehnung von mehreren Gigaparsec sind ausgiebig in der Literatur diskutiert worden, da sie eine mögliche Alternative zu den standardmäßig betrachteten, räumlich homogenen Friedmann Modellen darstellen. In diesem Zusammenhang wird das lokale Universum um unsere Galaxie durch die exakte Lemaître-Tolman-Bondi Lösung der Einstein'schen Feldgleichungen beschrieben. Vorhersagen solcher Modelle sind in den letzten Jahren mit vielfältigen Beobachtungen konfrontiert worden, die jedoch weitgehend die detaillierte Information aus linearer Strukturbildung vernachlässigen oder teilweise geschickt umgehen. Als Erweiterung bisheriger Betrachtungen von Void Modellen soll in dieser Arbeit daher die vollständige Zeitentwicklung linearer, eichinvarianter Störungen der LTB Raumzeit im kosmologischen Zusammenhang untersucht werden. Relativistische Störungstheorie auf inhomogenen Raumzeiten ist erheblich komplizierter als in homogenen Modellen, da sich die gestörte Raumzeit bereits in linearer Ordnung dynamisch verhält und eichinvariante Störungen untereinander koppelt. Die einschlägige Arbeit von Clarkson u. a. aus dem Jahr 2009 zeigt, dass die Zeitentwicklung dieser Störungen durch ein System partieller Differentialgleichungen beschrieben wird, das im Allgemeinen numerisch gelöst werden muss. Zu diesem Zweck wird in der vorliegenden Arbeit ein entsprechendes Verfahren entwickelt, dass auf Methoden der finiten Elemente zurückgreift. Kosmologische Anfangsbedingungen werden im homogenen Friedmann Limit des Rückwärtslichtkegels als Gaußsches Zufallsfeld modelliert, das aus dem gut bekannten Powerspektrum des Bardeen Potentials hervorgeht. Diese Anfangsfluktuationen werden in Kugelflächenfunktionen zerlegt und dann numerisch in der Zeit entwickelt. Das Ergebnis sind Winkelpowerspektren der LTB eichinvarianten Störungen, die sich auf dem Rückwärtslichtkegel auswerten lassen. Dies ermöglicht die Berechnung der Kopplungsstärke von Störungen als statistische Größe. Im Falle tiefer und großer Voids, die zur Modellierung der Abstands-Rotverschiebungs-Beziehung von Supernovae herangezogen werden, lassen sich Kopplungsstärken von bis zu 25% feststellen. Eine besondere Schwierigkeit bei diesem Ansatz liegt in der physikalischen Interpretation der Ergebnisse. Eichinvariante Größen auf dem LTB Hintergrund sind rein physikalische Größen, allerdings sehr abstrakt nicht auf intuitive Observablen zurückführbar. Um dieses Problem zu umgehen wird eine relativistische Beschreibung für Lichtausbreitung in allgemeinen Raumzeiten herangezogen und auf gestörte LTB Modelle angewandt. In der Tat lassen sich auf diese Weise eichinvariante Größen über die Sachs-Gleichung auf Korrekturen zur Winkelentfernung abbilden. In diesem Zusammenhang werden die vollständigen Sachs-Gleichungen für ein gestörtes LTB Modell herleitet und im Fall vernachlässigbarer Kopplungen numerisch gelöst.

PUBLICATION

Some ideas and figures have appeared previously in the following publication:

Sven Meyer, Matthias Redlich, and Matthias Bartelmann. Evolution of linear perturbations in Lemaître-Tolman-Bondi void models, *arXiv:1412.3012*, December 2014, URL http://arxiv.org/abs/1412.3012, *accepted for publication in the Journal of Cosmology and Astro-Particle Physics (JCAP)*.

ACKNOWLEDGMENTS

This present work emerged from a more general project based on a DFG application that has been granted for our research group. I am very grateful to Matthias Bartelmann for providing me the opportunity to conduct this research. There have been difficult times in between for financing the position. I want to thank him for all the effort he made to get my PhD position financed till the end. Of course, I am also deeply grateful for all his advice, motivation and guide through this thesis work.

I am grateful to Luca Amendola for accepting to be the second referee and for the time he invests in correcting and grading this thesis. I also want to thank Volker Springel and Karlheinz Meier for completing my examination committee.

This work was substantially influenced by many conversations with members of the cosmology group at the ITA. I particularly want to thank Matthias Redlich for long discussions about various aspects of the project. Regarding the chapters on light propagation, I really benefited from the mathematical insight of Simon Hirscher and the long afternoons and evenings we spent with proving "only seemingly obvious" things and setting up the weak lensing formalism in a rigorous way.

I am grateful to Björn Schäfer for his advice in many ways and for the long evenings we spent discussing about fundamental physics which I really appreciated.

I want to thank Britta Zieser for pointing out and providing a very clear and efficient implementation of the Levin collocation method which substantially helped to set up appropriate initial conditions for gauge-invariant perturbations in LTB models.

I am very grateful to Peter Bastian for his remarkable helpfulness and support with the DUNE framework. In addition, I benefited from a very informative and well-organised DUNE/PDELab workshop on March 24-28, 2014 organised by the DUNE project team. Furthermore, I want to thank Martin Reinecke for help with the Healpix C++-implementation.

Since I figured out that writing long passages in academic English is still quite a challenge for me, I particularly want to thank Matthias Redlich, Eleonora Sarli, and Heike Jablonsky for proofreading parts of the initial manuscript of this thesis and for very helpful comments both in scientific and stylistic aspects.

Part of this work was supported by the German *Deutsche Forschungsgemeinschaft, DFG*, project number BA 1359 / 20-1. Most simulations were performed on the bwGRiD cluster, member of the German D-Grid initiative, funded by the Ministry for Education and Research (Bundesministerium für Bildung und Forschung) and the Ministry for Science, Research and Arts Baden-Württemberg (Ministerium für Wissenschaft, Forschung und Kunst Baden-Württemberg).

During my PhD time, I have been a member of the Heidelberg Graduate School of Fundamental Physics (HGSFP) and the International Max Planck Research school (IMPRS-HD). I want to thank both graduate schools for providing an excellent research environment including very interesting and fruitful seminars, colloquia, and discussions. I particularly acknowledge financial support from the HGSFP for the final months of my thesis work.

I am deeply grateful to my research group for the great time we spent in the past three years. I really enjoyed our coffee and lunch breaks with all the chats, jokes, and foolish things we did.

I finally want to thank a fine group of friends, my family and especially my wife for supporting me in many ways and for giving me motivation and strength when things were not working as they should. I owe many of these people more than they probably think.

CONTENTS

I MAIN PART 1

1 INTRODUCTION 3

2 GENERAL CONCEPTS 7
2.1 Summary . . . 7
2.2 General relativity and FLRW cosmology . . . 7
2.3 Essentials of gauge-invariant linear perturbation theory in FLRW models . . . 10
2.3.1 Gauge transformations and gauge invariance . . . 11
2.3.2 Scalar-Vector-Tensor decomposition . . . 12
2.4 Initial seeds and the shape of the gravitational potential power spectrum . . . 14
2.5 General concepts of gravitational lensing . . . 16
2.5.1 Relativistic approach . . . 16
2.5.2 Application to perturbed FLRW models . . . 21

3 LTB MODELS 25
3.1 Summary . . . 25
3.2 Metric ansatz and field equations . . . 25
3.3 Time evolution and properties . . . 27
3.4 Background model implementation . . . 30
3.4.1 The role of the void density profile . . . 31

4 LINEAR PERTURBATION THEORY IN LTB MODELS 33
4.1 Summary . . . 33
4.2 Overview . . . 33
4.3 Metric approach of Clarkson et al. (2010) . . . 34
4.3.1 Spherical harmonic decomposition . . . 34
4.3.2 Metric ansatz and first order field equations for the polar branch . . . 35
4.3.3 Metric ansatz and first order field equations for the axial branch . . . 37
4.3.4 Properties of perturbations in LTB models in comparison to FLRW . . . 38

5 NUMERICAL APPROACH 41
5.1 Summary . . . 41
5.2 General statements on finite elements . . . 41
5.3 The Distributed Unified Numerics Environment (DUNE) . . . 42
5.4 Grid setup and boundary conditions . . . 42
5.5 Comparison to previous results in February et al. (2014) . . . 45

6 INITIAL CONDITIONS 51
6.1 Summary . . . 51
6.2 Gaussian sampling technique in configuration space . . . 51
6.2.1 Realisation of a Gaussian random field . . . 51
6.2.2 Healpix and spherical harmonic decomposition . . . 52
6.3 Multivariate sampling from angular covariance matrices . . . 55
6.3.1 Multivariate Gaussian sampling . . . 55
6.3.2 Covariance matrix . . . 56
6.3.3 Numerical treatment . . . 57

6.3.4 Sampling process . . . 59
6.4 Spherical harmonic coefficient profiles . . . 64

7 RESULTS AND DISCUSSION 67
7.1 Summary . . . 67
7.2 Angular power spectra . . . 67
7.3 Coupling strength a function of void depth and size . . . 69
7.4 Discussion . . . 73

8 A WEAK GRAVITATIONAL LENSING FORMALISM IN PERTURBED LTB MODELS 77
8.1 Summary . . . 77
8.2 Motivation . . . 77
8.3 Light propagation in LTB spacetimes . . . 77
8.4 Complete linearised Jacobi equation in perturbed LTB spacetimes . . . 81
8.5 Solution to the uncoupled case . . . 85
8.6 Outlook . . . 87

9 CONCLUSION AND OUTLOOK 91

II APPENDIX 95

A SOLUTION TO THE SACHS EQUATION IN LTB SPACETIMES 97

B A POSSIBLE SET OF GAUGE-INVARIANT PERTURBATIONS IN LTB SPACETIMES 99

C FLRW LIMIT OF GAUGE-INVARIANT PERTURBATIONS IN LTB MODELS 103

D LOCAL OPERATORS 105

BIBLIOGRAPHY 111

LIST OF FIGURES

Figure 2.1 Illustration of the formal construction of perturbations . . . 11
Figure 2.2 Construction of a screen space for a bundle of null geodesics . . . 18
Figure 3.1 Local coordinates in a spherically symmetric spacetime . . . 25
Figure 3.2 Spatial hypersurfaces of generic LTB spacetimes . . . 28
Figure 3.3 Illustration of the construction of the density profile of a given void model . . . 30
Figure 3.4 Color plots containing the spacetime evolution of the density $\rho(t,r)$, tangential Hubble rate $H_\perp(t,r)$ and the background shear . . . 31
Figure 5.1 Finite-element-approximation of an exemplary function $f(x)$ on a global interval Ω in one dimension . . . 42
Figure 5.2 Overview on different DUNE modules and their correspondences . . . 43
Figure 5.3 Illustration of the method of lines . . . 43
Figure 5.4 Schematic construction of the artificial boundary condition according to February et al. (2014) . . . 44
Figure 5.5 Schematic structure of the irregular spatial grid . . . 45
Figure 5.6 Initial Gaussian profile as applied by February et al. (2014) . . . 46
Figure 5.7 Space-time-evolution of the LTB gauge-invariants $\{\varphi, \varsigma, \chi\}$ with initial conditions according to Eqs. (5.3) and (5.4) for two exemplary modes $\ell = 2$ and $\ell = 10$ . . . 47
Figure 5.8 Space-time-evolution of the corresponding gauge-invariant fluid perturbations $\{\Delta, w, v\}$ . . . 48
Figure 6.1 Initial Bardeen potential power spectrum . . . 52
Figure 6.2 2d slices of the 3d Gaussian realisation of the Bardeen potential fluctuations . . . 53
Figure 6.3 Illustration of the Healpix discretization scheme . . . 54
Figure 6.4 Healpix Maps in Mollweide projection at different radii . . . 55
Figure 6.5 Covariance matrix entries C_{ij}^{ℓ} . . . 60
Figure 6.6 Estimates of angular power spectra from two different sampling techniques . . . 61
Figure 6.7 Mollweide projections of Healpix Maps that are constructed from the spherical harmonic coefficients obtained from two different sampling techniques . . . 62
Figure 6.8 Consecutive Healpix Maps around a fiducial radius . . . 63
Figure 6.9 Schematic summary of all modifications performed on the initial profiles . . . 64
Figure 6.10 Examples for initial radial profiles of $\varphi^{(\ell m)}$ for exemplary ℓ- and m-modes . . . 65
Figure 7.1 Angular power spectra of the metric perturbations $\{\varphi, \varsigma, \chi\}$ evaluated on the LTB backward lightcone . . . 68
Figure 7.2 Influence on artificial modifications on the initial profile . . . 69
Figure 7.3 Coupling strength ϵ^{ℓ} for the two gauge-invariants φ and Δ for different void depths at a fixed void size . . . 71

Figure 7.4 Coupling strength ϵ^ℓ for the two gauge-invariants φ and Δ for different void extensions at fixed void depth . . . 72
Figure 7.5 Averaged coupling strength $\langle\epsilon^\ell\rangle$ as function of void depth and size for decreasing redshifts . . . 73
Figure 8.1 Numerical results on the LTB backward lightcone relations . . . 80
Figure 8.2 Numerical solution of the Sachs equation at the background level in comparison to the areal radius as function of redshift z . . . 81
Figure 8.3 Linear perturbations Δ and φ on the backward lightcone . . . 87
Figure 8.4 First order corrections to the Jacobi Map as function of redshift at angular coordinates $(\theta, \phi) = (\pi/2, 0)$ . . . 88
Figure 8.5 Numerical results on the first order corrections to the area angular diameter distance in case of negligible perturbation coupling . . . 89

LIST OF TABLES

Table 1 Tables of LTB lightcone coordinates for three exemplary void models . . . 74

ACRONYMS

GR	General Theory of Relativity
FLRW	Friedmann-Lemaître-Robertson-Walker model
LTB	Lemaître-Tolman-Bondi model
EdS	Einstein-de Sitter universe
ΛCDM	Cold Dark Matter model with cosmological constant Λ
CMB	Cosmic Microwave background radiation
PNC	Past Null Cone
kSZ	kinetic Sunyaev Zel'dovic effect
BAO	Baryon Acoustic Oscillations
FFT	Fast Fourier Transform
SVT	Scalar Vector Tensor (perturbation types)
GMG	Gundlach and Martín-García (2000)
CCF	Clarkson, Clifton, and February (2009)
RW	Regge and Wheeler (1957)
DUNE	Distributed Unified Numerics Environment
ODE	Ordinary differential equation
PDE	Partial differential equation
FE	Finite Element
CLASS	Cosmic Linear Anisotropy Solving System
Healpix	Hierarchical Equal Area and iso-Latitude pixelisation scheme

- If not explicitly stated differently in the text, we will assume natural units with $c = \hbar = 1$.
- The sign convention of the preudo-Riemannian metric is given by $(-,+,+,+)$.
- Three dimensional Fourier transforms of a generic function $f(\vec{x})$ are applied according to the convention

$$\mathcal{F}(\vec{k}) = \int \mathrm{d}^3x\, f(\vec{x})\, e^{i\vec{k}\cdot\vec{x}}\,,$$
$$f(\vec{x}) = \int \frac{\mathrm{d}^3k}{(2\pi)^3}\, \mathcal{F}(\vec{k})\, e^{-i\vec{k}\cdot\vec{x}}\,.$$

- In a three dimensional, homogeneous and isotropic space, we define the power spectrum of a generic perturbations ζ as

$$\left\langle \zeta(\vec{k})\zeta^*(\vec{k}')\right\rangle = (2\pi)^3\, P_\zeta(k)\, \delta_D^{(3)}(\vec{k}-\vec{k}')\,.$$

- We apply the following definition of the spherical harmonic functions

$$Y^{(\ell m)}(\theta,\phi) = (-1)^m \sqrt{\frac{2\ell+1}{4\pi}\frac{(l-m)!}{(l+m)!}}\, P^{(\ell m)}(\cos\theta)\, e^{im\phi}\,,$$

  with the associated Legendre polynomials given by

$$P^{(\ell m)}(x) = \frac{(-1)^m}{2^\ell \ell!}\left(1-x^2\right)^{m/2} \frac{\mathrm{d}^{\ell+m}}{\mathrm{d}x^{\ell+m}}\left(x^2-1\right)^\ell\,.$$

Part I

MAIN PART

1

INTRODUCTION

The main motivation of the work laid out in this thesis can be concisely summarised by the following question: If we want to relax the assumptions of the standard cosmological model, but remain within the framework of General Relativity, can alternative cosmological models be constructed with properties that describe the observable universe more accurately?

Certainly, the standard cosmological model is remarkably successful. Based on General Relativity (GR) and two symmetry assumptions stating that (1) the universe is, on average, spatially isotropic around our position and (2) this position in the universe is not distinct, the generic class of Friedmann-Lemaître-Robertson-Walker (FLRW) models can be constructed. These particularly simple cosmological solutions do not only generally agree with observational data, but specific models can even be singled out. Recent observations of type Ia supernovae, the cosmic microwave background, gravitational lensing and large scale structure support the spatially flat ΛCDM model that describes the observable universe extremely well on a wide range of times and spatial scales (see [8] for a review).

Despite this extraordinary success, cosmological solutions based on FLRW models come at the high prize that the energy content of the universe is dominated by two hypothetical fluid species called *dark matter* and *dark energy* which are hitherto not confirmed by any direct detection. Whereas, in the framework of GR, there are strong hints for dark matter also on sub-cosmological scales, the physical nature of dark energy remains mysterious. In fact, the unexpected faintness of type Ia supernovae and resulting need to correct the luminosity distance-redshift relation seemingly requires an additional fluid component with negative pressure which, in the framework of homogeneous and isotropic models, accounts for a global accelerated expansion at late times. However, neither the question about its fundamental origin nor about its late time dominance (coincidence problem) can be answered in a satisfactory way. Although a cosmological constant represents a natural degree of freedom in General Relativity, quantum field theory predicts its energy scale to be utterly wrong by approximately 120 orders of magnitude. On the other hand, dynamical scalar field models of dark energy assume a time dependence in its equation of state for which we have actually no significant evidence in observational data (see [31]).

This profound lack of understanding of the physical nature of dark energy stimulates attempts to investigate alternative cosmological models that question the basic assumptions with the hope that well-motivated additional degrees of freedom may help to circumvent any need for dark energy and can nonetheless account for all observational data in an equally successful way.

Since we restrict ourselves to models described by General Relativity, the two symmetry assumptions are left to be relaxed. Statistical isotropy of the universe around our position is well confirmed by measurements of the cosmic microwave background and large scale structure. Hence, questioning spatial homogeneity seems the most reasonable attempt. Indeed, this model assumption relies on the so-called *Copernican Principle* which states that, when averaged over sufficiently large scales ($\geq$ 100Mpc), we are not placed at a special position in the universe. Being mainly philosophically motivated, this principle is very difficult to test observationally since we only have direct access to measurements on our past lightcone. A priori, there is consequently no way to distinguish temporal

evolution from spatial variations where the latter have simply been excluded by assumption in the standard model.

One possible approach to test spatial homogeneity is studying *Lemaître-Tolman-Bondi* (LTB) models (see [24, 57, 89] for original works and [23, 27, 40, 65] for detailed reviews) which constitute a class of cosmological models based on a radially inhomogeneous solution of Einstein's field equations. Their spatial hypersurfaces are spherically symmetric about a distinct central worldline. In fact, these models and especially a subclass with a homogeneous Big Bang and a vanishing cosmological constant[1] represent the simplest inhomogeneous generalization of the standard model based on an exact solution of General Relativity. If our galaxy is assumed to be located in a large underdense region of Gpc scale (a so-called *void*), cosmological models built upon this class of solutions are able to fit distance-redshift relations of type Ia supernovae without any need of dark energy (see [33, 42]). However, an off-centre observer would see a significant dipole amplitude in the cosmic microwave background (CMB) which has to be in agreement with the observed signal. Our position in the void region is therefore constrained to be close to the centre within a few tens of Mpc (see [2, 44] for corresponding CMB analyses), requiring a high degree of spatial fine tuning. LTB models were rigorously confronted with observations (see [19, 22, 26, 33, 46, 68, 94, 100, 101]), and their applicability to describe the local universe around our position was recently reanalysed in detail in [75]. All analyses agree that void profiles are indeed able to successfully reproduce local distance-redshift relations of supernovae, but the resulting local Hubble rate turns out to be too small to simultaneously account for global CMB measurements. Even very flexible void profiles as applied in [75] were not able to alleviate this issue as the resulting posterior distributions of Hubble constants have negligible overlap with the locally measured value and its uncertainty distribution. Moreover, various additional cosmological probes, such as the linear kinetic Sunyaev Zel'dovic effect ([99]), Baryon Acoustic Oscillations ([101]), and galaxy age measurements ([35, 96]) were reported to be in considerable tension with the simplest void models.

Current analyses, however, are limited to observables that do not depend on the details of linear structure formation since linear perturbation theory in LTB models is quite a challenge and therefore still under development. Nevertheless, structure formation in voids has to be taken into account in full generality in order to rule out these models on a solid basis. The reason for the utter complexity of the problem is that the evolution of linear perturbations on inhomogeneous backgrounds is substantially more complicated than in spatially homogeneous FLRW models because the decomposition into gauge-invariant 3-scalar-, 3-vector- and 3-tensor modes (SVT variables) is no longer straightforwardly possible. In addition, anisotropic and position-dependent structure growth causes gauge-invariant perturbation variables to couple already at first order, which is described by a system of coupled partial instead of ordinary differential equations. However, significant progress was made in the past few years on several approaches. Alonso et al (2010) ([3]) managed to set-up a Newtonian N-body simulation in the gravitational potential of a large Gpc void and studied Newtonian perturbations by comparing the simulated results with the theoretically predicted void profile of [46]. Nishikawa et al. (2012) (see [70] and also [71, 72]) studied the evolution of density perturbations in void models by applying secondary linear perturbations on top of a primary, isotropically perturbed FLRW model that accounts for the void. Zibin (2008) (see [98] and further application in [37]) used a covariant 1+1+2 formalism for scalar perturbations in LTB spacetimes and obtained evolution equations and matter transfer functions in the so-called *silent approximation* by neglecting the magnetic part of the Weyl tensor and effectively the coupling of scalar to tensor modes.

Clarkson et al. (2009) (see [29] for a remarkable paper in this context) obtained a full set of gauge-invariant perturbation variables in spherically symmetric dust spacetimes. They present first order evolution equations given by linear partial differential equations containing the full coupling of the perturbations on inhomogeneous backgrounds. Their results build on earlier studies of gauge-invariant perturbations in general spherically symmetric configurations, using a 2+2 split of the background spacetime (see [49, 50, 51, 84] and [90] for a cosmological application). The first order field

1 These issues will be clarified in Chapt. (3)

equations were evaluated in a covariant perfect fluid frame by Gundlach & Martin-García ([54, 67]) in the context of perturbed stellar collapse. Clarkson et al. specified these equations to dust solutions and even performed the FLRW limit showing the complicated mixing of FLRW scalar, vector, and tensor degrees of freedom in each LTB gauge-invariant quantity. However, numerics of the corresponding system of partial differential equations is very challenging. In case of negligible coupling, February et al. (2013) ([43]) managed to predict the two-point density correlation function in LTB void universes. A first test run of a full numerical solution of the system was performed by February et al. (2014) ([41]). Their numerical scheme is based on combined second-order finite differencing in space and fourth-order time integration. Starting with a void profile of Gaussian shape, they ran several test cases by initialising each perturbation variable separately by five Gaussian peaks that are placed at equidistant positions in the void.

However, estimating the relevance of perturbation coupling in a realistic cosmological environment is still an unsolved issue and represents the current state of research where this thesis work is going to set in. We extend the approach of February et al. (2014) by generating realistic initial conditions and evolve the system from an initial FLRW state. By assuming the universe to be sufficiently homogeneous and isotropic at early times, we sample initial conditions from a power spectrum of the Bardeen potential Ψ in the matter-dominated era. This enables us to study the spacetime evolution of perturbations in LTB models in a statistical way by comparing angular power spectra of each gauge-invariant quantity at different redshifts on the past null cone. We developed a new numerical scheme to solve the underlying partial differential equation system based on a finite element technique for the spatial discretisation in each timestep. This approach has proven to be more flexible than finite differences, since the grid structure can easily be adapted to the problem itself. In addition, we use a numerical implementation of the LTB background model (as also applied in [75]) such that we are not limited to strictly hyperbolic background models and very flexible in the choice of the void density profile.

This overall setup allows us to perform detailed studies of the evolution of gauge-invariant perturbations in LTB models and to investigate coupling effects, which are the main distinguishing feature from the spatially homogeneous FLRW models. So far, numerical studies presented in this thesis are still restricted to a general proof of concept and therefore have not yet been applied to observationally constrained void models. This is, of course, the next important step to be performed. The reason for this restriction lies in the mathematical structure of LTB gauge-invariant perturbations which represent complicated mixings of scalar, vector and tensor modes in the FLRW limit. Although these quantities contain, by construction, only physical degrees of freedom that are principally accessible by observations, their reduction to physically meaningful variables is a highly non-trivial task and is not yet fully understood.

A general formalism for light propagation in perturbed LTB spacetimes constitutes a very promising approach to circumvent the physical interpretation of single gauge-invariants since it actually accounts for their combined effect. Certainly, metric and fluid variables appear as sources in the Sachs equation that constrains the evolution of the Jacobi Map of a bundle of null geodesics. This formalism can, in fact, be used to compute observable corrections to the angular diameter distance caused by deviations of the central observer's lightcone from isotropy. Quantifying these corrections is essential to strengthen the results from previous analyses of void models since all cosmological measurements, apart from very few exceptions, rely on observational data on the past null cone.

The thesis is organised as follows: An introductory chapter outlines very general concepts that are widely applied throughout this work. Starting with a short introduction to General Relativity and FLRW cosmology, gauge-invariant perturbations on homogeneous and isotropic backgrounds are discussed. A simple framework of light propagation in arbitrary spacetimes is outlined in some detail and exemplarily applied to perturbed FLRW models. General properties of LTB spacetimes as well as an efficient numerical implementation of these models are described in Chapt. (3). Following the metric approach of Clarkson et al. (2009), a possible set of gauge-invariant perturbations and corresponding evolution equations are subsequently introduced in Chapt. (4). The numerical treatment of

the resulting linear partial differential equation system and corresponding boundary and initial conditions are laid out at length in Chapts. (5) and (6). Chapt. (7) contains the final angular power spectra and statistical estimation of the coupling strengths which are presented and discussed in some detail. The general weak lensing formalism introduced in Chapt. (2) can now straightforwardly be applied to perturbed LTB models. Based on considerations of light propagation in the background spacetime, the full Sachs equation in perturbed LTB models is derived. For simplicity, only the case of negligible coupling has been numerically addressed so far. We present first order corrections to the angular diameter distances within this approximation and provide some overview on ongoing extensions and improvements in this field. General conclusions are drawn in Chapt. (9).

2

GENERAL CONCEPTS

2.1 SUMMARY

This introductory chapter is meant to summarize general concepts that are widely be applied throughout the present work. Starting with a short overview of General Relativity and the standard cosmological model, gauge-invariant linear perturbation theory on homogeneous and isotropic backgrounds is introduced. The main focus is set on gauge transformations and the importance of gauge invariance to construct purely geometrical linear perturbations without coordinate degrees of freedom. Analogous techniques are going to be applied to construct gauge-invariant perturbations of LTB spacetimes. The inflationary origin of cosmic structures is pointed out which leads to the final shape of the dark matter power spectrum. This is a crucial ingredient to generate initial conditions for LTB gauge-invariant quantities in the homogeneous limit. A framework of light propagation in arbitrary spacetimes is discussed in detail as it provides a valuable tool to relate abstract gauge-invariant metric perturbations to meaningful observable quantities, e. g. corrections to the angular diameter distance.

2.2 GENERAL RELATIVITY AND FLRW COSMOLOGY

The General Theory of Relativity (GR) is a metric theory of gravity and has been worked out by A. Einstein at the beginning of the 20th century. Based on the Equivalence Principle, it has proven to be remarkably successful in reproducing measurements from solar system scales to cosmological solutions. The Newtonian force representation of gravity is replaced by a spacetime that behaves dynamically and can be curved by energy and momentum distributions. This novel description of the phenomenon of gravity includes a General Principle of Relativity and allows to formulate full covariant laws of nature which makes this theory one of the most impressive achievements in physics ever made. For a generally comprehensive and well-written introduction to GR, the interested reader is referred to [39].

Since a covariant theory of gravity necessarily has to be tensorial (see [87]), its exact mathematical formulation requires concepts developed in the field of differential geometry. In comparison to special relativity, the rigid metric tensor $\eta_{\mu\nu}$ or, equivalently, the line element

$$\mathrm{d}s^2 = \eta_{\mu\nu}\mathrm{d}x^\mu \mathrm{d}x^\nu \tag{2.1}$$

are replaced by a dynamical field $g_{\mu\nu}(x^\alpha)$ that characterises spacetime as a four dimensional pseudo-Riemannian manifold $\mathcal{M}$. Mathematically, a spacetime is therefore described by the pair $(\mathcal{M}, g)$. Based on the Levi-Civita connection ∇, parallel transport and corresponding covariant derivatives can be introduced for adequate mathematical operations on this object. The metric field is constrained by Einstein's field equations assembling a system of ten second order, non-linear partial differential equations which can compactly be written as

$$G_{\mu\nu} + \Lambda g_{\mu\nu} = 8\pi G T_{\mu\nu}\,, \tag{2.2}$$

with the Einstein tensor

$$G_{\mu\nu} = R_{\mu\nu} - \frac{1}{2} R g_{\mu\nu} \,. \tag{2.3}$$

The Ricci tensor $R_{\mu\nu}$ and the Ricci scalar R are contractions of the Riemann tensor $R_{\mu\nu\kappa\lambda}$ that determines the curvature of spacetime in an intrinsic and coordinate invariant way[1]. The second contracted Bianchi identity states that

$$\nabla_\mu G^{\mu\nu} = 0 \,, \tag{2.4}$$

ensuring that local energy-momentum conservation $\nabla_\mu T^{\mu\nu} = 0$ is generically contained in Eq. (2.2). In words, the field equations state that spacetime curvature encoded in the Einstein tensor $G_{\mu\nu}$ is sourced by general energy and momentum distributions $T_{\mu\nu}$ in the spacetime. On the other hand, curvature "back-reacts" on the dynamics of the spacetime content which is shown in the nonlinearity of Eq. (2.2). Due to a mathematical freedom, Einstein's field equations can be augmented by a term proportional to the metric tensor that contains the so-called cosmological constant Λ. According to a remarkable theorem proven by Lovelock in 1972 (see [64]), the form of Eq. (2.2) is unique in four dimensions for very general preconditions that are well fulfilled within the framework of GR.

Because of the obvious complexity of the theory, it is hard to find proper analytical solutions of the field equations in general. However, there are two important approaches to approximate those solutions that are relevant for the work considered here.

- If strong symmetry constraints are applied to the spacetime ab initio, a general parametric ansatz for the metric and energy-momentum tensor can be constructed that, when inserted into Eq. (2.2), yields analytically solvable differential equations in the parameters. Famous examples are the Schwarzschild solution ([83]), the Friedmann-Lemaître-Robertson-Walker (FLRW) solution ([45, 58, 77, 95]), or the Lemaître-Tolman-Bondi (LTB) solution ([24, 58, 89]) which are all subclasses of the Lemaître solution ([58]).
- More complicated spacetimes can be obtained by a perturbative ansatz. By constructing small perturbations on a well-known (probably highly symmetric) background spacetime, first order linear differential equations in terms of these perturbations can be deduced. Linear perturbation theory in GR has become a valuable tool for the description of various relativistic effects like frame dragging, light-deflection or gravitational waves. In cosmology, it has been established as a standard technique for the description of structure formation in the universe at sufficiently large scales and/or early times.

While perturbative treatments of spacetimes are discussed in detail in the following section, we continue with a short overview of the FLRW solution and its application to physical cosmology. Being remarkably successful in describing the observable universe, it it is also called *standard model* of cosmology.

It has already been pointed out in the introduction that, apart from GR, the FLRW cosmological model is based on two strong symmetry assumptions which are denoted as *Cosmological Principle*:

1. When averaged over sufficiently large scales, the universe is spatially isotropic. Mathematically, a spacetime $(\mathcal{M}, g)$ will be called spatially isotropic about a point $p \in \mathcal{M}$ if there exists a congruence of time-like geodesics through p with tangent vectors u (defining worldlines of local, so-called fundamental observers) such that two vectors v_1, v_2 orthogonal to u can be transformed into each other while u, g and p are left invariant. Thus, there is no dependence of spatial directions in the description of the spacetime seen by fundamental observers.

1 The trace-free contribution $C_{\mu\nu\kappa\lambda}$ to the Riemann tensor is known as Weyl tensor and describes the non-local part of curvature. For instance, this genuinely relativistic degree of freedom affects the propagation of light rays in the spacetime as will be outlined in Sect. (2.5).

2. The position of our galaxy in the universe is not unique (*Copernican Principle*). In combination with local isotropy, the Copernican Principle implies spatial homogeneity, i. e. there exists a family of spacelike hypersurfaces Σ_t that foliate $\mathcal{M}$ in a way that two points $p, q \in \Sigma_t$ can be transformed into each other while the metric is left invariant.

It can be shown that the Cosmological Principle restricts the spatial sections of $\mathcal{M}$ to hypersurfaces of constant curvature k. In local coordinates (t, r, θ, ϕ) of fundamental observers, the most general metric ansatz can be formulated as

$$\mathrm{d}s^2 = -\mathrm{d}t^2 + a^2(t)\, h\,, \quad \text{with} \quad h = \frac{\mathrm{d}r^2}{1-kr^2} + r^2 \mathrm{d}\Omega^2\,. \tag{2.5}$$

In fact, Eq. (2.5) describes generically curved spatial sections that can isotropically expand or contract mediated by a time-dependent scale factor $a(t)$. By choosing a different radial coordinate defined by

$$\mathrm{d}w = \frac{\mathrm{d}r}{\sqrt{1-kr^2}}\,, \tag{2.6}$$

Eq. (2.5) can equivalently be written as

$$\mathrm{d}s^2 = -\mathrm{d}t^2 + a^2(t) \left(\mathrm{d}w^2 + f_\mathrm{k}^2(w) \mathrm{d}\Omega^2\right)\,, \tag{2.7}$$

with

$$f_\mathrm{k}(w) = \begin{cases} \dfrac{1}{\sqrt{k}} \sin\left(\sqrt{k}\, w\right) & , k > 0 \\ w & , k = 0 \\ \dfrac{1}{\sqrt{-k}} \sinh\left(\sqrt{-k}\, w\right) & , k < 0\,, \end{cases} \tag{2.8}$$

depending on the sign of the spatial curvature.

The most general energy-momentum tensor that is compatible with the Cosmological Principle describes a perfect fluid

$$T_{\mu\nu} = (\rho + p)\, u_\mu u_\nu + p g_{\mu\nu}\,, \tag{2.9}$$

with contributions of energy density ρ and isotropic pressure p which depend on the coordinate time only. Einstein's field equations can then be reduced to the Friedmann equations given by

$$\left(\frac{\dot{a}}{a}\right)^2 = \frac{8\pi G}{3}\rho + \frac{\Lambda}{3} - \frac{k}{a^2}\,, \tag{2.10}$$

$$\left(\frac{\ddot{a}}{a}\right) = -\frac{4\pi G}{3}(\rho + 3p) + \frac{\Lambda}{3}\,. \tag{2.11}$$

According to Eq. (2.4), local energy-momentum conservation $\nabla_\mu T^{\mu\nu} = 0$ is already contained in these equations and reduces to the continuity equation of the matter distribution

$$\dot{\rho} = -3\left(\frac{\dot{a}}{a}\right)(\rho + p)\,. \tag{2.12}$$

This equation can be closed by assuming an equation of state $p = w\rho$ where the equation-of-state parameter w either represents a constant or a function of time. The resulting solution $\rho(a)$ can then be inserted into Eq. (2.10) which is then solved for $a(t)$. Equivalently, Eqs. (2.10) and (2.11) can be closed using the equation of state and right away be solved for $a(t)$ and $\rho(t)$. By convention, we assume a scale factor of unity today. A general solution to Eq. (2.12) is then given by

$$\rho(a) = \rho^{(0)} \exp\left(-3\int_1^a \left(1 + w(a')\right)\frac{\mathrm{d}a'}{a'}\right), \tag{2.13}$$

where $\rho^{(0)}$ denotes the matter energy density at $a = 1$.

In case of a pressureless fluid, we obtain a simple mass conservation law

$$\rho(a) = \rho^{(0)} a^{-3} \tag{2.14}$$

in an isotropically expanding space.

The relative expansion rate $\dot{a}/a$ defined by Eq. (2.10) is denoted as Hubble function $H(a)$. Its value today defines the Hubble constant H_0. Conveniently, Eq. (2.10) can be slightly rewritten as

$$\begin{aligned} H^2(a) = H_0^2 E^2(a)\,, \quad \text{with} \quad E^2(a) &= \frac{8\pi G}{3H_0^2}\rho^{(0)}a^{-3} + \frac{\Lambda}{3H_0^2} - \frac{k}{a^2H_0^2} \\ &= \Omega_m^{(0)}a^{-3} + \Omega_\Lambda^{(0)} + \Omega_k^{(0)}a^{-2}\,, \end{aligned} \tag{2.15}$$

where today's relative contributions of matter, cosmological constant and curvature are effectively expressed in terms of the density parameters

$$\Omega_m^{(0)} = \frac{8\pi G}{3H_0^2}\rho^{(0)}\,, \quad \Omega_\Lambda^{(0)} = \frac{\Lambda}{3H_0^2}\,, \quad \text{and} \quad \Omega_k^{(0)} = -\frac{k}{a^2H_0^2} = 1 - \Omega_m^{(0)} - \Omega_\Lambda^{(0)}\,.$$

Eq. (2.10) can be integrated yielding

$$t = \int_1^a \frac{\mathrm{d}a}{aH} = \frac{1}{H_0}\int_1^a \frac{\mathrm{d}a'}{\sqrt{\Omega_m^{(0)}a^{-1} + \Omega_\Lambda^{(0)}a^2 + \Omega_k^{(0)}}}\,, \tag{2.16}$$

which is used to compute the global age of the universe in terms of the cosmological parameters.

One particular example of FLRW models is the so-called Einstein-deSitter (EdS) universe that will account for the asymptotic limit of the LTB void model described in Chapt. (3). It is given by a spatially flat spacetime and vanishing cosmological constant that solely constains pressureless matter (so-called dust) described by $\Omega_m^{(0)} = 1$.

2.3 ESSENTIALS OF GAUGE-INVARIANT LINEAR PERTURBATION THEORY IN FLRW MODELS

As already mentioned in the previous section, approximate descriptions of spacetimes can be obtained by perturbative solutions of Einstein's field equations. The basic idea is to impose small perturbations on top of a well-known and in most cases highly symmetric background spacetime. Taking only first order contributions to the field equations into account reduces the problem to solving a system of linear differential equations that, in many cases, is still tractable in comparison to full GR. More precisely, we assume that the full spacetime $(\mathcal{M}, g)$ is close to an averaged background spacetime $(\overline{\mathcal{M}}, \bar{g})$. This means that there exists a local coordinate system in $\mathcal{M}$ such that the metric g can be written as

$$g_{\mu\nu} = \bar{g}_{\mu\nu} + \delta g_{\mu\nu}\,, \tag{2.17}$$

where $\delta g_{\mu\nu}$ and corresponding first and second partial derivatives are assumed to be small. In fact, this construction is non-trivial as the general averaging problem of GR is not fully solved yet. However, we do not want to go into details here and assume that an admissible averaged background spacetime exists. A short discussion of this issue can be found in [38].

Correspondingly, the Einstein and energy-momentum tensor on $\mathcal{M}$ can be constructed as

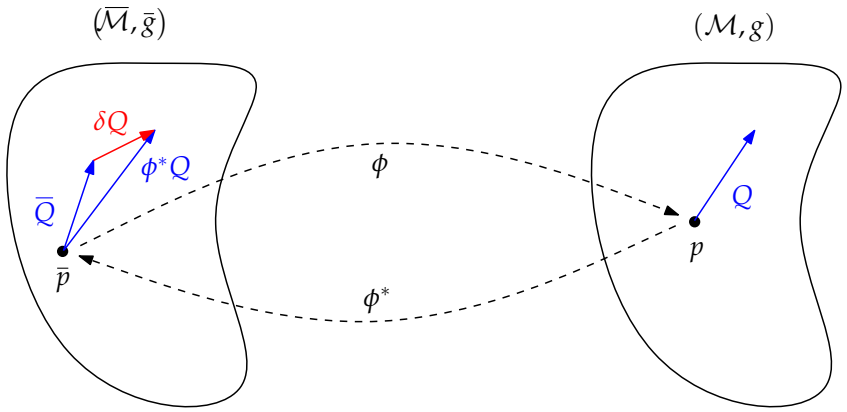

Figure 2.1: Illustration of the formal construction of perturbations using the pointwise correspondence between the perturbed and background spacetime mediated by a diffeomorphism.

$$G_{\mu\nu} = \overline{G}_{\mu\nu} + \delta G_{\mu\nu}\,, \tag{2.18}$$
$$T_{\mu\nu} = \overline{T}_{\mu\nu} + \delta T_{\mu\nu}\,, \tag{2.19}$$

with $\delta G_{\mu\nu}$ and $\delta T_{\mu\nu}$ being small as well. Einstein's field equations in the two spacetimes

$$G_{\mu\nu} = 8\pi G T_{\mu\nu}\,, \text{ and } \quad \overline{G}_{\mu\nu} = 8\pi G \overline{T}_{\mu\nu}$$

can now be subtracted from each other yielding first order equations in the perturbations

$$\delta G_{\mu\nu} = 8\pi G \delta T_{\mu\nu}\,. \tag{2.20}$$

Those generically represent a system of linear partial differential equations in the metric perturbation $\delta g_{\mu\nu}$.

2.3.1 *Gauge transformations and gauge invariance*

The subtraction of quantities that are defined on different manifolds requires a one-to-one correspondence between them. This correspondence is mediated by a diffeomorphism, i. e. a bijective, smooth map with a smooth inverse, between the perturbed and the background spacetime. Considering a fiducial diffeomorphism ϕ that maps the point $\bar{p} \in \overline{\mathcal{M}}$ uniquely to the point $p \in \mathcal{M}$, any tensor field Q defined on p can be compared to its averaged counterpart $\overline{Q}$ at $\bar{p}$ using the pull-back of Q with respect to ϕ (see Fig. (2.1)). Hence, a generic linear perturbation of $\overline{Q}$ can be constructed by subtracting both quantities correspondingly:

$$\delta Q(\bar{p}) = \phi^* Q(\bar{p}) - \overline{Q}(\bar{p})\,, \tag{2.21}$$

where, in accordance with Eqs. (2.17) - (2.19), δQ (and eventually its first and second partial derivatives) are assumed to be small with respect to $\overline{Q}$.

By construction, perturbations are then evaluated at points in background spacetime, but several equivalent descriptions exist (see [38] or [69] for reviews). A coordinate invariant treatment is discussed in [86]. Once coordinate charts are chosen in both spacetimes, the diffeomorphism also fixes the correspondence between these local coordinate systems at $\bar{p}$ and p. In this manner, the ϕ can be interpreted as a coordinate transformation between these two frames.

According to the General Principle of Relativity, the choice of local coordinates in both spacetimes is irrelevant and must not have any physical meaning. Certainly, local coordinates of the background spacetime are somehow singled out by fundamental observers that respect the given symmetry properties. We therefore fix the coordinate frame in the background spacetime. However, there exist infinitely many diffeomorphisms ϕ (and therefore local coordinate systems in the perturbed spacetime), so-called *gauges*, that lead to physically equivalent perturbations $\delta Q = \phi^* Q - \overline{Q}$ fulfilling Eq. (2.21). Hence, the quantity δQ is gauge-dependent and contains additional coordinate degrees of freedom. It is therefore crucial to be able to distinguish physical perturbations from coordinate effects. Transformations between perturbations in different gauges are defined by the correspondence between the generating diffeomorphisms. To first order, this correspondence can be mapped to infinitesimal coordinate changes $x^\mu \to x^\mu + \zeta^\mu$ in the perturbed spacetime that are mediated by a four vector field ζ^μ (see [69] for a rigorous treatment). In fact, it can then be shown that perturbations δQ_1 and δQ_2 in two different gauges are related by the Lie derivative of the background quantity along ζ^μ:

$$\delta Q_2 = \delta Q_1 + \mathcal{L}_\zeta \overline{Q} \,. \tag{2.22}$$

Equation (2.22) allows to derive explicit expressions for gauge transformations that only depend on the background quantity $\overline{Q}$. Gauge degrees of freedom of generic perturbations can directly be characterised and separated from physical degrees of freedom. This means that constructing perturbations being invariant under Eq. (2.22) effectively eliminates all dependence on the coordinate choice. This particular subclass of so-called *gauge-invariant perturbations* is essential for any physical statements deduced from linear perturbation theory as solely true geometric deviations from the background quantities are taken into account. To leading order, those gauge-invariants are given by linear combinations of gauge-dependent perturbations and derivatives thereof. However, reducing gauge-invariant perturbations to quantities that are accessible by observations becomes a non-trivial task in case of more complicated background spacetimes which will be discussed in detail when considering linear perturbation theory on top of LTB backgrounds (see Chapt. (4) and App. (B)). For spatially homogeneous and isotropic models, this construction is, in fact, simpler and will briefly be discussed in the following.

2.3.2 *Scalar-Vector-Tensor decomposition*

This section can only provide a very short summary on gauge-invariant perturbation theory in FLRW models. Detailed computations and rigorous mathematical treatment can be found in the lecture notes of Kurki-Suonio (see [88]) which are itself based on the work of Mukhanov et al. (1992) (see [69]) and the book of Liddle & Lyth (see [63]).

By introducing a conformal time τ defined by $\mathrm{d}\tau = \mathrm{d}t/a(t)$, the FLRW line element in Eq. (2.5) can be written in a more convenient form given by

$$\mathrm{d}s^2 = a^2(\tau)\left[-\mathrm{d}\tau^2 + \gamma_{ij}\mathrm{d}x^i\mathrm{d}x^j\right] , \tag{2.23}$$

where γ_{ij} denotes the comoving spatial part as obtained in Eqs. (2.5) or (2.7).

General perturbations of the metric and energy-momentum tensor can now be constructed in the formal way outlined above. We therefore obtain linear perturbations

$$g_{\mu\nu} = \bar{g}_{\mu\nu} + \delta g_{\mu\nu} \,, \tag{2.24}$$

$$T_{\mu\nu} = \overline{T}_{\mu\nu} + \delta T_{\mu\nu} \,, \tag{2.25}$$

with $\bar{g}_{\mu\nu}$ and $\overline{T}_{\mu\nu}$ describing the FLRW metric- and energy-momentum tensor. We restrict ourselves to the metric perturbations here, but fluid perturbations can be set up in an analogous way.

The local time coordinate of a fundamental observer singles out an underlying homogeneous and isotropic 3-space such that generic scalar, vector and tensor (SVT) perturbations in FLRW spacetimes are characterised by their transformation property regarding coordinate changes in that 3-space.

In a general gauge, the final metric tensor is then given by (see [29] and [88])

$$(g_{\mu\nu}) = a^2(\tau) \cdot \begin{pmatrix} -(1+2\phi) & \nabla_i B - S_i \\ \nabla_i B - S_i & (1-2\psi)\,\gamma_{ij} + 2\nabla_i\nabla_j E + 2\nabla_i F_j + h_{ij} \end{pmatrix} . \tag{2.26}$$

In fact, general metric perturbations can be decomposed into

1. Four scalars: ϕ, ψ, B, E (four degrees of freedom)
2. Two divergence-free 3-vectors: $(F_i), (S_i)$ (four degrees of freedom)
3. One divergence-free and trace-free 3-tensor: (h_{ij}) (two degrees of freedom)

Since $\delta g_{\mu\nu}$ is a symmetric tensor in four dimensions, it contains ten intrinsic degrees of freedom that have effectively been distributed over scalar, vector and tensor quantities defined on a spacelike hypersurface perpendicular to the local time direction.

By constructing the gauge transformation for the metric perturbation $\delta g_{\mu\nu}$ according to Eq. (2.22), corresponding expressions for each perturbation quantity can be deduced. It turns out that the following expressions

$$\Phi = \phi + \mathcal{H}\,(B - \partial_\tau E) + \partial_\tau\,(B - \partial_\tau E)\ , \tag{2.27}$$
$$\Psi = \psi - \mathcal{H}\,(B - \partial_\tau E)\ , \tag{2.28}$$
$$V_i = S_i + \partial_\tau F_i\ , \tag{2.29}$$

with $\mathcal{H} = \partial_\tau a/a$ are manifestly gauge-invariant (see for example Bardeen (1980) ([6]), Mukhanov et. al. (1992) ([69]), and Durrer (2005) ([38]) for detailed calculations). The tensor perturbation (h_{ij}) is automatically gauge-invariant since no gauge transformation of a symmetric traceless tensor can be generated by a vector field ζ^μ. In this manner, six physical degrees of freedom have been singled out and separated from the four coordinate degrees of freedom contained in ζ^μ. The two scalar functions Φ and Ψ are commonly known as Bardeen potentials according to Bardeen (1980) (see [6]).

There exists a particular gauge known as *longitudinal* or *conformal Newtonian gauge* where ζ^μ is fixed such that $E = B = F_i = 0$. According to Eqs. (2.27) - (2.29), perturbations in conformal Newtonian gauge directly correspond to the gauge-invariants and the line element becomes

$$\mathrm{d}s^2 = a^2(\tau)\left[-(1+2\Phi)\,\mathrm{d}\tau^2 - 2V_i\,\mathrm{d}\tau\mathrm{d}x^i + (1-2\Psi)\,\gamma_{ij} + h_{ij}\,\mathrm{d}x^i\mathrm{d}x^j\right] . \tag{2.30}$$

An important aspect to be mentioned here is that the gauge-invariant quantities have pure scalar, vector and tensor transformation properties on the underlying 3-space. Thus, transforming to gauge-invariant quantities does not mix different perturbation types. This is caused by the high degree of spatial symmetry in FLRW models. Scalar perturbations can therefore physically be interpreted as gravitational potentials, vector perturbations as velocity potentials and tensor perturbations as gravitational wave modes. However, in less symmetric models, gauge-invariant quantities are very complicated mathematical structures with non-trivial physical interpretation.

Analogously, perturbations in the energy-momentum tensor can be constructed in a gauge-invariant way and evaluated in conformal Newtonian gauge. Inserting the perturbed metric ansatz and energy-momentum tensor into Einstein's field equations yields a full system of first order evolution equations for the metric perturbations. In case of perturbed perfect fluids without anisotropic stress, this system separates into homogeneous (dynamical) equations and inhomogeneous (constraint) equations

where the latter contain source terms provided by the matter perturbations. The dynamical part decouples into separate evolution equations for scalars, vectors and tensors (see [38] and [69] for details) such that each metric perturbation type evolves independently in time and can be treated as if other perturbation types were absent. In case of a spatially flat background spacetime, perturbations are typically expanded into plane wave modes so that the evolution equations are transformed to ordinary differential equations per Fourier-mode. In absence of anisotropic stress, one then finds $\Psi = \Phi$ to first order (see [38]). Vector perturbations decay like a^{-2} in this environment whereas tensor perturbations obey a wave equation that contains a damping term due to the background expansion.

In Chapt. (4), gauge-invariant perturbations of spherically symmetric dust spacetimes will be considered which are characterised according to their transformation behaviour on $\mathcal{S}^2$. As a consequence of radial inhomogeneity, gauge-invariants are then non-trivial objects that inherently couple during spacetime evolution and are complicated mixtures of Scalar-Vector-Tensor perturbations in the FLRW limit. Since no separate treatment of perturbation variables is possible, the full linear evolution equations have to be evolved numerically. In comparison to the spatially flat FLRW case, perturbations can be expanded into spherical harmonics yielding partial differential equations in the coordinate time and radius for each angular scale ℓ and orientation m.

2.4 INITIAL SEEDS AND THE SHAPE OF THE GRAVITATIONAL POTENTIAL POWER SPECTRUM

The theory of cosmological inflation was proposed as a natural solution to disambiguities in the current cosmological model at early times which are known as horizon and flatness problem. Within this framework, the early universe undergoes a phase of exponential expansion which lasts sufficiently long to obtain a physically required increase of the scale factor by approximately 60 e-folds. Among more complicated configurations, this behaviour can be achieved by assuming the energy density of the early universe at Planck times to be dominated by a single scalar field ϕ which is commonly known as *inflaton*. Considering energy scales in this Planck era, quantum effects of ϕ are certainly important and have to be taken into account. As a consequence, quantum fluctuations of the inflaton field at the beginning of inflation are quickly driven out of causal contact and freeze in. As soon as inflation stops (which is generally described by the violation of the slow-roll conditions) it is assumed that the inflaton field can couple to ordinary matter which allows to transfer its energy density back to different constituents of the post-inflationary universe. This process is known as reheating and has not been completely understood so far. Nonetheless it states that initial seeds for the metric and matter perturbations are inherited from primordial quantum fluctuations of the inflaton field. Those perturbations then evolve in time on a homogeneous and isotropic background. Given an initial scalar metric potential Ψ, it can be shown from the vacuum expectation value of the inflaton field that (see [7])

$$k^3 P_\Psi(k) \sim \left(\frac{H^2}{\dot{\phi}}\right) \approx \text{const}\,. \tag{2.31}$$

Since density fluctuations are given by $\delta \sim k^2\Psi$ due to Poisson's equation, the initial density power spectrum obeys

$$P_{\text{ini}}(k)\, k^3\, \frac{1}{k^4} \approx \text{const} \quad \Rightarrow P_{\text{ini}}(k) \sim k^n\,, \tag{2.32}$$

with $n \approx 1$ denoting the spectral index. As perturbations generated by the inflaton field are assumed to be small, their evolution can be described by linear perturbation theory of a background FLRW model with sufficient accuracy. The high degree of spatial symmetry causes different Fourier modes to evolve independently (typically characterised by a scale-independent growth factor $D_+(a)$) and therefore density fluctuations in real space arise from superpositions of large numbers of statistically independent plane waves. According to the central limit theorem, this leads to a Gaussian random field with a vanishing mean and a variance proportional to the Fourier transform of the initial power spectrum $P_{\text{ini}}(k)$.

When inflation stops, the horizon starts shrinking and Fourier modes get into causal contact at different times depending on their wavelength. Modes that enter the horizon within the radiation dominated era experience the radiation pressure that almost completely stops their growth. Hence, small scale modes which correspond to large k-values are strongly suppressed. Large scale modes however, that get into causal contact at matter domination, are not affected by the radiation pressure and continue growing in amplitude. These effects strongly influence the shape of the density power spectrum which is mediated by a transfer function (see [4])

$$T(k,a) := \frac{D_+(a_{\mathrm{ini}})}{D_+(a)} \frac{\delta(k,a)}{\delta(k,a_{\mathrm{ini}})} \,. \tag{2.33}$$

Effectively, $T(k,a)$ relates the initial amplitude of $\delta(k)$ at a_{ini} to the final amplitude at a while excluding the growth provided by the linear growth factors. In case of smaller redshifts ($z \leq 100$), the transfer function depends negligibly on the scale factor since no significant influence of radiation pressure is present in this region.

The general form of the density power spectrum is given by

$$P(k,a) = \left(\frac{D_+(a)}{D_+(a_{\mathrm{ini}})} \right)^2 T^2(k,a) P_{\mathrm{ini}}(k) \begin{cases} \sim k & , \, a \ll a_{\mathrm{eq}} \\ \sim k^{-3} & , \, a \gg a_{\mathrm{eq}} \,, \end{cases} \tag{2.34}$$

where the asymptotic limits refer to modes that entered the horizon long before and after matter-radiation equality a_{eq}.

In general, the transfer function has to be determined numerically, but accurate analytic fitting formulae exist for various scenarios. For a universe that is dominated by cold dark matter and adiabatic initial conditions, the fitting formula developed in Bardeen et al. (1986) (see [5]) can be applied. It is given by

$$T(k) = \frac{\ln(1+2.34q)}{2.34q} \left[1 + 3.89q + (16.1q)^2 + (5.46q)^3 + (6.71q)^4 \right] \,, \tag{2.35}$$

with $q = k/\Omega_m^{(0)}\,\mathrm{Mpc}/h$.

In Fourier space, we obtain (using again Poisson's equation)

$$-k^2 \Psi(k,a) = 4\pi G \rho_b a^2 \delta(k,a) = \frac{3}{2} \frac{\Omega_m^{(0)} H_0^2}{a} \delta(k,a) \,, \tag{2.36}$$

where the definition of the matter density parameter has been applied (see Sect. (2.2)).

Hence, the potential power spectrum and its asymptotic limits are given by

$$P_\Psi(k,a) = \frac{9}{4} \frac{\Omega_m^{(0)} H_0^4}{a^2 k^4} P_\delta(k,a) \begin{cases} \sim k^{-3} & , \, a \ll a_{\mathrm{eq}} \\ \sim k^{-7} & , \, a \gg a_{\mathrm{eq}} \,. \end{cases} \tag{2.37}$$

We can define the effective potential growth factor $G_+(a) = D_+(a)/a$ such that all dependence on the scale factor is separated, yielding

$$P_\Psi(k,a_{\mathrm{fin}}) = \frac{G_+^2(a_{\mathrm{fin}})}{G_+^2(a_{\mathrm{ini}})} P_\Psi(k,a_{\mathrm{ini}}) \,, \tag{2.38}$$

that completely describes the time evolution of the power spectrum between fiducial scale factors a_{ini} and a_{fin}.

It is important to note that, in the particular case of EdS cosmology, $G_+(a) = 1$ and Ψ does not evolve in time.

In absence of anisotropic stress, the two linear Bardeen potentials are equal and can be identified with the Newtonian gravitational potential considered here. Hence, the statistics of linear scalar metric perturbations in FLRW spacetimes is Gaussian and initial fluctuations in the matter-dominated era can be constructed as a realisation of a Gaussian random field with vanishing mean and a variance given by Eq. (2.37). This procedure will be applied and discussed in detail in Chapt. (6).

2.5 GENERAL CONCEPTS OF GRAVITATIONAL LENSING

This section provides a detailed introduction to light propagation in arbitrary spacetimes starting from a bundle of null geodesics and the equation of geodesic deviation. General results are then exemplarily applied to perturbed FLRW models and linear corrections to the angular diameter distance are computed. The concepts presented in this section are essential tools for studying weak gravitational lensing in perturbed LTB models which will be laid out in detail in Chapt. (8). Derivations closely follow the approaches of Bartelmann (2010) ([9]) and Clarkson et al. (2012) ([30]) since both authors develop a relativistic formalism that can readily be adapted to spherically symmetric dust solutions of Einstein's field equations. A slightly different and more mathematically oriented treatment can be found in [73].

2.5.1 *Relativistic approach*

We consider an infinitesimal bundle of null geodesics (see [73] for an exact definition) that is propagating in an arbitrary spacetime and converges at a freely falling observer with four-velocity u_{obs}. One particular geodesic of the bundle can be singled out as a so-called *fiducial ray* and parametrised by an *affine parameter* λ. Given the observer's local coordinates x^μ, we define the ray's wave vector as

$$k^\mu = \frac{\mathrm{d}x^\mu}{\mathrm{d}\lambda} \tag{2.39}$$

and choose λ such that a unit projection of k on u_{obs} is obtained. Effectively, this corresponds to a normalisation of the wave vector by the observed frequency of the light ray. Starting from

$$\langle k, u_{\mathrm{obs}} \rangle = -\omega_{\mathrm{obs}}\,, \tag{2.40}$$

we transform $k^\mu \longrightarrow \tilde{k}^\mu = -k^\mu/\omega_{\mathrm{obs}} \equiv k^\mu$ such that

$$\langle k, u_{\mathrm{obs}} \rangle = 1\,. \tag{2.41}$$

The reason for this parametrisation is two-fold:

1. In the rest frame of the observer, an affine parameter that fulfills Eq. (2.41) corresponds to the Euclidian distance in her local neighborhood. This can be seen by direct evaluation of the projection. Given $u^\mu_{\mathrm{obs}} = (1,\,0,\,0,\,0)^T$ in the observer's local rest frame, we have

$$k_\mu u^\mu_{\mathrm{obs}} = -\frac{\mathrm{d}t}{\mathrm{d}\lambda} = 1 \;\Rightarrow -\mathrm{d}t = \mathrm{d}\lambda\,. \tag{2.42}$$

   In a freely falling frame of reference, spacetime is described by the Minkowski metric and therefore the null condition of k^μ is given by

$$k_\mu k^\mu = -\left(\frac{\mathrm{d}t}{\mathrm{d}\lambda}\right)^2 + \left(\frac{\mathrm{d}x^i}{\mathrm{d}\lambda}\right)\left(\frac{\mathrm{d}x_i}{\mathrm{d}\lambda}\right) = 0\,. \tag{2.43}$$

   Choosing spatial coordinates such that the light ray moves along one coordinate $\mathrm{d}r$ yields

$$\mathrm{d}\lambda^2 = \mathrm{d}t^2 = \mathrm{d}x^i\mathrm{d}x_i = \mathrm{d}r^2 \;\Rightarrow |\mathrm{d}\lambda| = |\mathrm{d}t| = |\mathrm{d}r|\,. \tag{2.44}$$

2. If Eq. (2.41) holds, the redshift of a fictitious source with respect to the observer can be defined as

$$\langle k, u_s \rangle = 1 + z\,, \tag{2.45}$$

where u_s denotes the source's four-velocity. By direct computation, we see

$$k_\mu u^\mu_{\text{obs}} = \frac{-\omega_{\text{obs}}}{-\omega_{\text{obs}}} = 1 \;\Rightarrow k_\mu u^\mu_s = \frac{-\omega_s}{-\omega_{\text{obs}}} = 1 + z\,. \tag{2.46}$$

In addition, the redshift of a comoving source at the observer's position is normalised to zero being physically plausible choice[2].

We now consider the spacelike plane perpendicular to k and u_{obs} which defines a screen in the rest frame of the observer. An orthonormal basis of this screen is generally given by the two vectors ${n^\mu}_a$ $(a = 1, 2)$ which are commonly referred to as *Sachs basis*. By construction, the Sachs basis vectors then fulfill the following identities[3]:

$$k_\mu {n^\mu}_a = 0\,, \tag{2.47}$$
$$u_\mu {n^\mu}_a = 0\,, \tag{2.48}$$
$$n_{\mu,a} {n^\mu}_b = \delta_{ab}\,. \tag{2.49}$$

Having set-up the Sachs basis system at $\lambda = 0$, the basis vectors at arbitrary affine parameters can be obtained by parallel transport ($\nabla_k n_a = 0$) of the initial basis system along the fiducial ray. Given the Riemannian connection, Eq. (2.47) - (2.49) are not affected by this procedure.

A general vector in the screen space can be constructed by defining a second affine parameter σ and a corresponding spacelike curve $\gamma(\sigma)$ that connects the fiducial ray with neighboring geodesics (see Fig. (2.2)). By assumption, $\gamma(\sigma)$ is entirely contained in the screen space such that the tangent vector

$$\eta^\mu = \left.\frac{\mathrm{d}\gamma^\mu}{\mathrm{d}\sigma}\right|_{\sigma=0} \tag{2.50}$$

can be expanded in the Sachs basis

$$\eta^\mu = \eta_1 {n^\mu}_1 + \eta_2 {n^\mu}_2\,. \tag{2.51}$$

For a proper choice of the affine parameter σ, η^μ measures the physical size and shape of the bundle when parallel-transported along the fiducial ray. The evolution of η^μ is given by the equation of geodesic deviation

$$k^\alpha k^\beta \nabla_\alpha \nabla_\beta \eta^\mu = {R^\mu}_{\nu\alpha\beta} k^\alpha k^\beta \eta^\nu\,, \tag{2.52}$$

containing the generic Riemann tensor of the spacetime.

We insert Eq. (2.51) into Eq. (2.52) which yields an expression for the evolution of the vector components η_a with respect to the Sachs basis. After some algebra, we obtain

2 Note that in case of FLRW models, the well-known relation of redshift to scale factor, i. e. $1 + z = a^{-1}$, can directly be inferred from Eq. (2.46) using the correspondence

$$\frac{\omega_s}{\omega_{\text{obs}}} = \frac{a(t_{\text{obs}})}{a(t_s)} \equiv \frac{1}{a(t_s)}$$

between a photon frequency emitted by a fundamental source (a source being at rest with respect to a fundamental observer at its spacetime position) at coordinate time t_s and the one received by a fundamental observer at t_{obs}.

3 We will denote the observers four velocity as u^μ in the following and drop the subscript.

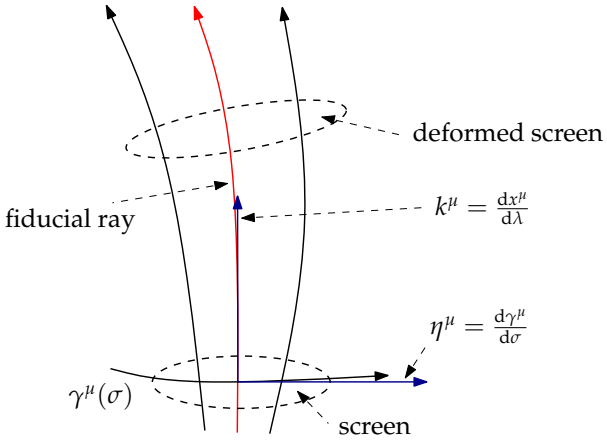

Figure 2.2: Construction of a screen space for a bundle of null geodesics: The evolution of the geodesic bundle can be mapped to the corresponding deformation of the screen when parallel-transported along the fiducial ray.

$$\frac{d^2\eta_a}{d\lambda^2} = R_{\mu\nu\alpha\beta} n^\mu{}_a k^\nu k^\alpha n^\beta{}_b \eta_b = \mathcal{T}_{ab}\eta_b\,, \tag{2.53}$$

where summation over b is implied[4]. The object $\mathcal{T}_{ab}$ is the so-called *optical tidal matrix* as it connects the evolution of the geodesic bundle with the curvature of spacetime. It can be decomposed by splitting the Riemann tensor into its trace and trace-free parts given by (see for example [87])

$$R_{\mu\nu\alpha\beta} = C_{\mu\nu\alpha\beta} + g_{\mu[\alpha}R_{\beta]\nu} - g_{\nu[\alpha}R_{\beta]\mu} - \frac{R}{3}g_{\mu[\alpha}g_{\beta]\nu}. \tag{2.54}$$

The optical tidal matrix then separates into two distinct contributions

$$\mathcal{T}_{ab} = -\frac{1}{2}R_{\alpha\beta}k^\alpha k^\beta \delta_{ab} + C_{\mu\nu\alpha\beta} n^\mu{}_a k^\nu k^\alpha n^\beta{}_b\,, \tag{2.55}$$

which define the so-called *Ricci* and *Weyl focussing* terms. The Ricci focussing originates from matter inside the bundle that causes η^μ to increase or decrease isotropically. On the other hand, the Weyl focussing is generated by matter located outside the bundle giving rise to shear effects on the screen. The role of the two different contributions will be discussed below in more detail.

Since Eq. (2.53) describes a second order linear differential equation in the affine parameter λ, any solution is constrained by two initial conditions given by the initial value and the initial first derivative of η^μ. As assumed readily at the beginning, the bundle converges at the freely falling observer placed at $\lambda = 0$ which fixes η^μ to vanish there. The final solution can therefore only depend on the initial rate $d\eta^\mu/d\lambda|_{\lambda=0}$. In case of a linear differential equation, the solution can only linearly depend on the initial conditions which yields the mapping

$$\eta_a(\lambda) = D_{ab}(\lambda)\frac{d\eta_b}{d\lambda}\bigg|_{\lambda=0}\,, \tag{2.56}$$

with the *Jacobi Map* D_{ab} that contains all information on the evolution of the geodesic bundle with respect to λ. Hence, the full initial value problem can be formulated in terms of the Jacobi Map

4 Since it turns out to be impractical to apply Einstein's sum convention for the screen coordinates, we use the convention that each screen index appearing twice implies a sum.

$$\begin{aligned} \frac{\mathrm{d}^2 D_{ab}}{\mathrm{d}\lambda^2} &= \mathcal{T}_{ac} D_{cb}\,, \\ D_{ab}|_{\lambda=0} &= 0\,, \\ \left.\frac{\mathrm{d}D_{ab}}{\mathrm{d}\lambda}\right|_{\lambda=0} &= \delta_{ab}\,, \end{aligned} \tag{2.57}$$

which is independent of the initial rate of η_a. Eq. (2.57) is a very convenient representation of the equation of geodesic deviation and is often referred to as *Sachs equation* in the literature. We have chosen the affine parameter λ to coincide with the local Euclidean distance in the observer's rest frame. Thus, the initial rate can locally be interpreted as the opening angle

$$\theta_a = \left.\frac{\mathrm{d}\eta_a}{\mathrm{d}\lambda}\right|_{\lambda=0} \tag{2.58}$$

in this particular frame. Integrating Eq. (2.57) from the observer to a fiducial source located at a position corresponding to the affine parameter λ_s leads to

$$\eta_a(\lambda_s) = D_{ab}(\lambda_s) \left.\frac{\mathrm{d}\eta_b}{\mathrm{d}\lambda}\right|_{\lambda=0} = D_{ab}(\lambda_s)\theta_b\,. \tag{2.59}$$

This means that the Jacobi Map relates cross-sectional diameters of the bundle at the source position to angular diameters at the observer which defines an angular diameter distance. Precisely, this definition only holds for infinitesimal bundles with circular cross section. In case of general elliptical cross sections, D_{ab} can be diagonalised yielding two extremal angular diameter distances $D_+(\lambda_s)$ and $D_-(\lambda_s)$. In fact, a circular image of angular size θ seen by an observer has an elliptical cross-section with main axes $|D_\pm(\lambda_s)| \cdot \theta$ at the source position (see [73] for details). Therefore, the angular diameter distance shall be replaced by the so-called area distance that relates the cross-sectional area of the lightbundle at the source position to the solid angle seen by the observer. Involving the geometric interpretation of the determinant, the area distance can be defined as (see [30, 73])

$$D_A(\lambda_s) = \sqrt{(\det D_{ab})(\lambda_s)} = \sqrt{D_+(\lambda_s) D_-(\lambda_s)}\,. \tag{2.60}$$

Due to its general applicability, this definition will be considered as angular diameter distance in the following. D_A is an important physical quantity as it can directly be inferred from observations. Once a physical length scale of a particular source is known, the opening angle can be measured and D_A readily estimated. On the other hand, D_A is related to the Jacobi Map which is itself a solution to the Sachs equation. It is therefore sensitive to the spacetime geometry due to the Weyl and Ricci focussing terms in the optical tidal matrix. Effects of gauge-invariant perturbations of the background spacetime can therefore be mapped to a physically meaningful observable. This is a most welcome property in case of more abstract gauge-invariants such as those appearing in LTB perturbation theory (see Chapt. (4)).

The Jacobi Map can be related to the Jacobian matrix A_{ab} of the lens mapping (see [9]) which is also denoted as *lensing amplification matrix*. We recover again Eq. (2.58) since it defines the angle under which a source is seen at the observer's position. The angular position β_a of the source without focussing effects is given by

$$\beta_a = \frac{\eta_a(\lambda_s)}{\overline{D}_A(\lambda_s)}\,, \tag{2.61}$$

where $\overline{D}_A(\lambda_s)$ is the area angular diameter distance of a background spacetime in which focussing effects due to perturbations are studied. If all focussing effects are taken into account, $\overline{D}_A$ will trivially be given in Minkowski spacetime. For cosmological applications, $\overline{D}_A$ expresses angular distances in FLRW or, respectively, LTB spacetimes. When combining Eqs. (2.59) and (2.61), we obtain the lens

map that relates the angular position of the source to the observed angular position due to focussing effects:

$$\beta_a = \frac{\eta_a(\lambda_s)}{\overline{D}_A(\lambda_s)} = \frac{D_{ab}(\lambda_s)}{\overline{D}_A(\lambda_s)}\theta_b = A_{ab}(\lambda_s)\theta_b. \tag{2.62}$$

Hence, the lensing amplification matrix is generally expressed as

$$A_{ab}(\lambda) = \frac{D_{ab}(\lambda)}{\overline{D}_A(\lambda)}\,, \tag{2.63}$$

which can be decomposed into a trace and trace-free part

$$(A_{ab}) = \begin{pmatrix} 1-\kappa & 0 \\ 0 & 1-\kappa \end{pmatrix} - \begin{pmatrix} \gamma_1 & \gamma_2 \\ \gamma_2 & -\gamma_1 \end{pmatrix}. \tag{2.64}$$

The convergence and shear coefficients are then given by

$$\kappa = 1 - \frac{1}{2}\frac{D_{11}+D_{22}}{\overline{D}_A}\,, \tag{2.65}$$

$$\gamma_1 = \frac{1}{2}\frac{D_{22}-D_{11}}{\overline{D}_A}\,, \tag{2.66}$$

$$\gamma_2 = -\frac{1}{2}\frac{D_{12}+D_{21}}{\overline{D}_A}\,, \tag{2.67}$$

that also determine the lensing magnification to be the inverse determinant of A

$$\mu = \frac{1}{|\det A|} = \frac{1}{(1-\kappa)^2 - \gamma_1^2 - \gamma_2^2}\,. \tag{2.68}$$

The general effect of Ricci and Weyl focussing on the geodesic bundle can be illustrated by a slightly different, but equivalent description of the equation of geodesic deviation. We start with ansatz

$$\frac{\mathrm{d}\eta_a}{\mathrm{d}\lambda} = \left(\hat{\theta}\delta_{ab} + \hat{\sigma}_{ab}\right)\eta_b\,, \tag{2.69}$$

that introduces the so-called Sachs optical scalars $\hat{\theta}$ and $\hat{\sigma}$ (see [79] for the original work and [25] for a cosmological application). Physically, Eq. (2.69) means that any change of the Sachs basis components of a vector in screen space can either be caused by isotropic focussing $\hat{\theta}$ of the bundle or by anisotropic distortion mediated by $\hat{\sigma}$. The optical scalars are therefore referred to as convergence and shear which should not be confused with the weak lensing expressions of convergence and shear introduced above. However, both sets of variables can be directly related as shown in [30].

Inserting Eq. (2.69) into the equation of geodesic deviation and separating convergence and shear contributions yields, after some computation,

$$\frac{\mathrm{d}\hat{\theta}}{\mathrm{d}\lambda} + \hat{\theta}^2 + \hat{\sigma}_{ab}\hat{\sigma}^{ab} = -\frac{1}{2}R_{\alpha\beta}k^\alpha k^\beta\,, \tag{2.70}$$

$$\frac{\mathrm{d}\hat{\sigma}_{ab}}{\mathrm{d}\lambda} + 2\hat{\theta}\hat{\sigma}_{ab} = C_{\alpha\beta\gamma\delta}n^\alpha{}_a k^\beta k^\gamma n^\delta{}_b\,. \tag{2.71}$$

These expressions are equivalent to Eq. (2.53) and show explicitly that changes in the convergence $\hat{\theta}$ along the fiducial ray are caused by the Ricci focussing whereas the shear $\hat{\sigma}_{ab}$ is sourced by the non-local Weyl focussing term.

2.5.2 *Application to perturbed FLRW models*

The concepts laid out in the previous section can now readily be applied to perturbed FLRW models which sketches the standard approach for solving the Sachs equation in a cosmological context. Derivations are again closely related to methods discussed in Bartelmann (2010) ([9]).

We start from a perturbed FLRW metric introduced in Sect. (2.3.2),

$$\mathrm{d}s^2 = a^2(\tau)\left[-(1+2\Psi)\mathrm{d}\tau^2 + (1-2\Psi)(\mathrm{d}w^2 + f_k(w)^2\mathrm{d}\Omega^2)\right], \tag{2.72}$$

and a pure dust-filled spacetime with $T_{\mu\nu} = \rho(\tau)u_\mu u_\nu$. For simplicity, we restrict ourselves to scalar perturbations mediated by the Bardeen potential Ψ.

Since the spacetime can be split into a background contribution and a linear perturbation, the linear optical tidal matrix and Jacobi Map can be split in a similar way:

$$\mathcal{T}_{ab} = \mathcal{T}^{(0)}_{ab} + \mathcal{T}^{(1)}_{ab}, \tag{2.73}$$

$$D_{ab} = D^{(0)}_{ab} + D^{(1)}_{ab}. \tag{2.74}$$

Precisely, the full first order correction to the background Jacobi Map additionally involves a perturbation in the affine parameter $\lambda \to \lambda_0 + \delta\lambda$. However, this contribution is neglected as conceptually only perturbations in the spacetime, but not in the screen and wave vectors are taken into account. This particular approximation will be discussed below.

Inserting Eqs. (2.73) and (2.74) into the full Sachs equation and separating the background and first order contributions yield

$$\frac{\mathrm{d}^2 D^{(0)}_{ab}}{\mathrm{d}\lambda} = \mathcal{T}^{(0)}_{ac} D^{(0)}_{cb}, \tag{2.75}$$

$$\frac{\mathrm{d}^2 D^{(1)}_{ab}}{\mathrm{d}\lambda} = \mathcal{T}^{(1)}_{ac} D^{(0)}_{cb} + \mathcal{T}^{(0)}_{ac} D^{(1)}_{cb}. \tag{2.76}$$

We start solving the Sachs equation for the background FLRW model and use the results to construct a formal solution to the first order equation. An important simplification to realize is that a space of constant curvature leads to a vanishing Weyl tensor and therefore only Ricci focussing has to be considered at the background level. By taking Einstein's field equations into account, we obtain

$$\begin{aligned}
\frac{\mathrm{d}^2 D^{(0)}_{ab}}{\mathrm{d}\lambda} &= -\frac{1}{2} R_{\mu\nu} k^\mu k^\nu \delta_{ac} D^{(0)}_{cb} \\
&= -4\pi G \left(T_{\mu\nu} - \frac{1}{2} g_{\mu\nu} T\right) k^\mu k^\nu D^{(0)}_{ab} \\
&= -4\pi G \left(\rho\langle k, u\rangle + \frac{1}{2}\rho\langle k, k\rangle\right) \\
&= -4\pi G\rho \cdot (1+z)^2 = -4\pi G\rho_0 \cdot (1+z)^5 .
\end{aligned} \tag{2.77}$$

The high degree of symmetry of the FLRW spacetime allows to derive a particularly simple relation between the affine parameter and the lightcone coordinates of radial null geodesics. Combining the null condition $k^\mu k_\mu = 0$ and the definition of redshift $k^\mu u_\mu = 1 + z = a^{-1}$ yields

$$|\mathrm{d}\tau| = |\mathrm{d}w|, \ |\mathrm{d}\lambda| = a^2|\mathrm{d}\tau| \quad \Rightarrow \quad |\mathrm{d}\lambda| = a^2|\mathrm{d}w| = a^2|\mathrm{d}\tau|, \tag{2.78}$$

which allows to transform between these quantities in a trivial way. We want to stress that this is a particular simplification in FLRW models which does not hold for radially inhomogeneous LTB backgrounds.

The LHS of Eq. (2.77) can now be expressed in terms of the comoving radius w:

$$\frac{\mathrm{d}^2 D^{(0)}_{ab}}{\mathrm{d}\lambda^2} = \frac{1}{a^2}\frac{\mathrm{d}}{\mathrm{d}w}\left(\frac{1}{a^2}\frac{\mathrm{d}}{\mathrm{d}w}D^{(0)}_{ab}\right) = \frac{1}{a^4}\left(\frac{\mathrm{d}^2 D^{(0)}_{ab}}{\mathrm{d}w^2} - 2\left(\frac{a'}{a}\right)\frac{\mathrm{d}}{\mathrm{d}w}D^{(0)}_{ab}\right), \tag{2.79}$$

where $a' \equiv \mathrm{d}a/\mathrm{d}w$ on the observer's backward lightcone. Involving Friedmann's equations (see Eqs. (2.10) and (2.11)) on the lightcone, namely

$$a'^2 = \frac{8\pi G}{3}\rho_0 a + \frac{\Lambda}{3}a^4 - ka^2\,, \text{ and} \tag{2.80}$$

$$a'' = \frac{4\pi G}{3}\rho_0 - ka + \frac{2\Lambda}{3}a^3\,, \tag{2.81}$$

yields

$$\frac{\mathrm{d}^2 D^{(0)}_{ab}}{\mathrm{d}\lambda^2} = \frac{1}{a^3}\left(\frac{\mathrm{d}^2}{\mathrm{d}w^2}\left(\frac{D^{(0)}_{ab}}{a}\right) - \frac{kD^{(0)}_{ab}}{a} + 4\pi G\rho_0\frac{D^{(0)}_{ab}}{a^2}\right). \tag{2.82}$$

Thus, the zeroth order Jacobi map simplifies to

$$\left(\frac{\mathrm{d}^2}{\mathrm{d}w^2} + k\right)\left(\frac{D^{(0)}_{ab}}{a}\right) = 0\,, \tag{2.83}$$

which is trivially solved by

$$D^{(0)}_{ab}(w) = a(w)f_k(w)\delta_{ab}\,. \tag{2.84}$$

This result is physically meaningful since light rays propagating in homogeneous and isotropic spacetimes experience an isotropic Ricci focussing that depends on the sign of the spatial curvature and the background expansion.

The first order equation can now be simplified using the results derived so far. One particular approximation applied here is the fact that deflection angles along the line of sight are small and therefore linear corrections to the Jacobi Map can be computed by integrating along the unperturbed light ray. This so-called *Born approximation* is consistent with the assumption of small gravitational potentials Ψ and is typically very accurate (see [16, 81]). One particular consequence is that perturbations in the affine parameter can be neglected. In fact, this has already been applied in Eq. (2.76) as this equation has been expressed in terms of the background affine parameter λ. Eqs. (2.76) and (2.83) can now be combined to a simplified expression

$$\left(\frac{\mathrm{d}^2}{\mathrm{d}w^2} + k\right)\left(\frac{D^{(1)}_{ab}(w)}{a}\right) = a(w)f_k(w)\mathcal{T}^{(1)}_{ab}(w)\,. \tag{2.85}$$

We can formally derive a solution to this equation by applying the Green's function $G(w-w')$ of the linear operator $\mathcal{L} = (\mathrm{d}^2/\mathrm{d}w^2 + k)$ given by (see [9]):

$$G(w-w') = \frac{1}{\sqrt{k}}\sin\left(\sqrt{k}(w-w')\right)\Theta(w-w') = f_k(w-w')\Theta(w-w')\,. \tag{2.86}$$

The first order solution to the Sachs equation can therefore be obtained by the integral

$$D^{(1)}_{ab}(w) = \int_0^w a(w')f_k(w')\mathcal{T}^{(1)}_{ab}(w')f_k(w-w')\,\mathrm{d}w'\,. \tag{2.87}$$

Assuming that perturbations are well-localised, meaning that their spatial extent is much smaller than the curvature scale of the background universe, the first order Ricci and Weyl focussing terms assemble

$$\mathcal{T}^{(1)}_{ab} = -2\partial_a\partial_b\Psi\,, \tag{2.88}$$

where ∂_x indicates a partial derivative along the Sachs basis vector n_x. Given the isotropy of the background spacetime, the area distance is, in fact, trivial and obtained by $D_A(w) = a(w)f_k(w)$. Thus, within the approximations discussed here, the full solution to the Sachs equation in perturbed FLRW spacetimes is given by

$$D_{ab}(w) = D_A(w)\delta_{ab} - 2\int_0^w f_k(w-w')D_A(w')\partial_a\partial_b\Psi\,\mathrm{d}w'\,. \tag{2.89}$$

Physically, this expression describes the first order correction to the angular diameter distance sourced by the Bardeen potential tidal field perpendicular to the fiducial ray. In case of perturbed LTB spacetimes, the derivation is analogous, but technical complications occur as the transformation between lightcone coordinates and the affine parameter is only given by linear differential equations and no analytical Green's function of the background Sachs equation can be found. This enforces a numerical solution of Eq. (2.76). Detailed computations and numerical results on light propagation in perturbed LTB spacetimes are presented in Chapt. (8) where the concepts introduced in this section are readily applied.

3

LTB MODELS

3.1 SUMMARY

The present chapter contains an overview of the Lemaître-Tolman-Bondi (LTB) solution and its cosmological application. Basic properties of these models are reviewed that are essential for the understanding of the propagation of linear perturbations on radially inhomogeneous backgrounds. The particular LTB realisation applied throughout this analysis requires additional, restrictive assumptions that can be motivated in a cosmological context. Accordingly, only a subclass of LTB solutions with homogeneous Big Bang and asymptotic FLRW limit are considered. The final setup and practical implementation of the background LTB model is laid out in the final section.

3.2 METRIC ANSATZ AND FIELD EQUATIONS

The Lemaître-Tolman-Bondi solution is a radially inhomogeneous dust solution of Einstein's field equations with spatial hypersurfaces being spherically symmetric about a central worldline. Spherical symmetry means that the full manifold $(\mathcal{M}, g)$ contains the isometry group $SO(3)$ such that the group orbits are two-dimensional spacelike hypersurfaces represented by two-spheres (see [87] for a detailed and rigorous construction of general spherically symmetric spacetimes). For each point $p \in \mathcal{M}$, we select the group orbit $\Omega(p)$ (the intersecting two-sphere) and consider all possible geodesics emerging perpendicular to that group orbit. This yields a set $N(p)$ which can be characterised by two coordinates (t, r). On the group orbits themselves, we choose coordinates (θ, ϕ) that coincide with the polar and azimuthal angles on the two-sphere (see Fig. (3.1)). In fact, this allows to construct a full set of local coordinates (t, r, θ, ϕ) such that the metric g can be written as

$$g = \tilde{g} + R^2(t, r)\left(\mathrm{d}\theta^2 + \sin^2\theta \mathrm{d}\phi^2\right) , \tag{3.1}$$

with a conformal factor $R(t, r)$. At fixed t and r, this factor is defines the area $S = 4\pi R^2$ of the corresponding spherical hypersurface. It is therefore referred to as *areal radius*.

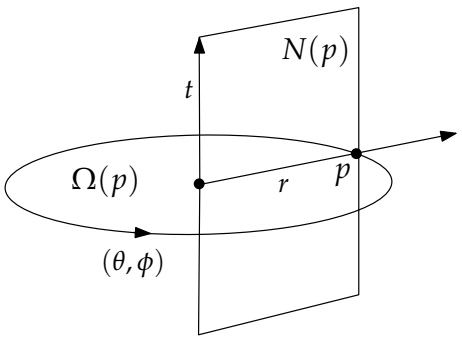

Figure 3.1: This sketch illustrates the choice of local coordinates for a point p in a spherically symmetric spacetime.

The form of Eq. (3.1) indicates that the manifold $\mathcal{M}$ can be foliated into orbits of $SO(3)$, e. g. $\mathcal{M} = \mathcal{M}^2 \times S^2$ where $\mathcal{M}^2$ denotes an arbitrary pseudo-Riemannian manifold. It can be shown (see [87]) that, without loss of generality, $\tilde{g}$ can be written as

$$\tilde{g} = -e^{2a(t,r)}\mathrm{d}t^2 + e^{2b(t,r)}\mathrm{d}r^2\,, \tag{3.2}$$

with free functions $a(t,r)$ and $b(t,r)$. Hence, the general line element for the description of a spherically symmetric spacetime is given by

$$\mathrm{d}s^2 = -e^{2a(t,r)}\mathrm{d}t^2 + e^{2b(t,r)}\mathrm{d}r^2 + R^2(t,r)\left(\mathrm{d}\theta^2 + \sin^2\theta\,\mathrm{d}\phi^2\right)\,. \tag{3.3}$$

The fact that the spherically symmetric spacetime is filled with pure dust allows further simplifications. We consider an ideal fluid with vanishing pressure, that leads to a particularly simple energy-momentum tensor (see also Eq. (2.9)), i. e.

$$T_{\mu\nu} = \rho(t,r)u_\mu u_\nu\,, \tag{3.4}$$

with a density field ρ and a four-velocity field u which both obey spherical symmetry. We change the time coordinate t for u being proportional to ∂_t which is always possible as u is timelike. In order to keep the normalisation ($\langle u,u\rangle = -1$), we have $u = e^{-a}\partial_t$. In the next step, we absorb the exponential in the definition of the time coordinate which is non-trivial as it may introduce off-diagonal metric components in the (t,r)-part of the metric. Thus, we obtain

$$\tilde{g} = -\mathrm{d}t^2 + g_{tr}\,\mathrm{d}t\mathrm{d}r + g_{rr}\,\mathrm{d}r^2\,. \tag{3.5}$$

Local energy-momentum conservation $\nabla_\mu T^{\mu\nu} = 0$ reduces to the expression $\nabla_u u = 0$ which, by construction of $u = \partial_t$, immediately implies

$$\Gamma^r_{tt} = \partial_t g_{tr} = 0\,. \tag{3.6}$$

The off-diagonal metric component is therefore time-independent. Thus, we choose new coordinates (t',r') defined by

$$t' = t + \int g_{tr}(r)\mathrm{d}r, \quad r' = r\,, \tag{3.7}$$

in which the metric ansatz reduces to the particularly simple form (dropping the primes)

$$\mathrm{d}s^2 = -\mathrm{d}t^2 + e^{2b(t,r)}dr^2 + R^2(t,r)\mathrm{d}\Omega^2\,, \tag{3.8}$$

with $\mathrm{d}\Omega^2 = \mathrm{d}\theta^2 + \sin^2\theta\,\mathrm{d}\phi^2$. Physically, these coordinates single out specific observers that are comoving with the dust fluid and have the same eigentime regardless of their spatial position. The latter coordinate frame is called *synchronous* (see [74] for details).

The given metric ansatz can be inserted into Einstein's field equations that give rise to four non-trivial expressions:

$$\frac{1}{R^2} + \frac{\dot{R}^2}{R^2} + \frac{2\dot{R}\dot{b}}{R} - e^{-2b}\frac{R'^2}{R^2} + 2e^{-2b}\frac{R'b'}{R} - 2e^{-2b}\frac{R''}{R} = 8\pi G\rho\,, \tag{3.9}$$

$$-\frac{1}{R^2} - \frac{\dot{R}^2}{R^2} - 2\frac{\ddot{R}}{R} + e^{-2b}\frac{R'^2}{R^2} = 0\,, \tag{3.10}$$

$$-\frac{\ddot{R}}{R} - \frac{\dot{b}\dot{R}}{R} - \dot{b}^2 - \ddot{b} - e^{-2b}\frac{b'R'}{R} + e^{-2b}\frac{R''}{R} = 0\,, \tag{3.11}$$

$$e^{-b}\left(-\frac{\dot{b}R'}{R} + \frac{\dot{R}'}{R}\right) = 0\,, \tag{3.12}$$

where $\dot{()}$ and $()'$ denote derivatives with respect to the LTB time and radial coordinates. Eq. (3.12) can readily be cast into

$$\partial_t \left(e^{-b} R' \right) = 0 \,. \tag{3.13}$$

This expression can be integrated while, for reasons that will be clarified below, we choose the corresponding free radial integration function to be $\sqrt{1+2E(r)}$. In this manner, we obtain

$$e^{2b} = \frac{R'^2}{1+2E(r)} \,, \tag{3.14}$$

which fixes the metric ansatz in Eq. (3.8) to be

$$\mathrm{d}s^2 = -\mathrm{d}t^2 + \frac{R'^2(t,r)}{1+2E(r)} \mathrm{d}r^2 + R^2(t,r) \mathrm{d}\Omega^2 \,. \tag{3.15}$$

The remaining three field equations now contain information on the space-time evolution of the areal radius and can effectively be reduced to two independent equations. We identify the expression

$$m(t,r) := R + R\dot{R}^2 - e^{-2b} R R'^2 \,, \tag{3.16}$$

such that the Eqs. (3.9) and (3.10) can be transformed to

$$m'(t,r) = 8\pi G \rho R^2(t,r) R'(t,r) \,, \tag{3.17}$$

$$\dot{m}(t,r) = 0 \,. \tag{3.18}$$

It can then be shown that Eq. (3.11) does not represent an independent degree of freedom as it is trivially fulfilled for generic solutions to Eqs. (3.17) and (3.18).

From Eq. (3.18), we see that $m = m(r)$ yielding

$$m(r) = 8\pi G \int_{r_0}^{r} \rho R^2 R' \, \mathrm{d}r = \int_{R_0}^{R} 8\pi G \rho \tilde{R}^2 \, \mathrm{d}\tilde{R} \,. \tag{3.19}$$

Due to the similarity of Eq. (3.19) to a mass profile of a spherical configuration, the function $m(r)$ is called active gravitational mass[1]. Inserting Eq. (3.14) into the original expression of the active mass in Eq. (3.16) yields an expression for the time evolution of the areal radius:

$$m(r) = \dot{R}^2 R - 2ER \Rightarrow \frac{\dot{R}^2}{R^2} = \frac{m}{R^3} + \frac{2E}{R^2} \,, \tag{3.20}$$

which is similar to the first Friedmann equation in the case of a spatially homogeneous and isotropic solution. In fact, dust FLRW solutions with scale factor $a(t)$ and constant spatial curvature k are a subclass of LTB solutions as they are described by the special choice of $R(t,r) = r\,a(t)$ and $2E(r) = -kr^2$.

3.3 TIME EVOLUTION AND PROPERTIES

In the following, we apply an equivalent notation for the LTB ansatz that turns out to be more convenient in the context of linear perturbation theory and can be motivated by the FLRW limit just mentioned. In fact, we introduce three functions

$$a_\perp(t,r) = R(t,r)/r \,, \quad \kappa(r) = -2E(r)/r^2 \,, \text{ and } \quad M(r) = 2m(r)/r^3 \,, \tag{3.21}$$

1 It should be mentioned that $m(r)$ is a priori an auxiliary function and its exact interpretation depends on the choice of gauge for the areal radius $R(t,r)$. However, as will be clarified below, $R(t,r)$ can be gauged in a way that $m(r)$ coincides with the mass contained in a sphere of radius r.

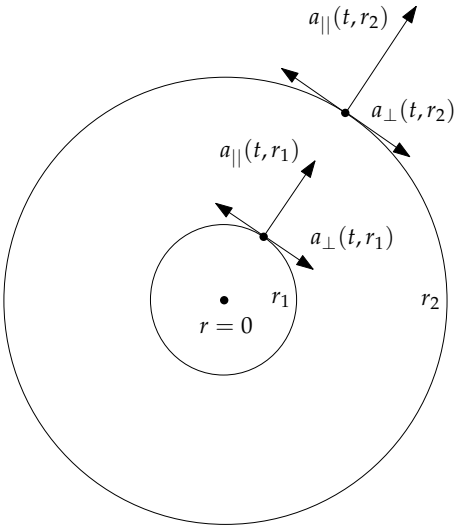

Figure 3.2: This sketch shows two exemplary spherical shells at radial coordinates r_1 and r_2. Each spherical shell has a different time evolutions as well as radial and tangential scale factor.

such that the LTB line element transforms into

$$\mathrm{d}s^2 = -\mathrm{d}t^2 + \frac{a_\parallel^2(t,r)}{1-\kappa(r)r^2}\mathrm{d}r^2 + r^2 a_\perp^2(t,r)\mathrm{d}\Omega^2\,, \tag{3.22}$$

with $a_\parallel(t,r) = (r a_\perp(t,r))'$.

In this particular notation proposed by Clarkson (2012) ([27]), differences with respect to the spatially homogeneous FLRW models can directly be identified and interpreted in a physical context. Since the LTB solution is constructed to be spherically symmetric about a central worldline, these models are isotropic around this centre and anisotropic everywhere else. This off-centre anisotropy causes the FLRW scale factor $a(t)$ to be replaced by two scale factors $a_\parallel(t,r)$ and $a_\perp(t,r)$ expressing the expansion parallel and perpendicular to the radial direction. The two scale factors induce two Hubble rates

$$H_\perp(t,r) = \frac{\dot{a}_\perp(t,r)}{a_\perp(t,r)}\,, \quad H_\parallel(t,r) = \frac{\dot{a}_\parallel(t,r)}{a_\parallel(t,r)}\,, \tag{3.23}$$

that depend on the time and radial position. In addition, there exists a radially dependent curvature profile $\kappa(r)$. As a consequence, the spatial sections of the LTB spacetime consist of spherical shells characterised by the radial coordinate r that each experience a different time evolution and a different radial and tangential expansion rate (see Fig. (3.2)). Spacetime anisotropy can be quantified by the normalised shear (see ([48])) which is given by the deviation of the radial from the tangential Hubble rate weighted by the total expansion in tangential and radial directions:

$$\epsilon = \frac{H_\parallel(t,r) - H_\perp(t,r)}{H_\parallel(t,r) + 2H_\perp(t,r)}\,. \tag{3.24}$$

Equation (3.17) for the active mass transforms into

$$\frac{(M(r)r^3)'}{r^2 a_\perp^2(t,r)a_\parallel(t,r)} = 8\pi G\rho(t,r) \tag{3.25}$$

and the time evolution of the scale factor $a_\perp(t,r)$ in terms of mass and curvature profile is constrained by

$$H_\perp^2(t,r) = \frac{M(r)}{a_\perp^3(t,r)} - \frac{\kappa(r)}{a_\perp^2(t,r)}\,. \tag{3.26}$$

In fact, this equation can be integrated to

$$t - t_B(r) = \int_0^{ra_\perp} \frac{\mathrm{d}(r\tilde{a}_\perp)}{\sqrt{-2\kappa(r)r^2 + \frac{2M(r)}{r\tilde{a}_\perp}}}\,, \tag{3.27}$$

with an integration constant $t_B(r)$ that is known as *bang time function* in the literature. General LTB models allow for inhomogeneous Big Bangs as shells of different radial coordinates r can reach zero scale factor at different times. However, for consistency with the standard inflationary paradigm, we decided to drop this additional degree of freedom and assume a synchronous Big Bang by setting $t_B(r) = 0$ for all radii. It can be shown (see [85, 100]) that fluctuations in the bang time function lead to decaying modes in the density and curvature contrast of an asymptotic, linearly perturbed FLRW regime. Physically, this results in large inhomogeneities at early times which would be highly inconsistent with the observed remarkable uniformity of the CMB last scattering surface. Hence, we require the LTB solution to be asymptotically embedded into a FLRW model at large radii and early times. In fact, this assumption yields a homogeneous Big Bang automatically.

Equation (3.27) can be solved parametrically depending on the sign of the spatial curvature profile $\kappa(r)$:[2]

$\kappa(r) > 0$ (elliptic evolution):

$$a_\perp(t,r) = \frac{M(r)}{2\kappa(r)}\left[1 - \cos(\eta)\right]\,, \tag{3.28}$$

$$\eta - \sin(\eta) = \frac{2[\kappa(r)]^{3/2}}{M(r)}\,t\,, \tag{3.29}$$

$\kappa(r) = 0$ (parabolic evolution):

$$a_\perp(t,r) = \left[\frac{9}{4}M(r)\,t^2\right]^{1/3}\,, \tag{3.30}$$

$\kappa(r) < 0$ (hyperbolic evolution):

$$a_\perp(t,r) = \frac{M(r)}{-2\kappa(r)}\left[\cosh(\eta) - 1\right]\,, \tag{3.31}$$

$$\sinh(\eta) - \eta = \frac{2[-\kappa(r)]^{3/2}}{M(r)}\,t\,. \tag{3.32}$$

The line element and all previous formulae are invariant under the coordinate transformation $r = f(r')$ which is a gauge freedom in this context. For consistency with the standard FLRW models discussed in Sect. (2.2), we fix this gauge such that $a_\perp(t_0,r) = 1$.

The mass profile is then simply given by

$$M(r) = \frac{8\pi}{r^3}\int_0^r r'^2\rho(t_0,r')\mathrm{d}r'\,. \tag{3.33}$$

2 Note that a homogeneous Big Bang has already been assumed here.

In general, a fiducial observer in the LTB spacetime can only access information from her past null cone (PNC)[3]. In what follows we assume throughout that observers are moving on the central worldline of the LTB spacetime which seems plausible regarding the small dipole signal of the CMB. Inward radial null geodesics are then described by the following system of equations

$$\frac{\mathrm{d}t(r)}{\mathrm{d}r} = -\frac{a_{\parallel}(t(r),r)}{\sqrt{1-\kappa(r)r^2}}\,, \tag{3.34}$$

$$\frac{1}{1+z(r)}\frac{\mathrm{d}z(r)}{\mathrm{d}r} = \frac{\dot{a}_{\parallel}(t(r),r)}{\sqrt{1-\kappa(r)r^2}}\,, \tag{3.35}$$

which can be integrated numerically. By interpolation, we can effectively invert the result in order to transform arbitrarily between redshift and LTB coordinates on the PNC. While Eq. (3.34) can easily be inferred from the metric ansatz in Eq. (3.22), Eq. (3.35) involves the definition of redshifts in LTB spacetimes. A heuristic derivation is given here and the reader is referred to Chapt. (8) for more general arguments. Assuming two light rays being emitted at a fictitious source at times $t_1(r) = T(r)$ and $t_2(r) = T(r) + \tau(r)$, both rays have to obey Eq. (3.34). In the case of $\tau(r) \ll T(r)$, we can expand $a_{\parallel}(t_2, r)$ yielding

$$a_{\parallel}(T(r)+\tau(r),r) = a_{\parallel}(T(r),r) + \tau(r)\dot{a}_{\parallel}(T(r),r).$$

Thus, we obtain

$$\frac{\mathrm{d}\tau(r)}{\mathrm{d}r} = -\tau(r)\frac{\dot{a}_{\parallel}(T(r),r)}{\sqrt{1-\kappa(r)r^2}}\,. \tag{3.36}$$

We define the redshift of the signals with respect to the central observer as the ratio of the observed and emitted time difference $\tau(r_{\mathrm{obs}})/\tau(r_{\mathrm{em}}) = 1 + z(r_{\mathrm{em}})$. When inserting this expression into Eq. (3.36), we immediately find Eq. (3.35).

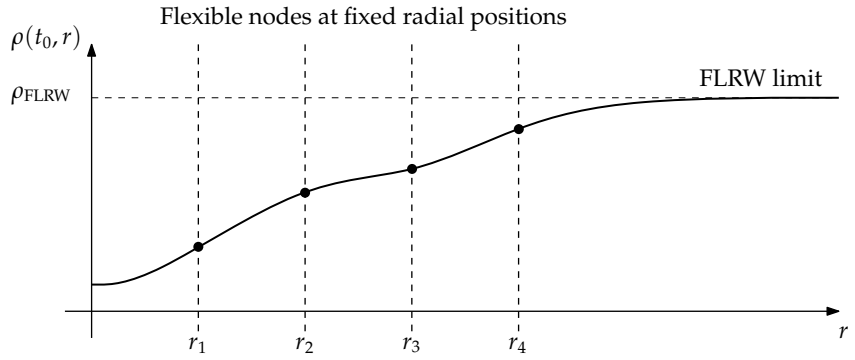

Figure 3.3: Illustration of the construction of the density profile of a given void model: Using nodes at flexible radial positions and an appropriate interpolation between them, very general void profiles can be constructed that are asymptotically embedded into a background FLRW model.

3.4 BACKGROUND MODEL IMPLEMENTATION

For a practical implementation of the background model, we adapted the algorithm outlined in Redlich et al. (2014) (see [75]) which shall be shortly summarised here. For a more detailed discussion of this issue, we refer to the corresponding paper.

1. Since we neglect fluctuations in the bang time function and assume an initially homogeneous universe, the background FLRW solution and the LTB patch have the same global age t_0 given by

3 In fact, this statement is true for any spacetime.

$$t_0 = \frac{1}{H_0}\int_0^1 \frac{\sqrt{a}}{\sqrt{\Omega_m + \Omega_k a}}\mathrm{d}a\,. \tag{3.37}$$

2. We fix a density profile $\rho(t_0, r)$ at the present time which determines the mass profile according to Eq. (3.33). The curvature profile $\kappa(r)$ is implicitly defined by Eq. (3.27) and has to be computed numerically. Using Eq. (3.27) in combination with a proper root finder (see [75]), we solve for $\kappa(r)$ as function of t_0, r and $M(r)$.

3. With the mass and curvature profiles at hand, the time evolution of the background model is completely determined by Eq. (3.26) which is integrated backwards to an initial hypersurface of constant time t_{ini}. All necessary coefficients of the LTB perturbation equations are then fixed on the full (t, r)-domain of interest and can be accessed by 2d linear interpolation.

4. Eqs. (3.34) and (3.35) can be integrated in a similar way.

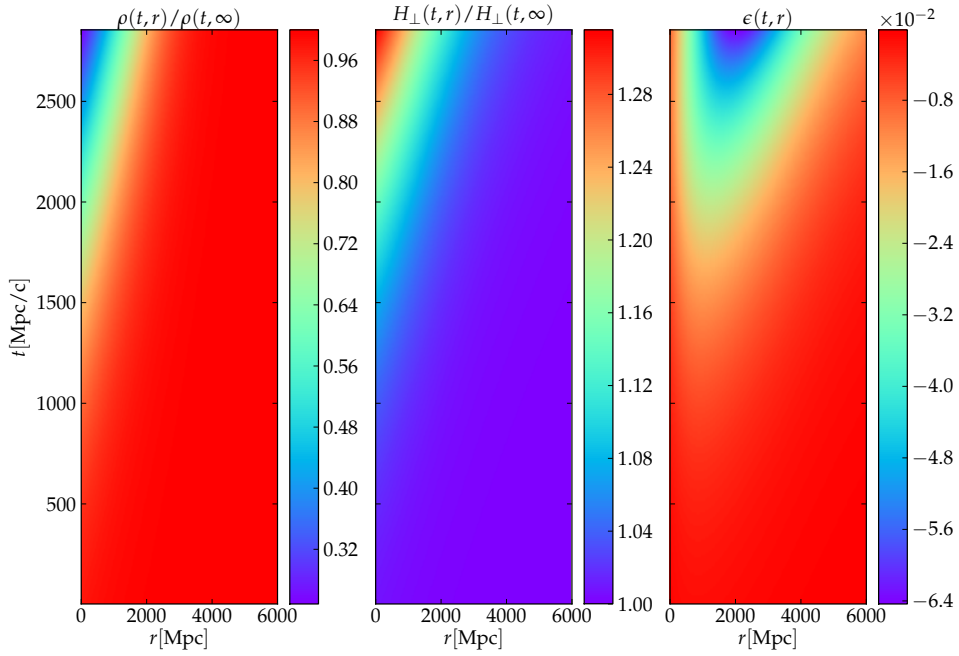

Figure 3.4: Color plots containing the spacetime evolution of the density $\rho(t, r)$, tangential Hubble rate $H_\perp(t, r)$ and the background shear: The density and tangential expansion rate are weighted by their asymptotic values for appropriate visualisation. On the left panel, we directly observe the void formation which leads to significant depth at late times that is connected to a local increase of the tangential expansion rate shown in the mid panel. This effect makes these model applicable to the prediction of distance-redshift relations of local SN measurements. The late-time intrinsic shear plotted in the right panel reaches significant values at radial positions where the density profile obeys its maximum slope. Results were obtained for a Gaussian-shaped void profile described by Eq. (3.38) with parameters $\Omega_{\mathrm{in}} = 0.2$ and $L = 2000$ Mpc. The LTB patch was asymptotically embedded into a background EdS model.

3.4.1 *The role of the void density profile*

As can be seen from Eqs. (3.25) - (3.27), LTB models are generically characterised by three free radial functions $t_B(r)$, $M(r)$, and $\kappa(r)$ that have to be specified individually. By demanding a spatially homogeneous universe at early times, we have already fixed the bang time function. In addition, we set a

proper gauge for the tangential scale factor ($a_\perp(t_0, r) = 1$) which allows us to integrate Eq. (3.25) and determines the mass profile as functional of the density profile $\rho(t_0, r)$ on the t_0-hypersurface. Since the gauge choice also specifies the upper integral boundary in Eq. (3.27), the curvature profile is fixed as function of t_0 and $M(r)$. Consequently, the void density profile at $t = t_0$ is sufficient to characterise the LTB model at all times and radial distances from the centre.

The density profile at $t = t_0$ is constructed in a flexible way using nodes placed at given radial positions in the void. Appropriate interpolation between these points yields void profiles of arbitrary shape (see Fig. (3.3) and [75] for details) which asymptotically tend to the background FLRW value at large radii. However, in accordance with previous studies in [42, 43], we assume a Gaussian shaped void of the form $\rho(t_0, r) = f(r)\bar{\rho}(t_0)$ with radial profile

$$f(r) = 1 + \left(\frac{\Omega_{\mathrm{in}}}{\Omega_{\mathrm{out}}} - 1\right) \exp\left(-\frac{r^2}{L^2}\right) , \tag{3.38}$$

which allows to characterise basic void properties by a simple three-parameter model. The void extension L as well as the central- and asymptotic density parameters Ω_{in} and Ω_{out} can be varied individually. As standard example for our study, we choose a 2 Gpc void with $\Omega_{\mathrm{in}} = 0.2$ that is asymptotically embedded into an Einstein-deSitter (EdS) model ($\Omega_{\mathrm{out}} = 1$) with a Hubble parameter of $h = 0.7$. Regarding this particular void profile, Fig. (3.4) shows numerical results on the spacetime evolution for the density, tangential Hubble rate and normalised shear.

If the density and expansion rate are normalised by their radially asymptotic values, the void formation and corresponding local increase in the Hubble rate can clearly be observed at late times. This effect induces correct predictions of the distance-redshift relations of supernovae for Gpc scale voids. The normalised shear (as introduced in Eq. (3.24)) is an important quantity in the context of LTB perturbation theory as it is one of the main sources of coupling of different perturbation types. It can be seen that significant shear values are obtained in regions where a large slope of the density profile is present. However, shear is negligible close to the void centre and therefore the LTB solution may there be approximated by an open FLRW model. We will test this approximation quantitatively in Chapt. (7) by considering coupling strengths of perturbations at small redshifts on the LTB past null cone.

4

LINEAR PERTURBATION THEORY IN LTB MODELS

4.1 SUMMARY

Properties of linear perturbations on spherically symmetric dust backgrounds are laid out in detail in the present chapter. Current approaches in the literature are again wrapped up at the beginning in order to give an overview of different attempts to investigate linear structure formation on LTB backgrounds. In the following, the metric approach of Clarkson et al. (2010) is singled out as it represents the most complete description of the evolution of all possible perturbation types. Considering the spherical symmetry of the background model, it is convenient to decompose perturbations into spherical harmonics. The metric ansatz and evolution equations are presented in detail that contain fundamental properties of LTB perturbations which are not present in the FLRW regime. As these differences are important features to distinguish LTB from FLRW models in the first place, the final section contains a comparison of both cosmological models in this context.

4.2 OVERVIEW

As briefly mentioned in Chapt. (1), LTB models have been analysed in detail by taking various observable probes into account. However, an important unsolved problem is the exact modeling of structure formation on radially inhomogeneous backgrounds (see [27, 28] for a short discussion). Nonetheless, it provides valuable additional information that can help to constrain and eventually rule out void models on a broad scientific basis. Due to its inherent complexity, the problem has not yet been solved in full generality, but promising approaches that have already been referred to in the Introduction shall be briefly summarized again:

- Making use of the similarity of Eq. (3.26) to the total energy of a spherical configuration (see also [24]), trajectories of test particles can be traced in a Newtonian gravitational potential of a huge Gpc void. Alonso et al. (2010) [3] successfully managed to set up a corresponding Newtonian N-body simulation and studied structure formation therein.

- Nishikawa et al. (2010) (see [71] and [72]) succeeded in imposing second order perturbations on top of a first order, isotropically perturbed FLRW model which accounts for the void. Detailed calculations were performed and promising results obtained, but it remains to be checked whether this approximation is an accurate description of linear structure formation on an exact, radially inhomogeneous cosmological solution.

- Perturbations in LTB models can be studied in an adapted form of the gauge-invariant fluid approach (see [93] for a review). This leads to a covariant 1+1+2 split of the spacetime. Although the full set of evolution equations has not been found yet, some effort has been put into the so-called *silent approximation* where the magnetic part of the Weyl-tensor is neglected. In fact, this reduces the evolution equations to a coupled system of ordinary differential equations which have been successfully applied to predict transfer functions of the linear matter power spectrum (see [68, 98]).

- A 2+2 covariant split of the background spacetime known from stellar and black hole physics can effectively be restricted to spherically symmetric dust spacetimes. By constructing a possible

set of gauge-invariant metric and matter perturbations, the full master and constraint equations of these quantities can be derived that contain the complete dynamical information of the perturbed spacetime to first order. This system was first derived by Clarkson et. al. (2010) in [29] and actually represents the most general description of the evolution of linear perturbations on LTB backgrounds. First numerical attempts to solve these equations can be found in [41] and [43].

Since it describes today's most elaborate approach in the field, all studies presented in the present work are based on the 2+2 covariant framework. Correspondingly, this approach is discussed in some detail in the following.

4.3 METRIC APPROACH OF CLARKSON ET AL. (2010)

Perturbations on homogeneous backgrounds have extensively been studied and are well-understood (see again [17], [38], and [69] for detailed discussions and Sect. (2.3.2) for a short summary). Perturbation variables can be split into scalars, vectors and tensors due to their transformation properties on the underlying homogeneous and isotropic 3-space. The main simplifying property of these models is that the high degree of symmetry causes gauge-invariant metric perturbations to decouple at first order such that their time evolution can be studied separately. This is no longer the case on general spherically symmetric backgrounds. In fact, the radial dependence and off-centre anisotropy of structure growth causes all perturbation types to couple already at first order which makes their modeling and physical interpretation highly difficult.

4.3.1 *Spherical harmonic decomposition*

As suggested by spherical symmetry of the background model, one possible approach is a covariant 2+2 split of the spacetime ($\mathcal{M}^4 = \mathcal{M}^2 \times \mathcal{S}^2$) at the background level. Perturbations can then be characterised according to their transformation properties on $\mathcal{S}^2$ which is analogous, but not equivalent, to the homogeneous and isotropic case. In fact, they decouple into a polar (even parity) and an axial (odd parity) branch which roughly corresponds to their covariant curl- and divergence-free parts on the two-sphere. It is convenient to separate the angular parts by expanding perturbations into an appropriate family of orthonormal basis functions that take all possible degrees of freedom into account. The most suitable choice on a spherically symmetric background are spherical harmonics and covariant derivatives thereof as they are eigenfunctions of the Laplace operator in spherical coordinates. In the following, greek indices $(\mu, \nu, \ldots)$ denote spacetime coordinates whereas lower case Roman letters $(a, b, \ldots)$ mark indices on the two-sphere. Coordinates of the remaining two-dimensional Lorentzian submanifold $\mathcal{M}^2$ are described by capital Roman letters $(A, B, \ldots)$.

General perturbations $\phi(x^A, x^a)$ of a spherically symmetric background model contain five different degrees of freedom that are modeled by corresponding basis functions of the right transformation property on $\mathcal{S}^2$. Considering the polar branch, we have

1. scalars: $Y^{(\ell m)}(\theta, \phi)$,
2. vectors: $Y_a^{(\ell m)} = \nabla_a Y^{(\ell m)}(\theta, \phi)$, $(\ell \geq 1)$, and
3. tensors: $Y_{ab}^{(\ell m)} = \nabla_a \nabla_b Y^{(\ell m)}(\theta, \phi) + \frac{\ell(\ell+1)}{2} \gamma_{ab} Y^{(\ell m)}(\theta, \phi)$, $(\ell \geq 2)$,

whereas, for the axial branch, there are

1. pseudovectors: $\bar{Y}_a = \epsilon_a{}^b \nabla_b Y^{(\ell m)}(\theta, \phi)$, $(\ell \geq 1)$, and
2. pseudotensors[1]: $\bar{Y}_{ab} = -2\epsilon^d{}_{(a} \nabla_{b)} \nabla_d Y^{(\ell m)}(\theta, \phi)$, $(\ell \geq 2)$.

1 The round parentheses denote symmetrisation

Spherical symmetry of the background model naturally causes the evolution of perturbations to separate into spherical harmonic modes (ℓ, m). By suitable combinations of the expansion coefficients, sets of gauge-invariant metric and fluid perturbations and corresponding evolution equations can be derived. The formalism was first developed by Gerlach & Sengupta (1979) ([51]) for general spherically symmetric spacetimes and reformulated in perfect fluid frames by Gundlach & Martín-García (2000) (GMG) (see [54, 67]) to study anisotropic stellar collapse.

In a remarkable work following up this approach, Clarkson, Clifton and February (CCF) ([29]) specified GMG's approach to dust solutions and obtained a full set of LTB gauge-invariant perturbation variables and corresponding master and constraint equations. Their work and recent applications in [41, 43] can be considered as the key theoretical background for our analysis. In analogy to the conformal Newtonian gauge in FLRW models, there exists a special gauge, the Regge-Wheeler (RW) gauge (see [76]), in which the perturbation variables correspond to the gauge-invariants. The final metric ansatz and a possible set of gauge-invariant variables is presented in the following. For details on their construction and on the metric ansatz, we refer to the corresponding papers ([29, 49, 54]). In addition, a brief summary is provided in App. (B).

4.3.2 *Metric ansatz and first order field equations for the polar branch*

For the polar sector, we can define a set of four metric perturbations $\{\eta^{(\ell m)}, \chi^{(\ell m)}, \varphi^{(\ell m)}, \varsigma^{(\ell m)}\}$ and three fluid perturbations $\{\Delta^{(\ell m)}, w^{(\ell m)}, v^{(\ell m)}\}$ that enter into the general form of the perturbed LTB metric and energy momentum tensor. In RW gauge, we have (see [29])

$$\begin{aligned} ds^2 = &-\left[1 + (2\eta^{(\ell m)} - \chi^{(\ell m)} - \varphi^{(\ell m)})Y^{(\ell m)}\right] \mathrm{d}t^2 - \frac{2a_\parallel \varsigma^{(\ell m)} Y^{(\ell m)}}{\sqrt{1-\kappa r^2}} \mathrm{d}t\mathrm{d}r \\ &+ \frac{a_\parallel^2}{1-\kappa r^2}\left[1 + (\chi^{(\ell m)} + \varphi^{(\ell m)})Y^{(\ell m)}\right] \mathrm{d}r^2 + r^2 a_\perp^2 \left[1 + \varphi^{(\ell m)} Y^{(\ell m)}\right] \mathrm{d}\Omega^2 , \end{aligned} \tag{4.1}$$

$$\rho = \rho^{\mathrm{LTB}} \left(1 + \Delta^{(\ell m)} Y^{(\ell m)}\right) , \tag{4.2}$$

$$u_\mu = \left[u_A + \left(w^{(\ell m)} n_A + \frac{1}{2} k_{AB} u^B\right) Y^{(\ell m)}, v^{(\ell m)} Y_b^{(\ell m)}\right] , \tag{4.3}$$

with sums over (ℓ, m) implied. Each perturbation variable is therefore a spherical harmonic coefficient and a free function of t and r. The unit vectors in time and radial direction are given by $u_A = (-1, 0)$ and $n_A = (0, a_\parallel / \sqrt{1-\kappa r^2})$. k_{AB} corresponds to the metric perturbation in the (t, r)-submanifold.

Inserting the perturbed quantities in Eqs. (4.1) - (4.3) into Einstein's field equations and dropping terms of $\mathcal{O}(Y^2)$ yields first order evolution equations for the gauge-invariants. In case of $\ell \geq 2$, the resulting system of equations can be reduced to a closed system of master equations[2]:

$$\ddot{\chi} = \frac{\chi'' - C\chi'}{Z^2} - 3H_\parallel \dot{\chi} + \left[A - \frac{(\ell-1)(\ell+2)}{r^2 a_\perp^2}\right] \chi + \frac{2\sigma}{Z} \varsigma' + \frac{2}{Z}\left[H_\parallel' - 2\sigma \frac{a_\parallel}{r a_\perp}\right] \varsigma - 4\sigma\dot{\varphi} + A\varphi , \tag{4.4}$$

$$\ddot{\varphi} = -4H_\perp \dot{\varphi} + \frac{2\kappa}{a_\perp^2}\varphi - H_\perp \dot{\chi} + Z^{-2} \frac{a_\parallel}{r a_\perp} \chi' - \left[\frac{1-2\kappa r^2}{r^2 a_\perp^2} - \frac{\ell(\ell+1)}{2 r^2 a_\perp^2}\right] \chi + \frac{2}{Z} \frac{a_\parallel}{r a_\perp} \sigma \varsigma , \tag{4.5}$$

$$\dot{\varsigma} = -2H_\parallel \varsigma - \frac{\chi'}{Z} , \tag{4.6}$$

$$\eta = 0 \tag{4.7}$$

2 $\dot{()}$ denotes a derivative with respect to coordinate time t whereas $()'$ corresponds to a derivative with respect to LTB radial coordinate r. We dropped the (ℓ, m) superscript here.

and a constraining part of the field equations that describes the coupling to the fluid perturbations

$$\alpha w = \frac{1}{Z}\dot{\varphi}' - \frac{1}{Z}(\sigma - H_\perp)\varphi' - \frac{1}{Z}\frac{a_\parallel}{ra_\perp}\dot{\chi} + \frac{H_\perp}{Z}\chi' + \left[\frac{\ell(\ell+1)}{2r^2a_\perp^2} + D + \frac{\kappa}{a_\perp^2}\right]\varsigma\,, \tag{4.8}$$

$$\begin{aligned}\alpha\Delta = &-\frac{1}{Z^2}\varphi'' + \frac{1}{Z^2}\left(C - 4\frac{a_\parallel}{ra_\perp}\right)\varphi' + \left(H_\parallel + 2H_\perp\right)\dot{\varphi} + \frac{1}{Z^2}\frac{a_\parallel}{ra_\perp}\chi' + H_\perp\dot{\chi} \\ &+ \left[\frac{\ell(\ell+1)}{r^2a_\perp^2} + 2D\right](\chi+\varphi) - \frac{(\ell-1)(\ell+2)}{2r^2a_\perp^2}\chi + \frac{2H_\perp}{Z}\varsigma' + \frac{2}{Z}\left(H_\parallel + H_\perp\right)\frac{a_\parallel}{ra_\perp}\varsigma\,,\end{aligned} \tag{4.9}$$

$$\alpha v = \dot{\varphi} + \frac{\dot{\chi}}{2} + H_\parallel(\chi+\varphi) + \frac{1}{2Z}\varsigma'\,. \tag{4.10}$$

The coefficients are given by the following quantities of the background LTB model:

$$\begin{aligned}\alpha &= 8\pi G\rho = \frac{\kappa}{a_\perp^2}\left(1 + 2\frac{a_\parallel}{a_\perp}\right) + H_\perp\left(H_\perp + 2H_\parallel\right) + \frac{\kappa' r}{a_\perp a_\parallel}\,,\\ A &= 2\alpha - \frac{6M}{a_\perp^3} - 4H_\perp\sigma\,,\\ C &= \frac{a_\parallel'}{a_\parallel} + \frac{\kappa r + \frac{1}{2}\kappa' r^2}{1-\kappa r^2} + \frac{2a_\parallel}{ra_\perp}\,,\\ D &= -\frac{\alpha}{2} + H_\perp\left(H_\perp + 2H_\parallel\right)\,,\\ \sigma &= H_\parallel - H_\perp\,,\\ Z &= \frac{a_\parallel}{\sqrt{1-\kappa r^2}}\,.\end{aligned}$$

Local energy momentum conservation $\nabla_\mu T^\mu_{\ \nu} = 0$ leads to derivative constraints that the system naturally obeys:

$$\dot{w} = \frac{1}{2Z}\varphi' - H_\parallel\left(w + \frac{\varsigma}{2}\right)\,, \tag{4.11}$$

$$\dot{\Delta} = -\frac{\dot{\chi} + 3\dot{\varphi}}{2} + \frac{\ell(\ell+1)}{r^2a_\perp^2}v - \frac{1}{Z}\left[\left(w + \frac{\varsigma}{2}\right)' + \left(\frac{\alpha'}{\alpha} + \frac{2a_\parallel}{ra_\perp}\right)\left(w + \frac{\varsigma}{2}\right)\right]\,, \tag{4.12}$$

$$\dot{v} = \frac{\chi + \varphi}{2}\,. \tag{4.13}$$

Einstein's field equations to first order show that the metric perturbations η, χ, φ and ς are master variables of the system, i. e., if the solution to the system (4.4) - (4.7) is known for each angular scale ℓ, Eqs. (4.8) - (4.10) will reduce to simple identities for the fluid perturbation variables. The evolution in time and radius is constrained by linear partial differential equations that contain a non-trivial coupling caused by radially-dependent and off-center anisotropic structure growth. Among various expressions in the coupling terms, the background shear $\sigma = H_\parallel - H_\perp$ as well as gradients in the curvature profile, scale factors and Hubble rates can clearly be identified. As already pointed out in Sect. (4.3.1), orthonormality of the spherical harmonic basis causes the evolution equations to decouple into (ℓ, m) modes. In addition, the spherically symmetric background allows to apply the eigenvalue equation of the Laplace operator on $\mathcal{S}^2$ which can be written as

$$\nabla_a\nabla^a Y^{(\ell m)} = -\ell(\ell+1)Y^{(\ell m)}\,. \tag{4.14}$$

This way, all derivatives with respect to local coordinates (θ, ϕ) can be eliminated such that the four dimensional problem of solving perturbation equations on the full spacetime $(\mathcal{M}^4, g)$ is mapped to

a set of effectively two dimensional problems for the evolution of eigenvalues of the $\mathcal{S}^2$-Laplacian for each angular scale ℓ.

Regarding the special case of dipole perturbations ($\ell = 1$), there is a complication as Eqs. (4.4) - (4.8) take different forms. This is caused by the fact that, mathematically, there exist no dipole tensorial spherical harmonics which does not allow the trivial field equation $\eta = 0$ to hold anymore. Secondly, due to the missing tensorial components, all perturbation variables are only partially gauge-invariant and leave an additional degree of freedom to be fixed. This issue and possible solutions are discussed in detail by GMG in [54], but we do not want to focus on it here as we restrict our analysis to polar perturbations of $\ell \geq 2$.

4.3.3 *Metric ansatz and first order field equations for the axial branch*

Gauge-invariant perturbations of the axial branch are given by a vector metric perturbation $\{k_A^{(\ell m)}\}$ and an axial fluid velocity perturbation $\bar{v}^{(\ell m)}$ (see again App. (B)). Since perturbations that transform as scalars on the two-sphere naturally belong to the polar sector, axial perturbations are restricted to $\mathcal{S}^2$-vector and -tensor modes that, by construction, have to obey $\ell \geq 1$. Hence, there can only exist axial gauge-invariants which are at least of $\mathcal{S}^2$-vector type such as velocity- or metric vector perturbations. The ansatz for the perturbed metric and four-velocity including these gauge-invariants is given by

$$\mathrm{d}s^2 = -\mathrm{d}t^2 + \frac{a_\parallel^2}{1-\kappa r^2}\mathrm{d}r^2 + r^2 a_\perp^2 \mathrm{d}\Omega^2 + 2k_A^{(\ell m)}\overline{Y}_b^{(\ell m)}\mathrm{d}x^A\mathrm{d}x^b\,, \tag{4.15}$$

$$u_\mu = \left(u_A, \bar{v}^{(\ell m)}\overline{Y}_b^{(\ell m)}\right)\,. \tag{4.16}$$

Inserting both quantities into Einstein's equations, the first order evolution equations (for $\ell \geq 2$) reduce to[3]:

$$g^{AB}\nabla_A k_B = 0\,, \tag{4.17}$$

$$g^{CB}\nabla_C\left(r^4 a_\perp^4 D_{AB}\right) = (\ell-1)(\ell+2)k_A - 16\pi G\rho\,\bar{v}\,r^2 a_\perp^2 u_A\,, \tag{4.18}$$

with $D_{AB} = \partial_B\left(k_A/(r^2a_\perp^2)\right) - \partial_A\left(k_B/(r^2a_\perp^2)\right)$ being the covariant curl of k_A.

As first proposed in [51], a scalar quantity

$$\Pi = \epsilon^{AB}\nabla_B\left(\frac{k_A}{r^2a_\perp^2}\right) \tag{4.19}$$

can be defined which allows to obtain an equivalent system of equations given by

$$\dot{\bar{v}} = 0 \;\Rightarrow \bar{v} = \bar{v}(r)\,, \tag{4.20}$$

$$\ddot{\Pi} = \frac{1}{Z^2}\Pi'' - \frac{\bar{C}}{Z^2}\Pi' - \left(6H_\perp + H_\parallel\right)\dot{\Pi} - \left[2\alpha + \frac{(\ell+2)(\ell-3)}{r^2a_\perp^2}\right]\Pi + \frac{2\alpha}{r^2a_\perp^2 Z}\left(\bar{v}' + \frac{\alpha'}{\alpha}\bar{v}\right)\,, \tag{4.21}$$

using again coefficients

$$\alpha = 8\pi G\rho = \frac{\kappa}{a_\perp^2}\left(1 + 2\frac{a_\parallel}{a_\perp}\right) + H_\perp\left(H_\perp + 2H_\parallel\right) + \frac{\kappa' r}{a_\perp a_\parallel}\,,$$

3 The (ℓm) superscript will be dropped again

$$\bar{C} = \frac{a_\parallel'}{a_\parallel} + \frac{\kappa r + \frac{1}{2}\kappa' r^2}{1-\kappa r^2} - \frac{2a_\parallel}{r a_\perp}\,,$$
$$Z = \frac{a_\parallel}{\sqrt{1-\kappa r^2}}\,.$$

The first equation has been obtained by taking the covariant divergence of Eq. (4.18) and inserting Eq. (4.17). The second expression is essentially the covariant curl of Eq. (4.18).

A solution to Eqs. (4.20) and (4.21) can be transformed to the actual gauge-invariant metric perturbations k_A via Eq. (4.18)[4]

$$(\ell-1)(\ell+2)k_0 = -2\alpha r^2 a_\perp^2 \bar{v} - \frac{r^4 a_\perp^4}{Z}\left(\Pi' + 4\frac{a_\parallel}{r a_\perp}\Pi\right)\,, \tag{4.22}$$
$$(\ell-1)(\ell+2)k_1 = -r^4 a_\perp^4 Z\left(\dot{\Pi} + 4H_\perp \Pi\right)\,. \tag{4.23}$$

In case of $\ell = 1$, Eq. (4.17) is no longer fulfilled which does not allow a straightforward derivation of Eqs. (4.20) and (4.21). Nonetheless, Eqs. (4.22) and (4.23) can be integrated directly yielding

$$\Pi = -\frac{2}{r^4 a_\perp^4}\int \frac{\bar{v}(Mr^3)'}{\sqrt{1-\kappa(r)r^2}}\mathrm{d}r\,. \tag{4.24}$$

The metric perturbations k_A then have to be obtained by inverting Eq. (4.19) which causes additional degrees of freedom and does not permit a unique solution anymore.

4.3.4 *Properties of perturbations in LTB models in comparison to FLRW*

Although the polar master equations will look similar to their FLRW counterparts if the coupling terms are neglected (in fact, χ obeys a wave equation, φ a scalar, Bardeen-like equation and ς an a^{-2}-decay law), the physical interpretation of these gauge-invariants is more subtle. Scalar-vector-tensor decomposition does not naturally exist on spherically symmetric backgrounds and therefore LTB gauge-invariants are a priori strongly differ from FLRW gauge-invariants. In extensive calculations, CCF managed to perform the FLRW limit and showed that, intrinsically, these gauge-invariants are complicated mixtures of all FLRW perturbation types. Their results are briefly summarised in App. (C). Proper comparison of FLRW gauge-invariant quantities and LTB gauge-invariants in FLRW limit is non-trivial, because the RW gauge is not adapted to the description of perturbations in FLRW models. One therefore has to equate the perturbed FLRW metric with the perturbed LTB metric in a general gauge and express each LTB gauge-invariant in terms of its FLRW counterparts. In fact, it turns out that only χ is a genuine gravitational wave mode whereas ς contains vector and tensor degrees of freedom and φ as well as η obey degrees of freedom of all FLRW-perturbation types. The axial variable Π contains vector and tensor contributions. Similar results are obtained for the fluid variables (see appendices of [29] for details). It is therefore hard to disentangle these gauge-invariants aiming at a direct comparison with homogeneous and isotropic models. There is the possibility of constructing SVT variables that, in the FLRW limit, reduce to pure scalar, vector and tensor modes, but these ones are of complicated structure (see [28] for a brief review).

The following analysis is restricted to the polar branch, since it potentially obeys the more prominent coupling effects and contains the generalized scalar gravitational potential φ and density contrast Δ. These variables transform as scalars on the two-sphere and obey similar evolution equations compared to the FLRW metric potential and density contrast which allows an intuitive treatment. However, they obey a complicated FLRW limit containing scalar-, vector- and tensor contributions which makes their understanding highly difficult and requires great care in this context.

4 Note that the local time coordinate of the LTB background model is chosen such that $u_A = (-1, 0)$.

Notwithstanding any physical interpretation or comparison to spatially homogeneous models, the intrinsic coupling of the perturbation variables itself as seen in Eqs. (4.4) - (4.7) can directly be studied if the system is integrated numerically. By carrying out the FLRW limit, CCF showed that the scalar Bardeen potential Ψ is only contained in φ (see also App. (C)). Hence, starting from an initial scalar potential perturbation at early times, we can directly quantify the influence of coupling on the space-time evolution by comparing the fully coupled case with solutions in which coupling has generally been neglected. The latter was extensively studied in [43].

As already pointed out in the Introduction, the main intention of this work is to consider the full evolution of perturbation equations from realistic initial scalar perturbations and to investigate the strength of the coupling in a statistical way. A direct comparison of structure formation in LTB and FLRW models would be the next appreciable step and is addressed in Chapt. (8).

We finally want to stress that the axial branch is dynamically decoupled from the polar one and 3-scalar perturbations in FLRW spacetimes do not source any axial LTB quantities in the homogeneous limit (see App. (C) for details). Hence, the axial branch is trivial in this setup at all times and spatial scales and potential physical effects are solely described by polar perturbations. This justifies the restriction to the polar branch in particular.

5

NUMERICAL APPROACH

5.1 SUMMARY

As outlined in Chapt. (4), the evolution of linear perturbations in LTB models is constrained by a coupled system of partial differential equations that is formulated in the LTB time and radial coordinates for each spherical harmonic mode (ℓ, m). Attempts to obtain accurate approximations of the solution are therefore challenging as advanced computational methods, e. g. finite elements, have to be applied. This chapter is meant to discuss the numerical setup for the given system of partial differential equations and to motivate the choice of the numerical scheme used here. All methods have been preimplemented in the Distributed Unified Numerics Environment (DUNE) and can therefore readily be applied to our problem. We start with a short overview of finite element methods and the DUNE framework. Focussing on Eqs. (4.4) - (4.11), the grid setup and appropriate boundary conditions are laid out and motivated in the following. The final section contains results of a test run previously performed by February et al. (2014) in [41] that independently confirms the authors' findings and shows the correct performance of the numerical scheme.

5.2 GENERAL STATEMENTS ON FINITE ELEMENTS

Originating from developments in structural mechanics in the 1950s, finite element methods became a well-established technique to solve partial differential equations (PDEs) on very flexible and even unstructured grids. The basic idea consists of writing the model problem (PDE and boundary conditions on a given domain of interest) into so-called weak formulation and converting it to an equivalent variational problem. In this manner, the differential equation system is multiplied by a test function and integrated over the full domain of interest yielding functional relations to be minimised by variation (see App. (D) for details). The variational problem itself can then be solved by discretizing the domain of interest into finite elements and approximating the solution by suitable basis functions (polynomials in particular) on each element with coefficients to be determined (see Fig. (5.1)). This typically leads to large, but sparsely populated, linear equation systems for the expansion coefficients. Finite element methods are based on a solid mathematical background using techniques developed in functional analysis like weak derivatives and corresponding Sobolev spaces. Giving a complete overview on finite elements and their properties would be beyond the scope of this thesis. Some details that are important for this particular application are described in App. (D). However, a detailed discussion of the corresponding mathematical background can, for example, be found in [14] and [53].

In contrast to finite differencing methods applied in [41], finite elements are more flexible and also well-suited for irregular or locally refined grids[1]. In addition, higher accuracies can easily be achieved by increasing the basis polynomial degree (see App. (D) for details of the implementation). We decided to prefer finite elements to finite differences since the initial profiles for the spherical harmonic coefficients show considerable small scale fluctuation with increasing spherical harmonic ℓ-mode and we therefore need a robust scheme for numerical differentiation that also works on grids that can be adapted to properties of the solution itself. February et al. (2014) ([41]) have shown that their approach using second order finite differences works well for the series of test runs they performed on a regular

1 The term *grid* refers to the finite element discretization of domain of interest.

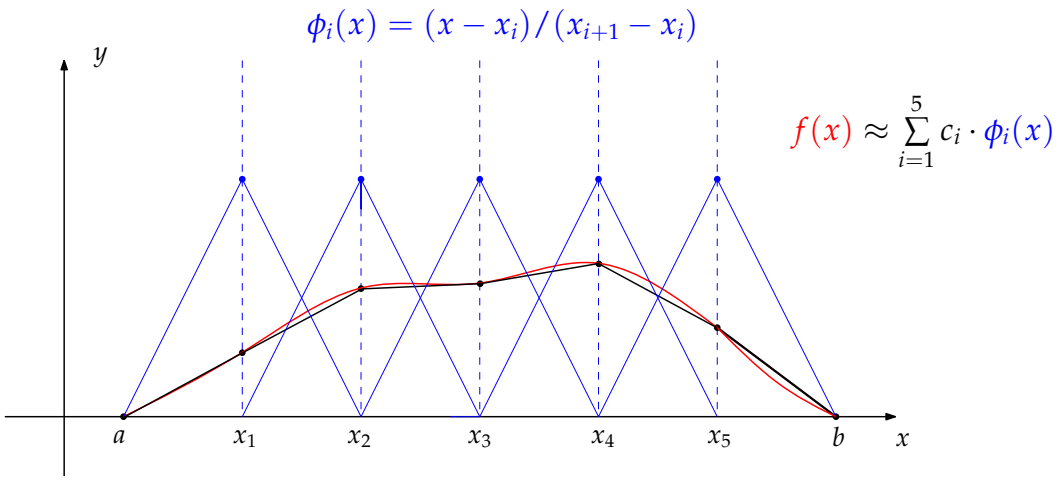

Figure 5.1: Approximation of an exemplary function $f(x)$ (shown in red) on a global interval $\Omega = [a, b]$ in one dimension: On subintervals $\Omega_i = [x_i, x_{i+1}]$ (so-called finite elements), linear Lagrangian basis polynomials (hat functions) are defined that are shown in blue. Once a proper set of coefficients $\{c_i\}_{i=1,\dots,5}$ and boundary conditions $\{f(a), f(b)\}$ are provided, a linear approximation (shown in black) of the functional shape can be obtained. The accuracy of this approximation can either be increased by refining the finite elements or by raising the basis polynomial degree.

grid. As will be shown in Sect. (5.5), we have been able to reproduce their results with a finite element setup.

5.3 THE DISTRIBUTED UNIFIED NUMERICS ENVIRONMENT (DUNE)

The *Distributed Unified Numerics Environment* (DUNE) (see [10, 11, 12, 21]) is a template-based, multi-purpose C++-library for the numerical solution of PDEs on arbitrary grids using finite element methods. The basic structure is divided into modules performing different tasks like grid setup (`dune-grid`), iterative solvers for equation systems (`dune-istl`), or efficient PDE discretization (`dune-pdelab`) (see [13] for details). It provides preimplemented basis polynomials, grid-based spatial solvers and time integrators designed to be very flexible and applicable to a wide range of PDE problems in basically arbitrary dimension (see Fig. (5.2) for an overview). For time-dependent problems, DUNE uses the well-known *method of lines* where the spatial derivatives are discretized and the time coordinate is left continuous. This results in a system of ordinary differential equations in time that assemble a large scale initial value problem. However, such a system can effectively be treated by appropriate ODE solvers (see Fig. (5.3)). We therefore perform a spatial discretization with finite elements in the radial coordinate which is then integrated in time using an implicit Alexander S-stable method (see [1].

5.4 GRID SETUP AND BOUNDARY CONDITIONS

The solution of a system of partial differential equations with time dependence is constrained by initial and boundary conditions. While the setup of initial conditions in a cosmological environment is a more extensive procedure and will be discussed in detail in Chapt. (6), boundary conditions can be chosen in a natural way by requiring regularity of the solution at the radial origin. We define a space-time *domain of interest* with spatial extend of (at least) three times the void size in which we want to study the forthcoming numerical solution. As proposed in [41], we impose an artificial spatial boundary condition at $r = r_*$ that is causally disconnected from the domain of interest in order to prevent any artificially reflected propagating modes to reenter (see Fig. (5.4)). By tracing null geodesics in the background spacetime and thereby following the characteristics of the system, we can integrate Eq. (3.34) given by

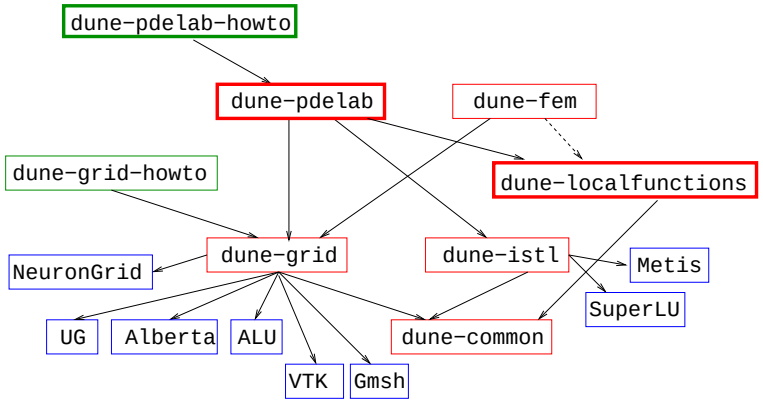

Figure 5.2: Overview on different DUNE modules and their correspondences: DUNE core modules are shown in red that perform different steps of the numerical scheme such as general assembling (`dune-common`), grid setup (`dune-grid`), iterative solvers (`dune-istl`), local polynomial bases (`dune-localfunctions`) as well as PDE discretization (`dune-pdelab` or `dune-fem`). The inclusion of secondary software like special grid managers (`ALU, UG, ...`), visualisation (`VTK, Gsmh`) or special solvers (`SuperLU, Metis`) is possible without problems. As we deal with a one dimensional problem in space, there is no need for any advanced grid manager or visualisation tool. However, `SuperLU` (see [36, 62]) turned out to be a powerful exact solver for the spatial discretization problem and was therefore successfully applied to our numerical setup. Discretization and general setup of the PDE system was performed using `dune-pdelab`. In fact, `dune-pdelab` and `dune-fem` are equivalent discretization modules, but `dune-pdelab` is developed and maintained at the Institute of Scientific Computing (IWR) in Heidelberg which allowed direct advise and support in an easy way (see also acknowledgments). This figure was taken from [13]).

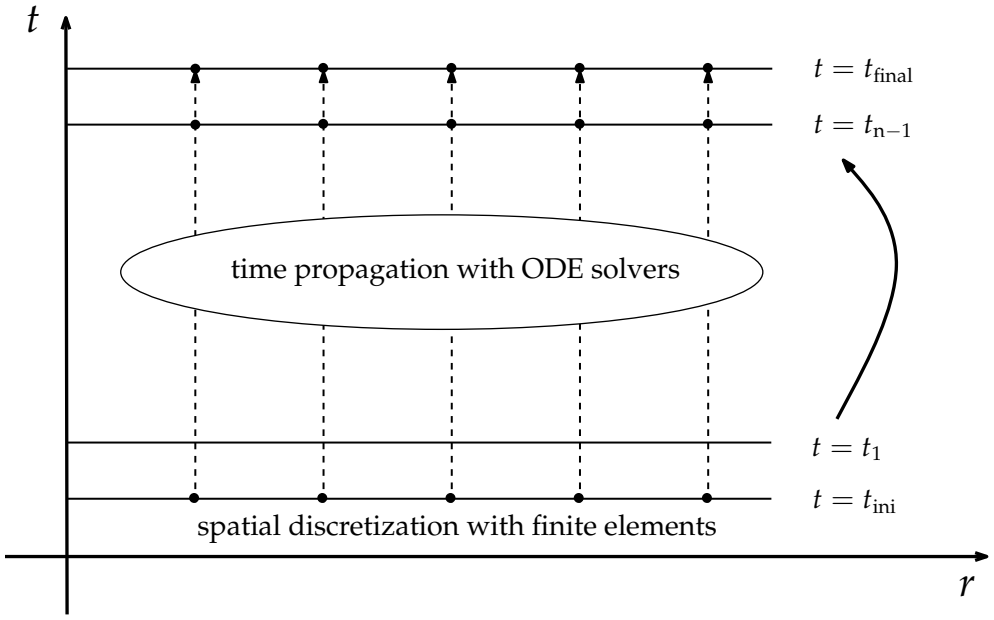

Figure 5.3: Illustration of the method of lines: The spatial discretization with finite elements is performed on each time slice and the resulting initial value problem is then propagated forward in time.

$$\frac{\mathrm{d}t(r)}{\mathrm{d}r} = \pm\frac{a_{\parallel}(t,r)}{\sqrt{1-\kappa(r)r^2}} = Z(t,r)\,,$$

with $t(r_{\max}) = t_{\mathrm{ini}}$ and obtain[2]

$$r_* = r_{\max} + \frac{1}{2}\int_{t_{\mathrm{ini}}}^{t_0} Z^{-1}(t, r_{\max})\mathrm{d}t\,. \tag{5.1}$$

As shown by GMG in [54], the solution to Eqs. (4.4) - (4.7) has to obey certain conditions for regularity at $r = 0$:

$$\chi = \bar{\chi}\, r^{\ell+2}\,,\ \varphi = \bar{\varphi}\, r^{\ell}\,,\ \varsigma = \bar{\varsigma}\, r^{\ell+1}\,,\ \Delta = \bar{\Delta}\, r^{\ell}\,,\ w = \bar{w}\, r^{\ell-1}\,,\ v = \bar{v}\, r^{\ell}\,,$$

where the barred quantities can be expanded in positive even powers of r. This enforces a zero Dirichlet boundary condition at the origin for $\ell \geq 2$. We require the solution to vanish at r_* as well such that no propagating modes to be generated there that can affect the results in the domain of interest.

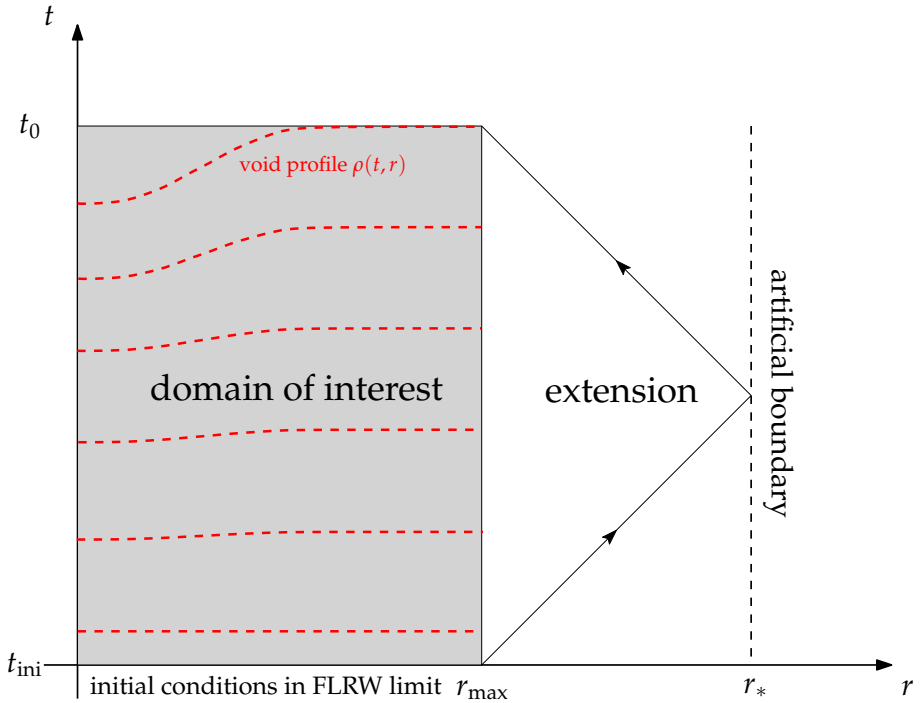

Figure 5.4: Schematic construction of the artificial boundary condition according to [41]: r_* is chosen to be causally disconnected from the domain of interest by integrating radial null geodesics in the background spacetime (see Eq. (5.2)). The void is fully contained in the domain of interest and deepens with increasing cosmic time.

Fig. (5.5) illustrates the construction of the spatial grid which is basically divided into three parts: In order to fulfill the regularity conditions with sufficient accuracy, we have a fine structured grid in the vicinity the origin, followed by an equidistant grid containing the domain of interest and a coarse grid covering the region between the outer boundary of the domain of interest and the artificial boundary.

Since we use an implicit time integration scheme, the Courant-Friedrichs-Levy (CFL) condition (see [32]) is not necessary for numerical stability, but nonetheless we assign the timesteps dynamically

2 We assume in addition that the unperturbed LTB metric in the region $[r_{\max}, r_*]$ is well-described by its asymptotic EdS limit.

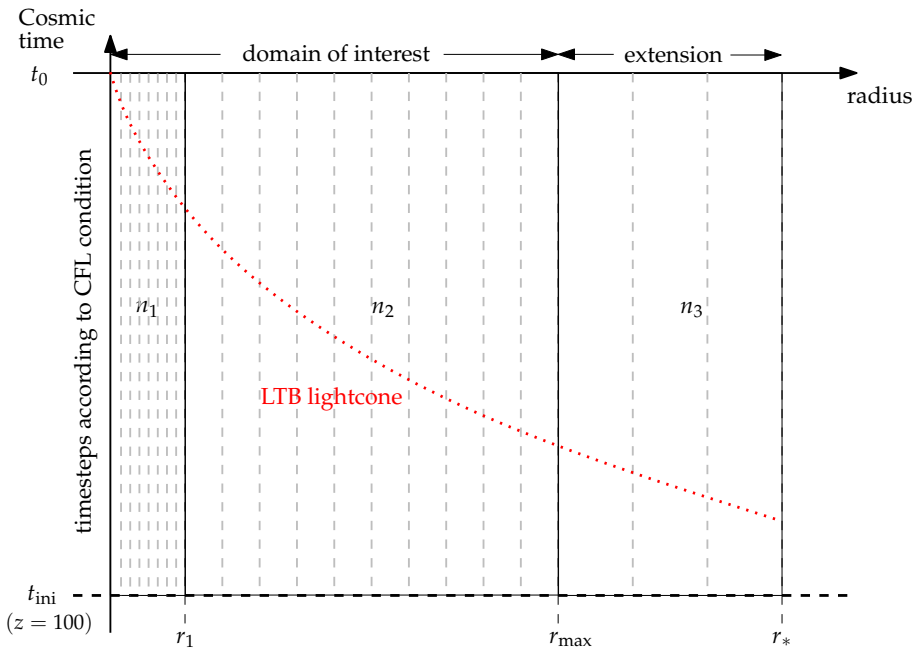

Figure 5.5: Schematic structure of the irregular spatial grid: At small radii, we apply a finely resolved grid discretizing the interval $[r_{\mathrm{min}}, r_1]$ with n_1 bins to recover the regularity condition precisely. This part is followed by a regular grid covering $[r_1, r_{\mathrm{max}}]$ with n_2 bins and a very coarse grid in the extension $[r_{\mathrm{max}}, r_*]$ with n_3 bins. The parameters r_1, n_1, n_2, and n_3 can be adjusted individually. For all test runs presented in Sects. (7.2) and (7.3), we have chosen $r_1 = 100$ Mpc, $n_1 = 50$, $n_2 = 256$ and $n_3 = 20$. Final results are interpolated on the LTB backward lightcone that is schematically shown for illustration.

according to this condition in order to adapt the time resolution to intrinsic timescales of the system. Using the system's characteristics again, we obtain

$$\frac{\Delta t(t)}{\Delta r} = 0.99 \cdot \min_{r_{\mathrm{min}} \leq r \leq r_{\mathrm{max}}} \left(Z(t,r)\right) \leq \min_{r_{\mathrm{min}} \leq r \leq r_{\mathrm{max}}} \left(Z(t,r)\right). \tag{5.2}$$

As motivated in Sect. (4.3.2), we concentrate on perturbations with even parity (polar branch) throughout this work. For each spherical harmonic mode (ℓ, m), Einstein's field equations then split into a closed set of master equations for the metric perturbations and corresponding constraint equations for the fluid perturbations. For fixed (ℓ, m), we therefore evolve Eqs. (4.4) - (4.7) in time and use the results in each timestep to constrain the fluid perturbations using the identities given by Eqs. (4.8) - (4.10). Grid structure, basic finite element map and the equation systems have to be passed to the DUNE interface that performs a residual calculation to solve the underlying linear equation system in each time step. For details of the implementation, the reader is referred to App. (D).

The corresponding procedure then has to be performed for a representative set of spherical harmonic modes such that final angular power spectra of each LTB gauge-invariant perturbation can be estimated (see Chapt. (7)). Computations were therefore parallelised using the well-established Open Message Passing Interface (Open MPI) and ported to the `bwGRiD` computing cluster of the state universities of Baden-Württemberg (see `http://www.bw-grid.de/en/the-bwgrid/` for details).

5.5 COMPARISON TO PREVIOUS RESULTS IN FEBRUARY ET AL. (2014)

February et al. (2014) ([41]) set up a numerical solution of the evolution equations for a simple test case by initializing each variable separately with five Gaussian peaks probing the behavior of the solution at different positions in the LTB patch. Starting from a Gaussian-shaped void outlined in Sect. (3.4.1) with $\Omega_{\mathrm{in}} = 0.2$ and $L = 2$ Gpc that is asymptotically embedded into an EdS model, initial conditions for one variable are given by

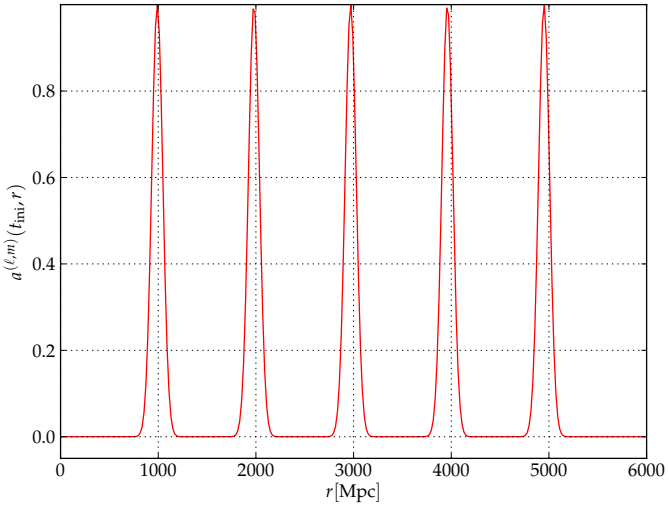

Figure 5.6: Initial Gaussian profile as applied by February et al. (2014) ([41])

$$a^{(\ell m)}(t_{\rm ini}, r) = \sum_{i=1}^{5} \exp\left(-\frac{(r-r_i)^2}{s^2}\right), \tag{5.3}$$

$$\dot{a}^{(\ell m)}(t_{\rm ini}, r) = 0\,, \tag{5.4}$$

with $r_i \in 0.99 \cdot \{1,2,3,4,5\}$ Gpc and $s = 0.08$ Gpc (see also Fig. (5.7)). All other variables and their time derivatives are set to zero. This initial configuration is placed on a spatial hypersurface that intersects the LTB backward lightcone at redshift $z = 100$. Hence, $t_{\rm ini}$ refers to the time coordinate on the PNC for this redshift. The PDE system is then numerically evolved in time till t_0 which corresponds to the global age of the LTB patch. The spatial extension $r_{\rm max}$ of the domain of interest is chosen to be 6 Gpc. In accordance with [41], the forthcoming results show the spacetime evolution of this setup for the two exemplary spherical harmonic modes $\ell = 2$ and $\ell = 10$. Since the regularity conditions mentioned in the previous section are trivially fulfilled by the initial profiles considered in this test case, the adapted grid structure shown in Fig. (5.4) is, for simplicity, replaced by an equidistant grid with 512 nodes.

We see from Fig. (5.7) that non-zero modes, while evolving in time, excite the remaining initially zero modes at a partly significant level. Although a rigorous interpretation of the results is physically subtle, we can qualitatively see the internal mode mixing of each gauge-invariant variable when considering the FLRW limit discussed in Sect. (4) and App. (C). Time evolution suggests that χ, as a purely tensorial mode in the FLRW limit, contains only propagating degrees of freedom, whereas ς and φ are mixtures of SVT perturbation types. On a homogeneous and isotropic background, ς reduces to vectorial and tensorial degrees of freedom. Similar behaviour can be seen on inhomogeneous backgrounds as we observe a decaying mode (Case 3 and 4) and propagating mode (Case 5 and 6) as well as modes similar to infall velocities (Case 1 and 2). φ contains scalar, vector and tensor modes in FLRW limit. Cases 1 and 2 suggest a time evolution of φ like a scalar Bardeen potential which decays inside the void (as $\kappa(r) < 0$) and stays constant in the EdS region. Nonetheless, there are also propagating modes as can clearly be seen in cases where it is excited from an initially zero state.

The corresponding fluid perturbations are presented in Fig. (5.8). The behaviour of the generalised density contrast Δ as well as the two gauge-invariant velocity perturbations w and v generally depends on the initialised metric perturbations. The strong decay of ς also causes the fluid perturbations to

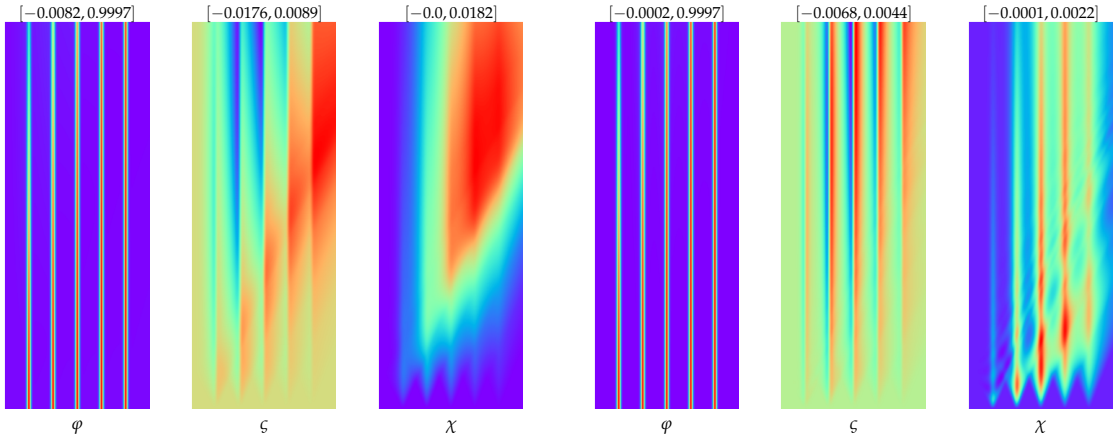

(a) Case 1: initialise φ for $\ell = 2$

(b) Case 2: initialise φ for $\ell = 10$

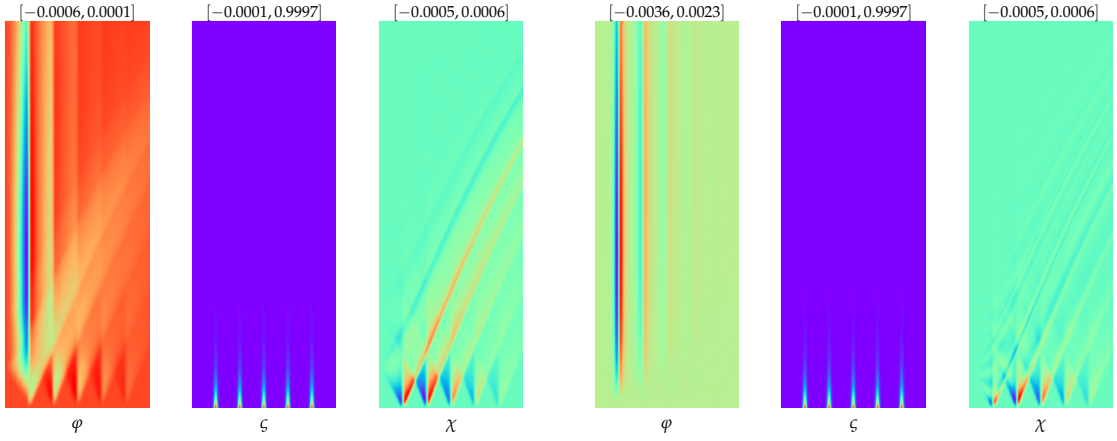

(c) Case 3: initialise ς for $\ell = 2$

(d) Case 4: initialise ς for $\ell = 10$

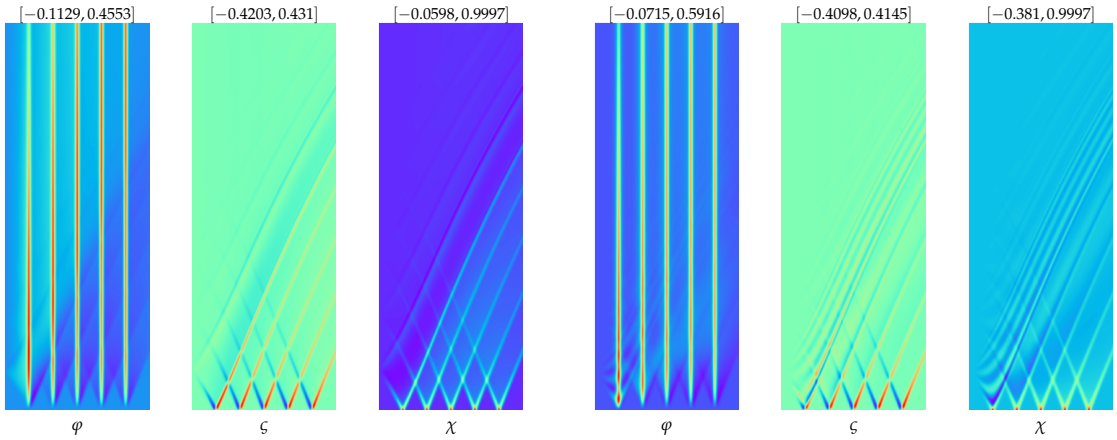

(e) Case 5: initialise χ for $\ell = 2$

(f) Case 6: initialise χ for $\ell = 10$

Figure 5.7: Space-time-evolution of the LTB gauge-invariants $\{\varphi, \varsigma, \chi\}$ with initial conditions according to Eqs. (5.3) and (5.3) for two exemplary modes $\ell = 2$ and $\ell = 10$: The minimum and maximum values of the space-time diagrams are provided in the headlines which also indicate the boundaries of the colorscale emerging from blue to red. Each panel covers the full domain of interest where the horizontal and vertical axes correspond to the LTB radial and time coordinate, respectively. We applied a Gaussian-shaped void density profile $\rho(t_0, r)$ with a density contrast of $\Omega_{\text{in}} = 0.2$ and $L = 2$ Gpc extension that is asymptotically embedded into an EdS model with $h = 0.7$. In accordance with [41], these results are obtained on an equidistant grid in radius with 512 nodes and time steps that are dynamically computed using the CFL condition (Eq. (5.2)).

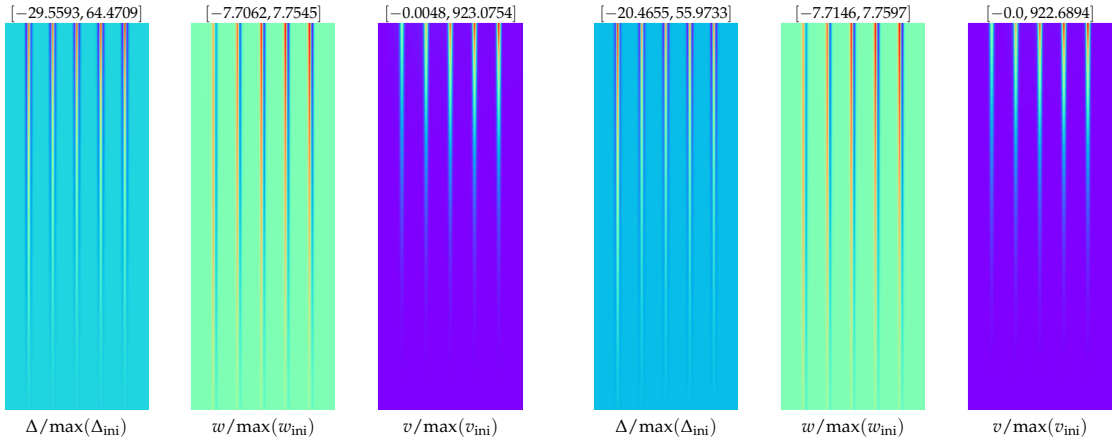

(a) Case 1: initialise φ for $\ell = 2$ (b) Case 2: initialise φ for $\ell = 10$

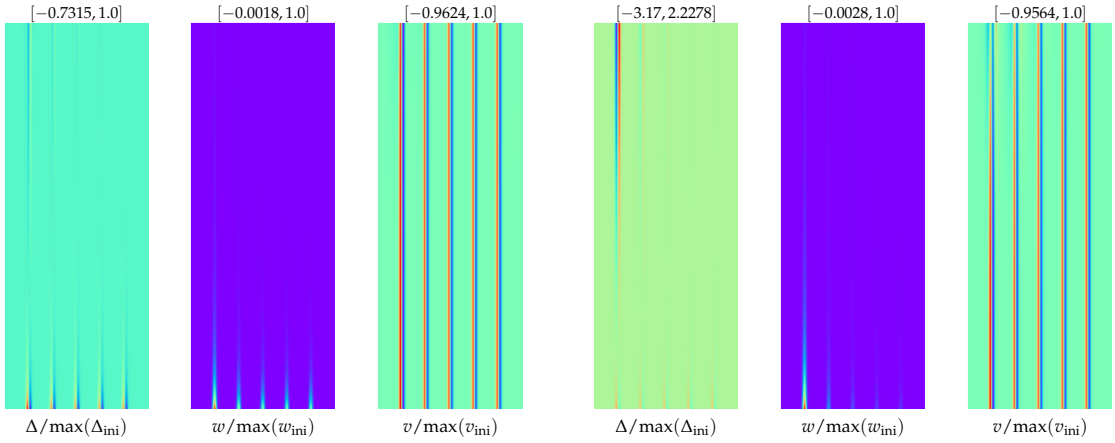

(c) Case 3: initialise ς for $\ell = 2$ (d) Case 4: initialise ς for $\ell = 10$

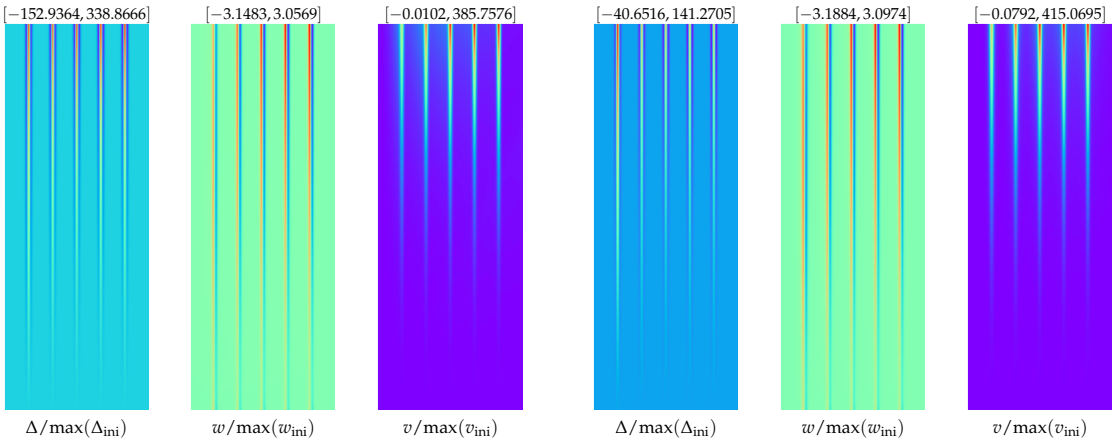

(e) Case 5: initialise χ for $\ell = 2$ (f) Case 6: initialise χ for $\ell = 10$

Figure 5.8: Space-time-evolution of the corresponding gauge-invariant fluid perturbations $\{\Delta, w, v\}$: We consider again two exemplary modes $\ell = 2$ and $\ell = 10$ as presented in [41]. The minimum and maximum values of the full spacetime diagram are given in the headlines where we have normalised each variable with respect to its maximum initial value.

decay whereas φ and χ source growing modes. Similar to the metric perturbations, these gauge-invariants are mixtures of scalar, vector and tensor degrees of freedom in the FLRW limit (see [29]).

We refrain from giving a detailed analysis of the behaviour of the time evolution of each perturbation variable here, since the results obtained are not new and have already been analysed in great detail in [41]. It is rather the main intention of this section to give an independent confirmation and to show that our numerical results are in agreement with previous works in the field.

Indeed, compared with results obtained by February et al. (2014), the spacetime diagrams agree well in shape for each initial configuration and the amplitudes of the excited perturbations are very similar. We have to point out here that the background model implementation of February et al. is slightly different from the one applied in this work. As outlined in Sect. (3.4.1), we fix the void density profile and the Hubble constant (respectively the global age) at the present time in the asymptotic FLRW regime. February et al. instead apply a functional shape of the matter density parameter profile $\Omega_{\mathrm{m}}(r)$ at the present time and fix the Hubble constant at the spatial origin. We believe that this causes the minor differences in the amplitudes of the perturbation variables. Nonetheless, the basic features of the spacetime evolution are clearly reproduced.

6

INITIAL CONDITIONS

6.1 SUMMARY

As pointed out in Chapt. (3), the LTB patch is constructed to be asymptotically embedded into a cosmological model of FLRW type. As a consequence, spatial hypersurfaces that are intersected by the LTB lightcone at large redshifts are statistically homogeneous and isotropic to a very high degree. In this asymptotic FLRW regime, we create cosmological initial conditions for the LTB master and constraint equations. For the cases analysed so far, we restrict ourselves to initial scalar perturbations described by the metric Bardeen potential $\Psi(t, \vec{x})$ since the transformation to LTB gauge-invariants in the homogeneous limit is particularly simple for this setup (see App. (C)). The present chapter outlines two possibilities to obtain initial spherical harmonic coefficient profiles for the scalar Bardeen potential. Both procedures make use of realisations of an initial Gaussian random field with vanishing mean and the underlying power spectrum $P_\Psi(k)$. In the first approach, potential fluctuations are sampled in configuration space, transformed to real space and decomposed into spherical harmonics using the Healpix scheme. The second approach was developed to overcome difficulties at small redshifts and angular scales. It uses direct multivariate Gaussian sampling of spherical harmonic coefficients with covariance matrices that are given by the theoretical angular power spectra.

6.2 GAUSSIAN SAMPLING TECHNIQUE IN CONFIGURATION SPACE

6.2.1 *Realisation of a Gaussian random field*

As we are dealing with a system of second order differential equations in time, we have to specify initial conditions for the variables themselves and their first time derivatives on an initial hypersurface $t = t_{\mathrm{ini}}$. Throughout, we assume vanishing initial rates for the perturbation variables[1] and specify the initial states as radial profiles. In accordance with the standard inflationary paradigm, we assume the early universe to be spatially homogeneous and isotropic and therefore apply standard FLRW perturbation theory. Hence, small initial density seeds for structure formation in the matter-dominated era obey nearly Gaussian statistics and are fully characterised by the linear power spectrum (see Sect. (2.4))

$$P_\delta(k, a) = \frac{D_+^2(a)}{D_+^2(a_{\mathrm{ini}})} \mathcal{P}(k) T^2(k)\,, \tag{6.1}$$

where $T(k)$ denotes the transfer function of Bardeen et al. (1986) (see [5]) that has already been introduced in Sect. (2.4). $\mathcal{P}(k)$ represents the primordial power spectrum right after inflation. By Poisson's equation, the power spectrum of the Bardeen potential Ψ yields

$$P_\Psi(k, a) = \frac{9}{4} \left(\frac{\Omega_m^{(0)} H_0^2}{a\, k^2} \right)^2 P_\delta(k, a)\,. \tag{6.2}$$

1 We can even assume this for the Bardeen potential since we constructed the LTB patch to be embedded into an EdS model in which Ψ does not obey any time dependence (see Sect. (2.4)).

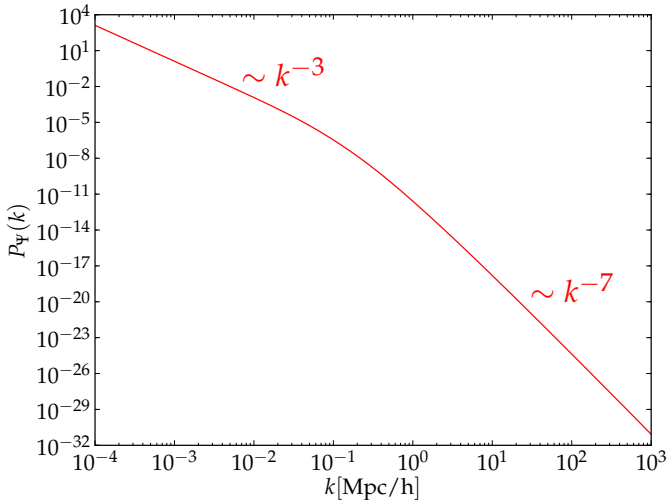

Figure 6.1: Initial potential power spectrum according to Eq. (6.2): Due to the asymptotic behaviour of k^{-7} on small scales, the resulting Gaussian random field is very smooth compared to the applied discretization scale.

We fix an exemplary initial hypersurface of constant time $t_{\rm ini}$ that intersects the LTB past lightcone at redshift $z_{\rm ini} = 100$ and is therefore placed well-within the FLRW matter-dominated era. At $t = t_{\rm ini}$, we draw a 3d realisation of the Gaussian random field describing the scalar Bardeen potential in a cubic box of scale $L_{\rm cube}$ with the following properties:

1. $\langle \Psi \rangle = 0$ in configuration space,
2. the variance in Fourier space is given by the potential power spectrum,
3. the cube is filled in a Hermitian conjugate way: $\Psi^*(k_x, k_y, k_z) = \Psi(-k_x, -k_y, -k_z)$.

Precisely, the variance in Fourier space is given by $\hat{\sigma}^2(k) = P_\Psi(k)/L^3_{\rm cube}$ as we have to take the dimensionless power spectrum into account. In comparison to previous applications in [18], we assume a prefactor $1/(2\pi)^3$ in the Fourier convention and define the power spectrum according to $\langle \Psi(\vec{k})\Psi(\vec{k}')^* \rangle = (2\pi)^3 P_\Psi(k)\, \delta^{(3)}_D(\vec{k} - \vec{k}')$. In fact, this yields the prefactor $1/L^3_{\rm cube}$ instead of $(2\pi)^3/L^3_{\rm cube}$ as obtained in [18].

Transforming back to real space[2] yields a discretized, real-valued potential field at nodes (x_i, y_j, z_k) in the 3d cube. Since the potential power spectrum shown in Fig. (6.1) behaves like k^{-7} on small scales, the resulting Gaussian random field is very smooth compared to the discretization scale. Four exemplary 2d slices of the 3d initial realisation are presented in Fig. (6.2).

6.2.2 *Healpix and spherical harmonic decomposition*

Within this cubic box, we draw concentric spheres around an arbitrary centre[3] and discretize each of them according to the Healpix pixelisation scheme described in [52]. The *Hierarchical Equal Area and Iso-Latitude pixelisation scheme (Healpix)* has originally been developed for data processing and analysis of large cosmic microwave background surveys. The idea is to arrive at a fast, accurate and efficient numerical integration on the sphere as well as optimal recursion of Legendre polynomials needed for spherical harmonic decomposition and angular power spectrum estimation. This can be achieved by an appropriate tesselation of the spherical surface that ensures equal pixel areas and an iso-latitudinal

2 A three-dimensional Fast Fourier Transform (FFT) was applied for this purpose.
3 For practical reasons we choose the central node of the cubic box.

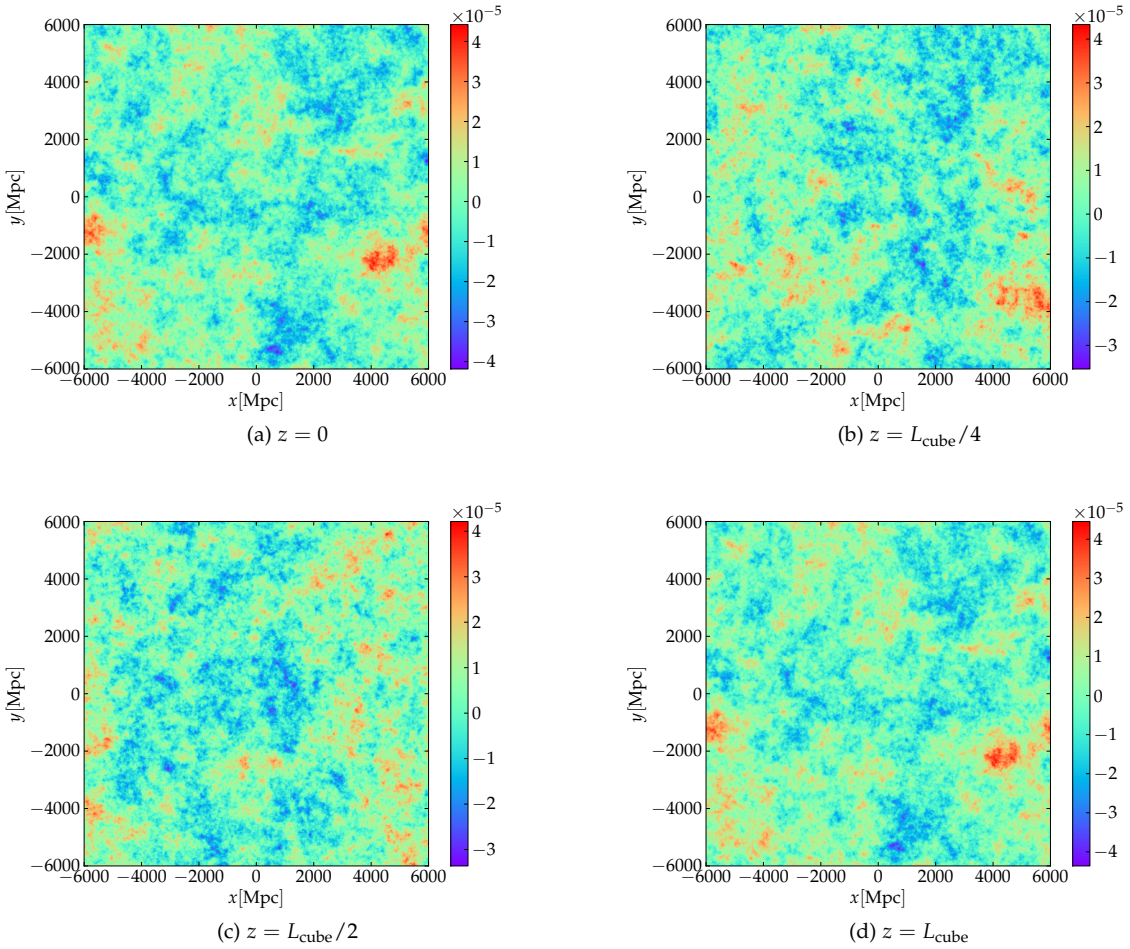

(a) $z = 0$ (b) $z = L_{\text{cube}}/4$

(c) $z = L_{\text{cube}}/2$ (d) $z = L_{\text{cube}}$

Figure 6.2: 2d slices of the 3d Gaussian realisation of the Bardeen potential fluctuations: In Cartesian coordinates, the xy surface is plotted for $z = 0$, $z = L_{\text{cube}}/4$, $z = L_{\text{cube}}/2$, and $z = L_{\text{cube}}$ in the corresponding subfigures (a), (b), (c), (d). We use $N_{\text{nodes}} = 1024^3$ with full spatial extension of $L_{\text{cube}} = 12$ Gpc. The obvious similarity of (a) and (d) is caused by periodic boundary conditions applied by the Fourier transform.

location of pixel centres. The Healpix grid consists of twelve base pixels with these properties that can be globally refined. By construction, the Healpix properties are conserved with respect to the refinement process. The number N_{side} of refinement steps determines the angular resolution of the spherical surface (so-called *Healpix Map*) which is then assembled by $N_{\text{pix}} = 12N_{\text{side}}^2$ pixels (see Fig. (6.3)).

As already mentioned, the Healpix grid allows fast and efficient numerical integration on $\mathcal{S}^2$ that is particularly useful for spherical harmonic decomposition

$$\Psi(t_{\text{ini}}, r, \theta, \phi) = \sum_{(\ell,m)} \Psi^{(\ell m)}(t_{\text{ini}}, r) Y^{(\ell m)}(\theta, \phi)\,, \tag{6.3}$$

with spherical harmonic coefficients being estimated by quadratures on the two sphere:

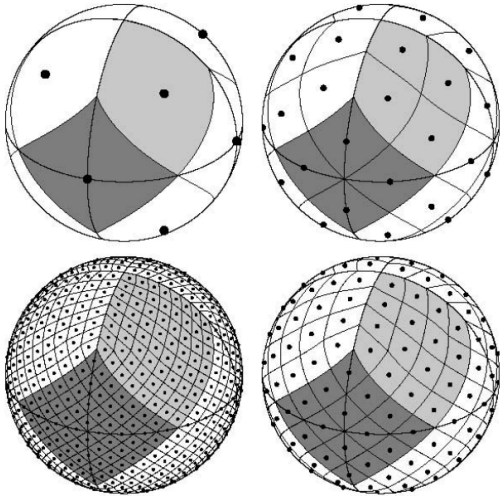

Figure 6.3: Illustration of the Healpix discretization scheme: Twelve base pixels of equal area and isolatitude pixel centers are globally refined with $N_{\rm side} = 1, 2, 4, 8$ such that these pixel properties are conserved. This figure has been taken from [52].

$$\begin{aligned}\Psi^{(\ell m)}(t_{\rm ini}, r) &= \int_\Omega \mathrm{d}\Omega\, \Psi(t_{\rm ini}, r, \theta, \phi)\, Y^{(\ell m)}(\theta, \phi)^* \\ &\approx \frac{4\pi}{N_{\rm pix}} \sum_{p=0}^{N_{\rm pix}} \Psi(t_{\rm ini}, r, \theta_p, \phi_p)\, Y^{(\ell m)}(\theta_p, \phi_p)^* \,.\end{aligned} \tag{6.4}$$

By placing concentric Healpix Maps at equidistant radial positions in the 3d cube, we finally obtain initial radial profiles for spherical harmonic coefficients of the Bardeen potential $\Psi^{(\ell m)}(t_{\rm ini}, r)$ for each angular scale ℓ and orientation m.

It shall be mentioned here that we effectively measure proper distances $d_p(t_{\rm ini}, r)$ between the centre and the spherical surfaces that do not reduce to the LTB radial coordinate in general. However, assuming the void depth to be negligible at $t = t_{\rm ini}$, we can write (see also [3, 43]):

$$\begin{aligned}d_p(t_{\rm ini}, r) = a(t_{\rm ini}) \cdot r_{\rm FLRW} &= \int_0^{r_{\rm LTB}} \frac{a_\parallel(t_{\rm ini}, r)}{\sqrt{1 - \kappa(r) r^2}}\, \mathrm{d}r \\ &\approx a_\perp(t_{\rm ini}, r_{\rm LTB}) \cdot r_{\rm LTB} \\ &\approx a(t_{\rm ini}) \cdot r_{\rm LTB} \,.\end{aligned} \tag{6.5}$$

Hence, in this particular limit, we can safely identify the LTB and FLRW radial coordinates.

Fig. (6.4) shows examples of Healpix Maps at increasing radii using Mollweide projection. As the spheres grow in radius, angular scales of fluctuations seem to decrease due to larger arc lengths with increasing radii. We want to point out at this stage that, in principle, the method can be extended to vector and tensor perturbations once a proper sampling technique is available. The Bardeen potential power spectrum itself can also be replaced correspondingly, if, for example, the primordial curvature perturbation (as applied in [43]) turns out to be a more realistic representation of potential fluctuations in the matter-dominated FLRW era.

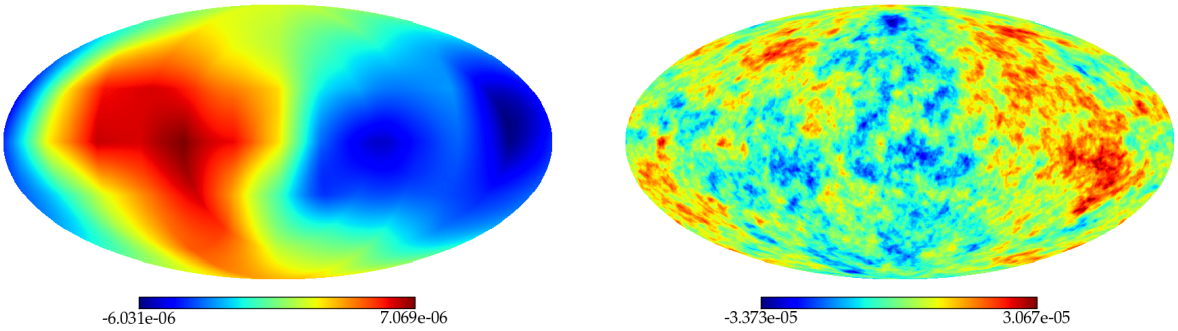

(a) $r = r_{\text{min}} = 1$ Mpc

(b) $r = r_{\text{max}}/4$

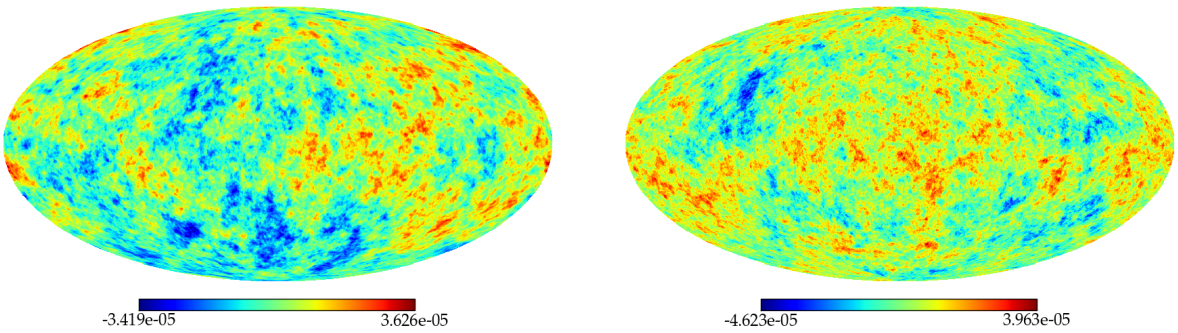

(c) $r = r_{\text{max}}/2$

(d) $r = r_{\text{max}}$

Figure 6.4: Healpix Maps in Mollweide projection at different radii given by fractions of $r_{\text{max}} = L_{\text{cube}}/2 = 6$ Gpc: By construction of the Healpix scheme (see [52]), Healpix Maps contain $12N_{\text{side}}^2$ pixel with $N_{\text{side}} = 512$ in this case. We apparently see fluctuations on smaller scales for spheres at increasing radius, since the spherical surface increases with the square of the radius.

6.3 MULTIVARIATE SAMPLING FROM ANGULAR COVARIANCE MATRICES

In the previous approach to obtain initial conditions for the LTB master and constraint equations, a realisation of a Gaussian potential field $\Psi(\vec{k})$ is created in a cubic box in configuration space. This procedure requires allocating a large 3d cube to store regularly placed nodes of the Bardeen potential in readiness for the FFT to real space. Due to memory limitations, the number of these regular nodes is bounded which determines a maximum resolution for the description of the potential field. This turns out to be problematic as we see significant resolution effects at small radii and large ℓ-modes (see Fig. (6.5)) which essentially rule out these regions for the forthcoming analysis of LTB perturbations. In addition, we have to convert cubic pixels to Healpix pixels which necessarily produces shot noise on small angular scales due to a finite cubic pixel size.

It is therefore worth investigating an alternative approach for the sampling technique that does not involve large 3d realisations. The idea is to use multivariate Gaussian sampling of the spherical harmonic coefficients with a covariance matrix given by the theoretical angular power spectra.

6.3.1 *Multivariate Gaussian sampling*

In general, a multivariate Gaussian distribution is given by

$$\mathcal{P}(\vec{y}) = \frac{1}{\sqrt{(2\pi)^n \det C}} \exp\left[-\frac{1}{2}\vec{y}^T \cdot C^{-1} \cdot \vec{y}\right] \tag{6.6}$$

for n-dimensional vectors $\vec{y} = \{y_i\}_{0 \leq i \leq n}$ and the corresponding covariance matrix

$$C_{ij} = \langle y_i y_j \rangle \,. \tag{6.7}$$

In order to obtain a finite realisation with the underlying distribution of Eq. (6.6), we first draw a vector $\vec{x}$ of n uncorrelated random numbers x_i with unit variance. Uncorrelated random numbers can be transformed to correlated ones by rotation in data space:

$$y_i = \sum_j \alpha_{ij} x_j \,. \tag{6.8}$$

In addition, it has to be ensured that the correlation between the $\{y_i\}$ is described by the given covariance matrix C. In fact, this constrains the shape of the coefficient matrix A. By direct calculation, we see

$$\begin{aligned} C_{ij} = \langle y_i y_j^* \rangle &= \sum_{k,l} \langle \alpha_{ik} \alpha_{jl} x_k x_l \rangle \\ &= \sum_{k,l} \alpha_{ik} \alpha_{jl} \underbrace{\langle x_k x_l \rangle}_{\delta_{kl}} \\ &= \sum_k \alpha_{ik} \alpha_{jk} = \sum_k \alpha_{ik} \alpha_{kj}^T \\ &= \left(A \cdot A^T \right)_{ij} \,. \end{aligned} \tag{6.9}$$

Hence, the coefficient matrix A can be obtained by taking the "square root" of the covariance matrix. Mathematically, this corresponds to the Cholesky decomposition as the covariance matrix is positive definite and symmetric. Given these properties, A and the corresponding linear map $\vec{x} \longrightarrow \vec{y}$ are uniquely defined.

6.3.2 *Covariance matrix*

In the particular case of spherical harmonic coefficients, the covariance matrix is given by

$$C_{ij} = \left\langle \Psi^{(\ell m)}(r) \Psi^{(\ell' m')}(r')^* \right\rangle_{ij} \,. \tag{6.10}$$

Correspondingly, the vector components are a priori correlated random numbers in the radius and in all spherical harmonic modes (ℓ, m).

In case of spatial flatness, Eq. (6.10) can be expressed in terms of spherical Bessel functions $j_\ell(x)$. Using the Rayleigh decomposition of plane waves

$$e^{\mathrm{i}\vec{k}\cdot\vec{r}} = 4\pi \sum_{\ell,m} \mathrm{i}^\ell \, j_\ell(kr) \, Y^{(\ell m)}(\hat{r}) \, Y^{(\ell m)}(\hat{k})^* \,, \tag{6.11}$$

with $\vec{k} = k \cdot \hat{k}$ and $\vec{r} = r \cdot \hat{r}$, the spherical harmonic coefficients can be obtained as

$$\Psi^{(\ell m)}(r) = \frac{\mathrm{i}^\ell}{2\pi^2} \int \mathrm{d}^3 k \, \Psi(\vec{k}) \, j_\ell(kr) \, Y^{(\ell m)}(\hat{k})^* \,. \tag{6.12}$$

We can use this result to compute the covariance matrix

$$\begin{aligned} \left\langle \Psi^{(\ell m)}(r) \Psi^{(\ell' m')}(r')^* \right\rangle &= \frac{\mathrm{i}^{\ell - \ell'}}{4\pi^4} \left\langle \int \mathrm{d}^3 k \, \Psi(\vec{k}) \, j_\ell(kr) Y^{(\ell m)}(\hat{k})^* \cdot \int \mathrm{d}^3 k' \, \Psi(\vec{k'})^* \, j_{\ell'}(k'r') \, Y^{(\ell' m')}(\hat{k'}) \right\rangle \\ &= \frac{2}{\pi} \int_0^\infty \mathrm{d}k \, k^2 P_\Psi(k) \, j_\ell(kr) \, j_\ell(kr') \cdot \delta_{\ell\ell'} \delta_{mm'} \\ &= C^\ell(r, r') \cdot \delta_{\ell\ell'} \delta_{mm'} \,, \end{aligned} \tag{6.13}$$

where the definition of the power spectrum

$$\left\langle \Psi(k)\Psi(k')^* \right\rangle = (2\pi)^3 \, P_\Psi(k) \, \delta_D^{(3)}(\vec{k} - \vec{k}')$$

and the orthogonality relation of the spherical harmonics

$$\int \mathrm{d}\Omega \, Y^{(\ell m)}(\hat{k}) \, Y^{(\ell' m')}(\hat{k})^* = \delta_{\ell\ell'}\delta_{mm'}$$

have been applied. According to Eq. (6.12), the covariance matrix decouples into separate blocks for each spherical harmonic mode (ℓ, m) which only contain the radial correlations at given ℓ-mode, i. e.

$$C^\ell(r_i, r_j) = \frac{2}{\pi} \int_0^\infty \mathrm{d}k \, k^2 \, P_\Psi(k) \, j_\ell(kr_i) \, j_\ell(kr_j) \,. \tag{6.14}$$

6.3.3 *Numerical treatment*

The numerical approximation of integral expressions like Eq. (6.14) is very challenging and expensive with standard quadrature techniques. Spherical Bessel functions show a rapidly oscillatory behaviour which requires a considerable amount of function evaluations to reach acceptable accuracies. An alternative approach was proposed by Levin (1996) in [60, 61] and is now established as the so-called *Levin collocation method*. In fact, the evaluation of oscillatory integrals is mapped to the problem of solving an ordinary differential equation system with no boundary conditions. The latter can be treated very efficiently by polynomial collocation. In the following, we briefly sketch this approach here, as it is an essential tool for computing the generic covariance matrices C_{ij}^ℓ for each angular scale.

The formalism addresses integrals of the form

$$I = \int_a^b \vec{f}(x)^T \vec{w}(x) \, \mathrm{d}x = \int_a^b \langle \vec{f}, \vec{w} \rangle \, \mathrm{d}x \,, \tag{6.15}$$

with $\vec{f} = (f_1(x), \ldots, f_m(x))^T \in \mathbb{R}^m$ being a vector of m non-oscillating functions and $\vec{w}(x) = (w_1(x), \ldots, w_m(x))^T \in \mathbb{R}^m$ a vector of linearly independent functions that show strong oscillations or even irregular rapid variations. We shall furthermore assume that the functions $\{w_i\}_{i=1,\ldots,m}$ satisfy the differential equation system

$$\vec{w}'(x) = A(x)\vec{w}(x) \,, \tag{6.16}$$

with an $m \times m$ matrix $A(x)$ containing entries that are varying non-rapidly. The principle of the Levin collocation method relies on finding a function vector $\vec{p}(x) = (p_1(x), \ldots, p_m(x))^T$ (or a least an approximation for it) such that $\langle \vec{p}, \vec{w} \rangle' \approx \langle \vec{f}, \vec{w} \rangle$. The integral can then readily be solved:

$$I = \int_a^b \langle \vec{f}, \vec{w} \rangle \mathrm{d}x \approx \int_a^b \langle \vec{p}, \vec{w} \rangle \mathrm{d}x = \vec{p}^T(b)\vec{w}(b) - \vec{p}^T(a)\vec{w}(a) \,. \tag{6.17}$$

The problem of evaluating Eq. (6.14) is therefore replaced by approximating the function vector $\vec{p}$ appropriately. Explicit calculation yields

$$\begin{aligned} \langle \vec{f}, \vec{w} \rangle = \langle \vec{p}, \vec{w} \rangle' &= \langle \vec{p}', \vec{w} \rangle + \langle \vec{p}, \vec{w}' \rangle \underbrace{=}_{\text{Eq. (6.16)}} \langle \vec{p}', \vec{w} \rangle + \langle \vec{p}, A\vec{w} \rangle \\ &= \langle \vec{p}', \vec{w} \rangle + \langle A^T \vec{p}, \vec{w} \rangle \\ &= \langle \vec{p}' + A^T \vec{p}, \vec{w} \rangle \,. \end{aligned} \tag{6.18}$$

Using the linear independence of the functions $\{w_i\}_{1<i<m}$, we infer that $\vec{p}$ is given by an approximate solution to the ordinary differential equation system

$$\vec{p}' + A^T \vec{p} = \vec{f}\,. \tag{6.19}$$

The numerical treatment of this system is feasible, since, by assumption, neither $\vec{f}$ nor A contain rapidly oscillatory components. A solution to the system can, for example, be found by collocation.

The function vector $\vec{p}$ is then approximated by a linear combination of basis polynomials

$$\left\{u_k^{(i)}\right\}_{i=1,\ldots,m}^{k=1,\ldots,n}$$

of degree n. An n-point approximation $p_i^{(n)}$ of the vector component p_i can be expressed as

$$p_i^{(n)}(x) = \sum_{k=1}^{n} c_k^{(i)} u_k^{(i)}(x)\,. \tag{6.20}$$

The coefficients $c_k^{(i)}$ have to be determined by a linear equation system set-up by the collocation conditions

$$\left(\partial_x + A^T\right) p^{(n)}(x_j) = f(x_j) \tag{6.21}$$

at properly chosen collocation points $\left\{x_j\right\}_{j=1,\ldots,n}$. The corresponding approximation of the integral is then

$$I \approx I^{(n)} = \sum_{i=1}^{m} p_i^{(n)}(b) w_i(b) - p_i^{(n)}(a) w_i(a)\,. \tag{6.22}$$

As proposed in [60], we apply the polynomial basis functions

$$u_k^{(i)}(x) = \left(x - \frac{a+b}{2}\right)^{k-1} \;;\; k = 1, \ldots, n \,;\; i = 1, \ldots, m \tag{6.23}$$

that are evaluated at equidistant collocation points

$$x_j = a + \left(\frac{j-1}{n-1}\right)(b-a) \,;\; j = 1, \ldots, n$$

in the integal domain $[a, b]$.

In case of products of two spherical Bessel functions with different arguments (as they appear in Eq. (6.14)), a closed equation system in the shape of Eq. (6.16) can be obtained by considering a four-component function vector given by

$$\vec{w} = \begin{pmatrix} j_\ell(kr_i)\, j_\ell(kr_j) \\ j_{\ell-1}(kr_i)\, j_\ell(kr_j) \\ j_\ell(kr_i)\, j_{\ell-1}(kr_j) \\ j_{\ell-1}(kr_i)\, j_{\ell-1}(kr_j) \end{pmatrix}. \tag{6.24}$$

In fact, regarding the recursive expressions of derivatives of spherical Bessel functions

$$j_\ell'(x) = j_{\ell-1}(x) - \frac{\ell+1}{x} j_\ell(x)\,, \tag{6.25}$$

$$j_{\ell-1}'(x) = -j_\ell(x) + \frac{\ell-1}{x} j_{\ell-1}(x)\,, \tag{6.26}$$

this yields a 4×4 matrix of the form

$$A = \begin{pmatrix} -2\frac{\ell+1}{k} & r_i & r_j & 0 \\ -r_i & -\frac{2}{k} & 0 & r_j \\ -r_j & 0 & -\frac{2}{k} & r_i \\ 0 & -r_j & -r_i & 2\frac{\ell-1}{k} \end{pmatrix}, \tag{6.27}$$

that fixes the differential equation system of Eq. (6.19).

The Levin collocation method is restricted to definite integrals with finite boundaries which is not the case in Eq. (6.14). Nonetheless, we perform a change of variable $k \longrightarrow kr_i \equiv \tilde{k}$ and approximate the integral by the expression

$$C^\ell(r_i, r_j) = \frac{2}{\pi r_i^3} \int_{\tilde{k}_{\min}}^{\tilde{k}_{\max}} \mathrm{d}\tilde{k}\, \tilde{k}^2\, P_\Psi(\tilde{k})\, j_\ell(\tilde{k})\, j_\ell\left(\tilde{k}\,\frac{r_j}{r_i}\right), \tag{6.28}$$

with suitably chosen boundaries $\tilde{k}_{\min}$ and $\tilde{k}_{\max}$. The lower boundary is taken at the ℓ-dependent "point of growth" of the spherical Bessel functions (see [92]) at which the first significant values larger than 10^{-10} are obtained. The cutoff $\tilde{k}_{\max}$ is given by the maximum sampling value of 10^6. Considering the asymptotic form of spherical Bessel functions for large $\tilde{k}$,

$$\lim_{\tilde{k}\longrightarrow\infty} j_\ell(\tilde{k}) = \frac{1}{\tilde{k}} \cos\left(\tilde{k} - \frac{\pi}{2}\,(\ell+1)\right), \tag{6.29}$$

and recovering that $P_\Psi(k) \sim k^{-7}$ for large k-modes, we see that the integrand decays like $\tilde{k}^{-7}$ in this regime. Hence, there is negligible dependence on the upper integral boundary once it is chosen sufficiently large. Fast and accurate approximations of the spherical Bessel-, or equivalently, Hyperspherical functions are provided by the CLASS library that uses a recursion and WKB scheme in combination with Hermite interpolation (see [59, 92]).

6.3.4 *Sampling process*

The sampling process for each spherical harmonic mode ℓ can be summarized as follows:

1. We compute the covariance matrix C_{ij}^ℓ with $j \leq i$ (as the covariance matrix is symmetric) for radial positions r_i, r_j.
2. The coefficient matrix A_{ij} is obtained by Cholesky decomposition of the covariance matrix.
3. We draw $2\ell + 1$ uncorrelated Gaussian random numbers with unit variance for $m = 0$ and variance 0.5 for each positive orientation m.
4. These uncorrelated variables can be transformed to the corresponding, radially correlated, random variables $\Psi_i^{(\ell m)}$ by linear combination

$$\Psi^{(\ell m)}(r_i) = \sum_j A_{ij} x_j^{(m)}.$$

Since spherical harmonic coefficients of a real-valued potential field $\Psi(\vec{r})$ are generally complex numbers for $m > 0$, we sample two random numbers with variance 0.5 for the real and imaginary parts. This ensures that the sampled coefficients account for the correct angular power spectrum C^ℓ. We restrict ourselves to orientations larger or equal zero, as these modes already contain the full information of a real-valued function on that angular scale[4]. In total, this leads $2\ell + 1$ random numbers to be drawn at given ℓ-mode.

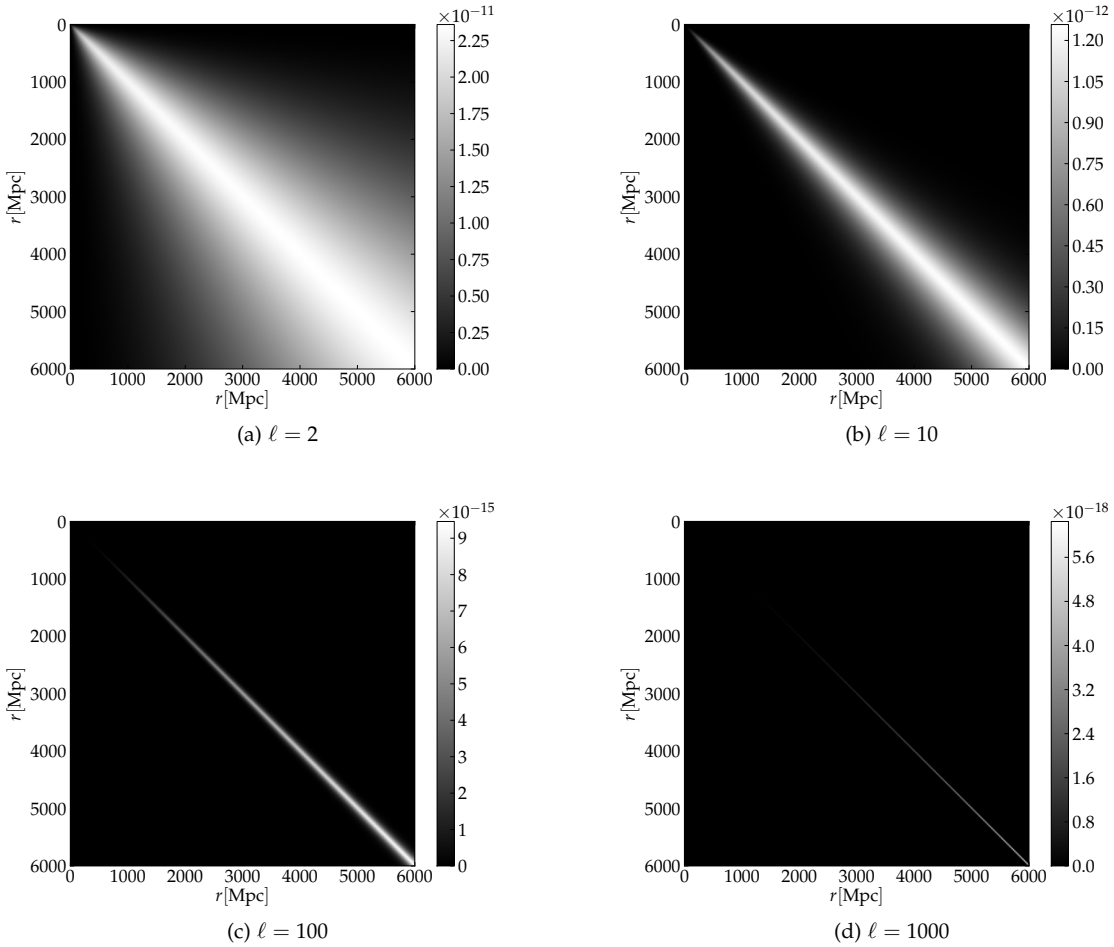

(a) $\ell = 2$ (b) $\ell = 10$

(c) $\ell = 100$ (d) $\ell = 1000$

Figure 6.5: These 2d plots show the covariance matrix entries that are assigned to the corresponding radii r_i and r_j given in Mpc. All matrices are diagonally dominant and amplitudes decrease with ℓ by almost seven orders of magnitude. The latter is caused by the strong decay of the initial power spectrum at large k-modes ($P_\Psi(k) \sim k^{-7}$). Radial correlation increases with distance from the centre which is expected as structures of given angular scale must have larger tangential extensions that itself lead to larger radial scales in a statistically isotropic initial universe. Radial correlation also increases for small ℓ-modes, as those describe angular patches corresponding to larger fluctuations in spatial scale.

The main advantages of this approach can be summarized by the following points:

- Since spherical harmonic coefficients are sampled directly, we do not have to allocate large 3d realisations of the Bardeen potential in real space. In addition, there is no conversion from cubic pixels to Healpix pixels with all complications at small radii and large ℓ-modes. Thus, small redshifts on the LTB lightcone are accessible which allows to study the coupling of LTB perturbation variables close to the void centre. Furthermore, perturbations in small voids of a few hundred Mpc extension can be studied without resolution problems.

- The memory-consuming part is now given by the Hermite interpolation of spherical Bessel functions performed in the CLASS library. The reason is a considerable amount of nodes that have to be stored in order to achieve sufficient accuracy. However, this can be controlled by proper subgroups of ℓ-modes for which the covariance matrices are computed simultaneously.

4 In fact, spherical harmonic coefficients of real-valued functions obey $a^{(\ell,-m)} = (-1)^m (a^{(\ell m)})^*$ and therefore coefficients with negative orientations m do not contain any additional degrees of freedom.

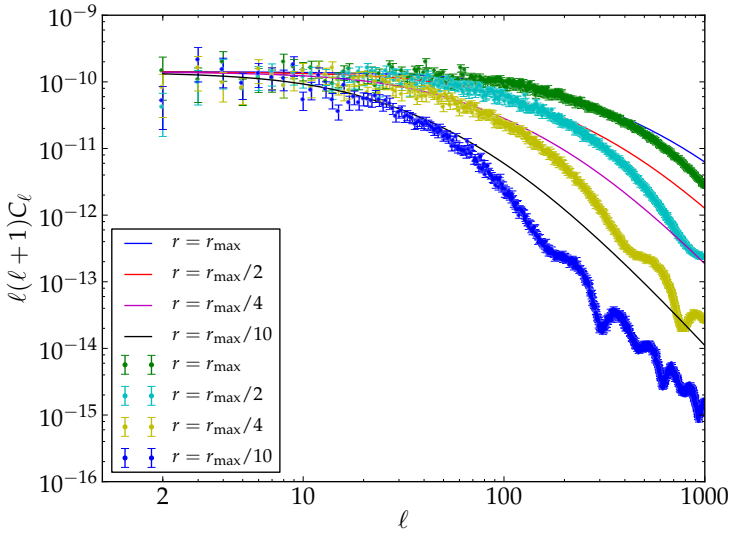

(a) 3d sampling and Healpix decomposition

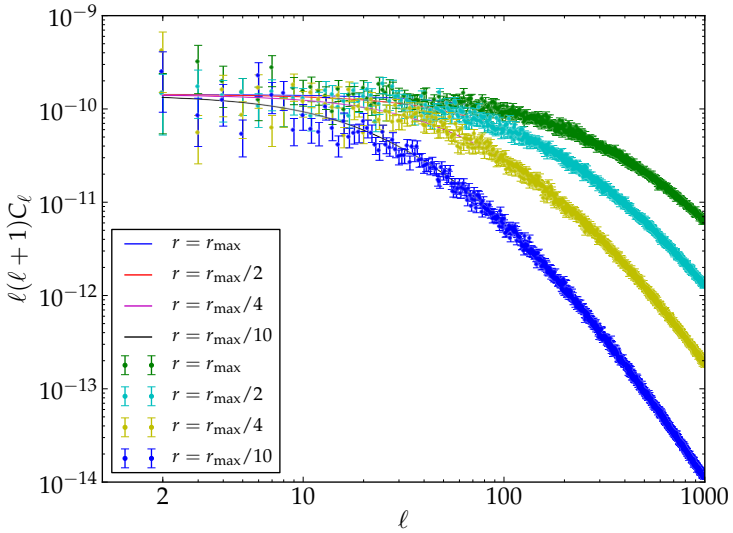

(b) Direct multivariate sampling

Figure 6.6: These figures show estimates of the angular power spectra from the spherical harmonic coefficients that have been sampled using the two different approaches. The theoretical spectra are plotted for comparison. In case of the decomposition of Healpix Maps in a 3d box, there is significant deviation from the theoretical spectra that seems to be caused by resolution problems on small angular scales.

- The generalization to asymptotically curved LTB models seems now straightforwardly possible as CLASS provides accurate approximations of Hyperspherical functions. It has been shown that LTB models of this kind partially remove the tension to observational data ([19, 101]). Thus, we are able to model the evolution of perturbations in these environments as well.
- The initial power spectrum can easily be exchanged in Eq. (6.14) such that alternative spectra of the primordial curvature perturbation or tensor modes can be considered. The only requirement for convergence is that the integrand decays sufficiently fast at large k-modes.

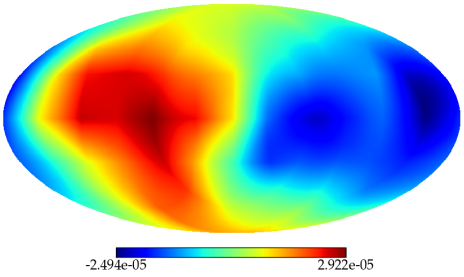

(a) 3d sampling: $r = r_{\mathrm{min}}$

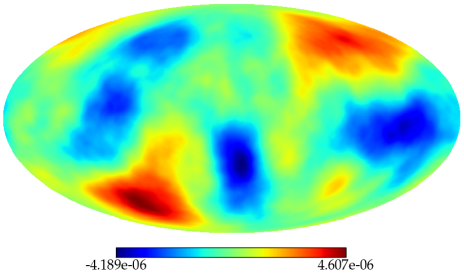

(b) Multivariate sampling: $r = r_{\mathrm{min}}$

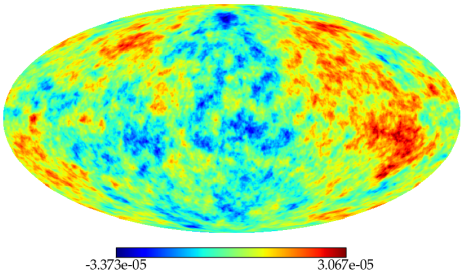

(c) 3d sampling: $r = r_{\mathrm{max}}/4$

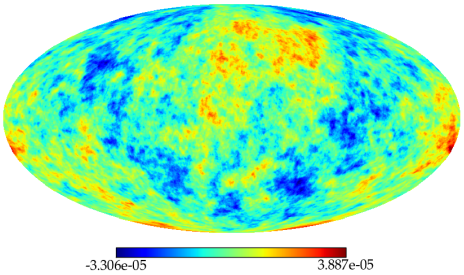

(d) Multivariate sampling: $r = r_{\mathrm{max}}/4$

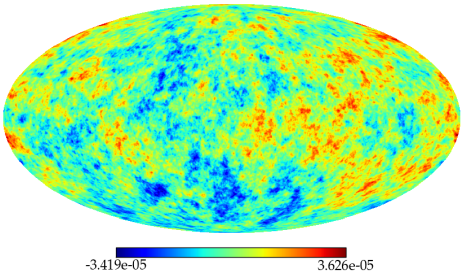

(e) 3d sampling: $r = r_{\mathrm{max}}/2$

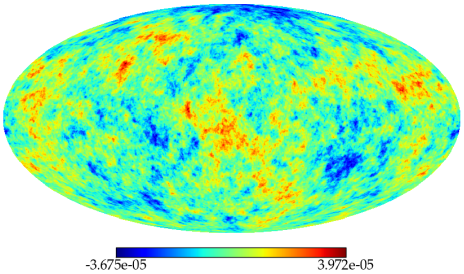

(f) Multivariate sampling: $r = r_{\mathrm{max}}/2$

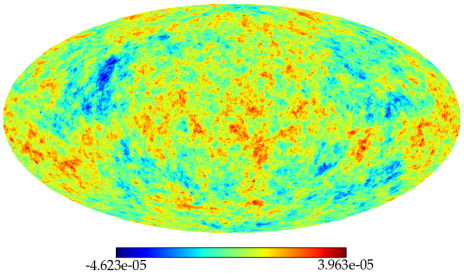

(g) 3d sampling: $r = r_{\mathrm{max}}$

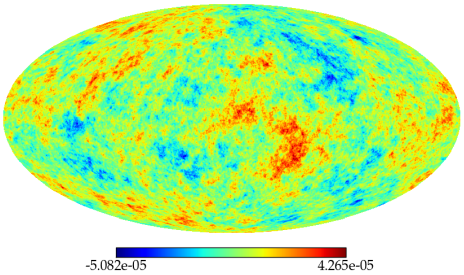

(h) Multivariate sampling: $r = r_{\mathrm{max}}$

Figure 6.7: These Mollweide projections show Healpix Maps that are constructed from the spherical harmonic coefficients obtained from either the 3d sampling technique or multivariate Gaussian sampling. Regarding subfigure (a), the angular resolution of structures on spherical shells of small radii is strongly limited by the resolution of the 3d cube, because even the pixel structure can be seen. This problem can be resolved with the new multivariate sampling technique as no 3d realisation is required anymore. At sufficiently large radii one cannot see any significant differences in the properties of the fluctuations although there are profound differences in the angular power spectra (see Fig. (6.6)).

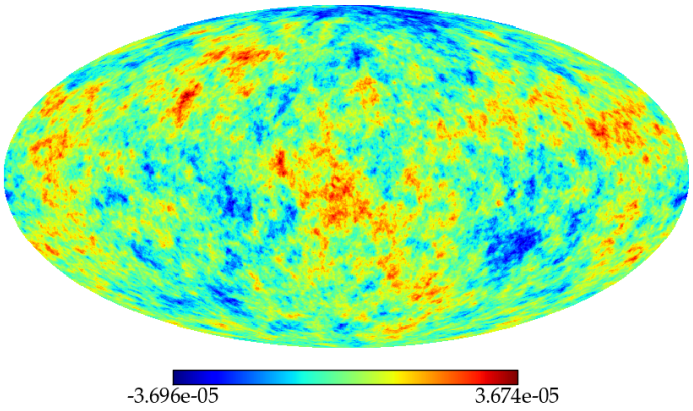

(a) $r = r_{\max}/2 - \Delta r$

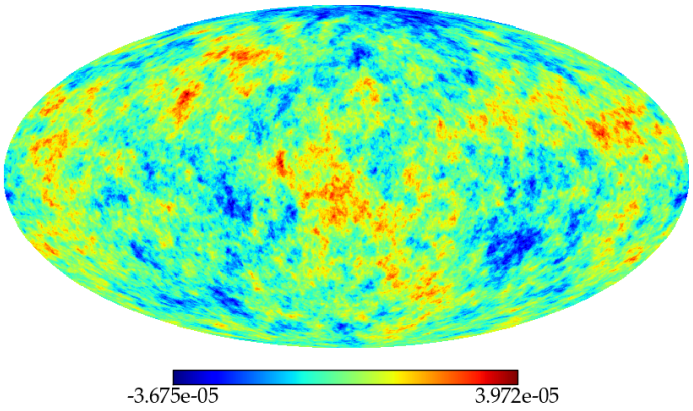

(b) $r = r_{\max}/2$

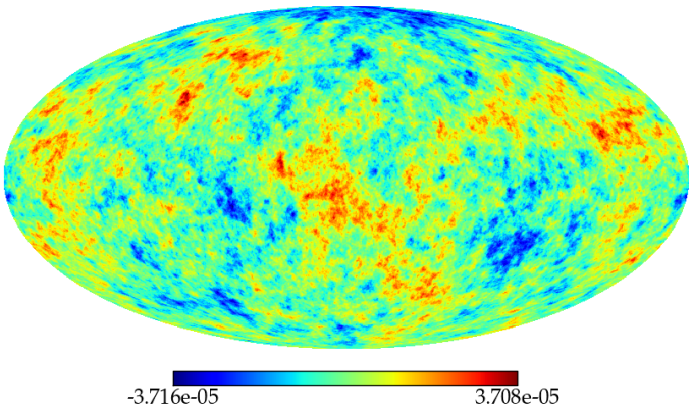

(c) $r = r_{\max}/2 + \Delta r$

Figure 6.8: These figures show consecutive Healpix Maps around a fiducial radius $r = r_{\max}/2 = 3000$Mpc with $\Delta r \sim 24$Mpc. The correlation of fluctuations of large angular scale can clearly be seen.

Although the last two points are worth being investigated, they are beyond the scope of this analysis and will be postponed to future work.

Using this technique, the Gaussian realisation reproduces the correct initial angular power spectrum also for large ℓ-modes and the resolution problem at small radii is resolved (see Figs. (6.6) and (6.7)). The covariance matrices for different ℓ-modes are shown in Fig. (6.5). The correlation is expected to increase with radius as fluctuations at large distances from the centre have to be larger in spatial scale in order to appear under the same angle. Fig. (6.7) shows Healpix Maps of spherical shells at appropriately chosen radii. Considering maps of increasing radius, one can see that potential fluctuations are indeed correlated. This correlation is more prominent on large angular scales (see Fig. (6.8)) as suggested by the shape of the covariance matrices.

6.4 SPHERICAL HARMONIC COEFFICIENT PROFILES

As shown by Clarkson et al. (2009) in [29], the only remaining gauge-invariant polar perturbation in the FLRW limit with initial scalar perturbations is $\varphi^{(\ell m)} = -2\Psi^{(\ell m)}$ (see also App. (C)). This turns out to be a very simple initial configuration for our case study. Nonetheless, initial coefficient profiles for LTB gauge-invariants have to obey certain regularity properties at the radial origin and need to be slightly adapted to the grid structure applied. We therefore, artificially, have to modify and extend the profiles in the following way (see also Fig. (6.9) for an illustration):

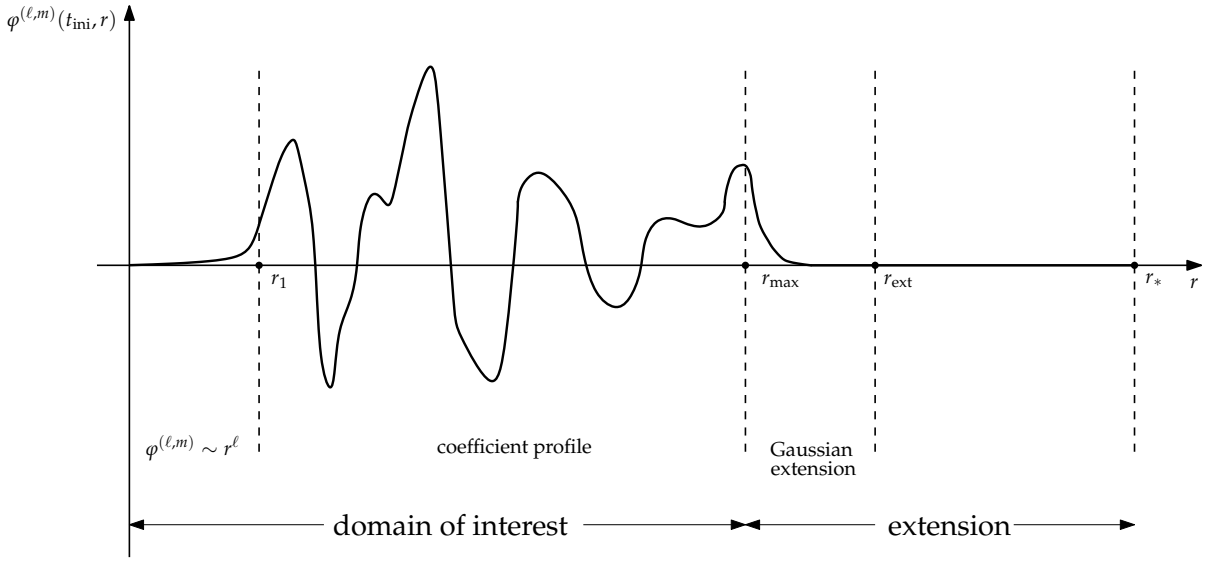

Figure 6.9: Schematic summary of all modifications performed on the initial profiles: At small radii, we require the regularity condition to hold which is then smoothly matched to the spherical harmonic coefficient profiles which were either extracted from Healpix Maps or sampled from the theoretical covariance matrix. In order to enforce the profile dropping to zero in a smooth way, a Gaussian extension is applied such that a vanishing initial profile is achieved in the extension region $[r_{\rm ext}, r_*]$.

1. As shown by GMG in [54], initial profiles have to obey $\varphi^{(\ell m)} \sim r^\ell$ close to the radial origin in order to represent regular solutions. We therefore modify the profile at small radii (typically up to the first radial bin) to enforce this functional shape. We then match this region smoothly to the exterior profile. However, for practical reasons, it is sufficient to require the first and second radial derivatives to vanish at the origin which can be achieved by setting the Bardeen potential amplitude to zero at the first two radial bins.

2. The boundary of the domain of interest $r_{\rm max}$ and the numerical boundary r_* are different, since the latter is constructed to be causally disconnected from $r_{\rm max}$ (see Chapt. (5)). In the region $[r_{\rm max}, r_*]$, all perturbation variables have to be initially zero such that no propagating mode can be excited in this region that influences the results in the domain of interest.

3. In order to achieve a smooth transition, we define a transition region $[r_{\max}, r_{\text{ext}}]$ where the initial profile is extended by a Gaussian function centered at $r_{\max}$ and a FWHM of one fifth of the size of the extension region.

The extension scale is obviously an arbitary parameter of the initial profiles. Its influence on the final results will be probed and quantified below.

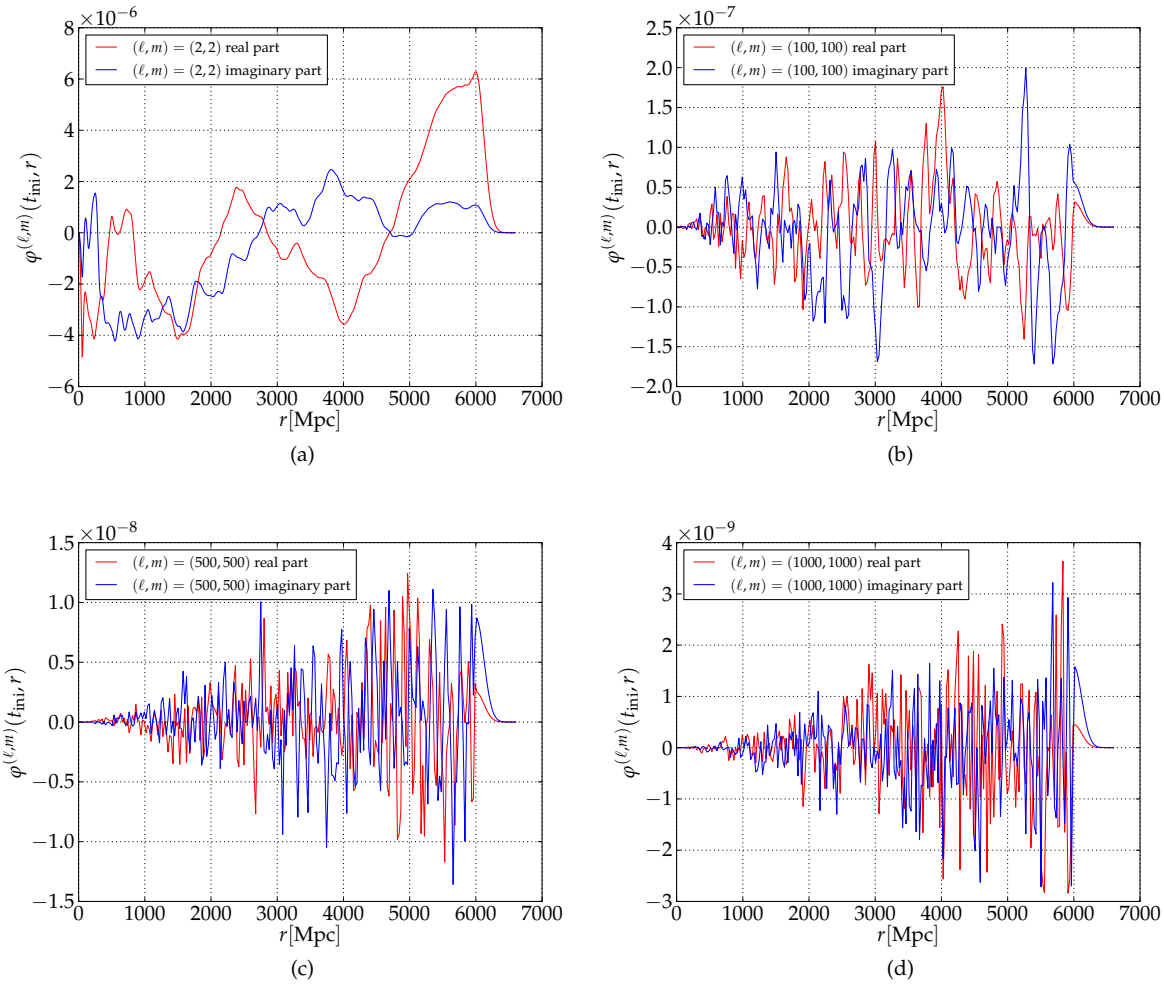

Figure 6.10: Examples for initial radial profiles of $\varphi^{(\ell m)}$ for exemplary ℓ- and m-modes: The amplitude of decreasing angular scales (increasing ℓ-modes) drops by almost three orders of magnitude. This is due to the steepness of the initial potential power spectrum ($P_\Psi(k) \sim k^{-7}$) on small scales that causes high ℓ-modes to be suppressed.

Summing up, we have overall initial conditions,

$$\begin{aligned} \varphi^{(\ell m)}(t_{\text{ini}}, r) &= -2\Psi^{(\ell m)}(t_{\text{ini}}, r)\,, \\ \chi^{(\ell m)}(t_{\text{ini}}, r) &= \varsigma^{(\ell m)}(t_{\text{ini}}, r) = 0\,, \\ \dot{\chi}^{(\ell m)}(t_{\text{ini}}, r) &= \dot{\varphi}^{(\ell m)}(t_{\text{ini}}, r) = \dot{\varsigma}^{(\ell m)}(t_{\text{ini}}, r) = 0\,, \end{aligned} \tag{6.30}$$

for the metric perturbations which respect the grid structure and boundary conditions posed by the problem itself. The initial fluid perturbations $(\Delta^{(\ell m)}, w^{(\ell m)}, v^{(\ell m)})$ are then constrained by Eqs. (4.8) - (4.10).

Examples of radial profiles of the spherical harmonic coefficients are shown in Fig. (6.10). Due to the strong decay of the initial potential power spectrum at large k-modes (recover again Eq. (6.2)), small angular scales are highly suppressed leading to a decrease of the coefficient amplitudes of nearly three orders of magnitude in the range from $\ell = 2$ to $\ell = 1000$.

7

RESULTS AND DISCUSSION

7.1 SUMMARY

The numerical scheme outlined in Chapt. (5) has been applied to the initial profiles which have been obtained using methods laid out in Chapt. (6). Corresponding results on the spacetime evolution of the given set of LTB gauge-invariant perturbations are shown in the present chapter. Starting from pure scalar perturbations in the asymptotic FLRW limit of the past null cone, spherical harmonic coefficients of perturbation variables have been evolved forward in time for a representative set of angular scales. Results are concisely presented in terms of angular power spectra that have been evaluated at different redshifts on the observer's backward lightcone. This allows to study statistical properties of the dynamical behaviour perturbed LTB spacetimes which is inherently different from perturbed FLRW spacetimes. In fact, power spectra at low redshifts show partially significant contributions of initially zero perturbation variables which have been excited during spacetime evolution. This generic coupling between different perturbation types is quantified in the following. By comparison to the case of uncoupled spacetime evolution for different void scenarios, the coupling strength for the generalized gravitational potential and density contrast is estimated. For deep voids with steep density slope, we find huge couplings of 28% to even 40% in extreme cases. We close this chapter with a detailed discussion of the results that have been presented so far.

7.2 ANGULAR POWER SPECTRA

Following the multivariate sampling approach outlined in Sect. (6.3), realisations of radially correlated spherical harmonic coefficients for the Bardeen potential can be obtained on an initial hypersurface being sufficiently homogeneous and isotropic. In comparison to the 3d Gaussian sampling described in Sect. (6.2), the multivariate sampling approach does not suffer from resolution problems and the corresponding initial profiles resemble the correct angular power spectra at all radii and angular scales (recover again Fig. (6.6)). For each spherical harmonic mode (ℓ, m), the radial coefficient profiles are numerically propagated forward in time. Since we deal with statistical information and want to explore general properties of the spacetime evolution of perturbations in void models, we compute estimates of the angular power spectra,

$$C^{\ell}(z) = \sum_{m=-\ell}^{\ell} \left| a^{(\ell m)}(t(z), r(z)) \right|^2 , \tag{7.1}$$

for all perturbation variables and evaluate them on the unperturbed LTB-lightcone described by Eqs. (3.34) and (3.35).

As we only consider a single Gaussian realisation of the spherical harmonic coefficients of the scalar potential field, we can just compute estimates of the angular power spectra and quantify their statistical error to be (similar to cosmic variance, see [78])

$$\langle (C^{\ell} - C^{\ell}_{\text{theor}})^2 \rangle = \frac{2}{2\ell + 1} (C^{\ell})^2 . \tag{7.2}$$

In this way, we can investigate the dynamical behavior of each perturbation variable at different redshifts z and angular scales ℓ.

It shall be mentioned that the derivation of Eq. (7.2) assumes Gaussianity of the corresponding 3d potential field which is generally not preserved over spacetime evolution on LTB backgrounds. However, since the perturbation equations (4.4) - (4.10) decouple into the spherical harmonic modes (ℓ, m), different modes are not correlated at first order. Thus, the spherical harmonic coefficients remain independent random variables for each radius r and time t such that Gaussianity is preserved in each spherical shell due to the central limit theorem. We can therefore safely compute the statistical error of the angular power spectra using Eq. (7.2) on the backward lightcone.

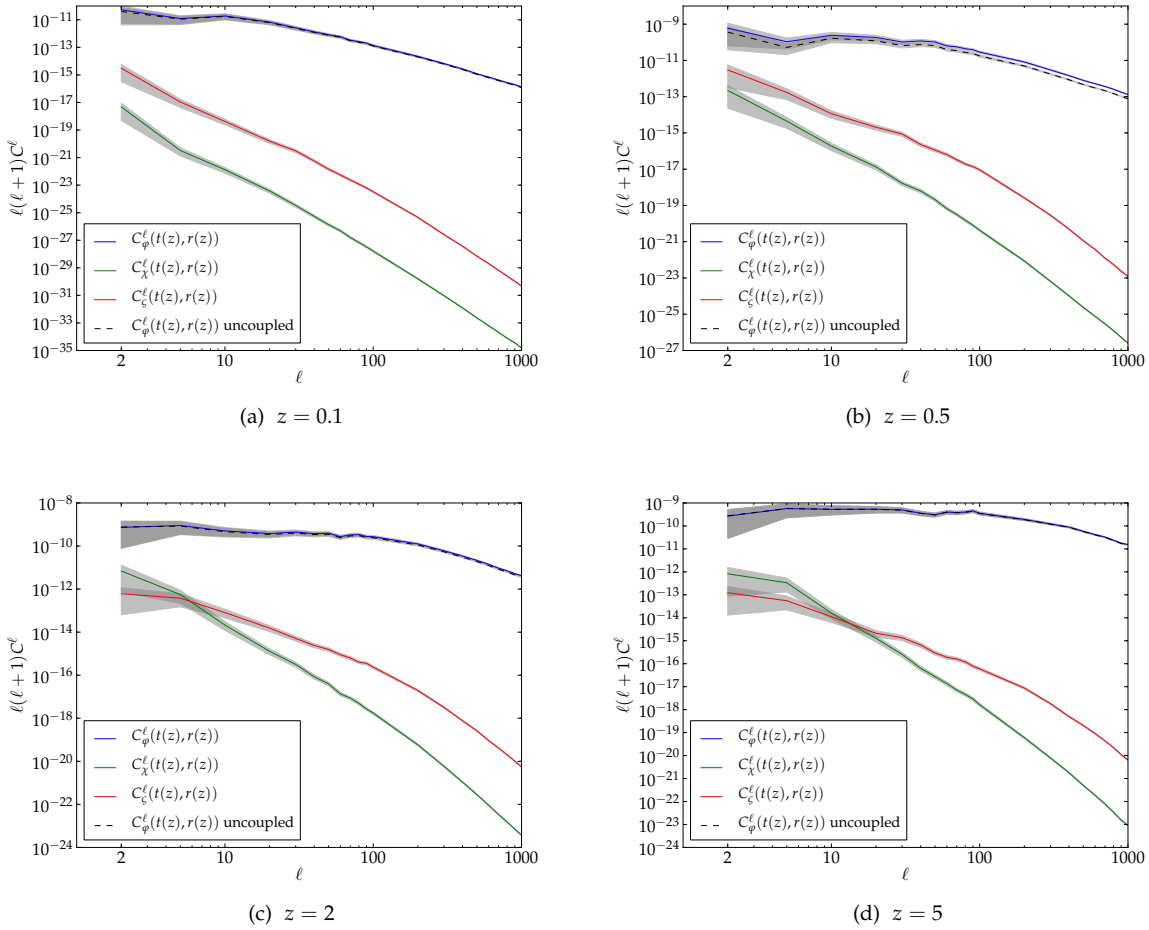

(a) $z = 0.1$ (b) $z = 0.5$

(c) $z = 2$ (d) $z = 5$

Figure 7.1: Angular power spectra of the metric perturbations $\{\varphi, \varsigma, \chi\}$ evaluated on the LTB backward lightcone for different redshifts: The gray-shaded areas indicate the uncertainty in the estimation of the power spectra due to statistical fluctuations in the finite sample. We consider a Gaussian-shaped void according to Eq. (3.38) with $\Omega_{\text{in}} = 0.2$ and $L = 2$ Gpc that is asymptotically embedded into an EdS model.

Fig. (7.1) shows angular power spectra for each LTB gauge-invariant at exemplary redshifts $z \in \{0.1, 0.5, 2.0, 5.0\}$. Starting from the initially sampled Bardeen potential that leads to a nontrivial contribution to φ, but to vanishing χ and ς variables, we clearly see excited modes of the latter at smaller redshifts. Since initial amplitudes of large k-modes are suppressed due to the form of the Bardeen potential power spectrum, we observe the same behavior in the angular power spectra on small angular scales. The solution to the uncoupled evolution equation for φ, which is constrained

by Eq. (7.3), is considered as well for completeness. It indicates the difference between the coupled and uncoupled cases for the spacetime evolution of φ. This difference is increasing with decreasing redshift as the void deepens significantly at small z. As a consequence, non-vanishing contributions of the remaining two gauge-invariants are excited that slow down the decay of φ in the interior of the void compared to the uncoupled solution[1]. The effects of coupling on the evolution of the generalised gravitational potential will be analysed in detail in Sect. (7.3). Interestingly, coupling decreases again significantly at $z = 0.1$, since the low shear limit is reached. Close to the void center, the background anisotropy is small and the LTB solution can be approximated as an open FLRW solution. Thus, no significant coupling can be expected in this region.

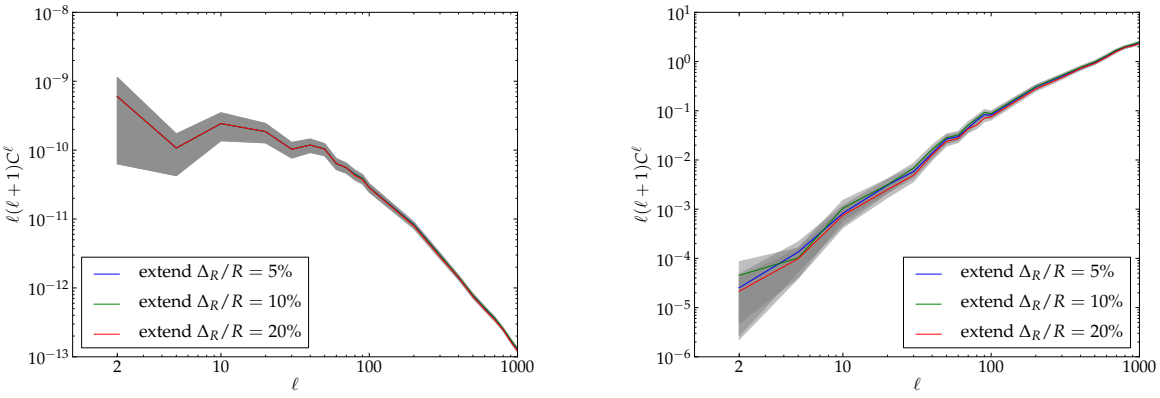

(a) C_φ^ℓ at $z = 0.5$

(b) C_Δ^ℓ at $z = 0.5$

Figure 7.2: Influence on artificial modifications on the initial profile (namely the extension factor Δ_R) on the angular power spectra for φ and Δ at redshift $z = 0.5$: This particular redshift has been chosen because Fig. (7.1) indicates that the strongest influence of the inhomogeneous background on the spacetime evolution can be expected in this region of the backward lightcone.

As outlined in Sect. (6.4), the initial profiles were augmented by a Gaussian tail that drops to zero within a small extension region. This way, the domain of interest and the outer region up to the artificial boundary condition can effectively be matched. This Gaussian extension is an artificial modification of the initial profiles and we need to investigate its influence on the final angular power spectra. For quantifying this influence, several runs for extensions $\Delta_R = 5\%$, 10%, and 20% of the size of the domain of interest have been performed. Whereas the results in Fig. (7.2) indicate that the extension scale has no significant influence on the final results of C_φ^ℓ, the amplitude of C_Δ^ℓ shows a small dependence on Δ_R. This can be expected as the extension scale introduces an artificial spatial gradient of φ at the boundary of the domain of interest. The master equations (4.4) - (4.7) do not contain any spatial gradients of φ, but the fluid constraint equations (4.8) - (4.10) strongly depend on φ' and φ''. However, deviations between different results for C_Δ^ℓ are well enclosed by the estimated statistical error. We can therefore safely apply an extension of 10% of the domain of interest.

7.3 COUPLING STRENGTH A FUNCTION OF VOID DEPTH AND SIZE

We finally want to quantify the coupling effects on the evolution of perturbation variables in a statistical way. Starting from an initial scalar perturbation as Gaussian random field with vanishing mean, we want to compare its evolution on different angular scales for the coupled and uncoupled case. As the gauge-invariant variables φ and Δ represent the generalized gravitational potential and density contrast (see [29] and Chapt. (4)), we restrict our analysis to these two variables in particular.

1 Since spatial hypersufaces of the LTB patch are negatively curved, we can expect gravitational potentials to decay.

Their uncoupled evolution is described by

$$\ddot{\varphi} = -4H_\perp \dot{\varphi} + \frac{2\kappa}{a_\perp^2}\varphi\,, \tag{7.3}$$

$$\alpha\Delta = -\frac{1}{Z^2}\varphi'' + \frac{1}{Z^2}\left(C - 4\frac{a_\parallel}{r a_\perp}\right)\varphi' + \left(H_\parallel + 2H_\perp\right)\dot{\varphi} + \left[\frac{\ell(\ell+1)}{r^2 a_\perp^2} + 2D\right]\varphi\,. \tag{7.4}$$

The fully coupled system of master and constraint equations given by Eqs. (4.4) - (4.10) is then evolved simultaneously in time while using the same initial coefficient profiles. We compute the corresponding angular power spectra C_φ^ℓ and $C_{\varphi,\mathrm{uc}}^\ell$ for both cases on the past null cone. In order to quantify the coupling strength, the relative deviation ϵ^ℓ of the square roots of the spectra

$$\epsilon^\ell(z) = \left|\frac{\sqrt{C_x^\ell\left(t(z), r(z)\right)} - \sqrt{C_{x,\mathrm{uc}}^\ell(t(z), r(z))}}{\sqrt{C_{x,\mathrm{uc}}^\ell(t(z), r(z))}}\right|\,, \text{ with } x = \varphi, \Delta \tag{7.5}$$

is computed with combined statistical errors given by

$$\Delta\epsilon^\ell = \frac{\epsilon^\ell}{\sqrt{C_{x,\mathrm{uc}}^\ell}}\sqrt{\left(\frac{\Delta C_{x,\mathrm{uc}}^\ell}{2C_{x,\mathrm{uc}}^\ell}\right) + \left(\frac{\Delta C_x^\ell}{2C_x^\ell}\right) + \frac{1}{2}\left(\frac{\Delta C_{x,\mathrm{uc}}^\ell}{C_{x,\mathrm{uc}}^\ell}\right)^2 \left|\sqrt{C_x^\ell} - \sqrt{C_{x,\mathrm{uc}}^\ell}\right|^2}\,. \tag{7.6}$$

The coupling strength can now be investigated as a function of the void size and void depth. For this purpose, we consider Gaussian-shaped density profiles described by Eq. (3.38) with variable central depth Ω_{in} and extension L. Each void profile is asymptotically embedded into a background EdS model with Hubble parameter $h = 0.7$. Considering exemplary redshifts of $z = 0.5$ and $z = 5$, we perform two runs with different configurations:

1. Case 1: fixed void size $L = 2000$ Mpc and modified void depth $\Omega_{\mathrm{in}} = 0.2,\ 0.4,\ 0.6,\ 0.8$, and 1.0 (FLRW limit)
2. Case 2: fixed void depth $\Omega_{\mathrm{in}} = 0.2$ and modified void size $L = 300,\ 500,\ 1000,\ 1200,\ 1500,\ 1800,\ 2000$ Mpc

The coupling strength in case of varying void depth (Case 1) and fixed void size of 2 Gpc is shown in Fig. (7.3). As expected, coupling increases with void depth as the background shear and curvature gradients decrease as well and the FLRW limit of vanishing coupling is correctly reproduced. Coupling decreases with increasing redshift as the void itself evolves in time and has significant depth only in the non-linear FLRW regime ($z \leq 1.0$). The huge deviations of the uncoupled and coupled case are nonetheless surprising as it rises up to nearly $\sim 30\%$ for a deep void with a density contrast of $\Omega_{\mathrm{out}} - \Omega_{\mathrm{in}} = 0.8$ with respect to the background EdS model. Deep voids cause large off-center anisotropies quantified by the difference between the radial and tangential Hubble rate (shear $\sigma \sim H_\parallel - H_\perp$). As laid out in Chapt. (4), this background shear can be identified as one of the main contributions to the coupling. In case of big voids of Gpc scale, this coupling is also present at large distances from the center. Coupling increases with angular scale as leading coupling terms scale quadratically with ℓ which was also found in [41].

Results on Case 2 are shown in Fig. (7.4). We see prominent coupling up to 30% for a large 2 Gpc void at redshift $z = 0.5$. In case of smaller voids, the coupling is not significant, since the radial coordinates on the backward lightcone yield $r(z = 0.5) \sim 1500$ Mpc (see Tab. (1)) and therefore the density contrast and the corresponding spacetime anisotropy are already small there. However, this does not mean that coupling is small in the interior of small voids. In fact, one observes the contrary for small redshifts as shown below. Nonetheless, as z increases, coupling decreases until it is not significantly measurable anymore at $z = 5$ when the lightcone approximates an FLRW shape.

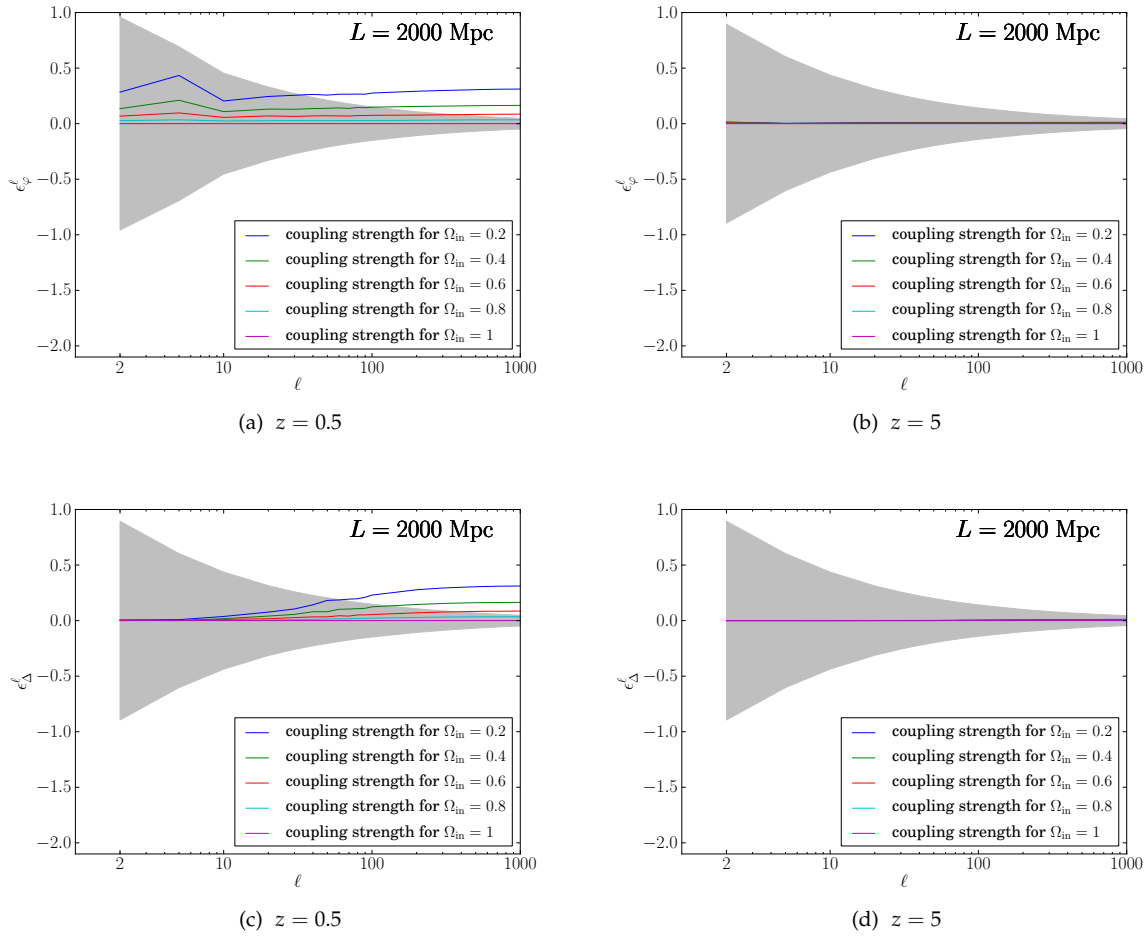

(a) $z = 0.5$ (b) $z = 5$

(c) $z = 0.5$ (d) $z = 5$

Figure 7.3: Coupling strength ϵ^ℓ for the two gauge-invariants φ and Δ (as defined in Eq. (7.1)) for different void depths $\Omega_{in} = 0.2,\ 0.4,\ 0.6,\ 0.8,\ 1.0$ at a fixed void size of $L = 2$ Gpc. The results are evaluated on the corresponding LTB past lightcones for two exemplary redshifts $z = 0.5$ and $z = 5$. The grey-shaded area marks the statistical error due to fluctuations in the finite sample that was estimated by Eq. (7.2) and presented here for the EdS limit. At redshift $z = 0.5$, we observe the coupling strength to increase with increasing void depth up to nearly 30% for the strongest deviation of $\Omega_{in} = 0.2$ from the EdS solution the void is embedded in. This is also significant regarding the statistical fluctuation in the finite sample. At higher redshifts, the coupling strength quickly drops as soon as the lightcone becomes FLRW-like. Coupling increases with void depth as expected, since the space-time induced anisotropy (quantified by the shear) and radial dependence of the curvature profile which are the main sources of perturbation coupling are also significantly increasing with void depth and density slope. We also see an increase with multipole order ℓ which can also be predicted, since one of the coupling terms in Eq. (4.5) as well as Eq. (4.9) scales quadratically with ℓ and quickly dominates the coupling strength on small angular scales. The FLRW limit of vanishing coupling is clearly reproduced in both cases.

Fig. (7.5) shows the coupling strength averaged over all angular scales as function of void depth and void size according to the two cases considered here. The results are shown for several redshifts on the LTB past null cone such that different stages of the void evolution can be probed. In case of varying void depth, we see significant couplings of, on average, 25% for deep voids of $\Omega_{in} = 0.2$. This value is decreasing with decreasing void depth as expected. Coupling also decreases with larger redshift for $z \geq 0.5$ which has already been observed in Fig. (7.3). However, at $z = 0.1$, there is considerably less coupling of just a few percent. This value is expected to decrease for even smaller redshifts. The LTB lightcone coordinates presented in Tab. (1) indicate that $z = 0.1$ is placed well within a void of 2 Gpc

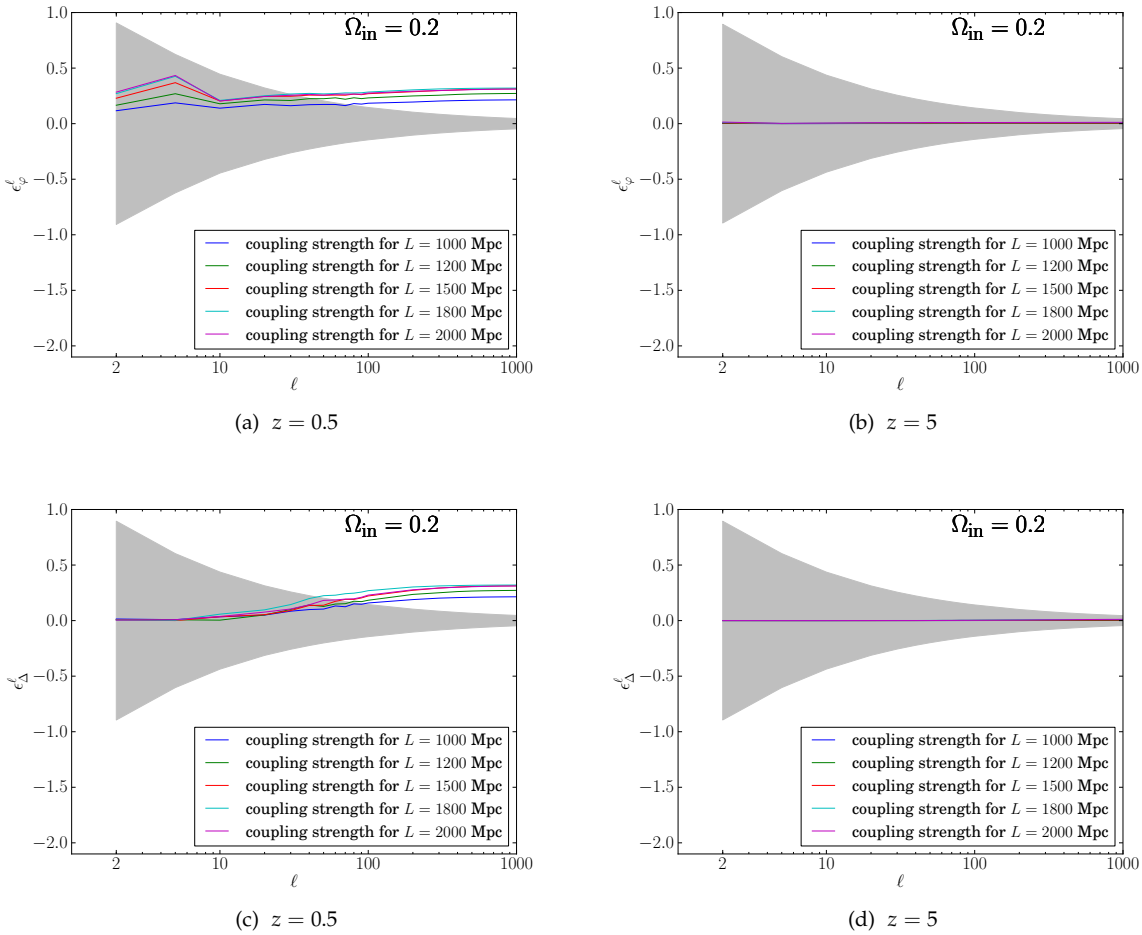

(a) $z = 0.5$ (b) $z = 5$

(c) $z = 0.5$ (d) $z = 5$

Figure 7.4: Coupling strength ϵ^ℓ for the two gauge-invariants φ and Δ for different void extensions $L = 1000$, 1200, 1500, 1800, and 2000 Mpc at fixed void depth. The results are evaluated on the LTB past lightcones for the two exemplary redshifts $z = 0.5$ and $z = 5$. The grey shaded areas mark again the statistical uncertainty of the coupling strength in case of EdS. As already observed in Fig. (7.3), we see couplings up to 30% at redshift $z = 0.5$ which drops to insignificant values at $z = 5$ as the lightcone is not strongly affected by the void in this region.

extension where no significant density slope and corresponding shear is present. Thus, in the vicinity of the void center, the perturbed LTB solution is well described by a perturbed FLRW solution with negative spatial curvature.

The averaged coupling strength as function of void size shows an increasing coupling with decreasing void size for $z = 0.1$. In case of small voids of a few hundred Mpc, the observed coupling raises up to 40% which is rapidly decreasing with redshift since the asymptotic FLRW limit is reached at comparably small z. However, even in this limit coupling is not completely vanishing as gravitational wave modes excited within the void propagate outwards and interact with perturbations φ in more distant regions from the center. At larger redshifts, we observe the coupling strength to increase with increasing void size since small scale voids do not obey a significant depth at radial positions corresponding to $z \geq 0.5$ on the PNC.

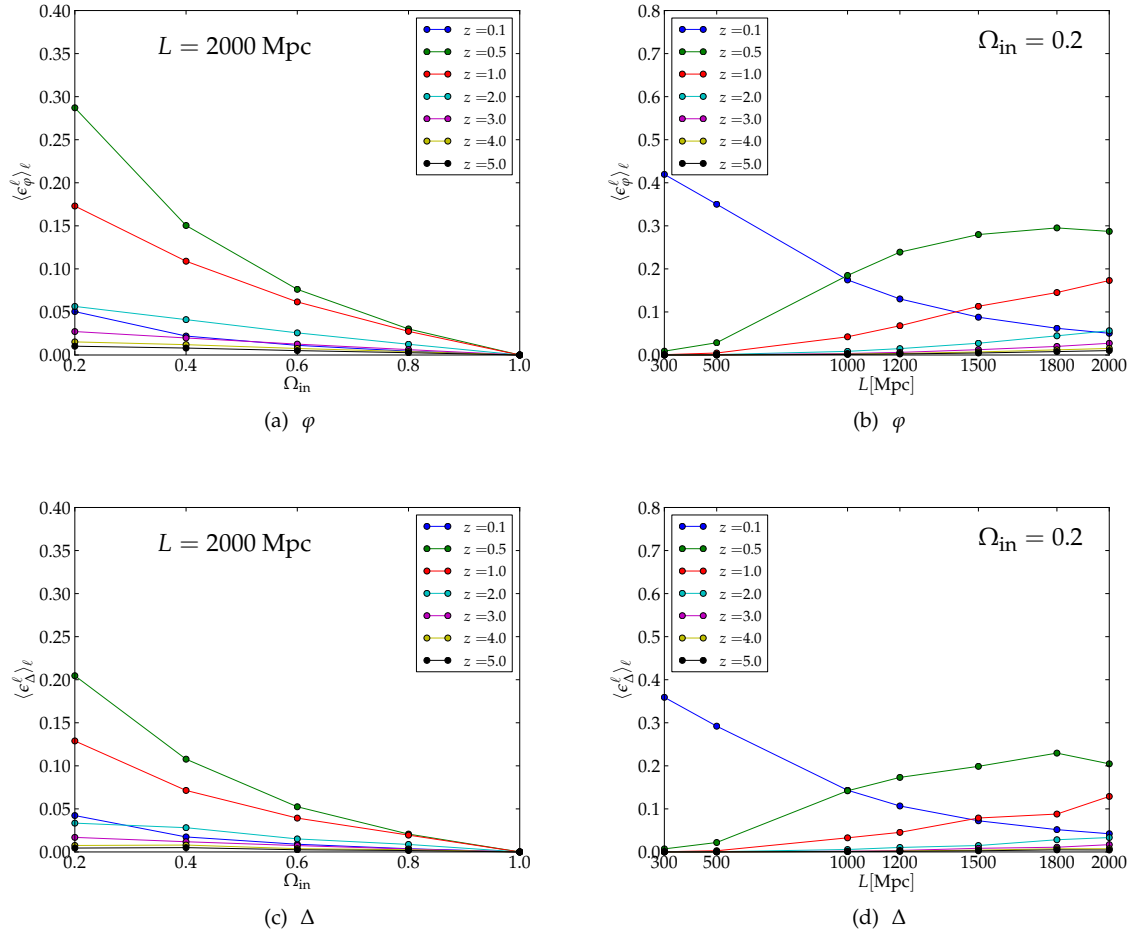

(a) φ (b) φ

(c) Δ (d) Δ

Figure 7.5: Averaged coupling strength $\langle \epsilon^\ell \rangle$ as function of void depth and size for decreasing redshifts: The coupling strength according to the definition of Eq. (7.5) is averaged over all angular scales and then plotted for the two different scenarios considered. (a) and (c) show the averaged coupling strengths as functions of void depth $\Omega_{\rm in}$ at fixed void size. The behaviour with void size at fixed void depth is shown in (b) and (d). As already observed in Figs. (7.3) and (7.4), coupling increases with void depth and also with decreasing redshift reaching averaged values of 28% in case of φ and 20% in case of Δ. For small redshifts ($z = 0.1$) in large voids, no significant couplings can be observed as perturbations are located well within the low shear limit close to the void centre. In case of a fixed void depth and varied void size, we see an increase in the coupling strength with void size for larger voids. This is caused by the fact these models still have significant depth at $z > 1$ whereas at larger redshifts we essentially probe the coupling in the asymptotic FLRW regime. Small and deep voids of sub-Gpc-scale show partially extreme values of the coupling strength up to 40% at small redshifts as the slope of the void density profile and hence the off-centre anisotropy are very strong there. However, coupling decreases significantly in these cases as the asymptotic FLRW regime is reached at smaller redshifts.

7.4 DISCUSSION

Perturbation theory in inhomogeneous backgrounds is inherently more complicated than in standard FLRW models. Not only the coupling of the gauge-invariant perturbations (necessarily described by partial instead of ordinary differential equations), but also their physical interpretation are very challenging. Nonetheless, it is necessary to perform this analysis in order to add further constraints on LTB models and, eventually, to rule them out on a solid basis. The present work does not yet address the physical interpretation of these results and therefore does not enable a direct comparison to FLRW

z	$r(z)$[Mpc]	$t(z)$[Mpc/c]
0.1	355.00	2515.76
0.5	1563.01	1557.57
1.0	2501.64	1011.02
2.0	3613.97	550.23
3.0	4276.95	357.97
4.0	4729.37	255.71
5.0	5063.32	194.52

(a) $\Omega_{\text{in}} = 0.2,\ L = 300$ Mpc

z	$r(z)$[Mpc]	$t(z)$[Mpc/c]
0.1	306.50	2563.17
0.5	1386.31	1729.35
1.0	2440.38	1115.76
2.0	3686.05	591.11
3.0	4403.68	380.11
4.0	4887.78	270.8
5.0	5243.44	205.54

(b) $\Omega_{\text{in}} = 0.2,\ L = 2000$ Mpc

z	$r(z)$[Mpc]	$t(z)$[Mpc/c]
0.1	398.62	2474.81
0.5	1571.80	1554.16
1.0	2508.78	1009.45
2.0	3620.21	549.48
3.0	4282.75	356.90
4.0	4734.89	255.37
5.0	5068.65	194.27

(c) FLRW limit

Table 1: Tables of LTB lightcone coordinates for three exemplary void models with different depths and sizes.

models. Carrying out an intermediate step, we analysed the coupling strength of the gauge-invariants in a cosmological environment starting from a dark matter power spectrum in the FLRW limit. As we are able to distinguish scalar-, vector- and tensor perturbations on initially homogeneous and isotropic hypersurfaces, we started from a scalar gravitational potential Ψ. By comparing perturbed FLRW metrics and perturbed LTB metrics in the FLRW limit in a general gauge, the FLRW Bardeen potential Ψ can be related to the LTB gauge-invariants (see [29] and App. (C)). It turns out that $\varphi = -2\Psi$ is the only remaining expression which yields a simple initial configuration for our setup. We can then study the coupling effect on the evolution of this generalized gravitational potential and the corresponding generalized density contrast Δ. For particularly deep and large voids (as needed to recover the distance redshift relation of type Ia SNe and measurements of the local Hubble rate ([33, 42, 75])), we find an averaged coupling strength 28% for the generalized gravitational potential and 20% for the generalised density contrast at redshifts $z < 1$. These results are in agreement with previous considerations of February et al. (2014) ([41]) as they find maximum deviations of the amplitudes of φ of around 30% well within deep voids at late times.

Analytical treatments in the framework of second order FLRW perturbations (see [72]) predict a non-negligible coupling as well. In fact, considering second order perturbations of a background EdS model in RW gauge yields very similar evolution equations for the corresponding second order quantities. The void itself is modeled by isotropic first-order perturbations and general second order perturbations are placed "on top" of these. However, a full analysis of this formalism with cosmological initial conditions has not yet been performed in RW gauge and therefore only general arguments about the growing and decaying modes of second order perturbations can be produced (see [72] for details). Although one can argue that, at second order, the influence of non-scalar perturbations on the scalar potential or density contrast are present and even growing in time, this does not allow any direct quantitative comparison with the exact treatment of linear perturbations in voids so far. Nonetheless, with the current numerical scheme at hand, such comparisons can, in principle, be made and the accuracy of the second order FLRW approach can directly be studied.

So far, coupling effects of perturbation variables or even linear structure growth in LTB models have been neglected in previous analyses as corrections due to the background shear were estimated to be of percent level. In fact, we found percent level corrections for voids that are not significantly deep, but those voids do not account for a sufficiently high local Hubble rate to describe the observed local universe without an exotic fluid assumption. In void models with appropriate depth however, coupling is indeed prominent and affects the evolution of the gauge-invariants in a significant way which should be taken into account when studying observational effects of linear structure formation in voids.

Although a careful analysis and comparison to FLRW models is still left to be done, coupling in the generalized metric potential φ would yield corrections in weak gravitational lensing measurements

and the integrated Sachs Wolfe effect that probe the metric perturbations on different angular scales. Previous studies of light propagation in perturbed LTB spacetimes were performed by Dunsby et al. (2010) ([37]) using the approach of [98]. In this framework, a model comparison is possible within the assumption of a negligible magnetic part of the Weyl tensor. Our results suggest that weak gravitational lensing based on the fully coupled perturbation equations should be investigated to assess possible corrections. One possible framework will be outlined in Chapt. (8). In case of the integrated Sachs Wolfe effect, there exists, to our knowledge, no direct analysis in perturbed LTB spacetimes. However, Tomita (2010) (see [91]) worked out a gauge-invariant treatment in generic spherically-symmetric spacetimes based on the formalism of [50].

Corrections in the generalised density contrast Δ are expected to be seen in the two-point correlation function of the galaxy distribution and to affect the BAO scales. This could be relevant for analysing typical galaxy surveys like BOSS-SDSS-III ([34]) or WhiggleZ ([20]) in the framework of large void models. BAOs have been used as an additional probe to constrain properties of void models (see [19, 48, 100, 101]) by taking the geometric distortion of the sound horizon due to the background shear into account, but not the effects of linear structure formation on inhomogeneous backgrounds. February et al. (2013) ([43]) modeled this effect using the uncoupled evolution described by Eqs. (7.3) and (7.4) with the assumption that the background shear is small and therefore causes negligible coupling. By direct comparison to the geometric approximation, the authors found that the influence of the structure formation model is, in fact, subdominant but nonetheless at percent level (see Figs. (7) and (8) in [43]) such that future large volume surveys like Euclid ([80]) and SKA ([82]) might be sensitive to it. Corrections to BAO scales due to a full treatment of perturbations in LTB models are expected to be of similar size and might therefore also be relevant for constraining void models with future surveys. Regarding our findings that coupling has a significant effect on the generalized density contrast Δ for deep voids, the effect on BAO measurements is worth to be investigated. However, any statements about observable predictions have to be considered with great caution in this context, as the notion of a physical density contrast in the framework of perturbed LTB models is poorly understood and a rigorous analysis is still left to be done.

Since we have taken the complete master- and constraint equations into account, we are not straightforwardly able to compute transfer functions for the theoretical angular power spectra (as done in [43] for the uncoupled case). We therefore have to draw a Gaussian realisation of spherical harmonic coefficients, evolve them forward in time, and compute estimates of the angular power spectra on the past null cone. Certainly, this approach has its limitation as the initial sample has a Gaussian statistical error which prevents us from making reliable statements about coupling strengths at small ℓ-modes which is similar to the cosmic variance limit in the CMB analysis. However, the statistical error can be reduced by considering several realisations in a row which is computationally very costly and the corresponding reduction of errors would only scale with the square root of the number of trials.

The master variables φ, ς, and χ are constructed to be gauge-invariant quantities and therefore contain only physical (in principle observable) degrees of freedom. Nonetheless, reducing them to "usable" observable constraints will be necessary for direct comparison to homogeneous models and for tests of the Copernican Principle. There are several promising approaches:

- Clarkson et al. (2009) ([29]) constructed perturbation variables that reduce to pure Scalar-Vector-Tensor variables in FLRW limit. Using these quantities, we might be able to directly compare large void models with best fit ΛCDM models and study the effects of coupling strengths.
- There exist conserved gauge-invariant quantities in LTB spacetimes that can be compared in initial FLRW states and in the LTB final state. Leithes & Malik (2015) (see [56]) identified the spatial metric trace perturbation ζ_{SMTP} to be conserved during spacetime evolution in spherically symmetric dust spacetimes.
- Weak gravitational lensing and the integrated Sachs Wolfe effect can extensively be studied. By tracing null geodesics in perturbed LTB spacetimes, we account for combined effects of all gauge-

invariant quantities summarized in first order Ricci and Weyl focusing terms in the optical tidal matrix.

A weak gravitational lensing formalism in perturbed LTB spacetimes will be laid out in Chapt. (8) that allows to predict observable corrections to the angular diameter distance in void models. Numerical tests have already been performed for the uncoupled evolution of perturbations and the application to the fully perturbed LTB spacetime is current work in progress.

Following on these possible approaches and in particular weak gravitational lensing, we would be able to add additional constraints to the void density profile from structure formation which would be an extension of recent work by Redlich et al. (2014) ([75]). However, it can also help to systematically rule out void models for the description of the late-time local universe. Combined multi-probe analyses of large void models with homogeneous Big Bang ([68, 75, 101]) showed strong tension with observations as even very flexible void profiles are not able to fit local (SNe, local H_0) and global measurements (CMB) of the Hubble rate simultaneously (see [75] and references therein). In addition, deviations from isotropy can directly be probed using the kinetic Sunyaev-Zel'dovich (kSZ) effect. The basic idea is to use the rescattering of CMB photons by hot electrons in galaxy clusters to access information from the interior of the observer's backward lightcone. As the corresponding galaxy cluster is placed at considerable radial distance from the void centre, it is exposed to a large spacetime anisotropy and therefore should see an anisotropic CMB signal (see [26, 47] for details). A related approach involves the so-called linear kSZ effect (or often referred to as Ostriker-Vishniac effect) that takes scattering of CMB photons at all evolving structures (linear density fluctuations) in the LTB patch into account. This effect allows to estimate corrections to the CMB angular power spectrum (see [97] for the original- and [99] for a fully relativistic treatment). In fact, the predicted linear kSZ power and corresponding corrections to the CMB power spectrum are much larger than actually observed. Although considerable effort has been made to approximate or circumvent linear structure formation in void models to describe this effect, a rigorous treatment requires proper modeling of the evolution of linear perturbations on the LTB background. In fact, deriving the angular power spectrum of the linear kSZ effect is then possible without scale dependent approximations for the growth factor of perturbations (as done in [99]) since spherical harmonic coefficients can be propagated in time directly.

We would like to stress again that any statement about the influence of evolution effects on inhomogeneous backgrounds goes beyond the scope of this work, as no direct expression for the scalar density contrast is available so far in gauge-invariant LTB perturbation theory. Nonetheless, it is worth being investigated and should be addressed in the future.

Considering the recent trends in the literature, we cannot expect linear structure formation to alleviate the problems, but rather to strengthen arguments against these models. One can therefore also think of a second application in testing the Copernican Principle with LTB models in combination with a cosmological constant Λ. As shown in [41], Eqs. (4.4) - (4.10) can be augmented by a cosmological constant and are therefore also valid in so-called ΛLTB models. Marra & Pääkonen (2010) ([66]), Valkenburg et al. (2012) ([94]), and Redlich et al. (2014) [75] performed detailed analyses of this kind of models to constrain local fluctuations in the radial density profile using combinations of several observational probes. In this context, a full treatment of linear structure growth in ΛLTB models would be a valuable extension of current methods to test the Copernican Principle, although we expect coupling effects to be less important due to smaller deviations of the density profile from the homogeneous ΛCDM model.

8

A WEAK GRAVITATIONAL LENSING FORMALISM IN PERTURBED LTB MODELS

8.1 SUMMARY

The present chapter outlines a relativistic formalism for light propagation in perturbed LTB models that is particularly useful to connect abstract LTB gauge-invariants to physically meaningful observables. We follow the approach laid out in Chapt. (2.5) and specialise it to perturbed spherically symmetric dust spacetimes. The Sachs equation, that constrains the evolution of thin bundles of null geodesics, is first derived at the LTB background level. It can be shown that the areal radius $R(t,r) = ra_\perp(t,r)$ generically solves this equation, although the shape of the lightcone can only be obtained numerically. In the following, the Sachs equation in perturbed LTB models is presented that take the full set of gauge-invariant perturbations into account. The final result yields first order corrections to the area angular diameter distance that can directly be used to probe effects of linear structure formation in void models. First numerical solutions are shown which, for simplicity, are restricted to negligible couplings between different LTB perturbation variables. We close this section with a brief outlook on further plans and improvements that are worth being investigated in future studies.

8.2 MOTIVATION

Although LTB gauge-invariant quantities are constructed to incorporate only physical, in principle observable degrees of freedom, they can, a priori, be very abstract mathematical objects that need to be interpreted in a physically meaningful way. In case of FLRW models, perturbations decouple into separate scalars, vectors and tensors on the underlying homogeneous and isotropic 3-space. Furthermore, these perturbation types do not couple over time because of the high degree of symmetry on each spatial hypersurface. Their physical interpretation is therefore trivial since, for example, initial scalar Bardeen potentials do not generate vector and tensor contributions, and can be regarded as physical gravitational potentials at all times and spatial scales. However, radially inhomogeneous spatial hypersurfaces are less symmetric and therefore gauge-invariant perturbations are intrinsically coupled. As shown by Clarkson et al. (2009) ([29]), assigning any physical interpretation to LTB gauge-invariants is a highly non-trivial task but necessary for observable predictions of linear structure formation in these spacetimes. One promising approach to circumvent this issue is weak gravitational lensing as it is sensitive to all metric and matter perturbations that are effectively mapped to Ricci and Weyl focussing effects in the Sachs equation. As outlined in Sect. (2.5), the solution to the Sachs equation can be related to the area angular diameter distance which is directly inferred from observations by comparing observation angles with physical length scales. For simplicity and consistency with the previous chapters, we assume the observer to be located at the centre of the LTB patch such that her worldline defines an isotropic local universe. Derivations in this chapter closely follow the steps in Sect. (2.5) and are readily applied to perturbed spherically symmetric dust models.

8.3 LIGHT PROPAGATION IN LTB SPACETIMES

We start from the LTB metric

$$\mathrm{d}s^2 = -\mathrm{d}t^2 + \frac{a_\parallel^2(t,r)}{1-\kappa(r)r^2}\mathrm{d}r^2 + r^2 a_\perp^2(t,r)\mathrm{d}\Omega^2\,, \tag{8.1}$$

with the corresponding energy momentum tensor $T_{\mu\nu} = \rho(t,r)u_\mu u_\nu$. As derived in Sect. (2.5), the general initial value problem for the Sachs equation is given by[1]

$$\begin{aligned} \frac{\mathrm{d}^2 D_{ab}}{\mathrm{d}\lambda^2} &= \mathcal{T}_{ac}D_{cb}\,,\\ D_{ab}|_{\lambda=0} &= 0\,,\\ \left.\frac{\mathrm{d}D_{ab}}{\mathrm{d}\lambda}\right|_{\lambda=0} &= \delta_{ab}\,. \end{aligned} \tag{8.2}$$

The optical tidal matrix $\mathcal{T}_{ab}$ splits into a Ricci and a Weyl focussing part

$$\mathcal{T}_{ab} = -\frac{1}{2}R_{\alpha\beta}k^\alpha k^\beta \delta_{ab} + C_{\alpha\beta\gamma\delta}n^\alpha{}_a k^\beta k^\gamma n^\delta{}_b\,, \tag{8.3}$$

which denote contractions of the Ricci and Weyl tensors with the photon wave vector k^μ and the Sachs basis vectors $n^\mu{}_a$ (see again Sect. (2.5) for details). Assuming an observer following the central worldline of the LTB spacetime, null geodesics are necessarily radial and the wave vector can be expressed as

$$k^\mu = \left(\frac{\mathrm{d}t}{\mathrm{d}\lambda}, \frac{\mathrm{d}r}{\mathrm{d}\lambda}, 0, 0\right)^T\,, \tag{8.4}$$

in the observer's local rest frame. A trivial choice for the Sachs basis vectors is then

$$n^\mu{}_1 = (0,0,1,0)^T\,,\ n^\mu{}_2 = (0,0,0,1)^T\,, \tag{8.5}$$

which yield the following Ricci and Weyl focussing contributions

$$-\frac{1}{2}R_{\alpha\nu}k^\alpha k^\beta = -4\pi G\rho(t,r)\,(1+z)^2\,, \tag{8.6}$$

$$C_{\alpha\beta\gamma\delta}n^\alpha{}_a k^\beta k^\gamma n^\delta{}_b = 0\,. \tag{8.7}$$

Due to spacetime isotropy seen by the central observer, no Weyl focussing contribution is present and the Sachs equation simplifies to

$$\frac{\mathrm{d}^2 D_{ab}}{\mathrm{d}\lambda^2} = -4\pi G\rho(t(\lambda), r(\lambda))\,(1+z(\lambda))^2\,D_{ab}(\lambda)\,. \tag{8.8}$$

In order to obtain the redshift and lightcone coordinates as function of the affine parameter λ, the null condition of k^μ and the definition of redshift can be properly combined. We obtain

$$k_\mu k^\mu = g_{\mu\nu}k^\mu k^\nu = -\left(\frac{\mathrm{d}t}{\mathrm{d}\lambda}\right)^2 + \frac{a_\parallel^2(t,r)}{1-\kappa(r)r^2}\left(\frac{\mathrm{d}r}{\mathrm{d}\lambda}\right)^2 = 0 \quad \Rightarrow \frac{\mathrm{d}t}{\mathrm{d}r} = -\frac{a_\parallel(t,r)}{\sqrt{1-\kappa(r)r^2}}\,, \tag{8.9}$$

$$k_\mu u^\mu = -\frac{\mathrm{d}t}{\mathrm{d}\lambda} = 1+z(\lambda)\,, \tag{8.10}$$

where no intrinsic velocity of the source has been assumed. For a source that is comoving with the dust fluid, we have $u^\mu = \delta^\mu_0$.

Hence, we obtain the following differential relations for the lightcone coordinates with respect to λ:

1 In accordance with the convention made in Sect. (2.5), we sum over two equal indices.

$$\frac{\mathrm{d}t}{\mathrm{d}\lambda} = -\left[1+z(\lambda)\right], \tag{8.11}$$

$$\frac{\mathrm{d}r}{\mathrm{d}\lambda} = \frac{\mathrm{d}r}{\mathrm{d}t}\frac{\mathrm{d}t}{\mathrm{d}\lambda} = \left[1+z(\lambda)\right]\frac{\sqrt{1-\kappa\left[r(\lambda)\right]r^2(\lambda)}}{a_{\parallel}\left[t(\lambda),r(\lambda)\right]}. \tag{8.12}$$

Relations containing the redshift involve the differentiation of Eq. (8.10). By direct computation, we see

$$\begin{aligned}\frac{\mathrm{d}z}{\mathrm{d}\lambda} = \frac{\mathrm{d}}{\mathrm{d}\lambda}\left(k^{\mu}u_{\mu}\right) &= k^{\nu}u_{\mu}\nabla_{\nu}k^{\mu} + k^{\nu}k^{\mu}\nabla_{\nu}u_{\mu}\\ &= k^{\nu}k^{\mu}\nabla_{\nu}u_{\mu}\\ &= -\Gamma^{\kappa}_{\mu\nu}k^{\mu}k^{\nu}u_{\kappa}\\ &= \Gamma^{0}_{\mu\nu}k^{\mu}k^{\nu}\\ &= \Gamma^{0}_{00}\left(\frac{\mathrm{d}t}{\mathrm{d}\lambda}\right)^2 + 2\Gamma^{0}_{01}\left(\frac{\mathrm{d}t}{\mathrm{d}\lambda}\right)\left(\frac{\mathrm{d}r}{\mathrm{d}\lambda}\right) + \Gamma^{0}_{11}\left(\frac{\mathrm{d}r}{\mathrm{d}\lambda}\right)^2.\end{aligned} \tag{8.13}$$

The Christoffel symbols result in

$$\Gamma^{0}_{00} = \Gamma^{0}_{01} = 0\,,\ \Gamma^{0}_{11} = \frac{a_{\parallel}\dot{a}_{\parallel}}{1-\kappa r^2}\,,$$

such that we finally obtain[2]

$$\frac{\mathrm{d}z}{\mathrm{d}\lambda} = \left[1+z(\lambda)\right]^2 H_{\parallel}\left[t(\lambda),r(\lambda)\right]. \tag{8.14}$$

Combining this result with Eq. (8.12) yields

$$\frac{\mathrm{d}z}{\mathrm{d}r} = \frac{\mathrm{d}z}{\mathrm{d}\lambda}\cdot\frac{\mathrm{d}\lambda}{\mathrm{d}r} = (1+z)^2\cdot\frac{\dot{a}_{\parallel}}{a_{\parallel}}\cdot\frac{a_{\parallel}}{\sqrt{1-\kappa(r)r^2}}\cdot\frac{1}{1+z} = \frac{(1+z)\dot{a}_{\parallel}}{\sqrt{1-\kappa(r)r^2}}, \tag{8.15}$$

which is consistent with the results found in Chapt. (3) where a more heuristic derivation was applied.

Summing up, light propagation in LTB spacetimes can be described by the following system of coupled linear differential equations:

$$\frac{\mathrm{d}^2 D_{ab}(\lambda)}{\mathrm{d}\lambda^2} = -4\pi G\rho\left[t(\lambda),r(\lambda)\right]\left[1+z(\lambda)\right]^2 D_{ab}(\lambda)\,, \tag{8.16}$$

$$\frac{\mathrm{d}t(\lambda)}{\mathrm{d}\lambda} = -\left[1+z(\lambda)\right], \tag{8.17}$$

$$\frac{\mathrm{d}r(\lambda)}{\mathrm{d}\lambda} = \left[1+z(\lambda)\right]\frac{\sqrt{1-\kappa\left[r(\lambda)\right]r^2(\lambda)}}{a_{\parallel}\left[t(\lambda),r(\lambda)\right]}, \tag{8.18}$$

$$\frac{\mathrm{d}z(\lambda)}{\mathrm{d}\lambda} = \left[1+z(\lambda)\right]^2 H_{\parallel}\left[t(\lambda),r(\lambda)\right]. \tag{8.19}$$

Initial conditions have to be chosen in a physically sensible way. As the observer's position is assumed to coincide with $\lambda = 0$, we have

$$\begin{aligned} D_{ab}|_{\lambda=0} &= 0\,,\\ \left.\frac{\mathrm{d}D_{ab}}{\mathrm{d}\lambda}\right|_{\lambda=0} &= \delta_{ab}\,,\end{aligned} \tag{8.20}$$

2 Different types of parentheses according to the convention $\{\ldots[\ldots(\ldots)\ldots]\ldots\}$ are used in the following where is turns out to appropriate for improved readability.

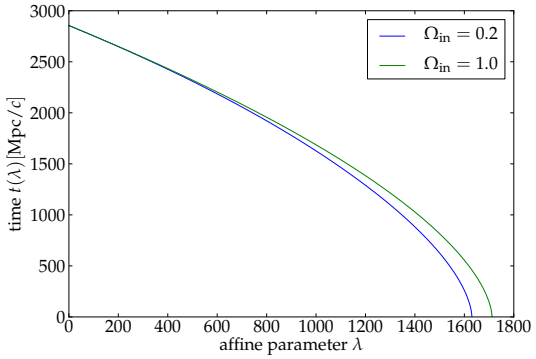

(a) Lightcone time vs. affine parameter

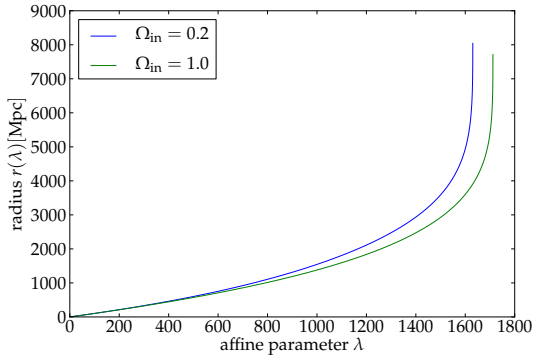

(b) Lightcone radius vs. affine parameter

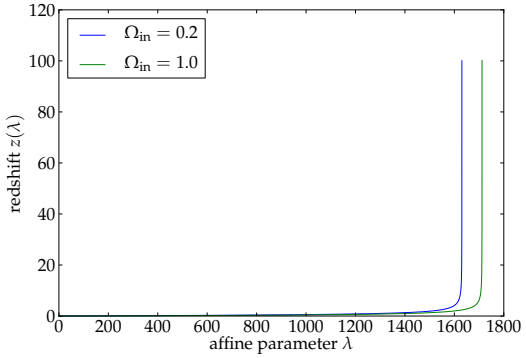

(c) Redshift vs. affine parameter

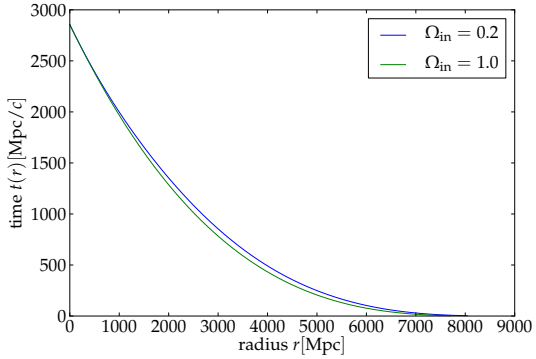

(d) Coordinate time vs. coordinate radius

Figure 8.1: Numerical results on time (a), radius (b) and redshift (c) with respect to the affine parameter λ and the t-r-shape of the lightcone (d): These results were obtained by evolving Eqs. (8.11), (8.17), and (8.19) starting from $\lambda = 0$ with corresponding initial conditions.

$$t|_{\lambda=0} = t_{\text{age}}\,, \tag{8.21}$$
$$r|_{\lambda=0} = 0\,, \tag{8.22}$$
$$z|_{\lambda=0} = 0\,, \tag{8.23}$$

where t_{age} denotes the age of the LTB patch. By construction, it corresponds to the age of the asymptotic FLRW background given by Eq. (3.37).

In comparison to the FLRW case, the main complication is the fact that radial inhomogeneity does not allow a direct relation between the LTB lightcone coordinates and the affine parameter. These relations are only given in a differential way which causes the Jacobi Map to be constrained by a coupled system of linear ordinary differential equations. In general, a system of this kind has to be numerically evolved in λ. However, it can be shown that the areal radius $R(t,r) = ra_{\perp}(t,r)$ that is referred to as angular diameter distance in LTB models formally solves this equation (see App. (A) for detailed calculations).

Physically, this is a direct consequence of the special position of the observer. Space is isotropic when projected onto the observer's worldline which causes emerging or incoming null geodesics to be necessarily radial and to experience only isotropic Ricci focussing. Starting with an initial solid angle Ω at the observer, any change in the cross-sectional area of the geodesic bundle at a fiducial source position has to be mediated by the angular part of the LTB metric. In fact, this is described by the areal radius $R(t,r) = ra_{\perp}(t,r)$ which then naturally corresponds to the area angular diameter distance (see also [37]). As a confirmation of the analytical treatment in App. (A), Fig. (8.2) shows the areal

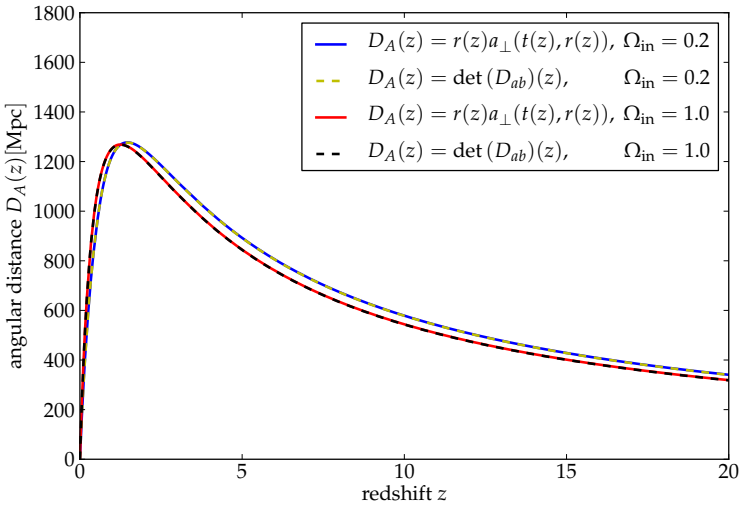

Figure 8.2: Numerical solution of the Sachs equation at the background level in comparison to the areal radius as function of redshift z: The results confirm that the areal radius $D_A(z) = r(z)a_\perp(t(z), r(z))$ indeed solves the Sachs equation for a central observer in LTB void models.

radius in comparison to the numerical solution of Eqs. (8.16) - (8.19) for a Gaussian shaped void with a depth of $\Omega_{\rm in} = 0.2$ and 2 Gpc extension that is asymptotically embedded into an EdS universe. We observe the well-known behaviour of the cosmological angular diameter distance. At small redshifts, we see an increase as a freely falling observer measures a local Euclidean distance in her vicinity. At larger redshifts however, cosmological expansion plays a role and the corresponding increase of the matter energy density on the backward lightcone enters into the Ricci focussing. The cross-sectional diameter of the geodesic bundle therefore shrinks with increasing redshift leading to a maximum in $D_A(z)$ followed by a long decrease.

Numerical solutions to the shape of the lightcone are shown in Fig. (8.1). Results are plotted for a homogeneous EdS solution and for the exemplary void model described above. In void models, we see that, at fixed affine parameters, time coordinates are smaller and radial coordinates are larger compared to the EdS solution. Although both effects compensate each other, the LTB lightcone is slightly bending outwards with respect to its FLRW counterpart which can clearly be seen in its t-r-shape. In fact, this behaviour can be expected in a negatively curved space. Redshift initially increases very slowly with λ in both models, but the relation steepens considerably at large affine parameters. This can be expected due to the shape of Eq. (8.19) since, at fixed spacing in λ, dz depends at least quadratically on the redshift position. In case of the EdS universe, it can be shown that it even increases like $(1+z)^{7/2}$. Redshift bins at large affine parameters are therefore highly stretched. In addition, the redshift is a model-dependent quantity as it refers to the backward lightcone of the spacetime. This should be kept in mind when analysing plots of angular diameter distances with respect to z. Due to the larger expansion rate in a locally underdense region, void models account for higher redshift values at fixed affine parameters when compared to the homogeneous EdS solution. The distance redshift-relations in Fig. (8.2) are therefore slightly shifted with respect to each other where the void model tends to larger redshifts.

8.4 COMPLETE LINEARISED JACOBI EQUATION IN PERTURBED LTB SPACETIMES

Generically perturbed LTB spacetimes do not obey any symmetries seen by observers moving on the LTB central worldline. Strictly speaking, even this special position in spacetime cannot be precisely singled out anymore. However, deviations from the spherically symmetric LTB solution are assumed to be small and therefore the following approximations can be made:

- The observer's worldline is approximated by a geodesic in the background LTB spacetime. Hence, the observer's rest frame and the corresponding central worldline can be expressed by the background metric only.
- In a similar manner as outlined in Sect. (2.5.2), Born's approximation can be applied and influences of perturbations on the propagation of null geodesics are integrated along the unperturbed lightpath. Since linear perturbation theory is applied and metric potentials are assumed to be small, this approximation is typically very accurate (see [16, 81]).
- Due to spherical symmetry of the background metric, all results can (for simplicity, but without loss of generality) be considered in the equatorial plane of the observer's local rest frame.

Referring to these approximations, deviations in the affine parameter λ, redshift, and lightcone coordinates from their background values can be neglected which allows us to adopt Eqs. (8.17) - (8.19) right away from the background model and consider only perturbations in the Sachs equation itself. This can also be done for the wave vector k^μ and the Sachs basis n^μ_a in the same manner.

In order to set up possible linear corrections to Eq. (8.16) in perturbed LTB spacetimes, we envisage the sets of polar gauge-invariant perturbations $\{\eta^{(\ell m)}, \chi^{(\ell m)}, \varphi^{(\ell m)}, \varsigma^{(\ell m)}\}$ for the metric and $\{\Delta^{(\ell m)}, w^{(\ell m)}, v^{(\ell m)}\}$ for the dust fluid that have been derived in Clarkson et al. (2009) ([29]) and laid out in Chapt. (4). For each spherical harmonic mode (ℓ, m), these quantities assemble the perturbed metric and energy momentum tensor

$$ds^2 = -\left[1 + (2\eta^{(\ell m)} - \chi^{(\ell m)} - \varphi^{(\ell m)})Y^{(\ell m)}\right] \mathrm{d}t^2 - \frac{2a_\parallel \varsigma^{(\ell m)} Y^{(\ell m)}}{\sqrt{1-\kappa r^2}} \mathrm{d}t\mathrm{d}r \tag{8.24}$$

$$+ \frac{a_\parallel^2}{1-\kappa r^2}\left[1 + (\chi^{(\ell m)} + \varphi^{(\ell m)})Y^{(\ell m)}\right] \mathrm{d}r^2 + r^2 a_\perp^2 \left[1 + \varphi^{(\ell m)} Y^{(\ell m)}\right] \mathrm{d}\Omega^2 \,, \tag{8.25}$$

$$\rho = \rho^{\mathrm{LTB}} \left(1 + \Delta^{(\ell m)} Y^{(\ell m)}\right) \,, \tag{8.26}$$

$$u_\mu = \left[u_A + \left(w^{(\ell m)} n_A + \frac{1}{2} k_{AB} u^B\right) Y^{(\ell m)}, v^{(\ell m)} Y_b^{(\ell m)}\right] \,. \tag{8.27}$$

Given the approximations made above, the Sachs equation can be separated into two second-order linear differential equations constraining the background evolution and the corresponding first order correction (see Sect. (2.5.2) for details)

$$\frac{\mathrm{d}^2 D^{(0)}_{ab}(\lambda)}{\mathrm{d}\lambda^2} = \mathcal{T}^{(0)}_{ac}(\lambda) D^{(0)}_{cb}(\lambda) \,, \tag{8.28}$$

$$\frac{\mathrm{d}^2 D^{(1)}_{ab}(\lambda,\theta,\phi)}{\mathrm{d}\lambda^2} = \mathcal{T}^{(1)}_{ac}(\lambda,\theta,\phi) D^{(0)}_{cb}(\lambda) + \mathcal{T}^{(0)}_{ac}(\lambda) D^{(1)}_{cb}(\lambda,\theta,\phi) \,. \tag{8.29}$$

First order quantities do not obey spherical symmetry and therefore generally depend of the azimuthal and polar angles. As we restrict ourselves fiducial light rays propagating in the observer's local equatorial plane, θ corresponds to $\pi/2$ throughout.

The system can effectively be reduced to Eq. (8.29) as the solution to the Sachs equation at the background level is analytically known as $D^{(0)}_{ab}(\lambda) = r(\lambda) a_\perp(t(\lambda), r(\lambda))\delta_{ab}$. Thus, the remaining first order correction to the Jacobi Map is constrained by

$$\begin{aligned}\frac{\mathrm{d}^2 D^{(1)}_{ab}(\lambda,\theta,\phi)}{\mathrm{d}\lambda^2} = &-4\pi G\rho\left[t(\lambda), r(\lambda)\right]\left[1 + z(\lambda)\right]^2 D^{(1)}_{ab}(\lambda,\theta,\phi) \\ &+ r(\lambda) a_\perp\left[t(\lambda), r(\lambda)\right] \mathcal{T}^{(1)}_{ab}(\lambda,\theta,\phi) \,.\end{aligned} \tag{8.30}$$

The geodesic bundle is assumed to converge at the observer's spacetime position at $\lambda = 0$ which conceptually implies the same boundary conditions for the Jacobi Map that have already been applied at the background level. In accordance with the approximations made above, the initial conditions of D_{ab} are unchanged at the background level. Correspondingly, the initial rate of the first order contribution $D^{(1)}_{ab}$ has to vanish such that the first derivative of the full Jacobi Map remains the identity matrix at the observer's position:

$$D^{(1)}_{ab}\Big|_{\lambda=0} = 0\,, \tag{8.31}$$

$$\frac{D^{(1)}_{ab}}{\mathrm{d}\lambda}\Big|_{\lambda=0} = 0\,. \tag{8.32}$$

The correction $\mathcal{T}^{(1)}_{ab}$ to the optical tidal matrix is now the only quantity left to be determined. Since its projection on the background central worldline does not yield a locally isotropic space at perturbation level, generic Ricci as well as Weyl focussing contributions in terms of the LTB gauge-invariants can be expected. In fact, detailed explicit computations result in the following first order contributions for each spherical harmonic mode (ℓ, m):

$$R^{(1)}_{\alpha\beta}k^\alpha k^\beta = 8\pi G\rho\,(1+z)^2\left(2w^{(\ell m)} + \Delta^{(\ell m)} + 2\eta^{(\ell m)} - \chi^{(\ell m)} - \varphi^{(\ell m)} - \varsigma^{(\ell m)}\right)Y^{(\ell m)}\,, \tag{8.33}$$

$$\begin{aligned} C^{(1)}_{\alpha\beta\gamma\delta}n^\alpha{}_1 k^\beta k^\gamma n^\delta{}_1 = (1+z)^2\left(\eta^{(\ell m)} - \chi^{(\ell m)} - \varphi^{(\ell m)} - \varsigma^{(\ell m)}\right)\Bigg[\left(\frac{8\pi G\rho}{3} - \frac{M}{a_\perp^3}\right)Y^{(\ell m)} \\ - \frac{1}{2r^2a_\perp^2}\left(\partial_\theta\partial_\theta Y^{(\ell m)} - \partial_\phi\partial_\phi Y^{(\ell m)}\right)\Bigg]\,, \end{aligned} \tag{8.34}$$

$$\begin{aligned} C^{(1)}_{\alpha\beta\gamma\delta}n^\alpha{}_2 k^\beta k^\gamma n^\delta{}_2 = (1+z)^2\left(\eta^{(\ell m)} - \chi^{(\ell m)} - \varphi^{(\ell m)} - \varsigma^{(\ell m)}\right)\Bigg[\left(\frac{8\pi G\rho}{3} - \frac{M}{a_\perp^3}\right)Y^{(\ell m)} \\ + \frac{1}{2r^2a_\perp^2}\left(\partial_\theta\partial_\theta Y^{(\ell m)} - \partial_\phi\partial_\phi Y^{(\ell m)}\right)\Bigg]\,, \end{aligned} \tag{8.35}$$

$$\begin{aligned} C^{(1)}_{\alpha\beta\gamma\delta}n^\alpha{}_1 k^\beta k^\gamma n^\delta{}_2 &= -\frac{(1+z)^2}{r^2a_\perp^2}\left(\eta^{(\ell m)} - \chi^{(\ell m)} - \varphi^{(\ell m)} - \varsigma^{(\ell m)}\right)\partial_\theta\partial_\phi Y^{(\ell m)} \\ &= C^{(1)}_{\alpha\beta\gamma\delta}n^\alpha{}_2 k^\beta k^\gamma n^\delta{}_1\,. \end{aligned} \tag{8.36}$$

Regarding the structure of these results, the first order correction to the optical tidal matrix can concisely be written as

$$\begin{aligned} \mathcal{T}^{(1)}_{ab} = \sum_{\ell=0}^{\infty}\sum_{m=-\ell}^{\ell} (1+z)^2\Bigg[-\frac{4\pi G\rho}{3}\left(6w^{(\ell m)} + 3\Delta^{(\ell m)} + 4\eta^{(\ell m)} - \varsigma^{(\ell m)} - \varphi^{(\ell m)} - \chi^{(\ell m)}\right) \\ - \frac{M}{a_\perp^3}\left(\eta^{(\ell m)} - \varsigma^{(\ell m)} - \varphi^{(\ell m)} - \chi^{(\ell m)}\right)\Bigg]Y^{(\ell m)}\delta_{ab} \\ - \frac{(1+z)^2}{r^2a_\perp^2}\left(\eta^{(\ell m)} - \varsigma^{(\ell m)} - \varphi^{(\ell m)} - \chi^{(\ell m)}\right)\Bigg[\frac{1}{2}\left(\partial_\theta\partial_\theta Y^{(\ell m)} - \partial_\phi\partial_\phi Y^{(\ell m)}\right)(\sigma_3)_{ab} \\ + \partial_\theta\partial_\phi Y^{(\ell m)}(\sigma_1)_{ab}\Bigg]\,, \end{aligned} \tag{8.37}$$

where the Pauli matrices

$$(\sigma_1) = \begin{pmatrix} 0 & 1 \\ 1 & 0 \end{pmatrix}, \text{ and } \quad (\sigma_3) = \begin{pmatrix} 1 & 0 \\ 0 & -1 \end{pmatrix}$$

have been applied.

The full system of equations constraining linear corrections to the Jacobi Map D_{ab} is then given by

$$\begin{aligned} \frac{\mathrm{d}^2 D^{(1)}_{ab}(\lambda,\theta,\phi)}{\mathrm{d}\lambda^2} &= -4\pi G\rho\left[t(\lambda),r(\lambda)\right]\left[1+z(\lambda)\right]^2 D^{(1)}_{ab}(\lambda,\theta,\phi) \\ &\quad + r(\lambda)a_\perp\left[t(\lambda),r(\lambda)\right]\mathcal{T}^{(1)}_{ab}(\lambda,\theta,\phi)\,, \end{aligned} \tag{8.38}$$

$$\frac{\mathrm{d}t(\lambda)}{\mathrm{d}\lambda} = -\left[1+z(\lambda)\right]\,, \tag{8.39}$$

$$\frac{\mathrm{d}r(\lambda)}{\mathrm{d}\lambda} = \left[1+z(\lambda)\right]\frac{\sqrt{1-\kappa\left[r(\lambda)\right]r^2(\lambda)}}{a_\parallel\left[t(\lambda),r(\lambda)\right]}\,, \tag{8.40}$$

$$\frac{\mathrm{d}z(\lambda)}{\mathrm{d}\lambda} = \left[1+z(\lambda)\right]^2 H_\parallel\left[t(\lambda),r(\lambda)\right]\,, \tag{8.41}$$

with $\mathcal{T}^{(1)}_{ab}$ determined by Eq. (8.37).

In comparison to the light propagation in perturbed FLRW models (see Sect. (2.5.2)), there is no analytical expression for the Green's function of the differential operator

$$\mathcal{L} = \frac{\mathrm{d}^2}{\mathrm{d}\lambda^2} + 4\pi G\rho\left[t(\lambda),r(\lambda)\right]\left[1+z(\lambda)\right]^2 \tag{8.42}$$

known so far. Therefore, Eqs. (8.38) - (8.41) have to the integrated numerically. Any possible solution yields

$$D_{ab}(\lambda,\theta,\phi) = r(\lambda)a_\perp\left[t(\lambda),r(\lambda)\right]\delta_{ab} + D^{(1)}_{ab}(\lambda,\theta,\phi)\,, \tag{8.43}$$

which can itself be transformed to the (area) angular diameter distance

$$\begin{aligned} D_A(\lambda,\theta,\phi) &= \sqrt{\det\left(D_{ab}\right)(\lambda,\theta,\phi)} \\ &= \sqrt{\det\left(D^{(0)}_{ab}\right)(\lambda) + \det\left(D_{ab}\right)(\lambda,\theta,\phi) - \det\left(D^{(0)}_{ab}\right)(\lambda)} \\ &\approx r(\lambda)a_\perp(t(\lambda),r(\lambda))\left(1+\delta D_A(\lambda,\theta,\phi)\right)\,. \end{aligned} \tag{8.44}$$

The expression

$$\delta D_A(\lambda,\theta,\phi) = \frac{1}{2}\frac{\Delta D_A(\lambda,\theta,\phi)}{r^2(\lambda)a^2_\perp\left[t(\lambda),r(\lambda)\right]} = \frac{1}{2}\left(\frac{\det(D_{ab})(\lambda,\theta,\phi)}{r^2(\lambda)a^2_\perp\left[t(\lambda),r(\lambda)\right]} - 1\right) \tag{8.45}$$

denotes the correction to the angular diameter distance due to first order contributions of the Ricci and Weyl focussing in perturbed LTB spacetimes.

Eq. (8.45) can be considered as the main theoretical result of this analysis, i. e., given suitable observational probes, D_A can be inferred observationally and compared to this theoretical prediction. In fact, the solution to Eq. (8.38) can be seen as an observational consequence of the combined effects of linear gauge-invariant perturbations in void models. Currently, a numerical solution to Eqs. (8.38) - (8.42) is work in progress and has therefore not been performed in full generality yet. However, as seen in Chapt. (7), the evolution equations of linear perturbations will simplify considerably if coupling effects are neglected. For this particular case, numerical investigations can be performed in a feasible way with less computational effort. First results of this test study are presented in the following section.

8.5 SOLUTION TO THE UNCOUPLED CASE

In case of negligible coupling, the evolution of linear scalar perturbations on top of the LTB background are described by the system (see Chapt. (7))

$$\ddot{\varphi}^{(\ell m)} = -4H_\perp \dot{\varphi}^{(\ell m)} + \frac{2\kappa}{a_\perp^2}\varphi^{(\ell m)}\,, \tag{8.46}$$

$$\begin{aligned}\alpha\Delta^{(\ell m)} = &-\frac{1}{Z^2}(\varphi^{(\ell m)})'' + \frac{1}{Z^2}\left(C - 4\frac{a_\parallel}{r a_\perp}\right)(\varphi^{(\ell m)})' + \left(H_\parallel + 2H_\perp\right)\dot{\varphi}^{(\ell m)} \\ &+ \left[\frac{\ell(\ell+1)}{r^2 a_\perp^2} + 2D\right]\varphi^{(\ell m)}\,.\end{aligned} \tag{8.47}$$

Within this approximation, initial 3-scalar perturbations do not excite any vector and tensor contributions over time evolution and therefore the metric potential φ and the density contrast Δ are the only non-trivial quantities of this setup[3]. The structure of Eq. (8.46) allows to introduce a growth factor $D_\varphi(t,r)$ that is independent of the angular scale and contains all information on the spacetime evolution of the metric potential. In fact, the spacetime evolution of a fiducial initial profile $\varphi_{\rm ini}(r)$ is given by

$$\varphi^{(\ell m)}(t,r) = D_\varphi(t,r)\cdot\varphi_{\rm ini}^{(\ell m)}(r)\,, \tag{8.48}$$

where D_φ satisfies the differential equation

$$\ddot{D}_\varphi = -4H_\perp\dot{D}_\varphi + \frac{2\kappa}{a_\perp^2}D_\varphi\,. \tag{8.49}$$

As we deal with a thin bundle of null geodesics, the metric potential and the density contrast are only needed in a small angular patch centered on the fiducial ray's angular coordinates, but with high precision in this region. Hence, spherical harmonic decomposition turns out to be impractical for this application as a superposition of a considerable amount of ℓ-modes would be required. We therefore apply an alternative technique that does not require any decomposition into orthonormal basis functions. Following the approach outlined in Sect. (6.2), we start from an initial 3d realisation of the Bardeen potential on a spatial hypersurface that intersects the lightcone well within its asymptotic FLRW limit and can therefore be considered as sufficiently homogeneous. We restrict this hypersurface to a cubic a box of sidelength $L_{\rm cube} = 10$ Gpc that contains the intersection with the central observer's backward lightcone at $z = 100$.

Transforming to spherical coordinates with respect to the centre of this cube yields an initial scalar metric potential $\varphi_{\rm ini}(t,r,\theta,\phi)$ which can be propagated in spacetime using the numerical solution to Eq. (8.49)[4]. The final result becomes

$$\varphi(t,r,\theta,\phi) = D_\varphi(t,r)\cdot\varphi_{\rm ini}(r,\theta,\phi) = -2D_\varphi(t,r)\cdot\Psi_{\rm ini}(r,\theta,\phi)\,, \tag{8.50}$$

which can easily be restricted to small angular patches with proper resolution. Inverting the eigenvalue equation of spherical harmonics presented in Chapt. (4), Eq. (8.47) can be transformed accordingly:

3 It can be shown that φ and Δ will indeed reduce to the scalar Bardeen potential and the gauge-invariant density contrast in the FLRW limit (see Sect. 4.1.1 of [29]) if no coupling terms are present. Strictly speaking, this approximation leads to disambiguities as the remaining perturbation quantities are too few degrees of freedom to obtain a closed set of perturbation equations on a radially inhomogeneous background. For instance, Eq. (4.8) implies that scalar metric potentials generate non-trivial radial velocity perturbations w which would again enter into the Sachs equation. For the sake of this example, we demand that velocities generated this way are negligible.

4 In fact, there exists a parametric solution to this equation applied in [29] and [43], but it turns out to be cumbersome when the curvature profile $\kappa(r)$ tends to small values or even changes sign. We therefore favored a numerical solution.

$$\begin{aligned}\alpha\Delta = &-\frac{1}{Z^2}\varphi'' + \frac{1}{Z^2}\left(C - 4\frac{a_\parallel}{r a_\perp}\right)\varphi' + \left(H_\parallel + 2H_\perp\right)\dot{\varphi} \\ &+ 2D\varphi - \frac{1}{r^2 a_\perp^2}\left(\partial_\theta\partial_\theta + \partial_\phi\partial_\phi\right)\varphi\,.\end{aligned} \tag{8.51}$$

The first order contribution to the optical tidal matrix then reduces to

$$\begin{aligned}\mathcal{T}^{(1)}_{ab} =&(1+z)^2\left[-4\pi G\rho\left(\Delta - \frac{\varphi}{3}\right) + \frac{M}{a_\perp^3}\varphi\right]\delta_{ab} + \frac{(1+z)^2}{r^2 a_\perp^2}\left[\frac{1}{2}\left(\partial_\theta\partial_\theta\varphi - \partial_\phi\partial_\phi\varphi\right)(\sigma_3)_{ab}\right. \\ &\left.+\partial_\theta\partial_\phi\varphi(\sigma_1)_{ab}\right]\,.\end{aligned} \tag{8.52}$$

Within this procedure, it has to be ensured that φ and Δ remain regular functions at the radial origin. While φ is well-defined at $r = 0$, Δ diverges quadratically (see Eq. (8.51)) which has to be caught up in order to avoid strong artifacts in the final solution. We neglect the influence of the monopole and dipole contributions of both variables on the geodesic bundle which should be well-fulfilled regarding its angular scale. Correspondingly, the regularity conditions derived in [54] and shown in Chapt. (5.4) enforce φ and Δ to grow at least with r^2 in the vicinity of the observer's central worldline. Practically, these conditions can be imposed by setting both variables artificially to zero in the first two radial bins which ensures their values and spatial gradients to vanish in this region.

In summary, all necessary information has been collected for the numerical treatment of Eqs. (8.38) - (8.41) for this particular scenario. Numerical investigations of the Sachs equation for negligible coupling have been performed by Simon Hirscher in the context of his Bachelor thesis.

The first order corrections δD_A to the angular diameter distance are shown in Fig. (8.5) for a Gaussian-shaped LTB patch of 2 Gpc extension and varying central density. The void profile is again asymptotically matched to a background EdS solution. We have singled out an exemplary fiducial ray reaching the central observer's position at angular coordinates $(\theta, \phi) = (\pi/2, 0)$. Results are shown as functions of the affine parameter and redshift. According to Fig. (8.1), the near and far regimes of the backward lightcone are then visualized in an appropriate way. Depending on the void model, corrections to the angular diameter distance are of sub-percent level which is observed to decrease with increasing void depth. This is physically meaningful since higher expansion rates in local underdense regions are expected to suppress linear structure growth. Numerical results for the metric potential and density contrast are shown in Fig. (8.3) for the given angular coordinates of the fiducial ray. We see typical potential fluctuation amplitudes of 10^{-5} whereas corresponding density fluctuations are considerably larger and are therefore expected to dominate the solution to the Sachs equation at small redshifts. In addition, gravitational potentials do not change significantly in the background EdS solution whereas density fluctuations encoded in Δ grow linearly with the scale factor. Similar behaviour can be expected in void models, although any firm analytical prediction seems impossible regarding the complicated shape of Eq. (8.51). Hence, the most significant influence of inhomogeneities can be expected at small redshifts where effects are almost completely determined by the density contrast. As Δ sources Ricci focussing of the geodesic bundle at first order, small expansions or contractions of its cross-section are present which cause the tiny wiggles of $\delta D_A(z)$ in this region. Note that, according to Fig. (8.1), small redshift intervals correspond to large intervals of the affine parameter in the low z regime such that these wiggles are fully resolved when considering $\delta D_A(\lambda)$ (see Fig. (8.5)).

At larger redshifts, the density contrast decreases rapidly and the first order contribution to the optical tidal matrix becomes less significant. The term $\sim \mathcal{T}^{(0)}_{ac} D^{(1)}_{cb}$ in the first order Sachs equation gains importance such that Eq. (8.38) is determined by a contribution being very similar to the right-hand-side of the background Sachs equation. Apart from possible sign changes caused by inhomogeneities at small redshifts and affine parameters, the components of the first order Jacobi Map adopt the

behaviour of the background solution at large redshifts. Corresponding numerical results on each component are shown in Fig. (8.4) for the EdS solution and the deepest void model. In fact, we overall observe a rapid decrease followed by a minimum and a slow increase at large redshifts. Obviously, a similar shape can be seen for $\delta D_A(z)$. This behaviour is independent of the central depth of each void model since lightcones are very close to the background FLRW shape in the high redshift regime ($z \geq 10$).

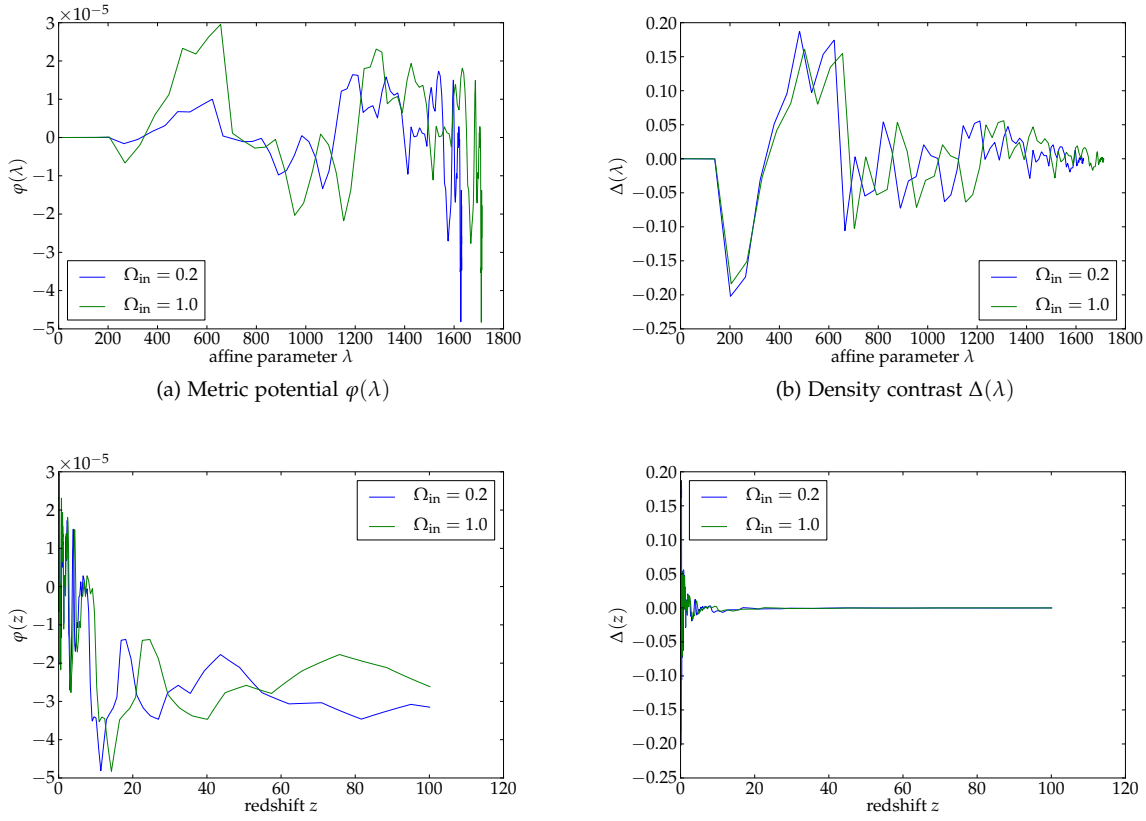

(a) Metric potential $\varphi(\lambda)$

(b) Density contrast $\Delta(\lambda)$

(c) Metric potential $\varphi(z)$

(d) Density contrast $\Delta(z)$

Figure 8.3: Linear perturbations Δ and φ on the backward lightcone that were interpolated at angular coordinates $(\theta, \phi) = (\pi/2, 0)$: Both results are shown as function of the affine parameter λ which enter into the Ricci and Weyl focussing contributions to the Sachs equation. In addition, a representation as function of redshift illustrates the strong decrease of Δ with increasing z. Whereas the density contrast $\Delta(\lambda)$ is of order 10^{-1}, $\varphi(\lambda)$ is considerably smaller by almost four orders of magnitude. The functional shape of the solution to the Sachs equation is therefore dominated by contributions of the density contrast.

8.6 OUTLOOK

Light propagation in LTB models is a promising approach to study observational effects of gauge-invariant perturbative quantities on radially inhomogeneous backgrounds. In fact, combined influences of metric and matter perturbations on null geodesics can be mapped to corrections to the area angular diameter distance that itself can directly be inferred from observations using, for example, cosmological standard rulers. As discussed in Chapts. (4) and (7), the notion of a generic scalar metric potential or a density contrast is inherently difficult on LTB backgrounds and corresponding gauge-invariant expressions have not been derived yet. Therefore, weak gravitational lensing seems the most useful alternative to obtain observable predictions from perturbed LTB models.

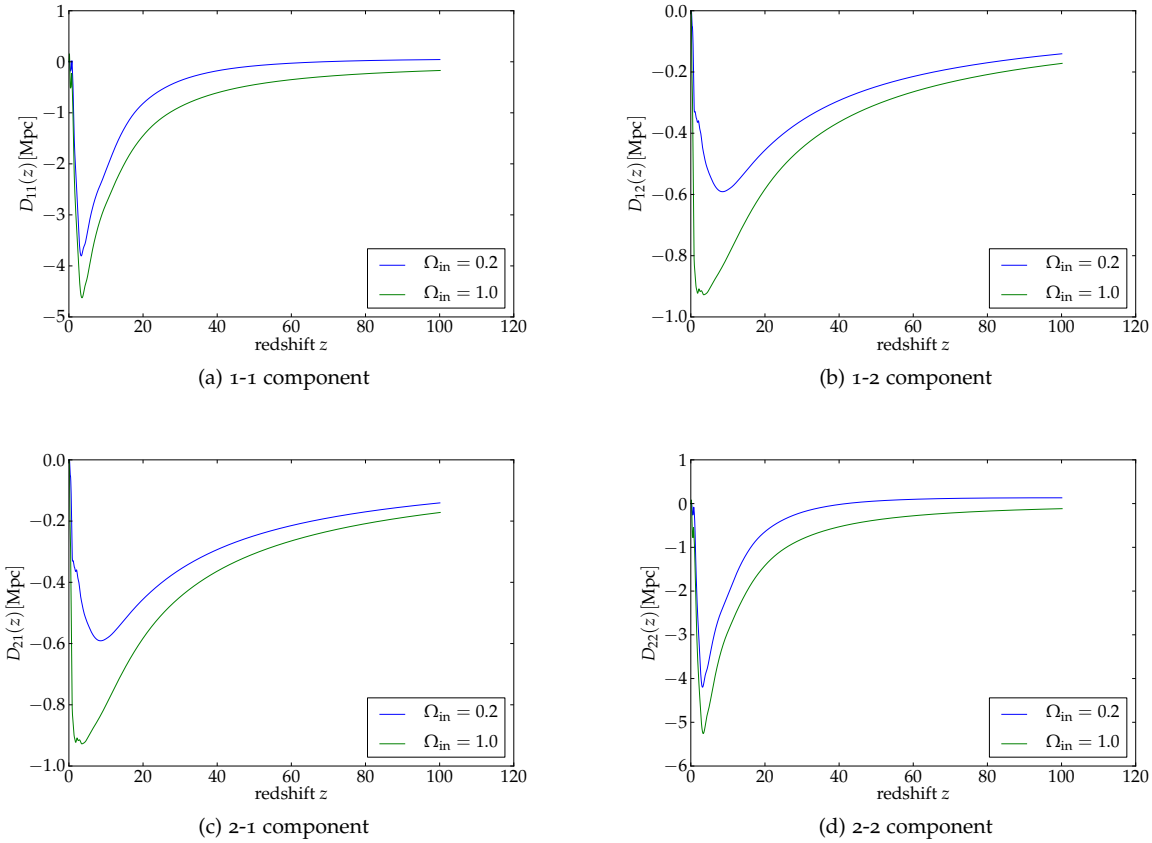

(a) 1-1 component (b) 1-2 component

(c) 2-1 component (d) 2-2 component

Figure 8.4: First order corrections to the Jacobi Map as function of redshift at angular coordinates $(\theta, \phi) = (\pi/2, 0)$: Results are shown for a deep void with $\Omega_{\rm in} = 0.2$ and $L = 2$ Gpc extension and for the homogeneous EdS model. Off-diagonal components are smaller by a factor of ten in amplitude as they are not sourced by the first-order Ricci focussing that is dominated by contributions of the density contrast.

In case of negligible coupling of perturbation types, the relevant equations and the corresponding numerical treatment simplify considerably since the spherical harmonic decomposition can be circumvented and the spacetime evolution of the scalar metric potential is solely described by a growth factor that is independent of the angular scale. Regarding these main simplifications, first numerical attempts to solve the Sachs equation were performed. However, the results presented in Chapt. (7) suggest that coupling of polar perturbations cannot be neglected for realistic void scenarios and therefore the complete set of polar perturbations have to be taken into account. This is current work in progress and we hope to obtain reliable results in the near future. The main complication lies in a sufficiently accurate modeling of perturbations along the line of sight which requires the numerical solution of the complete set of polar evolution equations for a considerable amount of ℓ-modes. This is computationally very costly as no universal transfer function to this equation system can be derived that could generically be applied to initial conditions at early times.

In addition, only polar degrees of freedom have been included into the analysis so far. This can be motivated by the fact that the polar and axial branches are dynamically decoupled and initial scalar perturbations do therefore not influence any vector or tensor perturbations in the axial branch. For the sake of initially vanishing vector and tensor fluctuations in FLRW limit, the restriction to the polar branch can be considered as sufficient for a complete description of light propagation in perturbed LTB models. However, once more general initial conditions are going to be applied, axial degrees

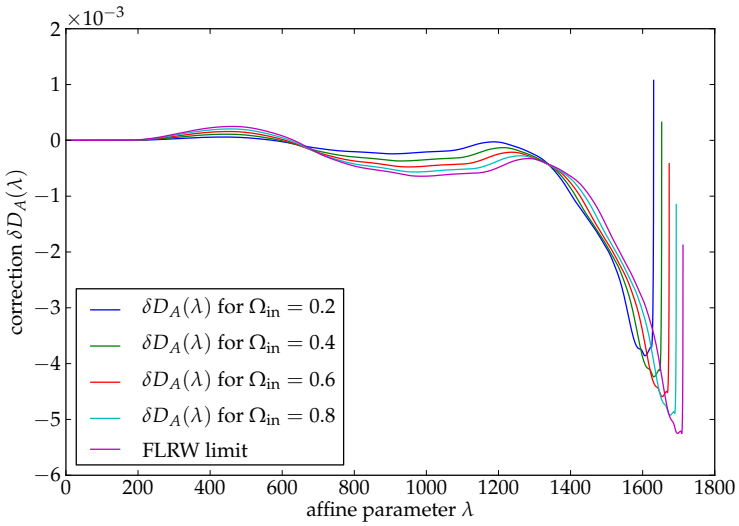

(a) Corrections δD_A with respect to the affine parameter

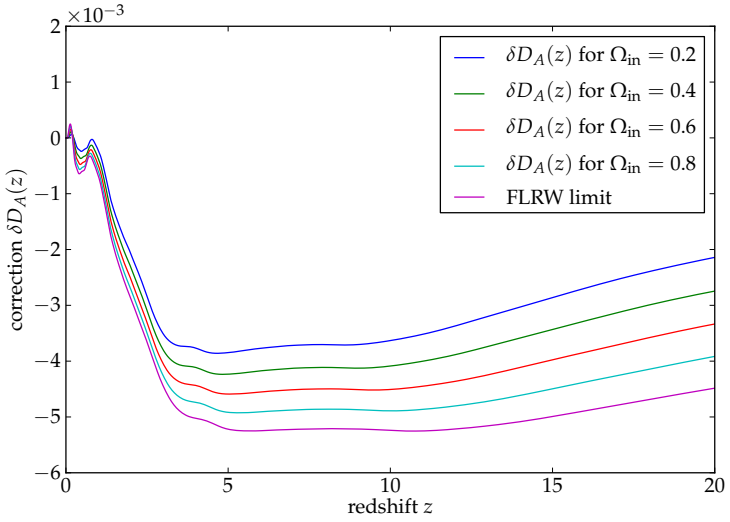

(b) Corrections δD_A with respect to redshift

Figure 8.5: Numerical results on the first order corrections to the area angular diameter distance in case of negligible perturbation coupling: Corrections are shown for Gaussian-shaped voids with 2 Gpc extension and varying depths. All void models are asymptotically embedded into an EdS universe. Figure (b) is restricted to redshifts $z \leq 20$ for better visualisation.

of freedom are relevant and have to be considered as a non-trivial contribution to the optical tidal matrix.

As already mentioned, the main observational probe for the estimation of angular diameter distances are Baryon Acoustic Oscillations (BAOs) or any comparable cosmological standard ruler. Since rigorous treatments of BAOs are still left to be done in void models, the length of the standard ruler has to be estimated in the asymptotic FLRW limit of the LTB lightcone. Once this physical length scale and the corresponding cross section can be determined, the observed solid angle yields an estimate of the area angular diameter distance. Regarding the smallness of the model-predicted amplitude of corrections, deviations of the backward lightcone from isotropy can well be neglected when constraining LTB models observationally. Although this result is still left to be confirmed by considering the

combined effects of all LTB gauge-invariants, we see that the difference in linear structure formation between void models and FLRW models does not affect shape of the backward lightcone in a significant way. Consequently there is no need to correct for these effects when analysing observational probes in the framework of large void models. Of course, there are strong arguments to neglect these effects right away as structure formation is expected to be suppressed in local underdense regions which even diminishes any effects of inhomogeneities on light propagation in comparison to the well-known FLRW case. However, regarding the complexity and subtleties of linear perturbation theory in void models, it is necessary to confirm those previous assumptions in a rigorous setup.

In order to augment constraints on LTB models from linear structure formation, it is inevitable to study the statistical information of these corrections which is contained in their angular correlations. In fact, Eq. (8.44) shows that $D_{ab}^{(1)}$ parametrically depends on the azimuthal and polar angles (θ, ϕ) on the celestial sphere. This suggests an expansion of the full angular diameter distance into spherical harmonics

$$D_A(\lambda, \theta, \phi) = \sum_{\ell=0}^{\infty} \sum_{m=-\ell}^{\ell} D_A^{(\ell m)}(\lambda) Y^{(\ell m)}(\theta, \phi)\,, \tag{8.53}$$

which allows to compute generic estimates of the angular power spectra $\langle D_A^{(\ell m)}(\lambda) D_A^{(\ell' m')}(\lambda') \rangle$ which can then directly be compared to observationally estimated spectra on different angular scales.

In a similar way, we can predict correlation functions of the convergence and shear coefficients (κ, γ) that have been introduced in Chapt. (2.5). The statistical properties of solutions to the Sachs equation can directly be compared to observed shear correlations. Relations of the Sachs optical scalars $\hat{\theta}$ and $\hat{\sigma}$ to the weak lensing amplification matrix A_{ab} (see [30]) can be applied to obtain direct estimates of the lensing angular power spectra in void models. Since we are confined to linear structure growth, those comparisons certainly need to be restricted to sufficiently large angular scales of at least $\sim 10'$. Existing datasets, notably from the Canada-France-Hawaii-Telescope-Legacy Survey (CFHTLS) (see [55]), can be involved for this purpose. As no analytical Green's function of the background Sachs equation has been found so far, those results have to be obtained numerically. This admittedly challenging procedure will be approached in the near future.

9

CONCLUSION AND OUTLOOK

The work condensed in this thesis aimed at investigating two main aspects of linear structure formation on radially inhomogeneous LTB spacetimes. First of all, we intended to study the evolution of polar, gauge-invariant perturbations starting from initial scalar fluctuations on a spatial hypersurface intersecting the past null cone well within the asymptotic FLRW limit. Secondly, we investigated how those perturbations quantitatively influence light propagation and thus the appearance and interpretation of observables.

In this context, we developed a new numerical scheme to solve the underlying system of partial differential equations that constrains the spacetime evolution for a possible set of gauge-invariant quantities on LTB backgrounds. The solution proved to be stable, physically meaningful and consistent with previously obtained results by February et al. (2014) ([41]). Initial scalar perturbations were sampled well within the matter-dominated FLRW era based on the power spectrum of the metric Bardeen potential. According to the standard inflationary paradigm, a finite realisation of a Gaussian random field for the metric potential Ψ was generated, related to the LTB gauge-invariants and those numerically evolved into the LTB regime. This approach extends previous studies performed in [41] in the sense that basic properties of the spacetime evolution, like dynamical coupling, can now be characterised for the full spectrum of initially Gaussian perturbations. The averaged coupling strength (as defined in Eq. (7.5)) were estimated to amount to 28% for large and deep voids needed to recover the observed distance redshift relation of SNe (see [41, 75]). This significant influence of couplings on the spacetime evolution represents a very important feature to constrain LTB models using structure formation and, eventually, ruling them out on a solid basis.

However, strong conceptual difficulties in constructing LTB and FLRW gauge-invariant quantities prevent a straightforward comparison of both models. As outlined in detail in Sect. (2.3.2) and App. (B), generic scalar, vector and tensor quantities are characterised according to their transformation properties on spatial hypersurfaces. In the case of Friedmann models, these spatial sections are homogeneous and isotropic 3-dimensional spaces whereas LTB models only admit 2-dimensional group orbits (two-spheres). Gauge transformations and corresponding gauge-invariant perturbations in LTB spacetimes are therefore inherently different from the FLRW case where gauge-invariants remain observable quantities. Instead, LTB perturbations are abstract mathematical objects that, although containing only physical degrees of freedom, are reduced to complicated mixings of scalar-vector-tensor variables in the FLRW limit (see App. (C)). The physical interpretation of those perturbations on fully inhomogeneous backgrounds is not clear at all.

In order to circumvent this problem, we successfully adapted a relativistic framework of light propagation to perturbed LTB models. Combined gauge-invariant metric and matter perturbations can effectively be mapped to the Ricci and Weyl focussing contributions in the optical Sachs equation. As laid out in Chapt. (8), the Sachs equation constrains the evolution of the cross section of a thin geodesic bundle that is parallel-transported along a fiducial light ray. By relating cross-sectional diameters at given affine parameter λ to solid angles at the observer's position, angular diameter distances can be deduced that incorporate small corrections due to metric and matter perturbations. Within the Born approximation, the full linear corrections to the Sachs equation were derived and numerically investigated in the case of negligible dynamical coupling. For instance, regarding an exemplary angular

direction, we found sub-percent level corrections to the angular diameter distance that are even decreasing with void depth. Hence, we found that linear perturbations along the line-of-sight produce negligible scatter in the distance-redshift relation of LTB models. This strengthens the arguments of previous analyses of void models that rely on observational data gathered from the backward lightcone. Although the full analysis with coupled LTB perturbations in a realistic void model still needs to be done, we are confident that influences of linear structures on the backward lightcone are by far not able to alleviate the tension between observational data and model predictions.

We want to stress that the main goal of this thesis work was to figure out whether it is possible to set up and maintain a numerical framework for linear perturbation theory in void models in the first place. Correspondingly, the results gathered so far are restricted to simple test cases and no direct comparison to observational data has been performed yet. More precisely, only scalar initial perturbations that evolve on a simple Gaussian-shaped void of variable depth and extension were taken into account. In addition, all LTB models considered in this thesis were asymptotically embedded into an EdS model serving as approximation of the matter-dominated era. Definitely, the results on the spacetime evolution need to be confirmed in an extended numerical setup that is fully adapted to cosmological observations. For instance, considering observationally constrained void models obtained from supernova data (see, for example [75]), Gaussian-shaped voids are certainly able to mimic sufficiently deep and large underdensities, but do not represent the profile sufficiently well at intermediate radii. Extending the analysis to these void profiles will therefore be most important and will be addressed in the near future.

As is well known, tensor perturbations in the matter-dominated era are small yet measurable and a firm prediction of many inflationary models (see [15] for a review). In fact, the latest measurements of upper bounds to the tensor-to-scalar ratio can help to predict initial tensor angular power spectra and corresponding initial tensor perturbations in the FLRW regime. This enables us to study their influence on the late-time evolution of perturbations on the LTB background. However, in order to arrive at a complete and consistent description of linear perturbations at all times and over all spatial scales, the numerical framework has to be extended to include axial perturbations, as initial tensor modes generate non-trivial contributions in this branch as well (see App. (B) for details).

The framework of light propagation in LTB models can certainly be improved by considering statistical properties of the solution to the Sachs equation. As a direct extension, angular correlations between two light rays and their analysis in spherical harmonic space might be adequate for comparison to observations providing additional constraints on LTB models. Of course, the solution to the full first-order Sachs equation has to be included in order to confirm previously obtained results on a solid foundation. Nonetheless, we do not expect severe changes of corrections as we only have access to the combined effect of LTB gauge-invariants. At a fixed angular scale, power is then simply exchanged between different gauge-invariants, which is not expected to alter the collective power significantly. However, it will be particularly interesting to study to what degree gravitational lensing effects in LTB models can convert E-mode to B-mode polarisation patterns. Since tensorial perturbation modes are naturally excited in LTB models and may even be fed by the decay of scalar perturbation modes, changes compared to the standard model could be substantial and should be carefully quantified.

Regarding the obvious complexity of the numerical modeling that has to be performed for a seemingly simple exclusion of void models, one can seriously ask whether it is really worth the effort. Careful comparison with observation data has shown that void models are in considerable tension with multiple observations. Hence, the understanding of linear structure growth in these models cannot be expected to alleviate this tension, but rather to strengthen it in a considerable way. In this manner, we think that observable predictions from linear perturbation theory are a very valuable extension to previous attempts of modeling and constraining the averaged structure of the local universe around our galaxy. If void models shall be ruled out in a scientifically substantial way, we are convinced that this information must be included, and we are going to address this issue in the near future.

We finally want to stress that, precisely, what has been ruled out by previous analyses is the assumption that the accelerated expansion might simply be an erroneous interpretation of observational data as the backward lightcone might be affected by a large underdense region around our spacetime position. Therefore, it seems that there is now even stronger evidence for a cosmological constant. But we know that, even within ΛCDM, there *are* voids, and we are able to calculate the evolution of linear perturbations in these voids as well. In this context, it is worth mentioning again that previous considerations can be extended to ΛLTB models which include a non-vanishing cosmological constant as an additional free parameter. These models are well motivated in the context of the Lovelock theorem (see [64]) and have been established to test the Copernican Principle due to deviations from the homogeneous ΛCDM model (see Sect. (7.4) for a brief discussion and [75] for a detailed analysis). As shown by [41], the polar master equations can easily be adapted to the ΛLTB regime. Detailed investigations have already been performed on the global properties of these models, and efficient numerical implementations are available. Porting our numerical scheme to ΛLTB models therefore seems to be a straightforward procedure. Coupling effects are, of course, expected to be substantially smaller but, nonetheless, linear perturbation theory may help to confirm the Copernican Principle and the remarkable success of the ΛCDM model using multiple observational probes.

Part II

APPENDIX

A

SOLUTION TO THE SACHS EQUATION IN LTB SPACETIMES

This section contains a short proof that the areal radius indeed solves the Sachs equation at the background level. Interestingly, this result can be obtained without exact knowledge of the shape of the backward lightcone since only differential relations between lightcone coordinates, redshift and affine parameter are going to enter.

We start again from the background LTB metric in the notation of Clarkson et. al. (2009) ([29]),

$$\mathrm{d}s^2 = -\mathrm{d}t^2 + \frac{a_\parallel^2(t,r)}{1-\kappa(r)r^2}\mathrm{d}r^2 + r^2 a_\perp^2(t,r)\mathrm{d}\Omega^2\,, \tag{A.1}$$

and the energy-momentum tensor $T_{\mu\nu} = \rho(t,r)u_\mu u_\nu$. Following [29], we define an auxiliary function $W(t,r)$ and a so-called radial frame derivative given by

$$W(t,r) := \frac{\sqrt{1-\kappa(r)r^2}}{r a_\perp(t,r)}\,, \tag{A.2}$$

$$(\ldots)' := \frac{\sqrt{1-\kappa(r)r^2}}{a_\parallel(t,r)}\partial_r(\ldots)\,. \tag{A.3}$$

Within this notation, the constraining equation for the mass profile (see Eq. (3.25))

$$\frac{\partial_r\left[M(r)r^3\right]}{r^2 a_\perp^2(t,r)a_\parallel(t,r)} = 8\pi G\rho(t,r)\,, \tag{A.4}$$

that has directly been inferred from Einstein's field equations, can be transformed into an equivalent expression

$$W' = -W^2 - 4\pi G\rho + H_\perp H_\parallel + \frac{M}{2a_\perp^3} \tag{A.5}$$

involving the tangential and radial Hubble rates $H_\perp$ and $H_\parallel$.

We now consider the Sachs equation for central observers in LTB spacetimes

$$\frac{\mathrm{d}^2 D_{ab}(\lambda)}{\mathrm{d}\lambda^2} = -4\pi G\rho\left[t(\lambda),r(\lambda)\right]\left[1+z(\lambda)\right]^2 D_{ab}(\lambda)\,. \tag{A.6}$$

Inserting $D_{ab} = R(t,r)\delta_{ab} = r a_\perp(t,r)\delta_{ab}$ into Eq. (A.6), we find, after some computation,

$$\begin{aligned}\frac{\mathrm{d}^2}{\mathrm{d}\lambda^2}\left\{r(\lambda)a_\perp\left[t(\lambda),r(\lambda)\right]\right\} &= (1+z)^2 H_\parallel\left(\sqrt{1-\kappa r^2} - r\dot{a}_\perp\right)\\ &+ (1+z)^2 r a_\perp\left[\frac{\sqrt{1-\kappa r^2}}{a_\parallel}\partial_r\left(\frac{\sqrt{1-\kappa r^2}}{r a_\perp}\right) + \frac{1-\kappa r^2}{r^2 a_\perp^2}\right]\\ &- (1+z)^2\sqrt{1-\kappa r^2}H_\parallel + (1+z)^2 r\ddot{a}_\perp\\ &\stackrel{!}{=} 4\pi G\rho(1+z)^2 r a_\perp\,,\end{aligned} \tag{A.7}$$

where the differential relations for redshift and lightcone coordinates with respect to λ have been applied (see Eqs. (8.17) - (8.19)).

Using Eqs. (A.2) and (A.3) as well as the definitions of the radial and tangential Hubble rates, the Jacobi equation can be transformed into

$$W' + W^2 - H_\parallel H_\perp + \frac{\ddot{a}_\perp}{a_\perp} = -4\pi G\rho\,, \tag{A.8}$$

which is very close to Eq. (A.5). In fact, considering the evolution of the tangential Hubble rate, namely

$$H_\perp^2(t,r) = \frac{M(r)}{a_\perp^3(t,r)} - \frac{\kappa(r)}{a_\perp^2(t,r)}\,, \tag{A.9}$$

and differentiating it with respect to time yields

$$\begin{aligned} \partial_t\left(H_\perp^2\right) = 2H_\perp\dot{H}_\perp &= 2\left(\frac{\ddot{a}_\perp}{a_\perp} - \frac{\dot{a}_\perp^2}{a_\perp^2}\right) \\ &\overset{!}{=} H_\perp\left(-3\frac{M(r)}{a_\perp^3} + 2\frac{\kappa(r)}{a_\perp^2}\right)\,, \\ \Rightarrow \frac{\ddot{a}_\perp}{a_\perp} - H_\perp^2 &= -\frac{3M}{2a_\perp^3} + 2\frac{\kappa(r)}{a_\perp^2} \\ \Rightarrow \frac{\ddot{a}_\perp}{a_\perp} &= -\frac{M}{2a_\perp^3}\,. \end{aligned} \tag{A.10}$$

The second time derivative in Eq. (A.8) can now be replaced and we finally obtain Eq. (A.5). Thus, we have managed to transform the Sachs equation to a well-known relation Einstein's field equations, once the areal radius is inserted. In order to uniquely identify $D_{ab}(\lambda)$ with $r(\lambda)a_\perp\left[t(\lambda), r(\lambda)\right]\delta_{ab}$, the initial conditions need to coincide as well. Since $r(\lambda = 0) = 0$ and $a_\perp(t,r)$ only weakly depends on r close to the void centre[1], we have

$$ra_\perp(t,r)\big|_{\lambda=0} = 0\,, \tag{A.11}$$

$$\begin{aligned} \frac{\mathrm{d}}{\mathrm{d}\lambda}ra_\perp(t,r)\bigg|_{\lambda=0} &= \partial_r\left[ra_\perp(t,r)\right]\frac{\mathrm{d}r}{\mathrm{d}\lambda}\bigg|_{\lambda=0} + \partial_t\left[ra_\perp(t,r)\right]\frac{\mathrm{d}t}{\mathrm{d}\lambda}\bigg|_{\lambda=0} \\ &= \sqrt{1-\kappa(0)r^2(0)}\left[1+z(0)\right] - r(0)a_\perp(t_{\mathrm{age}},0)\left[1+z(0)\right] \\ &= 1\,. \end{aligned} \tag{A.12}$$

Hence, $D_{ab}(\lambda) = r(\lambda)a_\perp\left[t(\lambda), r(\lambda)\right]\delta_{ab}$ uniquely solves the Sachs equation for central, freely-falling observers in generic LTB spacetimes.

1 As alternative, physical explanation it can be mentioned that a central, freely-falling observer locally experiences a Minkowski spacetime which automatically implies $ra_\perp(t,r)|_{\lambda=0} = r(\lambda = 0) = 0$.

B

A POSSIBLE SET OF GAUGE-INVARIANT PERTURBATIONS IN LTB SPACETIMES

The construction of gauge-invariant perturbations on generic spherically symmetric backgrounds was first performed by Gerlach & Sengupta in 1979 (see [51]). Their approach shall briefly be discussed here and then be specified to spacetimes sourced by pure dust matter. Derivations laid out in this appendix closely follow the steps outlined in Clarkson et al. (2009) (see Appendix of [29]).

As already pointed out in Chapt. (3), any 4-dimensional manifold $\mathcal{M}^4$ obeying spherical symmetry can naturally be splitted into $\mathcal{M}^4 = \mathcal{M}^2 \times \mathcal{S}^2$. The corresponding line element is then given by

$$\mathrm{d}s^2 = g_{AB}(t,r)\,\mathrm{d}x^A\mathrm{d}x^B + R^2(t,r)\gamma_{ab}\,\mathrm{d}x^a\mathrm{d}x^b\,. \tag{B.1}$$

In accordance with Chapt. (4), we again use Greek indices to denote coordinates on $\mathcal{M}^4$ whereas capital and lower case Roman indices refer to coordinates on $\mathcal{M}^2$ and $\mathcal{S}^2$, respectively. γ_{ab} is given by the metric on $\mathcal{S}^2$.

Linear perturbations away from Eq. (B.1) can be characterised regarding their transformation properties on underlying 2-spheres. Considering their behaviour with respect to parity transformations $(\theta,\phi) \longrightarrow (\pi-\theta,\pi+\phi)$ on $\mathcal{S}^2$, quantities additionally split into a separate polar (even) or an axial (odd) branch that are independent of each other. The metric and energy-momentum tensor of the full spacetime can therefore be written as

$$g_{\mu\nu} = \bar{g}_{\mu\nu} + \delta g^{\mathrm{polar}}_{\mu\nu} + \delta g^{\mathrm{axial}}_{\mu\nu}\,, \tag{B.2}$$

$$T_{\mu\nu} = \bar{T}_{\mu\nu} + \delta T^{\mathrm{polar}}_{\mu\nu} + \delta T^{\mathrm{axial}}_{\mu\nu}\,. \tag{B.3}$$

As introduced in Chapt. (4), spherical harmonics $Y^{(\ell m)}$ and corresponding covariant derivatives thereof assemble an orthonormal basis system on the unit sphere. Conveniently, spherical harmonics transform as scalars on $\mathcal{S}^2$ whereas the first and second covariant derivative obey vector and tensor properties, respectively. Hence, projecting generic linear perturbations onto these sets of basis functions allows to decompose them into $\mathcal{S}^2$-scalars, -vectors and -tensors in a natural way. Splitting vectors and tensors into their divergence-free and curl-free parts yields polar and axial contributions. For the axial branch, we obtain (see [51])

$$\delta g^{\mathrm{axial}}_{\mu\nu} = \begin{pmatrix} 0 & h^{\mathrm{axial}}_A\,\bar{Y}^{(\ell m)}_a \\ h^{\mathrm{axial}}_A\,\bar{Y}^{(\ell m)}_a & h\,\bar{Y}^{(\ell m)}_{ab} \end{pmatrix}, \tag{B.4}$$

$$\delta t^{\mathrm{axial}}_{\mu\nu} = \begin{pmatrix} 0 & \Delta t^{\mathrm{axial}}_A\,\bar{Y}^{(\ell m)}_a \\ \Delta t^{\mathrm{axial}}_A\,\bar{Y}^{(\ell m)}_a & \Delta t^{(1)}\,\bar{Y}^{(\ell m)}_{ab} \end{pmatrix}, \tag{B.5}$$

whereas polar perturbations can be decomposed into

$$\delta g^{\mathrm{polar}}_{\mu\nu} = \begin{pmatrix} h_{AB}\,Y^{(\ell m)} & h^{\mathrm{polar}}_A\,Y^{(\ell m)}_a \\ h^{\mathrm{polar}}_A\,Y^{(\ell m)}_a & R^2\left[K\,Y^{(\ell m)}\gamma_{ab} + G\,\nabla_a\nabla_b Y^{(\ell m)}\right] \end{pmatrix}, \tag{B.6}$$

$$\delta T^{\text{polar}}_{\mu\nu} = \begin{pmatrix} \Delta t_{AB}\, Y^{(\ell m)} & \Delta t^{\text{polar}}_{A}\, Y^{(\ell m)}_{a} \\ \Delta t^{\text{polar}}_{A}\, Y^{(\ell m)}_{a} & \Delta t^{(3)}\, Y^{(\ell m)}\, \gamma_{ab} + \Delta t^{(2)}\, Y^{(\ell m)}_{ab} \end{pmatrix} . \tag{B.7}$$

Results are presented for each spherical harmonic mode (ℓ, m).

In fact, Eqs. (B.4) - (B.7) define 12 gauge-dependent perturbations of the metric and energy-momentum tensor that contain 20 degrees of freedom in total. Each perturbation variable is given by a spherical harmonic coefficient being a function of the two remaining coordinates $x^A = (t, r)$. Following the exact same procedure as outlined in Chapt. (2), general gauge transformations of each quantity can be derived which allow to deduce expressions that are invariant under those transformations. Hence, a possible set of gauge-invariants is given by the following relations (see [51]):

- axial gauge-invariants:

$$k_A = h^{\text{axial}}_A - \nabla_A h + 2h v_A \,, \tag{B.8}$$

$$L_A = \Delta t^{\text{axial}}_A - \frac{h^{\text{axial}}_A}{2} \overline{T}^{d}{}_{d} \,, \tag{B.9}$$

$$L = \Delta t^{(1)} - \frac{h}{2} \overline{T}^{d}{}_{d} \,, \tag{B.10}$$

- polar gauge-invariants:

$$k_{AB} = h_{AB} - \nabla_B p_A - \nabla_A p_B \,, \tag{B.11}$$

$$\varphi = K - 2 v^A p_A \,, \tag{B.12}$$

$$t_{AB} = \Delta t_{AB} - p^C \nabla_C \overline{T}_{AB} - \overline{T}_{AC} \nabla_B p^C - \overline{T}_{BC} \nabla_A p^C \,, \tag{B.13}$$

$$t_A = \Delta t^{\text{polar}}_A - \overline{T}_{AC} p^C - R^2 \left(\frac{1}{4} \overline{T}^{d}{}_{d} \right) \nabla_A G \,, \tag{B.14}$$

$$t^{(2)} = \Delta t^{(2)} - \frac{p^C}{R^2} \nabla_C \left(\frac{1}{2} R^2 \overline{T}^{d}{}_{d} \right) , \tag{B.15}$$

$$t^{(3)} = \Delta t^{(3)} - \left(\frac{1}{2} R^2 \overline{T}^{d}{}_{d} \right) G \,, \tag{B.16}$$

where the definitions $v_A \equiv (\nabla_A R)/R$ and $p_A \equiv h^{\text{polar}}_A - R^2 \nabla_A G/2$ have been applied. ∇_A denotes a covariant derivative on the (t, r)-submanifold.

In the following, two main simplifications will be performed. First of all, we assume the background spacetime to be entirely sourced by pressureless dust which implies $\overline{T}^{d}{}_{d} = 0$. Secondly, we evaluate Eqs. (B.4) - (B.7) in Regge-Wheeler (RW) gauge (see [76]), i. e. the gauge-generating 4-vector field ζ^μ is chosen such that $h = h^{\text{polar}}_A = G = 0$. Considering Eqs. (B.8) - (B.16), we see that perturbations in RW gauge are identical to the gauge-invariants on spherically-symmetric backgrounds. In fact, this particular gauge is equivalent to the conformal Newtonian gauge which is conveniently applied to describe perturbed FLRW models. Perturbations of spherically symmetric dust solutions can therefore be identified as

$$\delta g^{\text{RW}}_{\mu\nu} = \begin{pmatrix} 0 & k_A\, \overline{Y}^{(\ell m)}_{a} \\ k_A\, \overline{Y}^{(\ell m)}_{a} & 0 \end{pmatrix} , \tag{B.17}$$

$$\delta T^{\text{RW}}_{\mu\nu} = \begin{pmatrix} 0 & L_A\, \overline{Y}^{(\ell m)}_{a} \\ L_A\, \overline{Y}^{(\ell m)}_{a} & L\, \overline{Y}^{(\ell m)}_{ab} \end{pmatrix} \tag{B.18}$$

for the axial branch and

$$\delta g^{\mathrm{RW}}_{\mu\nu} = \begin{pmatrix} k_{AB}\, Y^{(\ell m)} & 0 \\ 0 & r^2 a_\perp^2\, \varphi\, Y^{(\ell m)}\, \gamma_{ab} \end{pmatrix} , \tag{B.19}$$

$$\delta T^{\mathrm{RW}}_{\mu\nu} = \begin{pmatrix} t_{AB}\, Y^{(\ell m)} & t_A\, Y_a^{(\ell m)} \\ t_A\, Y_a^{(\ell m)} & r^2 a_\perp^2\, t^{(3)} Y^{(\ell m)}\, \gamma_{ab} + t^{(2)}\, Y_{ab}^{(\ell m)} \end{pmatrix} \tag{B.20}$$

for the polar branch. These quantities assemble a general metric ansatz that can be inserted into Einstein's field equations to obtain linear partial differential equations constraining their spacetime evolution. However, the general form of these equations turns out to be very abstract and therefore impractical for numerical treatment. For this reason, Gundlach & Martin-Garcìa (2000) (see [54]) additionally projected all perturbation variables on a covariant perfect fluid frame spanned by orthonormal basis vectors (u_A, n_A) in the (t, r)-submanifold. In fact, on a spherically symmetric background, the comoving four velocity u_μ can be written as

$$u_\mu = (u_A, 0) , \tag{B.21}$$

which defines the natural unit vectors u_A and $n_A = -\epsilon_{AB} u^B$ that are perpendicular to each other. ϵ_{AB} denotes the usual Levi-Civita tensor on $\mathcal{M}^2$. Physically, perturbations are then specified to observers comoving with the background fluid. In case of pressureless dust, this decomposition allows to separate density- from four-velocity perturbations which yields the general ansatz

$$\rho = \bar{\rho} \left(1 + \tilde{\Delta}\, Y^{(\ell m)}\right) , \tag{B.22}$$

$$\Delta u_\mu^{\mathrm{polar}} = \left[\left(\tilde{w}\, n_A + \frac{1}{2}\, h_{AB}\, u^B \right) Y^{(\ell m)},\, v\, Y_a^{(\ell m)} \right] , \tag{B.23}$$

$$\Delta u_\mu^{\mathrm{axial}} = \left(0,\, \bar{v}\, \bar{Y}_a^{(\ell m)}\right) . \tag{B.24}$$

The density perturbation Δ is scalar function and also transforms as scalar on $\mathcal{S}^2$. Hence, it naturally belongs to the polar branch. Four-velocity perturbations split into one n_A-component $\tilde{w}$ and two tangential components $\tilde{v}$ and $\bar{v}$. It can be shown that the general ansatz proposed in Eqs. (B.23) and (B.24) contains all three possible spatial velocity perturbations and additionally preserves the normalisation $g_{\mu\nu} u^\mu u^\nu = -1$ to first order. Evaluating general gauge transformations of these objects, one finds the following set of new quantities which are manifestly gauge-invariant

$$\Delta = \tilde{\Delta} - \frac{p^A \nabla_A \rho}{\rho} , \tag{B.25}$$

$$w = \tilde{w} - n^A p^B \nabla_B u_A + \frac{1}{2} n^A u^B \left(\nabla_B p_A - \nabla_A p_B\right) , \tag{B.26}$$

$$v = \tilde{v} - p^B u_B , \tag{B.27}$$

with the same definitions applied above. $\bar{v}$ turns out to be automatically gauge-invariant. Interestingly, the RW gauge reduces again all perturbation variables to the gauge-invariant ones which directly relates the density and velocity perturbations to the components of the energy momentum tensor defined in Eqs. (B.17) - (B.20), i. e.

$$L_A = \bar{v}\, \rho u_A , \tag{B.28}$$

$$t_A = v\, \rho u_A , \tag{B.29}$$

$$t_{AB} = \rho \left[\Delta\, u_A u_B + w \left(u_A n_B + n_A u_B\right) + \frac{1}{2} \left(k_{AC} u^C u_B - k_{BC} u^C u_A \right) \right] . \tag{B.30}$$

In absence of background pressure, no pressure perturbation in the form of anisotropic stress $\Sigma_{\mu\nu}$ is generated[1] which additionally leads to $t^{(2)} = t^{(3)} = L = 0$.

For convenience, the metric tensor k_{AB} in RW gauge can further be decomposed into components with respect to the fluid frame

$$k_{AB} = \eta\left(-u_A u_B + n_A n_B\right) + \phi\left(n_A n_B + u_A u_B\right) + \varsigma\left(u_A n_B + u_B n_A\right) , \tag{B.31}$$

which is equivalent to an expansion into Pauli matrices with scalar coefficient functions $\eta(t,r)$, $\phi(t,r)$, and $\varsigma(t,r)$. Introducing the new variable $\chi = \phi - \varphi - \eta$ finally yields

$$k_{AB} = \eta\left(-u_A u_B + n_A n_B\right) + \left(\chi + \varphi + \eta\right)\left(n_A n_B + u_A u_B\right) + \varsigma\left(u_A n_B + u_B n_A\right) . \tag{B.32}$$

For a dust-comoving observer, we obtain

$$u_A = (-1,\, 0)\,, \tag{B.33}$$

$$n_A = -\epsilon_{AB} u^B = \left(0,\, \frac{a_\parallel}{\sqrt{1-\kappa(r) r^2}}\right) , \tag{B.34}$$

where Eq. (3.22) has been applied.

Inserting k_{AB} into the general polar metric perturbation in Eq. (B.19) finally yields the metric ansatz specified in Eq. (4.1) for the polar branch. The full axial metric ansatz is already determined by Eq. (B.17).

1 Within this framework, any anisotropic stress would correspond to terms being quadratically in the velocity perturbation that are neglected in the first-order approach.

C

FLRW LIMIT OF GAUGE-INVARIANT PERTURBATIONS IN LTB MODELS

This short appendix outlines the basic procedure to obtain the homogeneous limit of the polar and axial LTB gauge-invariant perturbations. We will just report on the main aspects here and refer to Clarkson et al. (2009) (see [29]) for detailed calculations.

For expressing the homogeneous limit of LTB gauge-invariants in terms of FLRW gauge-invariants, the two different metrics somehow need to be matched. A main complication arises as the Regge-Wheeler gauge is not well adapted to the conformal Newtonian gauge and therefore components of the metric tensors cannot straightforwardly be identified. It is rather necessary to identify metric components in a general gauge and compute the gauge-invariant perturbations afterwards. Starting from the general perturbed metric presented in Eq. (2.26), the corresponding gauge-dependent 3-scalar, 3-vector and 3-tensor contributions need to be decomposed into spherical harmonics and can then componentwisely be identified with the expressions in Eqs. (B.4) - (B.7). For instance, we obtain

$$\Psi = \Psi\, Y^{(\ell m)}\,, \tag{C.1}$$

$$(S_i) = \left(S_r\, Y^{(\ell m)},\, S\, Y_a^{(\ell m)} + \bar{S}\, \bar{Y}_a^{(\ell m)}\right)\,, \tag{C.2}$$

$$(h_{ij}) = \begin{pmatrix} h_{rr}\, Y^{(\ell m)} & h_r\, Y_a^{(\ell m)} + \bar{h}_r\, \bar{Y}_a^{(\ell m)} \\ h_r\, Y_a^{(\ell m)} + \bar{h}_r\, \bar{Y}_a^{(\ell m)} & h\, Y^{(\ell m)}\, \gamma_{ab} + h^{(TF)}\, Y_{ab}^{(\ell m)} + \bar{h}\, \bar{Y}_{ab}^{(\ell m)} \end{pmatrix}\,, \tag{C.3}$$

where summation over (ℓ, m) is implied. By construction, (S_i) represents a divergence-free vector and (h_{ij}) a divergence- and trace-free tensor which both contain two remaining the degrees of freedom. Hence, the spherical harmonic coefficient functions in Eqs. (C.2) and (C.3) reduce to two independent degrees of freedom either (see [29] and Sect. (2.3.2) for details).

Identifying the expressions in Eqs. (B.4) - (B.7) with the spherical harmonic decomposition of Eq. (2.26) yields general, gauge-dependent polar and axial perturbations of spherically symmetric dust spacetimes in the homogeneous limit. Given these identifications, the gauge-invariant perturbations can directly be computed using the corresponding expressions outlined in App. (B). In accordance with this procedure, Clarkson et al. showed that the LTB gauge-invariants $\{\chi,\, \varphi,\, \varsigma,\, \eta,\, \Pi,\, \bar{v}\}$ can be written in terms of the FLRW gauge-invariants $\left\{\Phi,\, \Psi,\, (V_i),\, (h_{ij})\right\}$ in the following way:

$$\begin{aligned} \chi =& \left(1-\kappa r^2\right) h_{rr} + 2\left[-(1-\kappa r^2)\partial_r + \frac{1}{r}\right] h_r - \frac{1}{r^2} h^{(T)} \\ &+ \left[(1-\kappa r^2)\partial_r^2 - \frac{(3-2\kappa r^2)}{r}\partial_r - \frac{\ell(\ell+1) - 8 + 4\kappa r^2}{2r^2}\right] h^{(TF)}\,, \end{aligned} \tag{C.4}$$

$$\begin{aligned} \varphi =& -2\Psi - 2\mathcal{H}V - 2\frac{(1-\kappa r^2)}{r} h_r + \frac{1}{r^2} h^{(T)} \\ &+ \left[-\mathcal{H}\partial_\tau + \frac{(1-\kappa r^2)}{r}\partial_r + \frac{\ell(\ell+1) - 4(1-\kappa r^2)}{2r^2}\right] h^{(TF)}\,, \end{aligned} \tag{C.5}$$

$$\varsigma = \sqrt{1-\kappa r^2}\left[V_r - \partial_r V + \partial_\tau h_r - \left(\partial_r - \frac{1}{r}\right)\partial_\tau h^{(TF)}\right]\,, \tag{C.6}$$

$$\begin{aligned}\eta =&\Phi - \Psi - (\partial_\tau + 2\mathcal{H})\, V + \frac{1}{2}(1-\kappa r^2)h_{rr} + \left[-(1-\kappa r^2)\partial_r + \kappa r\right] h_r \\ &+ \frac{1}{2}\left[-\partial_\tau^2 - 2\mathcal{H}\partial_\tau + \frac{2}{r^2} - \frac{(2-\kappa r^2)}{r}\partial_r + (1-\kappa r^2)\partial_r^2\right] h^{(TF)}\,,\end{aligned} \tag{C.7}$$

$$\Pi = \frac{\sqrt{1-\kappa r^2}}{r^2 a^2(\tau)}\left[\left(\partial_r - \frac{2}{r}\right)\bar{V} + \partial_\tau \bar{h}_r\right]\,, \tag{C.8}$$

$$16\pi G a(\tau)\rho\bar{v} = \left[-(1-\kappa r^2)\partial_r^2 + \kappa r\partial_r + \frac{\ell(\ell+1) - 4\kappa r^2}{r^2}\right]\bar{V}\,, \tag{C.9}$$

where the constant spatial curvature κ, the conformal time τ, and the corresponding Hubble rate $\mathcal{H}$ have been involved.

Although being complicated differential relations, Eqs. (C.4) - (C.9) contain very profound information about the nature of LTB gauge-invariants in the FLRW limit. As outlined in Sect. (2.3.2), the physical interpretation of FLRW gauge-invariants is possible because of the high degree of spatial symmetry. Φ and Ψ denote generic scalar gravitational potentials whereas the 3-vector (V_i) gives rise to velocities and the 3-tensor (h_{ij}) to propagating modes, i. e. gravitational waves. In comparison, LTB gauge-invariants show complicated mixings between different perturbation types even on homogeneous backgrounds.

χ represents a genuine tensor quantity which explains its behaviour as propagating mode. ς does not contain any scalar part whereas φ incorporates the scalar metric perturbation known from perturbed FLRW models, but is also augmented by additional vector and tensor contributions. η actually corresponds to the difference of the Bardeen potentials plus corrections from vectors and tensors. Interestingly, the scalar limit of the evolution equation $\eta = 0$ exactly reflects the result $\Phi = \Psi$ in absence of anisotropic stress. By construction, axial perturbations do not contain any scalar parts. Π is constrained by a wave equation and so necessarily incorporates propagating modes. These are encoded in tensor contributions in the FLRW limit. Eq. (C.9) shows a generalised Poisson relation between the velocity potential $\bar{V}$ and the axial velocity perturbation $\bar{v}$.

We want to stress that all these statements rely on the FLRW limit of the LTB gauge-invariants. Any physical interpretation of these quantities on inhomogeneous backgrounds is far more complicated since, mathematically, no natural splitting into 3-scalars, 3-vectors and 3-tensors exists. In this case, only combined effects of all perturbation quantities have been studied so far (see Chapt. (8)).

To conclude this section, we want to draw attention a very important simplification of this setup. Assuming that the averaged initial universe is sufficiently homogeneous and isotropic and that deviations from this symmetries are mainly caused by scalar perturbations, the only non-trivial part of Eqs. (C.4) - (C.9) is given by $\varphi = -2\Psi$. Practically, this remarkably simple initial configuration allows to set up initial conditions for the LTB evolution equations which is laid out in detail in Chapt. (6). In addition, we see that the initial Bardeen potential does not source any axial modes. Since the axial branch is dynamically decoupled from the polar branch, these contributions can also not be generated during spacetime evolution. As already mentioned in Chapt (4), restricting the analysis to the polar branch does then already imply a complete description in this setup.

D

LOCAL OPERATORS

It was shortly discussed in Chapt. (5) that the basic idea behind finite element discretizations consists of writing the model problem (PDE and boundary conditions) into so-called weak formulation and converting it to a variational problem. The variational problem can then be solved by discretizing the domain of interest into finite elements and approximating the solution by suitable basis functions (polynomials in particular) on each element with coefficients to be determined. Regarding the evolution equations of polar perturbations on the LTB background, this procedure is explicitly outlined in this section. Regarding the broad applicability of the DUNE framework to various classes of PDE problems, the following derivations are admittedly quite abstract. However, all steps closely follow computations outlined in the documentation of the `dune-pdelab-howto` module edited by the DUNE project team (see `http://www.dune-project.org/pdelab/pdelab-howto-2.0.0.pdf`). Hence, we refer to this document for more details.

We consider the Eqs. (4.4) - (4.6) in the interior of full spatial domain $\Omega = (0, r_*)$ constructed in Chapt. (5). We first introduce auxiliary variables $\tilde{\varphi}$ and $\tilde{\chi}$ to convert the system into five first-order equations in time. For the spatial finite element problem, we then rewrite the system into *weak formulation* by multiplying with an ansatz function v and integrating over the domain Ω. The ansatz function is chosen to vanish at the boundary $\partial\Omega$ such that terms with second-order spatial derivatives are replaced by first-order spatial derivatives using partial integration.

For a test function $v \in \left(H^1(\Omega)\right)^5$ (5-dimensional first-order Sobolev space, called test space), we obtain:

$$\int_\Omega \dot{\chi}\, v_1 \,\mathrm{d}r = \int_\Omega \tilde{\chi}\, v_1 \,\mathrm{d}r\,, \tag{D.1}$$

$$\begin{aligned}\int_\Omega \dot{\tilde{\chi}}\, v_2 \,\mathrm{d}r = &-\int_\Omega \chi' \left(\frac{v_2}{Z^2}\right)' \mathrm{d}r + \int_\Omega \left[-\frac{C}{Z^2}\chi' - 3H_\parallel \tilde{\chi} + \left[A - \frac{(\ell-1)(\ell+2)}{r^2 a_\perp^2}\right]\chi\right. \\ &\left. + \frac{2\sigma}{Z}\varsigma' + \frac{2}{Z}\left[H_\parallel - 2H_\perp\right]'\varsigma - 4\sigma\tilde{\varphi} + A\varphi\right] v_2 \,\mathrm{d}r\,,\end{aligned} \tag{D.2}$$

$$\int_\Omega \dot{\varphi}\, v_3 \,\mathrm{d}r = \int_\Omega \tilde{\varphi}\, v_3 \,\mathrm{d}r\,, \tag{D.3}$$

$$\begin{aligned}\int_\Omega \dot{\tilde{\varphi}}\, v_4 \,\mathrm{d}r = \int_\Omega &\left[-4H_\perp\tilde{\varphi} + \frac{2\kappa}{a_\perp^2}\varphi - H_\perp\tilde{\chi} + Z^{-2}\frac{a_\parallel}{r a_\perp}\chi' - \left[\frac{1-2\kappa r^2}{r^2 a_\perp^2} - \frac{\ell(\ell+1)}{2r^2 a_\perp^2}\right]\chi\right. \\ &\left. + \frac{2}{Z}\frac{a_\parallel}{r a_\perp}\sigma\varsigma\right] v_4 \,\mathrm{d}r\,,\end{aligned} \tag{D.4}$$

$$\int_\Omega \dot{\varsigma}\, v_5 \,\mathrm{d}r = \int_\Omega -2H_\parallel \varsigma\, v_5 \,\mathrm{d}r - \int_\Omega \frac{\chi'}{Z}\, v_5 \,\mathrm{d}r. \tag{D.5}$$

The index $i \in \{1, 2, 3, 4, 5\}$ of the test function v expresses the components of the tuple

$$(v_1, v_2, v_3, v_4, v_5)^T \in \left(H^1(\Omega)\right)^5 .$$

We abbreviate the notation by combining all terms in the LHS to temporal residuals m_i and RHS terms to spatial residuals r_i:

$$\frac{d}{dt} m_1(\chi, v_1, t) = r_1(\tilde{\chi}, v_1, t) , \tag{D.6}$$
$$\frac{d}{dt} m_2(\tilde{\chi}, v_2, t) = r_2(\chi, \tilde{\chi}, \varphi, \tilde{\varphi}, \varsigma, v_2, t) , \tag{D.7}$$
$$\frac{d}{dt} m_3(\varphi, v_3, t) = r_3(\tilde{\varphi}, v_3, t) , \tag{D.8}$$
$$\frac{d}{dt} m_4(\tilde{\varphi}, v_4, t) = r_4(\chi, \tilde{\chi}, \varphi, \tilde{\varphi}, \varsigma, v_4, t) , \tag{D.9}$$
$$\frac{d}{dt} m_5(\tilde{\varsigma}, v_5, t) = r_5(\chi, \varsigma, v_5, t) . \tag{D.10}$$

We can then define the full temporal and spatial residuals by taking the sum of each

$$m = \sum_{i=1}^{5} m_i , \qquad r = \sum_{i=1}^{5} r_i . \tag{D.11}$$

The problem of solving the polar master equations can then be reformulated in terms of a residual (variational) problem

Find a solution $u = (\chi, \tilde{\chi}, \varphi, \tilde{\varphi}, \varsigma)^T \in \left(H^1(\Omega)\right)^5$ *(called trial space) such that*

$$\frac{\mathrm{d}}{\mathrm{d}t} m(u, v, t) - r(u, v, t) = 0$$

holds for each test function $v \in \left(H^1(\Omega)\right)^5$ *and for each time* $t \in [t_{\min}, t_{\max}]$.

In order to approach this problem numerically, we discretize the spatial domain of interest Ω and approximate the solution u and the test function v by polynomials of given degree on each spatial element. Therefore, we define general conforming finite elements Ω_e of the full domain Ω with $e \in E_h^0 = \{e_0, \ldots, e_{N_h^0 - 1}\}$ (finite element index set). The corresponding conforming finite-element-space is given by

$$U_h^k = \left\{ u \in C^0(\overline{\Omega}) \mid u_{|\Omega_e} \in P_k(\Omega_e) \ \forall e \in E_h^0 \right\} .$$

By construction, it is the function space of continuous, element-wise polynomial functions of degree k on the closed set $\overline{\Omega} = \Omega + \partial\Omega$. Since this function space is the same for each variable $\chi_h, \tilde{\chi}_h, \varphi_h, \tilde{\varphi}_h$ and ς_h, we have an overall 5-dimensional trial- and test space $(U_h^k)^5$. We assume the test and trial space to be equal (Galerkin approach).

Since `dune-pdelab` requires the so-called local residuals of each element as input, the local contributions of Eqs. (D.1) - (D.5) on each finite element need to be determined. These contributions are called *local operators* and will be computed for the present model problem in the following. For practical reasons, we define a reference finite element $\hat{\Omega}_e$ for all computations and an element transformation μ_e that maps the result to the actual element considered. We then fix a local polynomial basis

$$\left\{ \hat{\phi}_{e,l} = \left(\hat{\phi}_{e,l}^{(1)}, \hat{\phi}_{e,l}^{(2)}, \hat{\phi}_{e,l}^{(3)}, \hat{\phi}_{e,l}^{(4)}, \hat{\phi}_{e,l}^{(5)} \right) \right\}$$

on the reference element. Thus, each function of the conforming finite-element-subspace U_h^k can be expanded into this local basis

$$u_h^{(i)} = \sum_{e \in E_h^0} \sum_{l=0}^{n(e)-1} \mathbf{u}_{g(e,l)}^{(i)} \hat{\phi}_{e,l}^{(i)}(\mu_e^{-1}(x)) \chi_e(x) \in U_h^k \,,$$

where the following expressions have been applied:

- $n(e)$: number of polynomial basis functions on reference element $\hat{\Omega}_e$
- $\hat{\Omega}_e$: reference element of finite element e
- $\mu_e : \hat{\Omega}_e \longrightarrow \Omega_e$: element transformation
- $I_{U_h^k} = \{0, \ldots, N_{U_h^k - 1}\}$: global coefficient index set
- $g : E_h^0 \times \mathbb{N}_0 \longrightarrow \mathcal{I}_{U_h^k}$: local to global index map
- $\mathbf{u} \in \mathbb{R}^{\mathcal{I}_{U_h^k}}$: global coefficient vector
- χ_e: characteristic function of the finite element e ($\chi_e \equiv 1$ for our purposes)

Thus, the components of the full trial and test space read

$$\begin{aligned}
\chi_h &= \sum_{e \in E_h^0} \sum_{l=0}^{n(e)-1} \boldsymbol{\chi}_{g(e,l)} \hat{\phi}_{e,l}^{(1)}(\mu_e^{-1}(x)) \chi_e(x) \,, \\
\tilde{\chi}_h &= \sum_{e \in E_h^0} \sum_{l=0}^{n(e)-1} \tilde{\boldsymbol{\chi}}_{g(e,l)} \hat{\phi}_{e,l}^{(2)}(\mu_e^{-1}(x)) \chi_e(x) \,, \\
\varphi_h &= \sum_{e \in E_h^0} \sum_{l=0}^{n(e)-1} \boldsymbol{\varphi}_{g(e,l)} \hat{\phi}_{e,l}^{(3)}(\mu_e^{-1}(x)) \chi_e(x) \,, \\
\tilde{\varphi}_h &= \sum_{e \in E_h^0} \sum_{l=0}^{n(e)-1} \tilde{\boldsymbol{\varphi}}_{g(e,l)} \hat{\phi}_{e,l}^{(4)}(\mu_e^{-1}(x)) \chi_e(x) \,, \\
\varsigma_h &= \sum_{e \in E_h^0} \sum_{l=0}^{n(e)-1} \boldsymbol{\varsigma}_{g(e,l)} \hat{\phi}_{e,l}^{(5)}(\mu_e^{-1}(x)) \chi_e(x) \,,
\end{aligned}$$

and

$$v_h^{(i)} = \sum_{e \in E_h^0} \sum_{l=0}^{n(e)-1} \mathbf{v}_{g(e,l)}^{(i)} \hat{\phi}_{e,l}^{(i)}(\mu_e^{-1}(x)) \chi_e(x) \,, \text{ where } i = 1, \ldots, 5 \,.$$

We construct a global basis $\{\phi_j\}$ from the local reference basis $\{\hat{\phi}_{e,i}\}$ by defining

$$\Phi_{U_h^k} = \left\{ \phi_j(x) = \sum_{(e,l) : g(e,l) = j} \hat{\phi}_{e,l}(\mu_e^{-1}(x)) \chi_e(x) \;:\; j \in \mathcal{I}_{U_h^k} \right\}$$

such that $u_h \in U_h^k$ can be expanded into this global basis

$$u_h = \sum_{j \in \mathcal{I}_{U_h^k}} u_j \phi_j = \mathrm{FE}_{\Phi_{U_h^k}}(\mathbf{u}) \,,$$

with $\mathrm{FE}_{\Phi_{U_h^k}} : \mathbf{U} \subset \mathbb{R}^{\mathcal{I}_{U_h^k}} \longrightarrow U_h^k$ being the Finite-Element-Isomorphism.

Let us consider again the residual formulation of the problem

$$\frac{\mathrm{d}}{\mathrm{d}t} m(u,v,t) - r(u,v,t) = 0 \tag{D.12}$$

$$\Rightarrow \sum_{i=1}^{5} \left[\frac{\mathrm{d}}{\mathrm{d}t} m_i(u_i,v_i,t) - r_i(u_i,v_i,t) \right] = 0\,. \tag{D.13}$$

We set $v_i = \phi_j^{(i)}$ with $j \in \mathcal{I}_{U_h^k}$ which allows to write the residual as component of residual vectors $\mathcal{M}^{(i)}$ and $\mathcal{R}^{(i)}$:

$$m_i(u_h^{(i)}, \phi_j^{(i)}) = m_i(\mathrm{FE}(\mathbf{u}^{(i)}), \phi_j^{(i)}) = \mathcal{M}^{(i)}(\mathbf{u}^{(i)})_j\,,$$
$$r_i(u_h^{(i)}, \phi_j^{(i)}) = r_i(\mathrm{FE}(\mathbf{u}^{(i)}), \phi_j^{(i)}) = \mathcal{R}^{(i)}(\mathbf{u}^{(i)})_j\,.$$

We want to restrict ourselves to the local degrees of freedom. Therefore, the residual contributions of each element need to be separated and formulated in terms of local operators. Therefore, we define the subset $\mathbf{U}_e \subset \mathbf{U}$ of local degrees of freedom (coefficients of the local expansion) and the (linear) reduction map

$$R_e : \mathbf{U} \longrightarrow \mathbf{U}_e \quad \text{with } R_e(\mathbf{u})_l = \sum_j (R_e)_{lj}(\mathbf{u})_j = \mathbf{u}_{g(e,l)}\,.$$

The local operators can then be defined as maps

$$\alpha_{h,e} : \mathbf{U}_e \longrightarrow \mathbf{U}_e$$

such that they contain the local weak formulation of the problem.

In this way, the full residuals can be expressed in terms of a sum over the local residual contributions of each finite element:

$$\begin{aligned}
\mathcal{R}^{(i)}(\mathbf{u}^{(i)})_j &= \sum_{e \in E_h^0} R_e^{-1} \left[\left[\alpha_{h,e}(R_e(\mathbf{u}^{(i)})) \right]^{\mathrm{spat},i} \right] \\
&= \sum_{(e,l):g(e,l)=j} (R_e)_{lj} \left[\left[\alpha_{h,e}(R_e(\mathbf{u}^{(i)}) \right]^{\mathrm{spat},i} \right]_l \\
&= \sum_{e \in E_h^0} \mathbf{R}_e^T \left[\left[\alpha_{h,e}(R_e(\mathbf{u}^{(i)})) \right]^{\mathrm{spat},i} \right]\,,
\end{aligned}$$

$$\begin{aligned}
\mathcal{M}^{(i)}(\mathbf{u}^{(i)})_j &= \sum_{e \in E_h^0} R_e^{-1} \left[\left[\alpha_{h,e}(R_e(\mathbf{u}^{(i)})) \right]^{\mathrm{temp},i} \right] \\
&= \sum_{(e,l):g(e,l)=j} (R_e)_{lj} \left[\left[\alpha_{h,e}(R_e(\mathbf{u}^{(i)})) \right]^{\mathrm{temp},i} \right]_l \\
&= \sum_{e \in E_h^0} \mathbf{R}_e^T \left[\left[\alpha_{h,e}(R_e(\mathbf{u}^{(i)})) \right]^{\mathrm{temp},i} \right]\,.
\end{aligned}$$

By direct comparison to Eqs. (D.1) - (D.5), we obtain the following local operator expressions as integrals over reference elements in terms of the local reference basis $\hat{\phi}^{(i)}$:

temporal part:

$$[\alpha_{h,e}(R_e(\boldsymbol{\chi}))]_m^{\text{temp},1} = \int_{\hat{\Omega}_e} \sum_{l=0}^{n(e)-1} [R_e(\boldsymbol{\chi})]_l \; \hat{\phi}_{e,l}^{(1)}(\hat{x}) \, \hat{\phi}_{e,m}^{(1)}(\hat{x}) \; \det[\nabla \mu_e] \; \mathrm{d}\hat{x}\,, \tag{D.14}$$

$$[\alpha_{h,e}(R_e(\tilde{\boldsymbol{\chi}}))]_m^{\text{temp},2} = \int_{\hat{\Omega}_e} \sum_{l=0}^{n(e)-1} [R_e(\tilde{\boldsymbol{\chi}})]_l \; \hat{\phi}_{e,l}^{(2)}(\hat{x}) \, \hat{\phi}_{e,m}^{(2)}(\hat{x}) \; \det[\nabla \mu_e] \; \mathrm{d}\hat{x}\,, \tag{D.15}$$

$$[\alpha_{h,e}(R_e(\boldsymbol{\varphi}))]_m^{\text{temp},3} = \int_{\hat{\Omega}_e} \sum_{l=0}^{n(e)-1} [R_e(\boldsymbol{\varphi})]_l \; \hat{\phi}_{e,l}^{(3)}(\hat{x}) \, \hat{\phi}_{e,m}^{(3)}(\hat{x}) \; \det[\nabla \mu_e] \; \mathrm{d}\hat{x}\,, \tag{D.16}$$

$$[\alpha_{h,e}(R_e(\tilde{\boldsymbol{\varphi}}))]_m^{\text{temp},4} = \int_{\hat{\Omega}_e} \sum_{l=0}^{n(e)-1} [R_e(\tilde{\boldsymbol{\varphi}})]_l \; \hat{\phi}_{e,l}^{(4)}(\hat{x}) \, \hat{\phi}_{e,m}^{(4)}(\hat{x}) \; \det[\nabla \mu_e] \; \mathrm{d}\hat{x}\,, \tag{D.17}$$

$$[\alpha_{h,e}(R_e(\boldsymbol{\varsigma}))]_m^{\text{temp},5} = \int_{\hat{\Omega}_e} \sum_{l=0}^{n(e)-1} [R_e(\boldsymbol{\varsigma})]_l \; \hat{\phi}_{e,l}^{(5)}(\hat{x}) \, \hat{\phi}_{e,m}^{(5)}(\hat{x}) \; \det[\nabla \mu_e] \; \mathrm{d}\hat{x}\,, \tag{D.18}$$

spatial part:

$$\begin{aligned}
&[\alpha_{h,e}(R_e(\tilde{\boldsymbol{\chi}}))]_m^{\text{spat},1} \\
&= \int_{\hat{\Omega}_e} \sum_{l=0}^{n(e)-1} [R_e(\tilde{\boldsymbol{\chi}})]_l \; \hat{\phi}_{e,l}^{(2)}(\hat{x}) \, \hat{\phi}_{e,m}^{(1)}(\hat{x}) \; \det[\nabla \mu_e] \; \mathrm{d}\hat{x}\,,
\end{aligned} \tag{D.19}$$

$$\begin{aligned}
&[\alpha_{h,e}(R_e(\boldsymbol{\chi}), R_e(\tilde{\boldsymbol{\chi}}), R_e(\boldsymbol{\varphi}), R_e(\tilde{\boldsymbol{\varphi}}), R_e(\boldsymbol{\varsigma}))]_m^{\text{spat},2} \\
&= -\int_{\hat{\Omega}_e} \sum_{l=0}^{n(e)-1} R_e(\boldsymbol{\chi})_l \; \partial_{\hat{x}} \hat{\phi}_{e,l}^{(1)}(\hat{x}) \; \partial_{\hat{x}} \left(\frac{\hat{\phi}_{e,m}^{(2)}(\hat{x})}{Z^2} \right) \; (\partial_{\hat{x}} \mu_e)^{-2} \; \det[\nabla \mu_e] \; \mathrm{d}\hat{x} \\
&+ \int_{\hat{\Omega}_e} \sum_{l=0}^{n(e)-1} \Bigg[\left(-\frac{C}{Z^2} R_e(\boldsymbol{\chi})_l \; \partial_{\hat{x}} \hat{\phi}_{e,l}^{(1)}(\hat{x}) + \frac{2\sigma}{Z} R_e(\boldsymbol{\varsigma})_l \; \partial_{\hat{x}} \hat{\phi}_{e,l}^{(5)}(\hat{x}) \right) (\partial_{\hat{x}} \mu_e)^{-1} \\
&- 3H_{\parallel} R_e(\tilde{\boldsymbol{\chi}})_l \; \hat{\phi}_{e,l}^{(2)}(\hat{x}) + \left(A - \frac{(\ell-1)(\ell+2)}{\mu_e(\hat{x})^2 a_\perp^2} \right) R_e(\boldsymbol{\chi})_l \; \hat{\phi}_{e,l}^{(1)}(\hat{x}) \\
&+ \frac{2}{Z} \left[H_{\parallel} - 2H_{\perp} \right]' R_e(\boldsymbol{\varsigma})_l \; \hat{\phi}_{e,l}^{(5)}(\hat{x}) - 4\sigma R_e(\tilde{\boldsymbol{\varphi}}) \; \hat{\phi}_{e,l}^{(4)}(\hat{x}) + A R_e(\boldsymbol{\varphi})_l \; \hat{\phi}_{e,l}^{(3)}(\hat{x}) \Bigg] \hat{\phi}_{e,m}^{(2)}(\hat{x}) \\
&\det[\nabla \mu_e] \; \mathrm{d}\hat{x}\,,
\end{aligned} \tag{D.20}$$

$$\begin{aligned}
&[\alpha_{h,e}(R_e(\tilde{\boldsymbol{\varphi}}))]_m^{\text{spat},3} \\
&= \int_{\hat{\Omega}_e} \sum_{l=0}^{n(e)-1} [R_e(\tilde{\boldsymbol{\varphi}})]_l \; \hat{\phi}_{e,l}^{(4)}(\hat{x}) \, \hat{\phi}_{e,m}^{(3)}(\hat{x}) \; \det[\nabla \mu_e] \; \mathrm{d}\hat{x}\,,
\end{aligned} \tag{D.21}$$

$$\begin{aligned}
&[\alpha_{h,e}(R_e(\boldsymbol{\chi}), R_e(\tilde{\boldsymbol{\chi}}), R_e(\boldsymbol{\varphi}), R_e(\tilde{\boldsymbol{\varphi}}), R_e(\boldsymbol{\varsigma}))]_m^{\text{spat},4} \\
&= \int_{\hat{\Omega}_e} \sum_{l=0}^{n(e)-1} \Bigg[-4H_{\perp} R_e(\tilde{\boldsymbol{\varphi}})_l \; \hat{\phi}_{e,l}^{(4)}(\hat{x}) + \frac{2\kappa}{a_\perp^2} R_e(\boldsymbol{\varphi})_l \; \hat{\phi}_{e,l}^{(3)}(\hat{x}) - H_{\perp} R_e(\tilde{\boldsymbol{\chi}})_l \; \hat{\phi}_{e,l}^{(2)}(\hat{x}) \\
&- \left(\frac{1 - 2\kappa\mu_e(\hat{x})^2}{\mu_e(\hat{x})^2 a_\perp^2} - \frac{\ell(\ell+1)}{2\mu_e(\hat{x})^2 a_\perp^2} \right) R_e(\boldsymbol{\chi})_l \; \hat{\phi}_{e,l}^{(1)}(\hat{x}) + \frac{1}{Z^2} \frac{a_{\parallel}}{\mu_e(\hat{x}) a_\perp} R_e(\boldsymbol{\chi})_l \partial_{\hat{x}} \hat{\phi}_{e,l}^{(1)}(\hat{x}) \, (\partial_{\hat{x}} \mu_e)^{-1} \\
&+ \frac{2}{Z} \sigma \frac{a_{\parallel}}{\mu_e(\hat{x}) a_\perp} R_e(\boldsymbol{\varsigma}) \hat{\phi}_{e,l}^{(5)}(\hat{x}) \Bigg] \hat{\phi}_{e,m}^{(4)}(\hat{x}) \; \det[\nabla \mu_e] \, \mathrm{d}\hat{x}\,,
\end{aligned} \tag{D.22}$$

$$
\begin{aligned}
&[\alpha_{h,e}(R_e(\boldsymbol{\chi}), R_e(\tilde{\boldsymbol{\chi}}), R_e(\boldsymbol{\varphi}), R_e(\tilde{\boldsymbol{\varphi}}), R_e(\boldsymbol{\varsigma}))]_m^{\text{spat},5} \\
&= \int_{\hat{\Omega}_e} \sum_{l=0}^{n(e)-1} \left[-2H_{\|} R_e(\boldsymbol{\varsigma})_l \, \hat{\phi}_{e,l}^{(5)}(\hat{x}) - \frac{1}{Z} R_e(\boldsymbol{\chi})_l \, \partial_{\hat{x}} \hat{\phi}_{e,l}^{(1)}(\hat{x}) \, (\partial_{\hat{x}} \mu_e)^{-1} \right] \hat{\phi}_{e,m}^{(5)}(\hat{x}) \\
&\det [\nabla \mu_e] \, \mathrm{d}\hat{x} \, .
\end{aligned} \tag{D.23}
$$

These operators can directly be passed to the `dune-pdelab`-framework. The local operator formulation of the fluid system (given by Eqs. (4.8) - (4.10)) can be done analogously. If the spatial discretization is completed and residual contributions of all finite elements are known, Eq. (D.12) can be integrated as large scale ODE problem in time. All results in this work are obtained by using basis polynomials of degree 2 in space combined with a third-order time integrator[1]. Initial and boundary conditions are fixed according to the methods outlined in Chapts. (5) and (6).

In the one dimensional case we consider here, the general formulation is simplified considerably:

- The domain of interest is a 1d open interval $\Omega = (0, r_*)$.
- The finite elements are subintervals $\Omega_e = \left(r_j, r_{j+1}\right)$ with $e = j,\ r_0 = 0,$ and $r_{N_{U_h^k}} = r_*$.
- The reference element is the unit interval $(0, 1)$ and the transformation map μ_e is given by

$$
\begin{aligned}
\mu_e : \hat{\Omega}_e &\longrightarrow \Omega_e \\
\hat{x} &\longmapsto \left(r_{j+1} - r_j\right) \hat{x} + r_j \, .
\end{aligned}
$$

Therefore, the Jacobian is just a constant $\partial_{\hat{x}} \mu_e = r_{j+1} - r_j = \det [\nabla \mu_e]$.

1 Since the solution can be expected to be sufficiently smooth, the approximation using polynomials of degree 2 yields second-order convergence with respect to the H^1-Norm and even third-order convergence with respect to the L^2-Norm (see [14]).

BIBLIOGRAPHY

[1] Roger Alexander. Diagonally implicit Runge-Kutta methods for stiff O.D.E.'s. *SIAM Journal on Numerical Analysis*, 14(6):1006–1021, December 1977. ISSN 0036-1429, 1095-7170. doi: 10.1137/0714068. URL http://epubs.siam.org/doi/abs/10.1137/0714068.

[2] Havard Alnes and Morad Amarzguioui. CMB anisotropies seen by an off-center observer in a spherically symmetric inhomogeneous universe. *Physical Review D*, 74:103520, November 2006. ISSN 0556-2821. doi: 10.1103/PhysRevD.74.103520. URL http://adsabs.harvard.edu/abs/2006PhRvD..74j3520A.

[3] David Alonso, Juan García-Bellido, Troels Haugboelle, and Julián Vicente. Large scale structure simulations of inhomogeneous Lemaître-Tolman-Bondi void models. *Physical Review D*, 82(12):123530, December 2010. doi: 10.1103/PhysRevD.82.123530. URL http://link.aps.org/doi/10.1103/PhysRevD.82.123530.

[4] Christian Angrick. On the derivation of an X-ray temperature function without reference to mass and the prediction of weak-lensing number counts from the statistics of Gaussian random fields. *PhD dissertation, University of Heidelberg*, 2010.

[5] J. M. Bardeen, J. R. Bond, N. Kaiser, and A. S. Szalay. The statistics of peaks of Gaussian random fields. *The Astrophysical Journal*, 304:15–61, May 1986. ISSN 0004-637X. doi: 10.1086/164143. URL http://adsabs.harvard.edu/abs/1986ApJ...304...15B.

[6] James M. Bardeen. Gauge-invariant cosmological perturbations. *Physical Review D*, 22:1882–1905, October 1980. doi: 10.1103/PhysRevD.22.1882. URL http://adsabs.harvard.edu/abs/1980PhRvD..22.1882B.

[7] M. Bartelmann. Lecture notes on Cosmology. URL http://www.ita.uni-heidelberg.de/research/bartelmann/files/cosmology.pdf.

[8] Matthias Bartelmann. The dark Universe. *Reviews of Modern Physics*, 82(1):331–382, February 2010. doi: 10.1103/RevModPhys.82.331. URL http://link.aps.org/doi/10.1103/RevModPhys.82.331.

[9] Matthias Bartelmann. TOPICAL REVIEW Gravitational lensing. *Classical and Quantum Gravity*, 27:233001, December 2010. ISSN 0264-9381. doi: 10.1088/0264-9381/27/23/233001. URL http://adsabs.harvard.edu/abs/2010CQGra..27w3001B.

[10] P. Bastian, M. Droske, C. Engwer, R. Klöfkorn, T. Neubauer, M. Ohlberger, and M. Rumpf. Towards a unified framework for scientific computing. In R. Kornhuber, R. H. W. Hoppe, D. E. Keyes, J. Périaux, O. Pironneau, and J. Xu, editors, *Proceedings of the 15th Conference on Domain Decomposition Methods*, LNCSE, pages 167–174. Springer-Verlag, 2004.

[11] P. Bastian, M. Blatt, A. Dedner, C. Engwer, R. Klöfkorn, R. Kornhuber, M. Ohlberger, and O. Sander. A generic grid interface for parallel and adaptive scientific computing. Part II: implementation and tests in DUNE. *Computing*, 82(2-3):121–138, 2008. DOI 10.1007/s00607-008-0004-9.

[12] P. Bastian, M. Blatt, A. Dedner, C. Engwer, R. Klöfkorn, M. Ohlberger, and O. Sander. A generic grid interface for parallel and adaptive scientific computing. Part I: abstract framework. *Computing*, 82(2-3):103–119, 2008. DOI 10.1007/s00607-008-0003-x.

[13] P. Bastian, M. Blatt, A. Dedner, Ch. Engwer, J. Fahlke, C. Gräser, R. Klöfkorn, M. Nolte, M. Ohlberger, and O. Sander. *DUNE Web page*. 2011. URL http://www.dune-project.org.

[14] Peter Bastian. Finite Elemente Verfahren und schnelle Löser. 2008. URL http://conan.iwr.uni-heidelberg.de/teaching/scripts/fesarticle.pdf.

[15] Daniel Baumann. TASI Lectures on Inflation. *ArXiv e-prints*, 0907:5424, July 2009. URL http://adsabs.harvard.edu/abs/2009arXiv0907.5424B.

[16] Francis Bernardeau, Camille Bonvin, and Filippo Vernizzi. Full-sky lensing shear at second order. *Physical Review D*, 81:083002, April 2010. ISSN 0556-2821. doi: 10.1103/PhysRevD.81.083002. URL http://adsabs.harvard.edu/abs/2010PhRvD..81h3002B.

[17] Edmund Bertschinger. Cosmological perturbation theory and structure formation. *ArXiv Astrophysics e-prints*, page 1009, December 2000. URL http://adsabs.harvard.edu/abs/2001astro.ph..1009B.

[18] Edmund Bertschinger. Multiscale Gaussian random fields and their application to Cosmological simulations. *The Astrophysical Journal Supplement Series*, 137:1–20, November 2001. ISSN 0067-0049. doi: 10.1086/322526. URL http://adsabs.harvard.edu/abs/2001ApJS..137....1B.

[19] Tirthabir Biswas, Alessio Notari, and Wessel Valkenburg. Testing the void against cosmological data: fitting CMB, BAO, SN and Ho. *Journal of Cosmology and Astro-Particle Physics*, 2010(11): 030, November 2010. ISSN 1475-7516. doi: 10.1088/1475-7516/2010/11/030. URL http://iopscience.iop.org/1475-7516/2010/11/030.

[20] Chris Blake, Sarah Brough, Warrick Couch, Karl Glazebrook, Greg Poole, Tamara Davis, Michael Drinkwater, Russell Jurek, Kevin Pimbblet, Matthew Colless, Rob Sharp, Scott Croom, Michael Pracy, David Woods, Barry Madore, Chris Martin, and Ted Wyder. The WiggleZ dark energy survey. *Astronomy and Geophysics*, 49:19–5, October 2008. ISSN 1366-8781. doi: 10.1111/j.1468-4004.2008.49519.x. URL http://adsabs.harvard.edu/abs/2008A%26G....49e..19B.

[21] Markus Blatt and Peter Bastian. On the generic parallelisation of iterative solvers for the finite element method. *Int. J. Comput. Sci. Engrg.*, 4(1):56–69, 2008. doi: 10.1504/IJCSE.2008.021112. URL http://portal.acm.org/citation.cfm?id=1457168.1457174.

[22] Krzysztof Bolejko and J. Stuart B. Wyithe. Testing the Copernican Principle via cosmological observations. *Journal of Cosmology and Astro-Particle Physics*, 02:020, February 2009. ISSN 1475-7516. doi: 10.1088/1475-7516/2009/02/020. URL http://adsabs.harvard.edu/abs/2009JCAP...02..020B.

[23] Krzysztof Bolejko, Marie-Noëlle Célérier, and Andrzej Krasinski. Inhomogeneous cosmological models: exact solutions and their applications. *Classical and Quantum Gravity*, 28:164002, August 2011. ISSN 0264-9381. doi: 10.1088/0264-9381/28/16/164002. URL http://adsabs.harvard.edu/abs/2011CQGra..28p4002B.

[24] H. Bondi. Spherically symmetrical models in general relativity. *Monthly Notices of the Royal Astronomical Society*, 107:410, 1947. ISSN 0035-8711. URL http://adsabs.harvard.edu/abs/1947MNRAS.107..410B.

[25] Nikolaos Brouzakis, Nikolaos Tetradis, and Eleftheria Tzavara. The effect of large scale inhomogeneities on the luminosity distance. *Journal of Cosmology and Astro-Particle Physics*, 2007(02):013, February 2007. ISSN 1475-7516. doi: 10.1088/1475-7516/2007/02/013. URL http://iopscience.iop.org/1475-7516/2007/02/013.

[26] Philip Bull, Timothy Clifton, and Pedro G. Ferreira. Kinematic Sunyaev-Zel'dovich effect as a test of general radial inhomogeneity in Lemaître-Tolman-Bondi cosmology. *Physical Review D*, 85:024002, January 2012. ISSN 0556-2821. doi: 10.1103/PhysRevD.85.024002. URL http://adsabs.harvard.edu/abs/2012PhRvD..85b4002B.

[27] Chris Clarkson. Establishing homogeneity of the universe in the shadow of dark energy. *Comptes Rendus Physique*, 13:682–718, July 2012. ISSN 1631-0705. doi: 10.1016/j.crhy.2012.04.005. URL http://adsabs.harvard.edu/abs/2012CRPhy..13..682C.

[28] Chris Clarkson and Roy Maartens. Inhomogeneity and the foundations of concordance cosmology. *Classical and Quantum Gravity*, 27:124008, June 2010. ISSN 0264-9381. doi: 10.1088/0264-9381/27/12/124008. URL http://adsabs.harvard.edu/abs/2010CQGra..27l4008C.

[29] Chris Clarkson, Timothy Clifton, and Sean February. Perturbation theory in Lemaître-Tolman-Bondi cosmology. *Journal of Cosmology and Astro-Particle Physics*, 06:025, June 2009. doi: 10.1088/1475-7516/2009/06/025;. URL http://adsabs.harvard.edu/abs/2009JCAP...06..025C.

[30] Chris Clarkson, George F. R. Ellis, Andreas Faltenbacher, Roy Maartens, Obinna Umeh, and Jean-Philippe Uzan. (Mis)interpreting supernovae observations in a lumpy universe. *Monthly Notices of the Royal Astronomical Society*, 426:1121–1136, October 2012. ISSN 0035-8711. doi: 10.1111/j.1365-2966.2012.21750.x. URL http://adsabs.harvard.edu/abs/2012MNRAS.426.1121C.

[31] Planck Collaboration and P. A. R. Ade et al. Planck 2015 results. XIV. Dark energy and modified gravity. *arXiv:1502.01590 [astro-ph]*, February 2015. URL http://arxiv.org/abs/1502.01590. arXiv: 1502.01590.

[32] R. Courant, K. Friedrichs, and H. Lewy. On the partial difference equations of mathematical physics. *International Business Machines Corporation. Journal of Research and Development*, 11:215–234, 1967. ISSN 0018-8646. URL http://www.ams.org/mathscinet-getitem?mr=0213764.

[33] Marie-Noëlle Célérier. Do we really see a cosmological constant in the supernovae data? *Astronomy and Astrophysics*, 353:63–71, January 2000. ISSN 0004-6361. URL http://adsabs.harvard.edu/abs/2000A%26A...353...63C.

[34] Kyle S. Dawson and David J. et al. Schlegel. The Baryon Oscillation Spectroscopic Survey of SDSS-III. *The Astronomical Journal*, 145:10, January 2013. ISSN 0004-6256. doi: 10.1088/0004-6256/145/1/10. URL http://adsabs.harvard.edu/abs/2013AJ....145...10D.

[35] Roland de Putter, Licia Verde, and Raul Jimenez. Testing LTB void models without the cosmic microwave background or large scale structure: new constraints from galaxy ages. *Journal of Cosmology and Astro-Particle Physics*, 02:047, February 2013. ISSN 1475-7516. doi: 10.1088/1475-7516/2013/02/047. URL http://adsabs.harvard.edu/abs/2013JCAP...02..047D.

[36] James W. Demmel, Stanley C. Eisenstat, John R. Gilbert, Xiaoye S. Li, and Joseph W. H. Liu. A supernodal approach to sparse partial pivoting. *SIAM J. Matrix Analysis and Applications*, 20(3): 720–755, 1999.

[37] Peter Dunsby, Naureen Goheer, Bob Osano, and Jean-Philippe Uzan. How close can an inhomogeneous universe mimic the concordance model? *Journal of Cosmology and Astro-Particle Physics*, 06:017, June 2010. ISSN 1475-7516. doi: 10.1088/1475-7516/2010/06/017. URL http://adsabs.harvard.edu/abs/2010JCAP...06..017D.

[38] Ruth Durrer. Cosmological Perturbation Theory. volume 653, page 31, eprint: arXiv:astro-ph/0402129, 2005. ISBN 0075-8450. doi: 10.1007/978-3-540-31535-3_2. URL http://adsabs.harvard.edu/abs/2005LNP...653...31D.

[39] Albert Einstein. *Relativity: The Special and General Theory*. Methuen & Co Ltd, 1924, October 2009. URL http://www.gutenberg.org/ebooks/30155.

[40] Kari Enqvist. Lemaître Tolman Bondi model and accelerating expansion. *General Relativity and Gravitation*, 40:451–466, February 2008. ISSN 0001-7701. doi: 10.1007/s10714-007-0553-9. URL http://adsabs.harvard.edu/abs/2008GReGr..40..451E.

[41] S. February, J. Larena, C. Clarkson, and D. Pollney. Evolution of linear perturbations in spherically symmetric dust spacetimes. *Classical and Quantum Gravity*, 31:175008, September 2014. ISSN 0264-9381. doi: 10.1088/0264-9381/31/17/175008. URL http://adsabs.harvard.edu/abs/2014CQGra..31q5008F.

[42] Sean February, Julien Larena, Mathew Smith, and Chris Clarkson. Rendering dark energy void. *Monthly Notices of the Royal Astronomical Society*, 405:2231–2242, July 2010. ISSN 0035-8711. doi: 10.1111/j.1365-2966.2010.16627.x. URL http://adsabs.harvard.edu/abs/2010MNRAS.405.2231F.

[43] Sean February, Chris Clarkson, and Roy Maartens. Galaxy correlations and the BAO in a void universe: structure formation as a test of the Copernican Principle. *Journal of Cosmology and Astro-Particle Physics*, 03:023, March 2013. ISSN 1475-7516. doi: 10.1088/1475-7516/2013/03/023;. URL http://adsabs.harvard.edu/abs/2013JCAP...03..023F.

[44] Simon Foreman, Adam Moss, James P. Zibin, and Douglas Scott. Spatial and temporal tuning in void models for acceleration. *Physical Review D*, 82:103532, November 2010. ISSN 0556-2821. doi: 10.1103/PhysRevD.82.103532. URL http://adsabs.harvard.edu/abs/2010PhRvD..82j3532F.

[45] A. Friedman. On the Curvature of Space. *General Relativity and Gravitation*, 31:1991, December 1999. URL http://adsabs.harvard.edu/abs/1999GReGr..31.1991F.

[46] Juan Garcia-Bellido and Troels Haugboelle. Confronting Lemaître Tolman Bondi models with observational cosmology. *Journal of Cosmology and Astro-Particle Physics*, 04:003, April 2008. ISSN 1475-7516. doi: 10.1088/1475-7516/2008/04/003. URL http://adsabs.harvard.edu/abs/2008JCAP...04..003G.

[47] Juan Garcia-Bellido and Troels Haugboelle. Looking the void in the eyes — the kinematic Sunyaev Zeldovich effect in Lemaître Tolman Bondi models. *Journal of Cosmology and Astro-Particle Physics*, 09:016, September 2008. ISSN 1475-7516. doi: 10.1088/1475-7516/2008/09/016. URL http://adsabs.harvard.edu/abs/2008JCAP...09..016G.

[48] Juan Garcia-Bellido and Troels Haugboelle. The radial BAO scale and cosmic shear, a new observable for inhomogeneous cosmologies. *Journal of Cosmology and Astro-Particle Physics*, 09:028, September 2009. ISSN 1475-7516. doi: 10.1088/1475-7516/2009/09/028. URL http://adsabs.harvard.edu/abs/2009JCAP...09..028G.

[49] Ulrich H. Gerlach and Uday K. Sengupta. Homogeneous collapsing star: Tensor and vector harmonics for matter and field asymmetries. *Physical Review D*, 18(6):1773–1784, September 1978. doi: 10.1103/PhysRevD.18.1773. URL http://link.aps.org/doi/10.1103/PhysRevD.18.1773.

[50] Ulrich H. Gerlach and Uday K. Sengupta. Relativistic equations for aspherical gravitational collapse. *Physical Review D*, 18(6):1789–1797, September 1978. doi: 10.1103/PhysRevD.18.1789. URL http://link.aps.org/doi/10.1103/PhysRevD.18.1789.

[51] Ulrich H. Gerlach and Uday K. Sengupta. Gauge-invariant perturbations on most general spherically symmetric space-times. *Physical Review D*, 19:2268–2272, April 1979. doi: 10.1103/PhysRevD.19.2268. URL http://adsabs.harvard.edu/abs/1979PhRvD..19.2268G.

[52] K. M. Gorski and Eric Hivon. HEALPix: Hierarchical Equal Area isoLatitude Pixelization of a sphere. *Astrophysics Source Code Library*, page 1107.018, July 2011. URL http://adsabs.harvard.edu/abs/2011ascl.soft07018G.

[53] Christian Grossmann and Hans-Görg Roos. *Numerical Treatment of Partial Differential Equations*. Springer Science & Business Media, October 2007. ISBN 9783540715825.

[54] Carsten Gundlach and José M. Martín-García. Gauge-invariant and coordinate-independent perturbations of stellar collapse: The interior. *Physical Review D*, 61:84024, April 2000. doi: 10.1103/PhysRevD.61.084024;. URL http://adsabs.harvard.edu/abs/2000PhRvD..61h4024G.

[55] Catherine Heymans, Ludovic Van Waerbeke, Lance Miller, Thomas Erben, Hendrik Hildebrandt, Henk Hoekstra, Thomas D. Kitching, Yannick Mellier, Patrick Simon, Christopher Bonnett, Jean Coupon, Liping Fu, Joachim Harnois Déraps, Michael J. Hudson, Martin Kilbinger, Koenraad Kuijken, Barnaby Rowe, Tim Schrabback, Elisabetta Semboloni, Edo van Uitert, Sanaz Vafaei, and Malin Velander. CFHTLenS: the Canada-France-Hawaii Telescope Lensing Survey. *Monthly Notices of the Royal Astronomical Society*, 427:146–166, November 2012. ISSN 0035-8711. doi: 10.1111/j.1365-2966.2012.21952.x. URL http://adsabs.harvard.edu/abs/2012MNRAS.427..146H.

[56] Alexander Leithes and Karim A. Malik. Conserved quantities in Lemaître-Tolman-Bondi cosmology. *Classical and Quantum Gravity*, 32:015010, January 2015. ISSN 0264-9381. doi: 10.1088/0264-9381/32/1/015010. URL http://adsabs.harvard.edu/abs/2015CQGra..32a5010L.

[57] G. Lemaître. Expansion of the universe, The expanding universe. *Monthly Notices of the Royal Astronomical Society*, 91:490–501, March 1931. ISSN 0035-8711. URL http://adsabs.harvard.edu/abs/1931MNRAS..91..490L.

[58] Georges Lemaître. L'Univers en expansion. *Annales de la Societe Scietifique de Bruxelles*, 53:51, 1933. URL http://adsabs.harvard.edu/abs/1933ASSB...53...51L.

[59] Julien Lesgourgues and Thomas Tram. Fast and accurate CMB computations in non-flat FLRW universes. *Journal of Cosmology and Astro-Particle Physics*, 09:032, September 2014. ISSN 1475-7516. doi: 10.1088/1475-7516/2014/09/032. URL http://adsabs.harvard.edu/abs/2014JCAP...09..032L.

[60] David Levin. Fast integration of rapidly oscillatory functions. *Journal of Computational and Applied Mathematics*, 67(1):95–101, February 1996. ISSN 0377-0427. doi: 10.1016/0377-0427(94)00118-9. URL http://www.sciencedirect.com/science/article/pii/0377042794001189.

[61] David Levin. Analysis of a collocation method for integrating rapidly oscillatory functions. *Journal of Computational and Applied Mathematics*, 78(1):131–138, February 1997. ISSN 0377-0427. doi: 10.1016/S0377-0427(96)00137-9. URL http://www.sciencedirect.com/science/article/pii/S0377042796001379.

[62] Xiaoye S. Li. An overview of SuperLU: Algorithms, implementation, and user interface. *ACM Transactions on Mathematical Software*, 31(3):302–325, September 2005.

[63] Andrew R. Liddle and David H. Lyth. *Cosmological Inflation and Large-Scale Structure*. June 2000. URL http://adsabs.harvard.edu/abs/2000cils.book.....L.

[64] David Lovelock. The uniqueness of the Einstein field equations in a four-dimensional space. *Archive for Rational Mechanics and Analysis*, 33:54–70, January 1969. ISSN 0003-9527. doi: 10.1007/BF00248156. URL http://adsabs.harvard.edu/abs/1969ArRMA..33...54L.

[65] Valerio Marra and Alessio Notari. Observational constraints on inhomogeneous cosmological models without dark energy. *Classical and Quantum Gravity*, 28:164004, August 2011. ISSN 0264-9381. doi: 10.1088/0264-9381/28/16/164004. URL http://adsabs.harvard.edu/abs/2011CQGra..28p4004M.

[66] Valerio Marra and Mikko Pääkkönen. Observational constraints on the ΛLTB model. *Journal of Cosmology and Astro-Particle Physics*, 12:021, December 2010. ISSN 1475-7516. doi: 10.1088/1475-7516/2010/12/021. URL http://adsabs.harvard.edu/abs/2010JCAP...12..021M.

[67] José M. Martín-García and Carsten Gundlach. Gauge-invariant and coordinate-independent perturbations of stellar collapse. II. Matching to the exterior. *Physical Review D*, 64:24012, July 2001. doi: 10.1103/PhysRevD.64.024012;. URL http://adsabs.harvard.edu/abs/2001PhRvD..64b4012M.

[68] Adam Moss, James P. Zibin, and Douglas Scott. Precision cosmology defeats void models for acceleration. *Physical Review D*, 83:103515, May 2011. ISSN 0556-2821. doi: 10.1103/PhysRevD.83.103515. URL http://adsabs.harvard.edu/abs/2011PhRvD..83j3515M.

[69] V. F. Mukhanov, H. A. Feldman, and R. H. Brandenberger. Theory of cosmological perturbations. *Physics Reports*, 215:203–333, June 1992. doi: 10.1016/0370-1573(92)90044-Z. URL http://adsabs.harvard.edu/abs/1992PhR...215..203M.

[70] Ryusuke Nishikawa, Chul-Moon Yoo, and Ken-ichi Nakao. Evolution of density perturbations in a large void universe. *Physical Review D*, 85(10):103511, May 2012. doi: 10.1103/PhysRevD.85.103511. URL http://link.aps.org/doi/10.1103/PhysRevD.85.103511.

[71] Ryusuke Nishikawa, Chul-Moon Yoo, and Ken-ichi Nakao. Two-point correlation function of density perturbations in a large void universe. *Physical Review D*, 88:123520, December 2013. ISSN 0556-2821. doi: 10.1103/PhysRevD.88.123520. URL http://adsabs.harvard.edu/abs/2013PhRvD..88l3520N.

[72] Ryusuke Nishikawa, Ken-ichi Nakao, and Chul-Moon Yoo. Comparison of two approximation schemes for solving perturbations in a LTB cosmological model. *ArXiv e-prints*, 1407:4899, July 2014. URL http://adsabs.harvard.edu/abs/2014arXiv1407.4899N.

[73] Volker Perlick. Gravitational lensing from a spacetime perspective. *ArXiv e-prints*, 1010:3416, October 2010. URL http://adsabs.harvard.edu/abs/2010arXiv1010.3416P.

[74] Jerzy Plebanski and Andrzej Krasinski. *An Introduction to General Relativity and Cosmology*. September 2012. URL http://adsabs.harvard.edu/abs/2012igrc.book.....P.

[75] M. Redlich, K. Bolejko, S. Meyer, G. F. Lewis, and M. Bartelmann. Probing spatial homogeneity with LTB models: a detailed discussion. *Astronomy and Astrophysics*, 570:63, October 2014. ISSN 0004-6361. doi: 10.1051/0004-6361/201424553. URL http://adsabs.harvard.edu/abs/2014A%26A...570A..63R.

[76] Tullio Regge and John A. Wheeler. Stability of a Schwarzschild singularity. *Physical Review*, 108:1063–1069, November 1957. doi: 10.1103/PhysRev.108.1063. URL http://adsabs.harvard.edu/abs/1957PhRv..108.1063R.

[77] H. P. Robertson. Kinematics and World-Structure. *The Astrophysical Journal*, 82:284, November 1935. URL http://adsabs.harvard.edu/abs/1935ApJ....82..284R.

[78] Sysky Räsänen. Lecture notes on Cosmology I & II. Fall 2014. URL http://theory.physics.helsinki.fi/~cosmology.

[79] R. Sachs. Gravitational Waves in General Relativity. VI. The Outgoing Radiation Condition. *Royal Society of London Proceedings Series A*, 264:309–338, November 1961. ISSN 0080-4630. doi: 10.1098/rspa.1961.0202. URL http://adsabs.harvard.edu/abs/1961RSPSA.264..309S.

[80] R. Scaramella, Y. Mellier, J. Amiaux, C. Burigana, C. S. Carvalho, J. C. Cuillandre, A. da Silva, J. Dinis, A. Derosa, E. Maiorano, P. Franzetti, B. Garilli, M. Maris, M. Meneghetti, I. Tereno, S. Wachter, L. Amendola, M. Cropper, V. Cardone, R. Massey, S. Niemi, H. Hoekstra, T. Kitching, L. Miller, T. Schrabback, E. Semboloni, A. Taylor, M. Viola, T. Maciaszek, A. Ealet, L. Guzzo, K. Jahnke, W. Percival, F. Pasian, M. Sauvage, and the Euclid Collaboration. Euclid space mission: a cosmological challenge for the next 15 years. *ArXiv e-prints*, 1501:4908, January 2015. URL http://adsabs.harvard.edu/abs/2015arXiv150104908S.

[81] Björn Malte Schäfer, Lavinia Heisenberg, Angelos F. Kalovidouris, and David J. Bacon. On the validity of the Born approximation for weak cosmic flexions. *Monthly Notices of the Royal Astronomical Society*, 420:455–467, February 2012. ISSN 0035-8711. doi: 10.1111/j.1365-2966.2011.20051.x. URL http://adsabs.harvard.edu/abs/2012MNRAS.420..455S.

[82] Dominik J. Schwarz, David Bacon, Song Chen, Chris Clarkson, Dragan Huterer, Martin Kunz, Roy Maartens, Alvise Raccanelli, Matthias Rubart, and Jean-Luc Starck. Testing foundations of modern cosmology with SKA all-sky surveys. *ArXiv e-prints*, 1501:3820, January 2015. URL http://adsabs.harvard.edu/abs/2015arXiv150103820S.

[83] K. Schwarzschild. On the gravitational field of a mass point according to Einstein's theory. *Abh. Königl. Preuss. Akad. der Wissenschaften Jahre 1906,92, Berlin,1907*, 1916:189–196, 1916. URL http://adsabs.harvard.edu/abs/1916AbhKP1916..189S.

[84] Edward Seidel. Gravitational radiation from even-parity perturbations of stellar collapse: Mathematical formalism and numerical methods. *Physical Review D*, 42:1884–1907, September 1990. ISSN 0556-2821. doi: 10.1103/PhysRevD.42.1884. URL http://adsabs.harvard.edu/abs/1990PhRvD..42.1884S.

[85] J. Silk. Large-scale inhomogeneity of the Universe - Spherically symmetric models. *Astronomy and Astrophysics*, 59:53–58, July 1977. ISSN 0004-6361. URL http://adsabs.harvard.edu/abs/1977A%26A....59...53S.

[86] J M Stewart. Perturbations of Friedmann-Robertson-Walker cosmological models. *Classical and Quantum Gravity*, 7(7):1169–1180, July 1990. ISSN 0264-9381, 1361-6382. doi: 10.1088/0264-9381/7/7/013. URL http://iopscience.iop.org/0264-9381/7/7/013.

[87] Norbert Straumann. *General Relativity*. 2013. URL http://adsabs.harvard.edu/abs/2013gere.book.....S.

[88] Hannu K. Suonio. Lecture notes on cosmological perturbation theory. September 2012. URL http://www.helsinki.fi/~hkurkisu/CosPer.pdf.

[89] Richard C. Tolman. Effect of inhomogeneity on cosmological models. *Proceedings of the National Academy of Science*, 20:169–176, March 1934. doi: 10.1073/pnas.20.3.169. URL http://adsabs.harvard.edu/abs/1934PNAS...20..169T.

[90] Kenji Tomita. Perturbations in a spherically symmetric inhomogeneous cosmological model with the self-similar region. *Physical Review D*, 56(6):3341–3356, September 1997. doi: 10.1103/PhysRevD.56.3341. URL http://link.aps.org/doi/10.1103/PhysRevD.56.3341.

[91] Kenji Tomita. Gauge-invariant treatment of the integrated Sachs-Wolfe effect on general spherically symmetric spacetimes. *Physical Review D*, 81:063509, March 2010. ISSN 0556-2821. doi: 10.1103/PhysRevD.81.063509. URL http://adsabs.harvard.edu/abs/2010PhRvD..81f3509T.

[92] Thomas Tram. Computation of hyperspherical Bessel functions. *arXiv:1311.0839 [astro-ph, physics:physics]*, November 2013. URL http://arxiv.org/abs/1311.0839. arXiv: 1311.0839.

[93] Christos G. Tsagas, Anthony Challinor, and Roy Maartens. Relativistic cosmology and large-scale structure. *Physics Reports*, 465:61–147, August 2008. doi: 10.1016/j.physrep.2008.03.003;. URL http://adsabs.harvard.edu/abs/2008PhR...465...61T.

[94] Wessel Valkenburg, Valerio Marra, and Chris Clarkson. Testing the Copernican principle by constraining spatial homogeneity. *Monthly Notices of the Royal Astronomical Society*, 438:L6–L10, February 2014. ISSN 0035-8711. doi: 10.1093/mnrasl/slt140. URL http://adsabs.harvard.edu/abs/2014MNRAS.438L...6V.

[95] A. G. Walker. On Milne's Theory of World-Structure. *Proceedings of the London Mathematical Society*, s2-42(1):90–127, January 1937. ISSN 0024-6115, 1460-244X. doi: 10.1112/plms/s2-42.1.90. URL http://plms.oxfordjournals.org/content/s2-42/1/90.full.pdf+html?frame=sidebar.

[96] Xiao-Peng Yan, De-Zi Liu, and Hao Wei. Age Problem in Lemaître-Tolman-Bondi Void Models. *Physics Letters B*, 742:149–159, March 2015. ISSN 03702693. doi: 10.1016/j.physletb.2015.01.029. URL http://arxiv.org/abs/1411.6218. arXiv: 1411.6218.

[97] Pengjie Zhang and Albert Stebbins. Confirmation of the Copernican Principle at Gpc radial scale and above from the kinetic Sunyaev-Zel'dovich effect power spectrum. *Physical Review Letters*, 107:041301, July 2011. ISSN 0031-9007. doi: 10.1103/PhysRevLett.107.041301. URL http://adsabs.harvard.edu/abs/2011PhRvL.107d1301Z.

[98] J. P. Zibin. Scalar perturbations on Lemaître-Tolman-Bondi spacetimes. *Physical Review D*, 78: 043504, August 2008. ISSN 0556-2821. doi: 10.1103/PhysRevD.78.043504. URL http://adsabs.harvard.edu/abs/2008PhRvD..78d3504Z.

[99] J. P. Zibin and A. Moss. Linear kinetic Sunyaev-Zel'dovich effect and void models for acceleration. *Classical and Quantum Gravity*, 28:164005, August 2011. ISSN 0264-9381. doi: 10.1088/0264-9381/28/16/164005. URL http://adsabs.harvard.edu/abs/2011CQGra..28p4005Z.

[100] James P. Zibin, Adam Moss, and Douglas Scott. Can We Avoid Dark Energy? *Physical Review Letters*, 101:251303, December 2008. ISSN 0031-9007. doi: 10.1103/PhysRevLett.101.251303. URL http://adsabs.harvard.edu/abs/2008PhRvL.101y1303Z.

[101] Miguel Zumalacárregui, Juan García-Bellido, and Pilar Ruiz-Lapuente. Tension in the void: cosmic rulers strain inhomogeneous cosmologies. *Journal of Cosmology and Astro-Particle Physics*, 10:009, October 2012. ISSN 1475-7516. doi: 10.1088/1475-7516/2012/10/009. URL http://adsabs.harvard.edu/abs/2012JCAP...10..009Z.